universität wien

MASTERARBEIT / MASTER'S THESIS

Titel der Masterarbeit / Title of the Master's Thesis

„Metabolomics of the leaf nodulated species *Ardisia crenata* Sims (Primulaceae) and *Psychotria kirkii* (Rubiaceae), as well as the suspected to be leaf nodulated species *Dioscorea bulbifera* (Dioscoreaceae) via RP-HPLC-HRESIMS followed by natural product isolation from nodulated *Ardisia crenata* leaf tissue“

verfasst von / submitted by

Florian Schindler BSc

angestrebter akademischer Grad / in partial fulfilment of the requirements for the degree of

Master of Science (MSc)

Wien, 2019 / Vienna 2019

Studienkennzahl lt. Studienblatt / degree programme code as it appears on the student record sheet:	A 066 862
Studienrichtung lt. Studienblatt / degree programme as it appears on the student record sheet:	Masterstudium Chemie UG2002
Betreut von / Supervisor:	Univ.-Prof. Dr. Wolfram Weckwerth

Contents

I.1. Abstract

Leaf nodulation is a very intimate kind of symbiosis, where plants harbour bacterial endophytes inside specialized glandular tissue within their leaves. The symbiosis has been described for the diverse taxa of Primulaceae sensu lato, Rubiaceae and Styracaceae as dicot families and Dioscoraceae as monocot family. The bacterial endosymbionts identified so far, all belong within the order Burkholderiales inside the Betaproteobacteria. While previous work suggested that the bacteria fix atmospheric nitrogen for the plant akin to the root nodule symbiosis, or promote plant growth by synthesizing phytohormones, newer genomic analysis points towards secondary metabolite production as the primary symbiotic function. A consistent extraction method for different tissue types of the species *Ardisia crenata* Sims (Primulaceae), *Dioscorea bulbifera* (Dioscoreaceae) and *Psychotria kirkii* was developed in order to perform a metabolomics analysis of the methanolic plant extracts. Extracts of nodulated and non-nodulated tissues at varying developmental stages were subjected to RP-HPLC-HRESIMS measurement. Peak picking, alignment of *m/z* features and analyte identification on MS 2 level by database matching was performed by the in-house-developed software mzFun. Multivariate statistical analysis in the form of principal component analysis (PCA) and analysis of variance (ANOVA) revealed distinct differences in the metabolic composition of the varied tissue types. These results further point towards secondary metabolite production by the bacterial endophytes. Multiple analytes from both plant and bacterial origin could be identified on MS 2 level by database matching and manual investigation. Natural product isolation was atempted for nodulated tissue of the species *Ardisia crenata* to identify substances that contribute to the different metabolic composition of nodulated and non-nodulated tissues. *Ardisia crenata* belongs to the ethno-botanically used genus *Ardisia* in the family Primulaceae sensu lato, which is rich in biologically active substances with great chemo diversity. Genetic studies of the bacterial endosymbiont revealed the non-ribosomal peptide synthetase (frs) gene cluster. Expression of frs in *Escherichia coli* leads to the synthesis of the cyclic-depsipeptide FR900359, which displays strong and selective inhibition of Gq proteins. This makes it not only a promising drug candidate but also an interesting lead structure for the development of novel pharmaceuticals. Examination of MS data revealed that novel putative derivatives of FR900359 are under the PCA loadings which differentiate the most between nodulated and non-nodulated tissues. The following procedure aimed at isolating these new compounds. A novel depsipeptide candidate was isolated but it degraded before its structure could be elucidated. Other substances which were successfully isolated were catechin, epicatechin and the novel natural product epicatechin-3-hydroxy-2-methyl-propanoate.

I.2. Abstract (Deutsch)

Die Blattknöllchen-Symbiose stellt eine sehr enge Art der Symbiose dar, in der Bakterien spezielle Drüsen im Blatt einer Pflanze besiedeln. Die Symbiose wurde für die diversen Taxa Primulaceae sensu lato, Rubiaceae und Styracaceae, innerhalb der Eudikotyledonen und Dioscoraceae, innerhalb der Monokotyledonen, beschrieben. Sämtliche bis jetzt identifizierte Endophyten gehören zu der Ordnung Burkholderiales innerhalb der Betaproteobacteria. Erste Untersuchungen der Symbiose führten zu Annahmen, dass die Bakterien, ähnlich zur wurzelknollen Symbiose atmosphärischen Stickstoff fixieren, oder das Pflanzenwachstum durch Synthese von Phytohormone fördern. Neuere genomische Untersuchungen deuten jedoch auf die Produktion von Sekundärmetaboliten durch die Bakterien hin. Eine reproduzierbare Extraktionsmethode für unterschiedliche Gewebe der Spezies *Ardisia crenata* Sims (Primulaceae), *Dioscorea bulbifera* (Dioscoreaceae) und *Psychotria kirkii* wurde entwickelt, um eine metabolomische Analyse der methanolischen Pflanzenextrakte durchzuführen. Extrakte von nodulierten und nicht-nodulierten Geweben an unterschiedlichen Entwicklungsstadien wurden mittels RP-HPLC-HRESIMS gemessen. Die Auswahl der Peaks, das „Alignment“ von *m/z* features und die Identifikation der Analyte auf MS 2 Ebene durch Abgleich mit einer Datenbank wurde mithilfe der vorort-entwickelten Sofware mzFun durchgeführt. Eine multivariate statistische Analyse in Form von einer Hauptkomponentenanalyse (PCA) mit anschliessender Varianzanalyse (ANOVA) ergaben deutliche Unterschiede innerhalb der Metabolitzusammensetzung der unterschiedlichen Gewebe. Diese Ergebnisse verstärken die vorangegangenen Untersuchungen, dass die endophytischen Bakterien an der Produktion von Sekundärmetaboliten beteiligt sind. Diverse Analyte pflanzlichen und bakteriellen Ursprungs konnten mithilfe eines Datenbankabgleichs und durch manuelle Überprüfung auf MS 2 Ebene annotiert werden. Eine Naturstoffisolation aus dem nodulierten Gewebe der Spezies *Ardisia crenata* wurde durchgeführt um Substanzen zu identifizieren, welche zu den Unterschieden zwischen noduliertem und nicht-noduliertem Gewebe beitragen. *Ardisia crenata* gehört zum ethno-botanisch genutztem Genus *Ardisia* innerhalb der Familie Primulaceae sensu lato. Der Genus produziert eine Vielfalt an biologisch-aktiven Substanzen mit hoher chemischer Diversität. Genetische Studien des baktertiellen Endosymbionten wiesen den nicht-ribosomalen Peptidsythetase (frs) Gencluster nach. Die Expression dieses Genclusters in *Escherichia coli* führte zur Sythese des zyklischen Depsipeptids FR900359, welches starke und selektive Inhibition von Gq-Proteinen zeigt. Diese Eigenschaft macht FR900359 nicht nur zu einem potentiellen pharmakologischen Wirkstoff, sondern auch zu einer interessanten Leitstruktur zur Entwicklung neuer Medikamente. Die Analyse der MS-Daten deutet darauf hin, dass unbekannte vermutliche Derivate von FR900359 unter den „PCA-loadings“ sind, welche am meisten zwischen noduliertem und nicht-noduliertem Gewebe unterscheiden. Im folgenden Verfahren wurde versucht diese Substanzen zu isolieren. Ein neues vermutliches Depsipeptid konnte isoliert werden, jedoch dürfte sich die Substanz zersetzt haben, bevor ihre Struktur aufgeklärt werden konnte. Des Weiteren konnten die Substanzen Catechin, Epicatechin und die erstmalsbeschriebene Substanz Epicatechin-3-hydroxy-2-methyl-propanoate erfolgreich isoliert werden.

II. Introduction

Plants have been used for their natural products since time immemorial. Although already suspected, it was discovered, that certain previously from plant sources isolated natural products are actually produced by plant associated microbes. Therefore, plant associated microorganisms and microorganisms living in symbiosis with plants should be thoroughly investigated as source for novel biologically active natural products (Ludwig-Müller, 2015).

A very intimate kind of symbiosis between plant and bacteria is the leaf nodule endosymbiosis. The plants harbor their endosymbionts in specialized glandular tissue inside their leaves (HORNER JR and LERSTEN, 1972). Leaf nodule symbiosis has been reported in various genera of the three dicot families Primulaceae (*Amblyanthopsis*, *Amblyanthus*, and *Ardisia*) Rubiaceae (*Pavetta*, *Psychotria*, and *Sericanthe*) and Styracaceae (*Styrax*), as well as in the monocot family Dioscoreaceae (Dioscorea). So far around 530 nodulated species have been reported. The identified bacterial endophytes all belong to the order Burkholderiales within the Betaproteobacteria (Yang and Hu, 2018). Most endosymbionts have undergone evolutionary genome reduction as result of this symbiosis to an extend that they are no longer capable of freely living outside their host (Carlier et al., 2016; Carlier and Eberl, 2012). Interestingly, most host plants are also no longer capable of surviving without their endosymbionts. When the symbiotic bacteria are removed the plants lose vigor and subsequently die off. Because of this codependence of host and endosymbiont, the bacteria are transmitted vertically between host generations by infecting the developing ovule of the host (Pinto-Carbó et al., 2018).

At first nitrogen fixation and synthesis of phytohormones by the endosymbiont were reported (Becking, 1971; Silver et al., 1963). Newer results, however, point towards secondary metabolite production as the primary benefit of the symbiosis. Great potential as pharmaceutical lead structures can already be seen in the substances FR900359 and kirkamide isolated from the leaf nodulated plant species *A. crenata* and *P. kirkii* respectively (Crüsemann et al., 2018; Sieber et al., 2015).

Despite the enormous diversity and vast number of unique metabolic capabilities of bacteria, only few genera have been exploited for their natural products. Bacteria harbor great potential as a source for new bioactive and antibiotic substances. The non-ribosomal peptide synthetase (NRPS), polyketide synthase (PKS) and NRPS/PKS hybrid metabolic pathways account for a lot of biologically active substances with great chemo diversity (Challinor and Bode, 2015). Putative NRPS and PKS gene clusters have already been reported for *Candidatus Burkholderia crenata*, the endosymbiont of *A. crenata* (Carlier et al., 2016). With increasing antibiotic resistance of pathogens, the need for novel antibiotics arises. Most isolated bioactive and antibiotic compounds from bacterial origin so far, were isolated from environmental (soil, marine) bacteria or bacteria that are commensals or pathogens. Recently bacteria living in symbiosis with insects and nematodes have been investigated as source for novel bioactive natural products with promising results (Challinor and Bode, 2015).

Considering the metabolic capabilities of both, plants and bacteria suggests, that leaf nodulated plants might be a great resource for novel biologically active natural products. Potentially even substances produced in tandem by both symbiotic partners could be discovered. The vast number of antimicrobial and biologically active compounds produced by bacteria could suggest that by harboring symbiotic bacterial endosymbionts the plant could get access to their metabolic capabilities. This could lead to an expansion of the plants immune system against pathogens, as well as a general increase in defensive compounds against herbivory.

The following procedure aimed to investigate the metabolic differences of leaf tissue with and without bacterial endosymbionts at different developmental stages. The plant species investigated were the leaf nodulated species *Ardisia crenata* (Primulaceae) and *Psychotria kirkii* (Rubiaceae), as well as the suspected to be leaf nodulated species *Dioscorea bulbifera* (Dioscoreaceae) (Figure 1, Figure 2, Figure 3 and Figure 4).

Figure 1. Different development stages of *A. crenata* leaves. From left to right: young, old, very old. The endosymbiont harbouring glands can be seen on the leaf margins.

Figure 2. Different development stages of *D. bulbifera* leaves. From left to right: young, old. Note that the picture was taken after the experiment, therefore the colour of the young leaf has already changed from purple to green. The possibly endosymbiont harbouring glands can be seen on the leaf acumen.

Figure 3. Different development stages of *P. kirkii* leaves. From left to right: young, old. The endosymbiont harbouring glands can be seen distributed over the leaf.

Figure 4. Different development stages of *P. kirkii* leaves. From left to right: young, old. (Underside). The endosymbiont harbouring glands can be seen distributed over the leaf.

A. crenata is an evergreen shrub native to East Asia, which is cultivated for medicinal and ornamental purposes (Kitajima et al., 2006; Kobayashi and de Mejía, 2005).
P. kirkii is an understory shrub distributed through the subtropical regions of continental Africa and Madagascar (Carlier and Eberl, 2012). The plant was found to contain the cardiotoxic substance pavettamine, which is suspected to be the causing agent of gousiekte, a fatal poisoning of ruminants (Van Elst et al., 2013).
D. sansibarensis is a vine with its habitat being the tropical rainforest of West Africa (Miller and Reporter, 1987). Its bulbils are used in fishing for their ichthyotoxic constituents (Neuwinger, 2004).
D. bulbifera is a yam native to the subtropical and tropical regions of Africa and Asia. While the plant is widely cultivated as a crop in tropical regions, its wild form is considered poisonous because of the presence of alkaloids, oxalates and saponines (Ogbuagu, 2008). The plant is also used in traditional Chinese medicine (Li et al., 2015). Despite *D. bulbifera* not being recorded as leaf nodulated, the species was still chosen in the following experiment because of its prominent glandular structure on the leaf acumen. The leaf tip appears in stark physiological contrast compared to the rest of the leaf. Therefore, the presence of endosymbionts was considered as a possibility for this species.
A metabolomics approach using RP-HPLC-HRESIMS analysis coupled with data exploration using multivariate statistical methods was performed. The results show clear differences in the metabolic composition of the analyzed tissues.
To further investigate the substances responsible for the different metabolic composition of nodulated and non-nodulated tissues, a natural product isolation of *A. crenata* was attempted.
The leaves of *A. crenata* bear specialized structures on their margin containing symbiotic bacteria. Recently the genome of the symbiotic bacterium of *A. crenata*, *Candidatus B. crenata* was sequenced. It is the smallest genome from a species of the genus Burkholderia to date and contains a large amount of insertion sequences and pseudogenes. Such patterns are often found in symbiotic bacteria in comparison with non-symbiotic relatives. Free-living organisms are subjected to a greater variety of environmental parameters and therefore have to allocate a larger proportion of their genome to transcriptional regulators than host-restricted symbionts or pathogens (Cases et al., 2003). It was noticed that the genome of *Candidatus B. crenata* does not encode functions commonly associated with plant symbioses such as nitrogen fixation (nitrogenase) or plant hormone metabolism. In comparison to the genes belonging to the core genome of Burkholderiaceae and genes conserved within the endosymbionts of Primulaceae and Rubiaceae, the genome of *Candidatus B. crenata* also contains 24 unique genes. These genes are organized in two clusters localized on two different plasmids and encode for putative enzymes involved in polyketide- and non-ribosomal peptide synthesis. (Carlier et al., 2016). Heterologous expression of the frs gene cluster in *Escherichia coli* leads to the production of FR900359, therefore confirming it as the FR non-ribosomal peptide synthetase gene cluster (Crüsemann et al., 2018).
The cyclic depsipeptide FR900359 was first isolated from *A. crenata* and described in 1988 (Fujioka et al., 1988). FR900359 has the ability to interfere with cell signaling by selectively blocking heterotrimeric guanine nucleotide binding proteins (G proteins) (Crüsemann et al., 2018). Many essential processes in eukaryotic cells are regulated by Gq-mediated signaling pathways (Link and Müller, 2016). Therefore, FR900359 could have value as a pharmaceutical. G proteins are very important for homoeostasis in response to extracellular cues. Since the discovery of the G protein family no pharmacological agent that targets these proteins, is available yet (Schrage et al., 2015). Beside the cyclic depsipeptide YM254890 (Nishimura et al., 2010), FR900359 is the only available compound so far, which interdicts Gq signaling with high selectivity and potency (Schrage et al., 2015).
Besides pharmacological use and better understanding of the physiology of Gq-proteins and Gq-protein coupled receptors (GqPCRs), the ecological function of FR900359 *in planta* is of interest. A previous study showed that kirkamide, a metabolite of the nodule-bearing species *Psychotria kirkii* (Rubiaceae) is toxic to insects, which suggests a protective function against herbivory (Sieber et al., 2015). In a study the effects of FR900359 on mice and bean bug nymphs was tested. The results showed significant decrease in mouse blood pressure and lower survival rates of the nymphs. Toxic effects on insects were likely caused by the high affinity of FR900359 to Gq proteins of various pest insects. These results likewise suggest that FR900359 protects the host plant against herbivores (Crüsemann et al., 2018).

The following procedure aimed to isolate FR900359 and possible derivatives from fresh leaves of *A. crenata* and analyze the purified substances by RP-HPLC-UV, RP-HPLC-HRESIMS and nuclear magnetic resonance spectroscopy (NMR). A novel depsipeptide candidate was isolated but it degraded before its structure could be elucidated. Other substances which were successfully isolated were catechin, epicatechin and the novel natural product epicatechin-3-hydroxy-2-methyl-propanoate.

III. Metabolomics of the leaf nodulated species *Ardisia crenata* Sims (Primulaceae) and *Psychotria kirkii* (Rubiaceae), as well as the suspected to be leaf nodulated species *Dioscorea bulbifera* (Dioscoreaceae) via RP-HPLC-HRESIMS

Metabolomics of the leaf nodulated species *Ardisia crenata* Sims (Primulaceae) and *Psychotria kirkii* (Rubiaceae), as well as the suspected to be leaf nodulated species *Dioscorea bulbifera* (Dioscoreaceae) via RP-HPLC-HRESIMS

ARTICLE INFO

Keywords:
Ardisia crenata
Primulaceae
Dioscorea bulbifera
Dioscoreaceae
Psychotria kirkii
Rubiaceae
Burkholderiales
Depsipeptides
Metabolomics
Leaf nodule symbiosis
mzFun

ABSTRACT

Leaf nodulation is a very intimate kind of symbiosis, where plants harbour bacterial endophytes inside specialized glandular tissue within their leaves. The symbiosis has been described for the diverse taxa of Primulaceae sensu lato, Rubiaceae and Styracaceae as dicot families and Dioscoraceae as monocot family. The bacterial endosymbionts identified so far, all belong within the order Burkholderiales inside the Betaproteobacteria. While previous work suggested that the bacteria fix atmospheric nitrogen for the plant akin to the root nodule symbiosis, or promote plant growth by synthesizing phytohormones, newer genomic analysis points towards secondary metabolite production as the primary symbiotic function. A consistent extraction method for different tissue types of the species *Ardisia crenata* Sims (Primulaceae), *Dioscorea bulbifera* (Dioscoreaceae) and *Psychotria kirkii* was developed in order to perform a metabolomics analysis of the methanolic plant extracts. Extracts of nodulated and non-nodulated tissues at varying developmental stages were subjected to RP-HPLC-HRESIMS measurement. Peak picking, alignment of *m/z* features and analyte annotation on MS 2 level by database matching was performed by the in-house-developed software mzFun. Multivariate statistical analysis in the form of principal component analysis (PCA) and analysis of variance (ANOVA) revealed distinct differences in the metabolic composition of the varied tissue types. These results further point towards secondary metabolite production by the bacterial endophytes. Multiple analytes from both plant and bacterial origin could be annotated on MS 2 level by database matching and manual investigation.

III.1. Introduction

Plants have been used for their natural products since time immemorial. Although already suspected, it was discovered, that certain previously from plant sources isolated natural products are actually produced by plant associated microbes. Therefore, plant associated microorganisms and microorganisms living in symbiosis with plants should be thoroughly investigated as source for novel biologically active natural products (Ludwig-Müller, 2015).

A very intimate kind of symbiosis between plant and bacteria is the leaf nodule endosymbiosis. The plants harbor their endosymbionts in specialized glandular tissue inside their leaves (HORNER JR and LERSTEN, 1972). Leaf nodule symbiosis has been reported in various genera of the three dicot families Primulaceae (*Amblyanthopsis*, *Amblyanthus*, and *Ardisia*) Rubiaceae (*Pavetta*, *Psychotria*, and *Sericanthe*) and Styracaceae (*Styrax*), as well as in the monocot family Dioscoreaceae (*Dioscorea*). So far around 530 nodulated species have been reported. The identified bacterial endophytes all belong to the order Burkholderiales within the Betaproteobacteria (Yang and Hu, 2018). Most endosymbionts have undergone evolutionary genome reduction as result of this symbiosis to an extend that they are no longer capable of freely living outside their host (Carlier et al., 2016; Carlier and Eberl, 2012). Interestingly, most host plants are also no longer capable of surviving without their endosymbionts. When the symbiotic bacteria are removed the plants lose vigor and subsequently die off. Because of this codependence of host and endosymbiont, the bacteria are transmitted vertically between host generations by infecting the developing ovule of the host (Pinto-Carbó et al., 2018).

At first nitrogen fixation and synthesis of phytohormones by the endosymbiont were reported (Becking, 1971; Silver et al., 1963). Newer results, however, point towards secondary metabolite production as the primary benefit of the symbiosis. Great potential as pharmaceutical lead structures can already be seen in the substances FR900359 and kirkamide isolated from the leaf nodulated plant species *A. crenata* and *P. kirkii* respectively (Crüsemann et al., 2018; Sieber et al., 2015).

Despite the enormous diversity and vast number of unique metabolic capabilities of bacteria, only few genera have been exploited for their natural products. Bacteria harbor great potential as a source for new bioactive and antibiotic substances. The non-ribosomal peptide synthetase (NRPS), polyketide synthase (PKS) and NRPS/PKS hybrid metabolic pathways account for a lot of biologically active substances with great chemo diversity (Challinor and Bode, 2015). Putative NRPS and PKS gene clusters have already been reported for *Candidatus Burkholderia crenata*, the endosymbiont of *A. crenata* (Carlier et al., 2016). With increasing antibiotic resistance of pathogens, the need for novel antibiotics arises. Most isolated bioactive and antibiotic compounds from bacterial origin so far, were isolated from environmental (soil, marine) bacteria or bacteria that are commensals or pathogens. Recently bacteria living in symbiosis with insects and nematodes have been investigated as source for novel bioactive natural products with promising results (Challinor and Bode, 2015).

Considering the metabolic capabilities of both, plants and bacteria suggests, that leaf nodulated plants might be a great resource for novel biologically active natural products. Potentially even substances produced in tandem by both symbiotic partners could be discovered. The vast number of antimicrobial and biologically active compounds produced by bacteria could suggest that by harboring symbiotic bacterial endosymbionts the plant could get access to their metabolic capabilities. This could lead to an expansion of the plants immune system against pathogens, as well as a general increase in defensive compounds against herbivory.

The following procedure aimed to investigate the metabolic differences of leaf tissue with and without bacterial endosymbionts at different developmental stages. The plant species investigated were the leaf nodulated species *Ardisia crenata* (Primulaceae) and *Psychotria kirkii* (Rubiaceae), as well as the suspected to be leaf nodulated species *Dioscorea bulbifera* (Dioscoreaceae) (Figure 5, Figure 6, Figure 7 and Figure 8).

Figure 5. Different development stages of *A. crenata* leaves. From left to right: young, old, very old. The endosymbiont harbouring glands can be seen on the leaf margins.

Figure 6. Different development stages of *D. bulbifera* leaves. From left to right: young, old. Note that the picture was taken after the experiment, therefore the colour of the young leaf has already changed from purple to green. The possibly endosymbiont harbouring glands can be seen on the leaf acumen.

Figure 7. Different development stages of *P. kirkii* leaves. From left to right: young, old. The endosymbiont harbouring glands can be seen distributed over the leaf.

Figure 8. Different development stages of *P. kirkii* leaves. From left to right: young, old. (Underside). The endosymbiont harbouring glands can be seen distributed over the leaf.

A. crenata is an evergreen shrub native to East Asia, which is cultivated for medicinal and ornamental purposes (Kitajima et al., 2006; Kobayashi and de Mejía, 2005).

P. kirkii is an understory shrub distributed through the subtropical regions of continental Africa and Madagascar (Carlier and Eberl, 2012). The plant was found to contain the cardiotoxic substance pavettamine, which is suspected to be the causing agent of gousiekte, a fatal poisoning of ruminants (Van Elst et al., 2013).

D. sansibarensis is a vine with its habitat being the tropical rainforest of West Africa (Miller and Reporter, 1987). Its bulbils are used in fishing for their ichthyotoxic constituents (Neuwinger, 2004).

D. bulbifera is a yam native to the subtropical and tropical regions of Africa and Asia. While the plant is widely cultivated as a crop in tropical regions, its wild form is considered poisonous because of the presence of alkaloids, oxalates and saponines (Ogbuagu, 2008). The plant is also used in traditional Chinese medicine (Li et al., 2015). Despite *D. bulbifera* not being recorded as leaf nodulated, the species was still chosen in the following experiment because of its prominent glandular structure on the leaf acumen. The leaf tip appears in stark physiological contrast compared to the rest of the leaf. Therefore, the presence of endosymbionts was considered as a possibility for this species.

A metabolomics approach using RP-HPLC-HRESIMS analysis coupled with data exploration using multivariate statistical methods was performed. The results show clear differences in the metabolic composition of the analyzed tissues.

III.2. Results and discussion

III.2.1. Development and validation of the extraction procedure

To verify if a consistent extraction of methanol soluble metabolites was achieved by the extraction procedure, samples pooled from all tissue types of one species where extracted. Combined samples of *A. crenata*, *D. bulbifera* and *P. kirkii* were extracted. The weights of the dried methanolic extracts was plotted against the weight of the frozen plant material previous to extraction (see: III.4. Experimental, *III.4.3. Development and validation of the extraction procedure*, Figure 29). In the range of extracted plant material tested, a high linear correlation can be observed for all species and samples. This suggests a consistent extraction method was achieved. It can be concluded that not more than 60 mg of frozen plant material should be extracted with this method and that sonication during the extraction increases the extraction efficiency. To minimize the error of the extraction, an amount close to the 60 mg of frozen plant material limit should be extracted.

III.2.2. Extraction of the individual leaf tissue types

Because of the results of the extraction method evaluation, the amount of frozen plant material extracted for the metabolomics experiment was in the range of 29.0 mg to 50.4 mg and showed a similar linear correlation compared to the extracted combined samples. When the extracts were dissolved for the RP-HPLC-HRESIMS analysis, there were still insoluble substances present (likely carotenoids and chlorophylls). This could probably be accounted for the variability of the added standards due to matrix effects.

III.2.3. Principal component analysis (PCA) and analysis of variance (ANOVA) of the RP-HPLC-HRESIMS measurement data

After the RP-HPLC-HRESIMS measurements of the plant tissue extracts (see: III.4. Experimental, *III.4.5. RP-HPLC-HRESIMS analysis*, *III.4.6. Data extraction and analysis*) the initial data output after peak picking and alignment but before manual dataset reduction contained 260325 *m/z* features. A visualization of this highly complex dataset can be seen in the mzFun Heatmap of *m/z* features (Figure 9). After manual dataset reduction the amount of *m/z* features dropped to 6844 for all species and tissue types (2518 for *A. crenata*, 3242 for *D. bulbifera* and 2851 for *P. kirkii*).

The PCA summary of fit graphs displays 2 values. R2 is the percent of variation of the training set, a measure of how well the model fits the data. Q2 is the percent of variation of the training set according to cross validation, it indicates how well the model

predicts new data. Both values are plotted cumulatively (cum) for the principal components (PC) (see: III.7. Appendix, *III.7.1. Appendix A: PCA summary of fit graphs*, Figure 32, Figure 33, Figure 34 and Figure 35). The scores t_n are new variables summarizing the X-variables. The scores are orthogonal to each other. There are as many score vectors as there are components in the model. The tolerance ellipse is based on Hotelling's T2 and observations situated far outside the ellipse are outliers. Scores can be seen as weighted averages of the loadings (p_n). p_n are vectors with one element for each variable. The loadings express the dominating correlation structure of the X matrix. In the PCA a clear clustering of samples belonging to the same species and condition occurs and a distinct separation between the clusters is visible.

The PCA involving all species shows a clear separation between *A. crenata* and *P. kirkii* with *D. bulbifera* in PC1 within a 95 % confidence interval. This result could be attributed for by the different evolutionary development of the taxa of eudicots and monocots. A clear separation between all species can be seen in PC2 (Figure 10, Figure 11). For the ANOVA results (see: III.7. Appendix, *III.7.2. Appendix B: ANOVA graphs*, Figure 36 and Figure 37).

For *A. crenata* the PCA shows a clear separation between the old nodulated and very old nodulated tissues with all other tissue types in PC1 within a 95 % confidence interval. The results for PC2 indicate a gradual differentiation of the tissue types with age of development. It seems that the metabolic variation especially between nodulated and non-nodulated tissues increases most with age (Figure 12, Figure 13). For the ANOVA results (see: III.7. Appendix, *III.7.2. Appendix B: ANOVA graphs*, Figure 38 and Figure 39).

For *D. bulbifera* the PCA shows a clear separation between the leaf acumen tissue types, from here on out described as nodulated, and the leaf tissue types, from here on out described as non-nodulated, in PC1 within a 95 % confidence interval. The results for PC2 show a separation within samples of the same tissue types which most likely indicates statistical noise (Figure 14, Figure 15). For the ANOVA results (see: III.7. Appendix, *III.7.2. Appendix B: ANOVA graphs*, Figure 40 and Figure 41).

For *P. kirkii* the PCA shows a clear separation between the old and young leaf tissue types in PC1 within a 95 % confidence interval. The results for PC2 show a clear separation between nodulated and non-nodulated tissue types within a 95 % confidence interval. This result indicates a gradual differentiation of the tissue types with age, wherein the impact of nodulation on the metabolic makeup seems to be lesser than the state of development by age (Figure 16, Figure 17). For the ANOVA (see: III.7. Appendix, *III.7.2. Appendix B: ANOVA graphs*, Figure 42 and Figure 43).

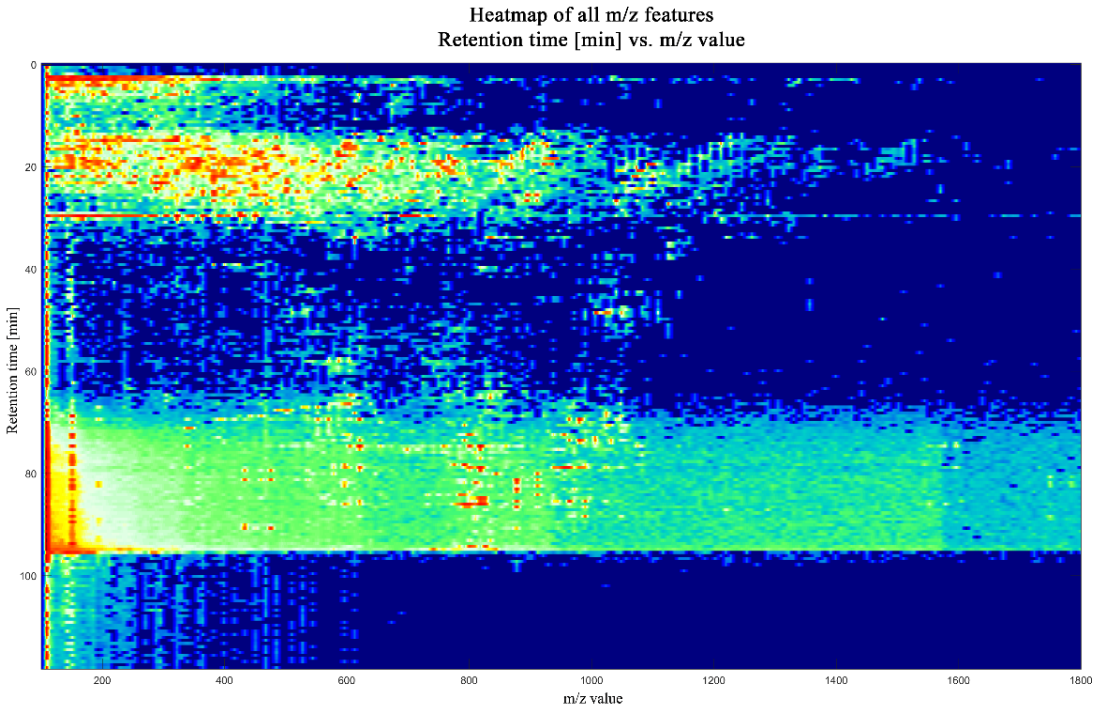

Figure 9. mzFun heatmap of all *m/z* features. Retention time [min] vs. *m/z* value.

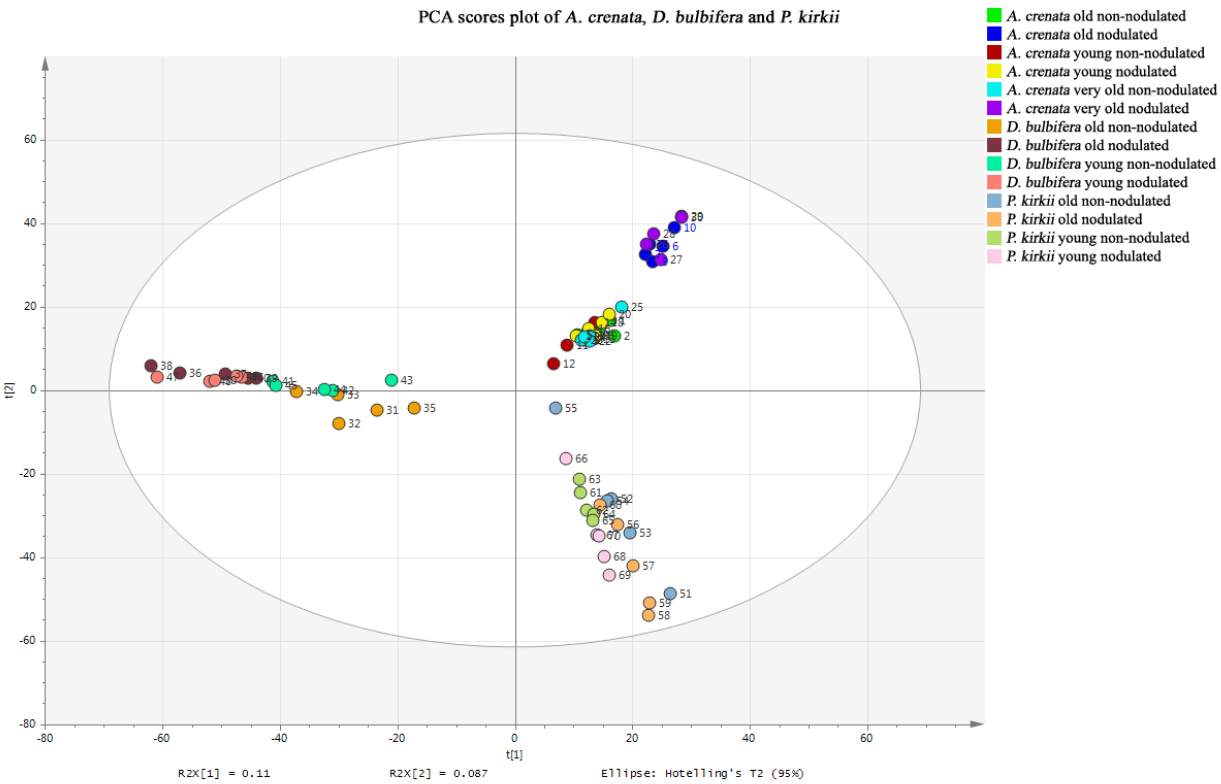

Figure 10. PCA scores plot of *A. crenata* tissues, *D. bulbifera* tissues and *P. kirkii* tissues.

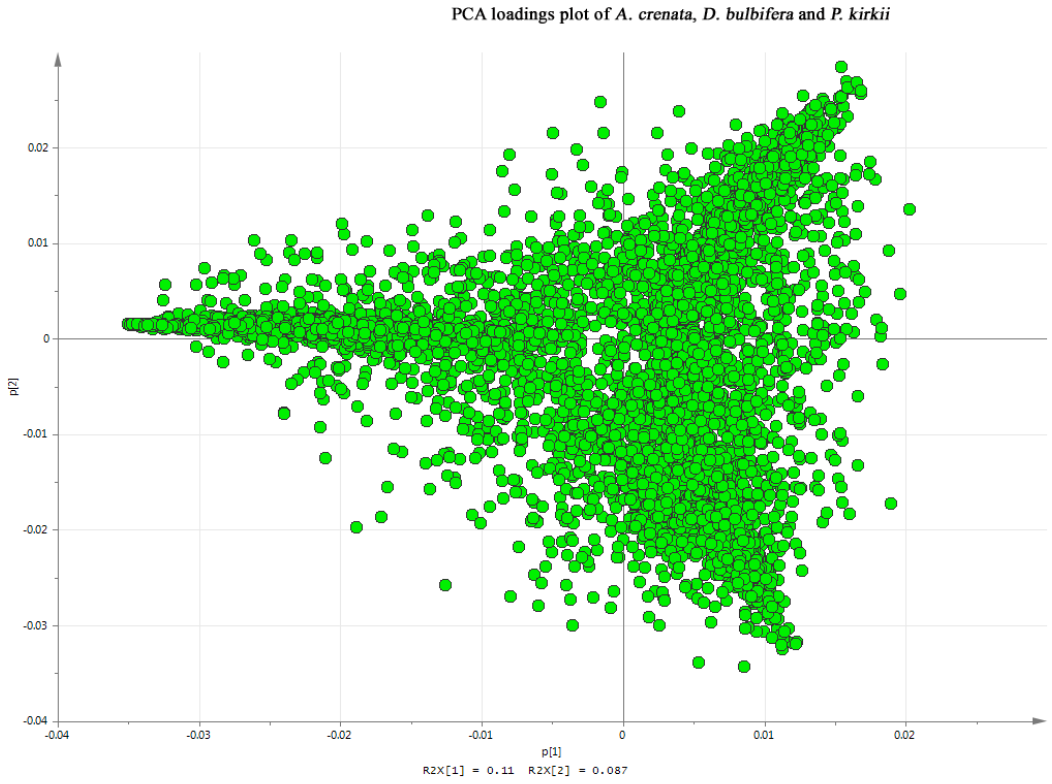

Figure 11. PCA loadings plot of *A. crenata* tissues, *D. bulbifera* tissues and *P. kirkii* tissues.

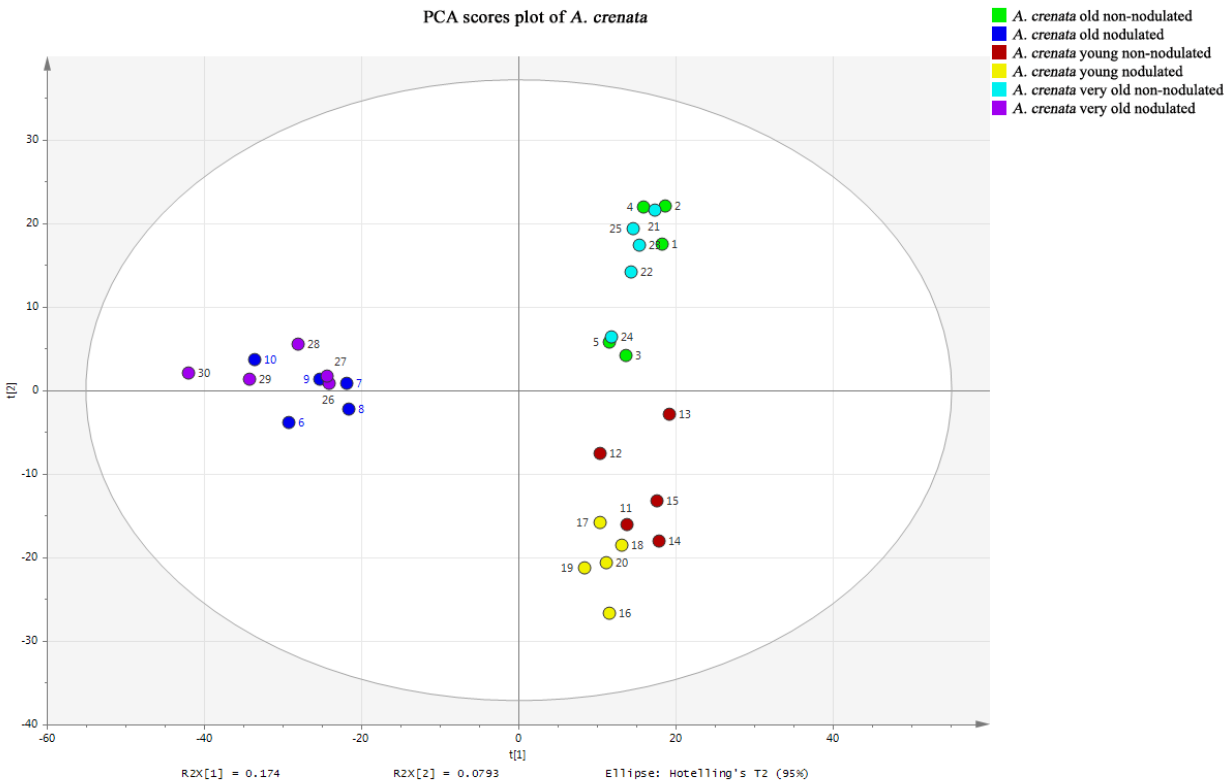

Figure 12. PCA scores plot of *A. crenata* tissues.

Figure 13. PCA loadings plot of *A. crenata* tissues.

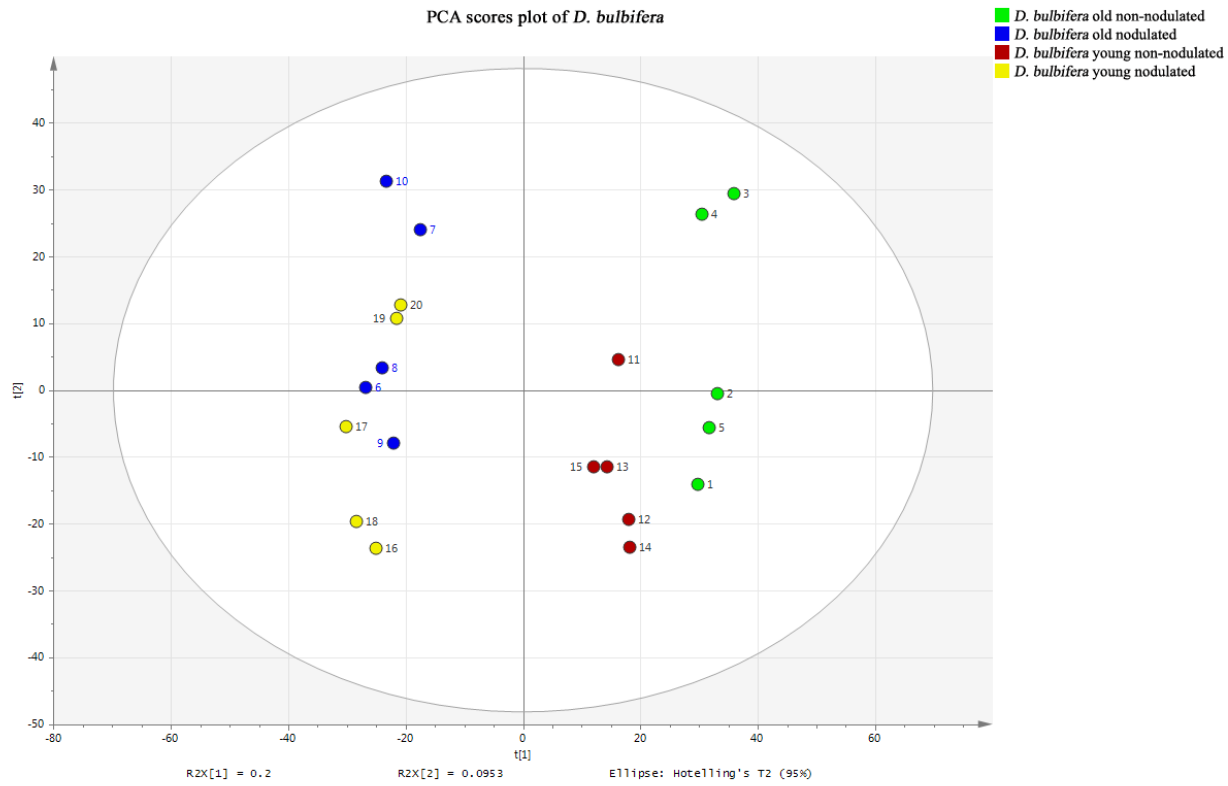

Figure 14. PCA scores plot of *D. bulbifera* tissues.

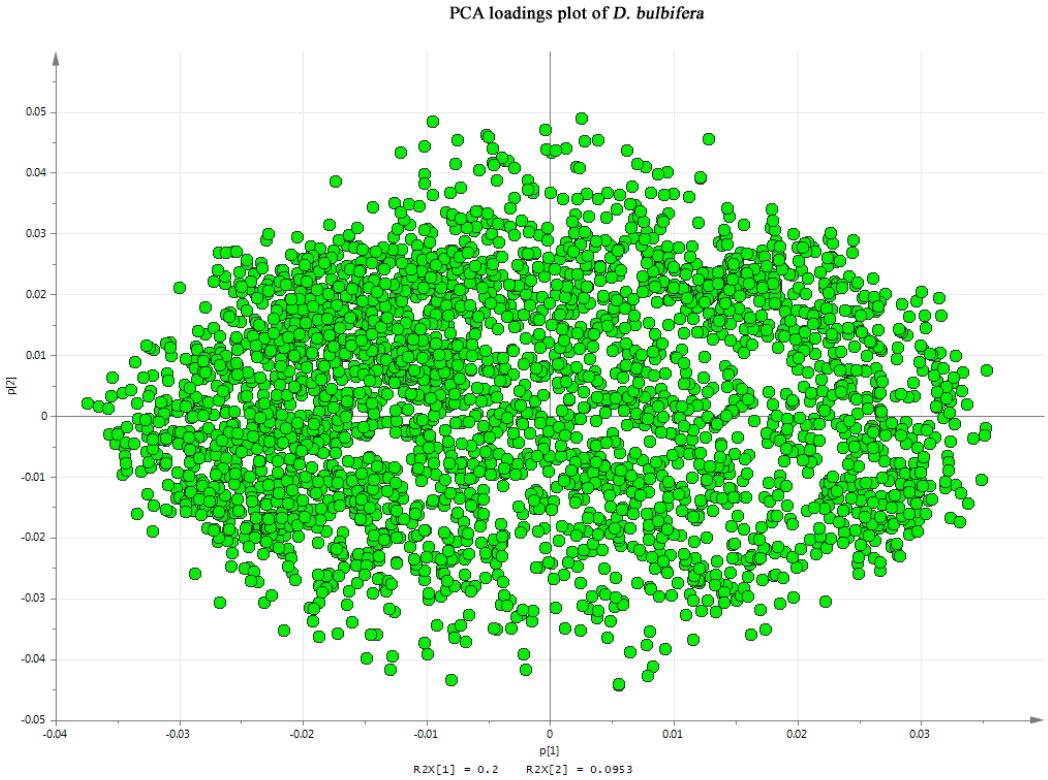

Figure 15. PCA scores plot of *D. bulbifera* tissues.

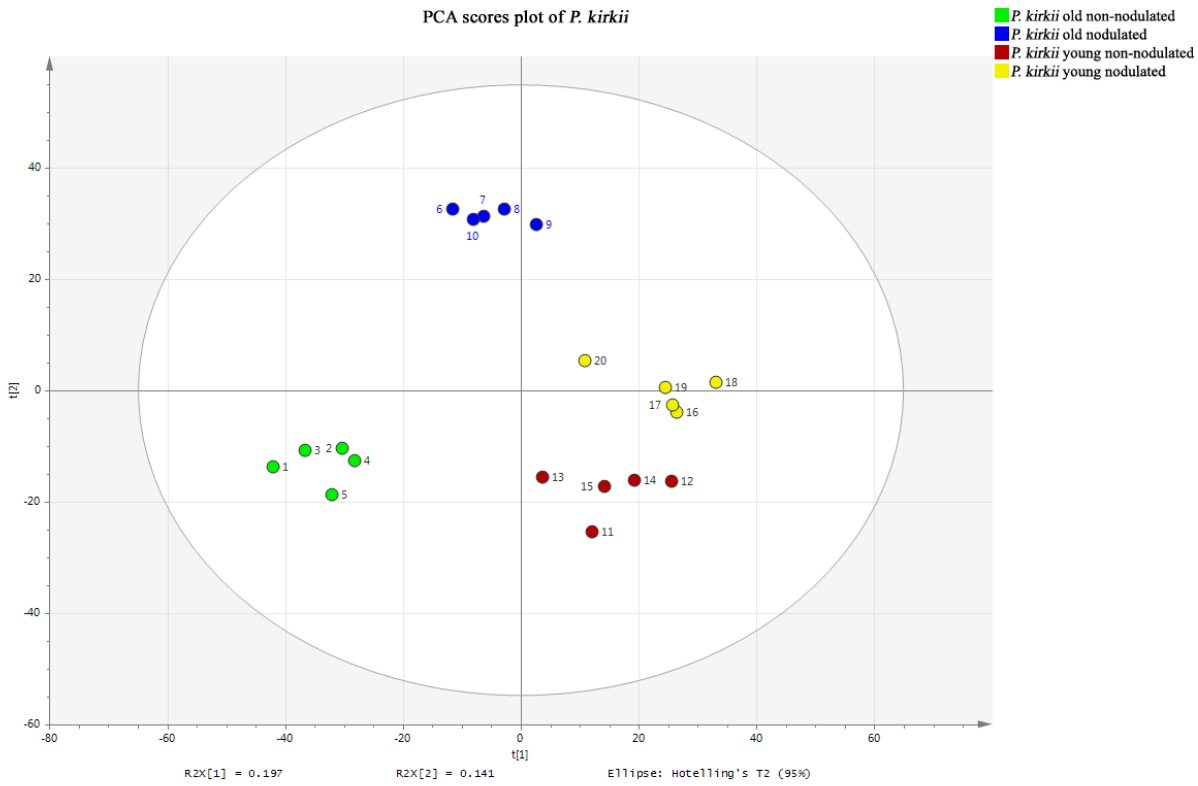

Figure 16. PCA scores plot of *P. kirkii* tissues.

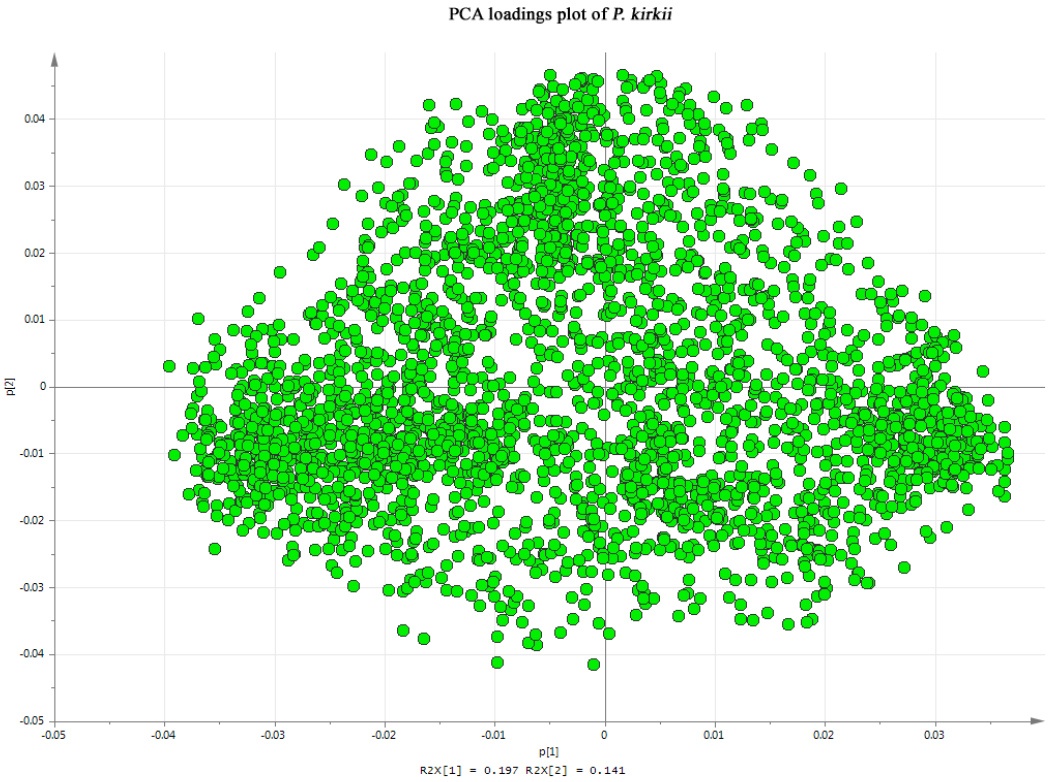

Figure 17. PCA loadings plot of *P. kirkii* tissues.

III.2.4. Targeted analysis of m/z features and annotation based on MS 2 matching with a database

Besides the non-targeted data output, the in-house developed software mzFun is also capable of matching *m/z* features with entries within selected databases. The database used within this experiment consists of locally measured standard compounds. However, the database used for *m/z* feature annotation can be tailored for individual needs. The following results were created by taking the targeted matching results and subjecting them to manual reevaluation (see: III.4. Experimental, *III.4.6. Data extraction and analysis*). The intensity of the signals with the highest score value (best match with reference spectrum) is shown (Table 1). After checking each original RP-HPLC-HRESIMS measurement on MS 1 and MS 2 level and confirmation with an external database only Coniferyl alcohol seemed to have been wrongfully annotated. The corresponding MS spectra are shown in the Appendix (see: III.7.3. Appendix C: MS 1 and MS 2 *spectra of* m/z features annotated by *targeted matching*, Figure 44, Figure 45, Figure 46, Figure 47, Figure 48, Figure 49, Figure 50, Figure 51, Figure 52, Figure 53, Figure 54, Figure 55, Figure 56, Figure 57, Figure 58, Figure 59, Figure 60, Figure 61, Figure 62 and Figure 63).

Table 1
Compounds annotated by subjecting the dataset to matching with a database. The intensity of the signals with highest score value is shown. The number after the tissue type represents the replicate.

Analyte intensity / Samples	Caffeoylquinic acid	Catechin	Coniferyl alcohol	Epicatechin	Naringenin	Quercetin-3-glucoside
A. crenata old non-nodulated 1	-	-	-	-	-	-
A. crenata old non-nodulated 2	-	1055852	-	1055852	-	62687
A. crenata old non-nodulated 3	-	386151	-	386151	-	14416
A. crenata old non-nodulated 4	-	351759	-	351759	-	23082
A. crenata old non-nodulated 5	-	-	-	-	-	-
A. crenata old nodulated 2	-	-	-	-	-	-
A. crenata old nodulated 3	-	-	-	-	-	-
A. crenata old nodulated 4	-	-	-	-	-	-
A. crenata old nodulated 5	-	-	-	-	-	-
A. crenata young non-nodulated 1	-	-	-	-	-	-
A. crenata young non-nodulated 2	-	415910	-	415910	111124	527526
A. crenata young non-nodulated 3	-	507197	-	507197	-	250541
A. crenata young non-nodulated 4	-	-	-	-	-	-
A. crenata young non-nodulated 5	-	-	-	-	-	-
A. crenata young nodulated 1	-	-	-	-	-	-
A. crenata young nodulated 2	-	-	-	-	-	-
A. crenata young nodulated 3	-	-	-	-	-	25290
A. crenata young nodulated 4	-	74659	-	74659	-	54695
A. crenata very old non-nodulated 1	-	1981233	-	1981233	-	72960
A. crenata very old non-nodulated 2	-	475311	-	475311	-	-
A. crenata very old non-nodulated 3	-	2373308	-	2373308	-	17223
A. crenata very old nodulated 1	-	-	-	-	-	-
A. crenata very old nodulated 2	-	336041	-	336041	-	22511
A. crenata very old nodulated 3	-	-	-	-	-	-
A. crenata very old nodulated 4	-	-	-	-	-	-
A. crenata very old nodulated 5	-	-	-	-	-	-
D. bulbifera old non-nodulated 1	2504725	21798	-	21798	-	-
D. bulbifera old non-nodulated 2	753633	48166	-	48166	123921	14134
D. bulbifera old non-nodulated 3	2469368	19847	-	19847	44718	17327
D. bulbifera old non-nodulated 4	41318	18986	-	18986	17995	7256
D. bulbifera old non-nodulated 5	205933	19477	-	19477	112123	21541
D. bulbifera old nodulated 1	1131211	10606229	-	10606229	123237	43674
D. bulbifera old nodulated 2	336736	38422	-	38422	-	-
D. bulbifera old nodulated 3	1033129	2937873	-	343938	-	31669
D. bulbifera old nodulated 4	-	107346	-	107346	-	-
D. bulbifera old nodulated 5	1580375	7704062	-	7704062	15140	25595

D. bulbifera young non-nodulated 1	166087	41428	-	69512	22278	73702
D. bulbifera young non-nodulated 2	943717	31202	-	31202	-	-
D. bulbifera young non-nodulated 3	1119498	4174974	-	59732	-	-
D. bulbifera young non-nodulated 4	866175	62233	-	62233	-	-
D. bulbifera young non-nodulated 5	872203	65683	-	65683	190958	710200
D. bulbifera young nodulated 1	385157	221857	-	221857	-	-
D. bulbifera young nodulated 2	1906759	9150194	-	9150194	18277	33846
D. bulbifera young nodulated 3	979169	23410	-	1062053	-	-
D. bulbifera young nodulated 4	532607	108314	-	108314	27319	-
D. bulbifera young nodulated 5	291434	158499	-	1335799	13666	20259
P. kirkii old non-nodulated 1	4569885	-	74630	-	-	44033
P. kirkii old non-nodulated 2	56058	-	14806	-	-	31810
P. kirkii old non-nodulated 3	-	-	47880	-	-	-
P. kirkii old non-nodulated 4	1305918	-	8846	-	-	26923
P. kirkii old non-nodulated 5	1598893	-	-	-	-	21071
P. kirkii old nodulated 1	673265	-	-	-	-	19263
P. kirkii old nodulated 2	1127079	-	-	-	-	32631
P. kirkii old nodulated 3	3489941	-	-	-	-	-
P. kirkii old nodulated 4	978240	-	-	-	-	32923
P. kirkii old nodulated 5	312208	-	-	-	-	-
P. kirkii young non-nodulated 1	759240	-	-	-	-	32227
P. kirkii young non-nodulated 2	788243	-	-	-	-	32608
P. kirkii young non-nodulated 3	47657	-	-	-	-	27033
P. kirkii young non-nodulated 4	9981	-	-	-	-	35523
P. kirkii young non-nodulated 5	256960	-	-	-	-	46567
P. kirkii young nodulated 1	1128151	-	-	-	-	36260
P. kirkii young nodulated 2	9960	-	-	-	-	20638
P. kirkii young nodulated 3	582033	-	-	-	-	55666
P. kirkii young nodulated 4	314966	-	-	-	-	-
P. kirkii young nodulated 5	765168	-	-	-	-	13405

III.2.5. Manual analysis of PCA loading and interpretation based on MS 2 fragmentation patterns

The *m/z* features of the measured spectra and PCA loadings were analyzed manually to gain further information about the dataset. This led to extra analyte annotation on MS 2 level. Epicatechin-3-hydroxy-2-methyl-propanoate, glutathione (GSH), glutathione disulfide (GSSG), pavettamine, FR900359, AC-1, AC-SC and five putative cyclic-depsipeptides were annotated. The corresponding MS spectra are shown in the Appendix (see: III.7.4. Appendix D: MS 1 and MS 2 spectra *of* m/z features annotated by manual analysis of the untargeted matching and alignment *data*, Figure 64,Figure 65, Figure 66, Figure 67, Figure 68, Figure 69, Figure 70, Figure 71, Figure 72, Figure 73, Figure 74, Figure 75, Figure 76, Figure 77, Figure 78, Figure 79, Figure 80, Figure 81, Figure 82, Figure 83, Figure 84, Figure 85, Figure 86 and Figure 87). It should be noted that for *D. bulbifera* a *m/z* feature corresponding to epicatechin-3-hydroxy-2-methyl-propanoate was also found at the same *m/z* value and rt, however manual analysis of the MS 2 spectra revealed that this is probably a different compound since the spectra differ from the MS 2 spectra from *A. crenata*. In the spectra of nodulated *P. kirkii* tissues three putative peptides were also found. These features have high intensity, but probably due to the spectral count of four (a spectral count of five was set as requirement to include *m/z* features into the output matrix) were not included into the untargeted dataset. The areas of these *m/z* features were integrated using the Quan Browser of the Xcalibur software. The corresponding MS spectra are shown in the Appendix (see: III.7.5. Appendix E: MS 1 and MS 2 spectra of *the* m/z features annotated as putative peptides found in the MS spectra *of P.* kirkii by manual *analysis*, Figure 88, Figure 89, Figure 90, Figure 91, Figure 92, Figure 93, Figure 94, Figure 95 and Figure 96). The area of the *m/z* features corresponding to the *m/z* features was plotted (see: III.7.6. Appendix F: Area of *the* m/z features annotated as putative peptides found in the MS spectra *of P.* kirkii by manual *analysis*, Figure 97, Figure 98 and Figure 99). These *m/z* features occur in all *P. kirkii* tissues but are more intense in the nodulated tissue types. Interestingly these *m/z* features were also found in *A. crenata* tissues where they also show a higher intensity in the nodulated tissue types. The *m/z* feature with the *m/z* value of 476.1871 and rt of 16.26 was annotated as putative peptide but in comparison to the other putative peptides no corresponding doubly protonated molecular ion species was found, therefore, this analyte might not in fact be a peptide.

III.2.6. PCA loadings plots showing the annotated compounds

The *m/z* values and retention times (rt) for the annotated compounds was compiled (

Table 2, Table 3, Table 4 and Table 5). After compound annotation the corresponding *m/z* features were selectively displayed in the original PCA loadings plots (Figure 18, Figure 19, Figure 20, Figure 21, Figure 22, Figure 23, Figure 24 and Figure 25). For *A. crenata* additional loadings plots of selected loadings were created which consider all *m/z* features corresponding to annotated cyclic-depsipeptides and putative cyclic-depsipeptides which also include doubly protonated molecular ions and isotope peaks (see: III.7.7. Appendix G: Selected loadings plots *of A.* crenata of *all m*/z features corresponding to annotated cyclic-depsipeptides and putative cyclic-depsipeptides including doubly protonated molecular ions and isotope *peaks*, Figure 100, Figure 101 and Figure 102). A table of the highest 25 and lowest 25 loadings for PC1 and PC2 for each species was created (see: III.7.8. Appendix H: Table of the highest 25 and lowest 25 PCA loadings for PC1 and PC2 for each *species*, Table 9, Table 10, Table 11, Table 12, Table 13, Table 14, Table 15 and Table 16).

Table 2
Table of the PCA loadings selectively displaying the annotated compounds for *A. crenata*, *D. bulbifera* and *P. kirkii*.

Analyte	Var ID (Primary)	Var ID (Var. Sec. ID:1) *m/z*	Var ID (Var. Sec. ID:2) rt [min]	M1.p[1]	M1.p[2]
putative cyclic-depsipeptide	190	1123.57	31.7596	0.0116579	0.0215277
putative cyclic-depsipeptide	191	1123.57	34.9693	0.0116719	0.0215906
putative cyclic-depsipeptide	192	1123.57	37.3035	0.0117514	0.0217621
AC-1	296	1032.56	44.3804	0.0111998	0.0195191
FR900359	329	1002.55	48.2338	0.0115165	0.0203444
putative cyclic-depsipeptide	343	988.534	45.5147	0.0116475	0.0208153
putative cyclic-depsipeptide	344	988.534	42.2279	0.0107882	0.019038
AC-SC	848	817.443	39.7074	0.00818704	0.0148766
Glutathione disulfide	1637	613.159	5.896	-0.0040231	-0.0258194
putative cyclic-depsipeptide doubly protonated	2019	562.289	35.044	0.0111013	0.0199054
putative cyclic-depsipeptide doubly protonated	2020	562.289	31.7364	0.0101769	0.0177118
putative cyclic-depsipeptide doubly protonated	2021	562.288	37.4817	0.0107313	0.0194068
AC-1 doubly protonated	2291	516.784	44.4802	0.00881098	0.0164171
FR900359 doubly protonated	2379	501.778	48.2881	0.0105952	0.0187161
Quercetin-3-glucoside	2643	465.103	20.706	0.00690446	-0.0113527
Quercetin-3-glucoside	2644	465.103	22.5747	0.0137885	0.0151725
Epicatechin-3-hydroxy-2-methyl-propanoate	3440	377.127	22.0175	0.00298066	0.00722054
Caffeoylquinic acid	3654	355.106	24.444	-0.00812924	0.00411643
Caffeoylquinic acid	3655	355.102	18.347	-0.0126041	-0.00478195
Caffeoylquinic acid	3657	355.102	18.0218	-0.00624361	-0.0247296
Caffeoylquinic acid	3658	355.102	15.9688	-0.000841134	-0.0281148
Glutathione	4236	308.091	3.619	-0.00412849	0.00343146
Glutathione disulfide doubly protonated	4254	307.083	5.7552	-0.00876562	-0.0137743
Glutathione disulfide doubly protonated	4255	307.083	5.8787	0.000939539	-0.0132467
Epicatechin	4449	291.089	19.7438	-0.00510731	0.0061547
Catechin	4450	291.087	18.0868	-0.0324004	0.00567933
Naringenin	4636	273.078	25.711	-0.00247984	0.0117229
Naringenin	4637	273.078	22.2728	0.0154477	0.0284368
Naringenin	4640	273.076	19.2069	-0.0198511	0.00136547
Pavettamine	4830	252.191	2.2785	0.00722433	-0.0176169

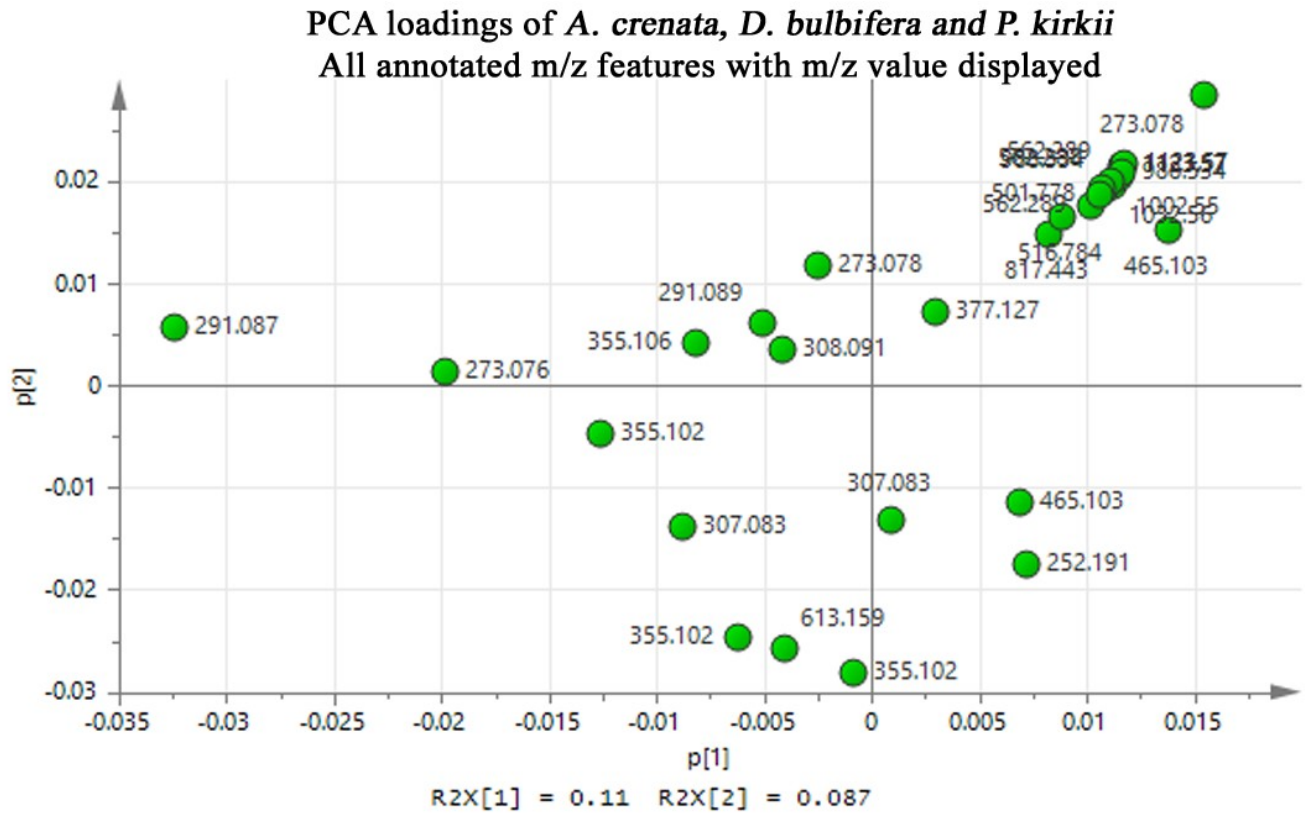

Figure 18. PCA loadings plot of *A. crenata* tissues, *D. bulbifera* tissues and *P. kirkii* tissues selectively displaying the annotated *m/z* features with their *m/z* values.

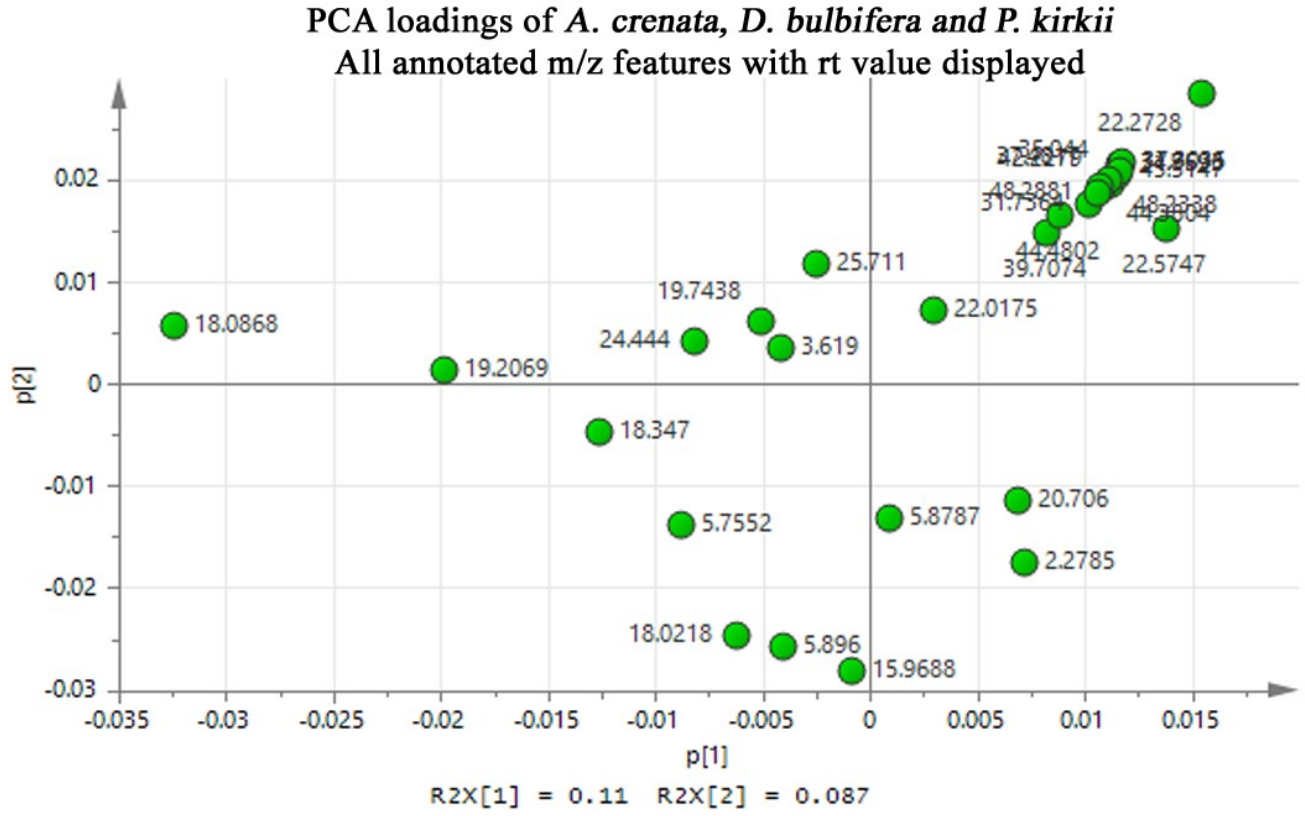

Figure 19. PCA loadings plot of *A. crenata* tissues, *D. bulbifera* tissues and *P. kirkii* tissues selectively displaying the annotated *m/z* features with their rt values.

Table 3
Table of the PCA loadings selectively displaying the annotated compounds for *A. crenata*.

Analyte	Var ID (Primary)	Var ID (Var. Sec. ID:1) *m/z*	Var ID (Var. Sec. ID:2) rt [min]	M1.p[1]	M1.p[2]
putative cyclic-depsipeptide	43	1123.57	31.7596	-0.0396058	0.00383047
putative cyclic-depsipeptide	44	1123.57	34.9693	-0.0402221	0.00282872
putative cyclic-depsipeptide	45	1123.57	37.3035	-0.0405466	0.00321936
AC-1	98	1032.56	44.3804	-0.0343354	-0.00273885
FR900359	115	1002.55	48.2338	-0.0361834	-0.00279426
putative cyclic-depsipeptide	121	988.534	45.5147	-0.0391503	0.00111865
putative cyclic-depsipeptide	122	988.534	42.2279	-0.0350214	-0.00138532
AC-SC	252	817.443	39.7074	-0.0259023	-0.00156194
putative cyclic-depsipeptide doubly protonated	627	562.289	35.044	-0.0348665	0.00186466
putative cyclic-depsipeptide doubly protonated	628	562.289	31.7364	-0.0324994	0.00236805
putative cyclic-depsipeptide doubly protonated	629	562.288	37.4817	-0.0344286	0.00113638
AC-1 doubly protonated	718	516.784	44.4802	-0.0278092	-0.000712842
FR900359 doubly protonated	758	501.778	48.2881	-0.0332297	-0.00201515
Quercetin-3-glucoside	853	465.103	20.706	-0.01552	-0.00339371
Quercetin-3-glucoside	854	465.103	22.5747	-0.000731688	-0.0355407
Epicatechin-3-hydroxy-2-methyl-propanoate	1138	377.127	22.0175	0.00112073	-0.0292754
Glutathione	1480	308.091	3.619	0.00346958	-0.0359243
Epicatechin	1570	291.089	19.7438	0.00769592	0.00408661
Catechin	1571	291.087	18.0868	0.01302	0.035515
Naringenin	1658	273.078	25.711	0.0243808	0.0117753
Naringenin	1659	273.078	22.2728	-0.0271751	-0.00393446

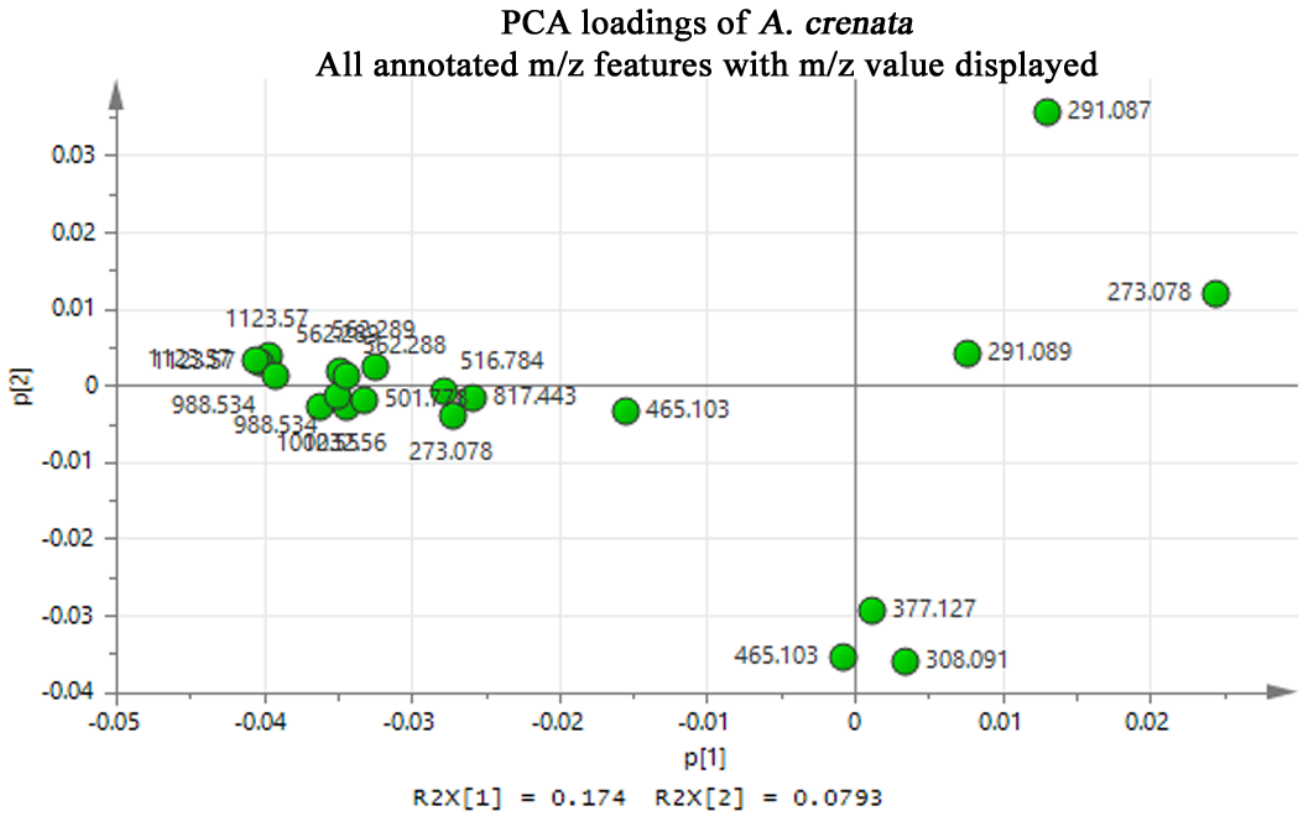

Figure 20. PCA loadings plot of *A. crenata* tissues selectively displaying the annotated *m/z* features with their *m/z* values.

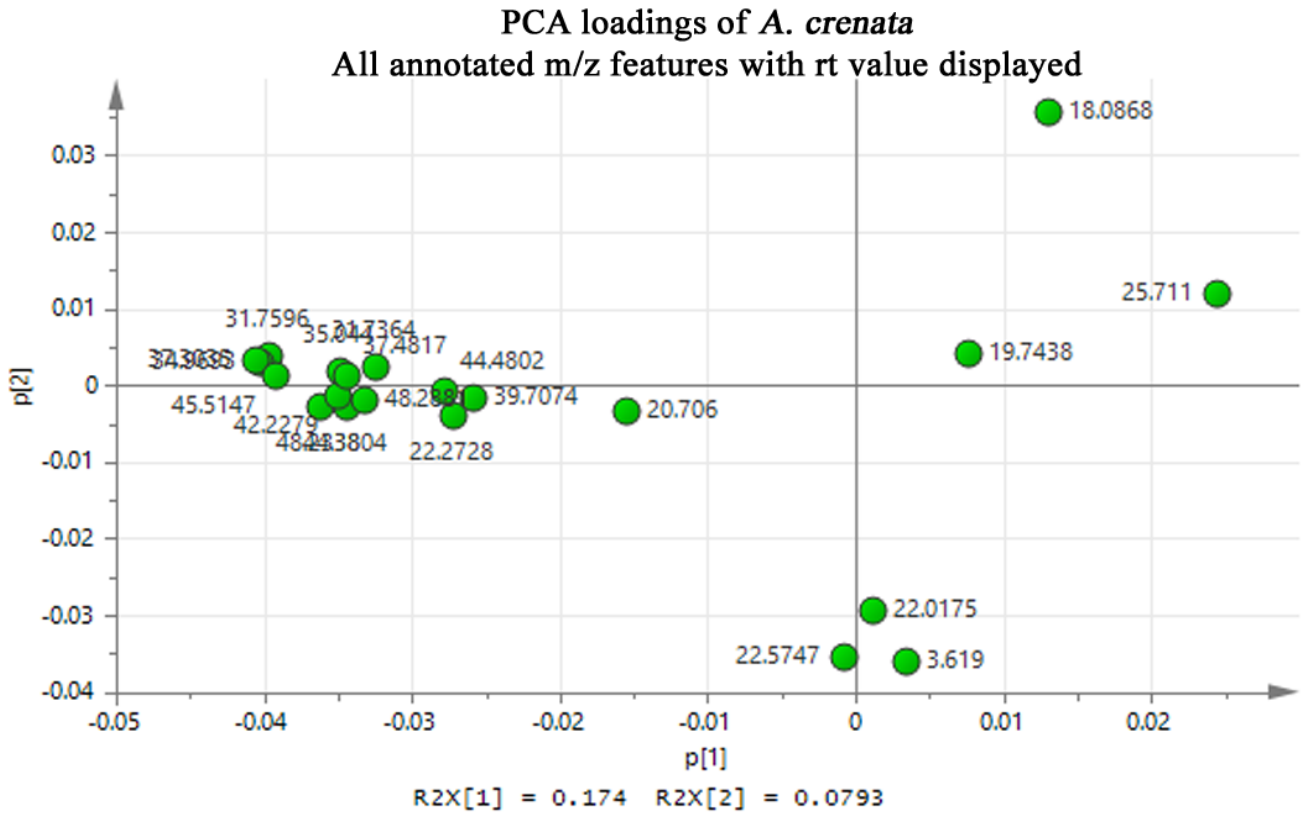

Figure 21. PCA loadings plot of *A. crenata* tissues selectively displaying the annotated *m/z* features with their rt values.

Table 4
Table of the PCA loadings selectively displaying the annotated compounds for *D. bulbifera*

Analyte	Var ID (Primary)	Var ID (Var. Sec. ID:1) *m/z*	Var ID (Var. Sec. ID:2) rt [min]	M1.p[1]	M1.p[2]
Glutathione disulfide	724	613.159	5.896	-0.00702177	-0.0228494
Quercetin-3-glucoside	1122	465.103	20.706	0.00179069	-0.0223299
Quercetin-3-glucoside	1123	465.103	22.5747	0.00852964	0.00200935
Caffeoylquinic acid	1552	355.106	24.444	0.0162707	-0.0359217
Caffeoylquinic acid	1553	355.102	18.347	0.00430866	-0.0188303
Caffeoylquinic acid	1554	355.102	18.0218	0.0265351	0.011404
Caffeoylquinic acid	1555	355.102	15.9688	0.0163835	0.00224175
Glutathione	1823	308.091	3.619	-0.00693221	-0.0235173
Catechin	1927	291.087	18.0868	-0.034285	-0.00431992
Naringenin	2016	273.078	22.2728	0.0184131	0.0264871
Naringenin	2018	273.076	19.2069	-0.0180706	0.00340048

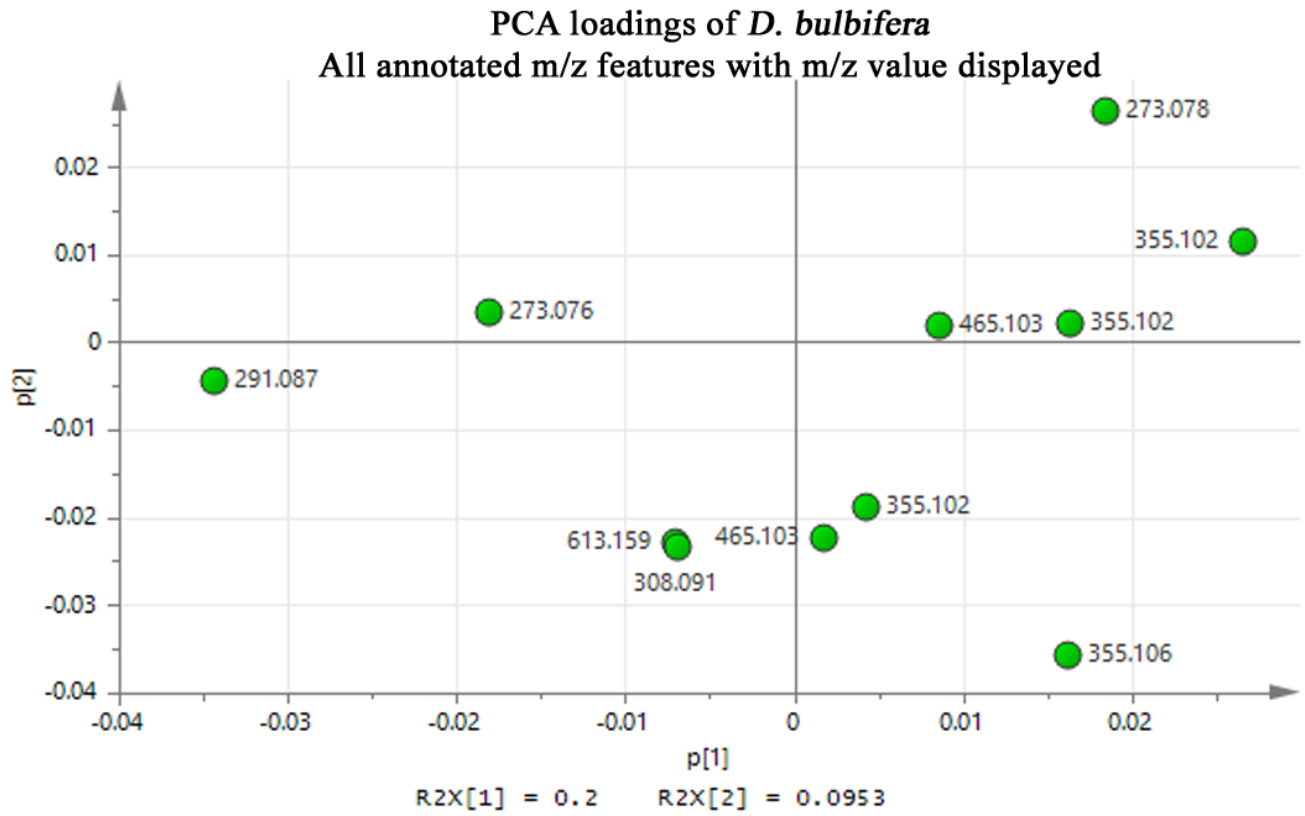

Figure 22. PCA loadings plot of *D. bulbifera* tissues selectively displaying the annotated *m/z* features with their *m/z* values.

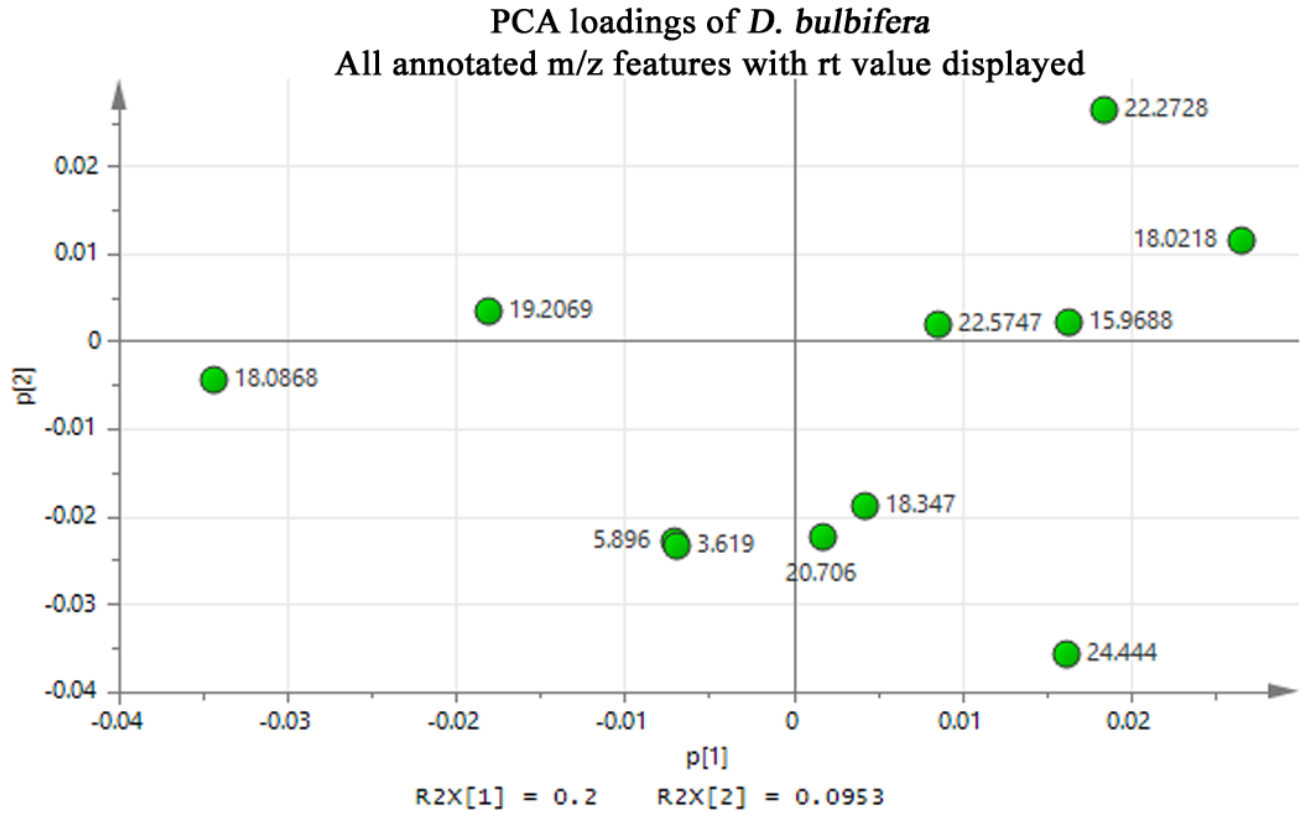

Figure 23. PCA loadings plot of *D. bulbifera* tissues selectively displaying the annotated *m/z* features with their rt values.

Table 5
Table of the PCA loadings selectively displaying the annotated compounds for *P. kirkii*.

Analyte	Var ID (Primary)	Var ID (Var. Sec. ID:1) *m/z*	Var ID (Var. Sec. ID:2) rt [min]	M1.p[1]	M1.p[2]
Glutathione disulfide	680	613.159	5.896	0.00347212	0.0447541
Quercetin-3-glucoside	1180	465.103	20.706	-0.00983083	-0.0129484
Quercetin-3-glucoside	1181	465.103	22.5747	-0.012852	-0.00957134
Caffeoylquinic acid	1575	355.102	18.347	-0.0156831	-0.00699426
Caffeoylquinic acid	1577	355.102	18.0218	-0.0284755	-0.0161331
Caffeoylquinic acid	1578	355.102	15.9688	-0.0364722	-0.0127729
Glutathione	1762	308.091	3.619	-0.0196611	-0.0304643
Pavettamine	1974	252.191	2.2785	-0.0217129	0.00508258

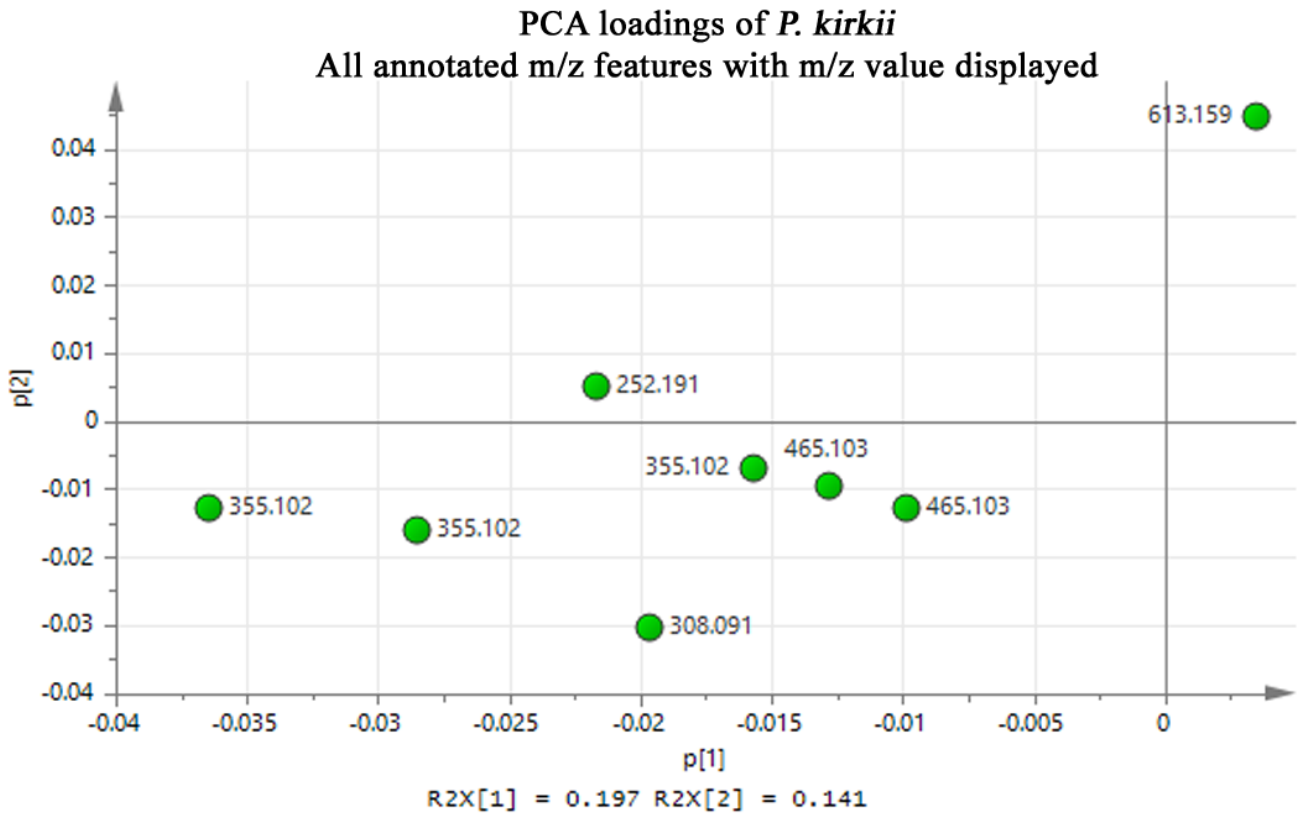

Figure 24. PCA loadings plot of *P. kirkii* tissues selectively displaying the annotated *m/z* features with their *m/z* values.

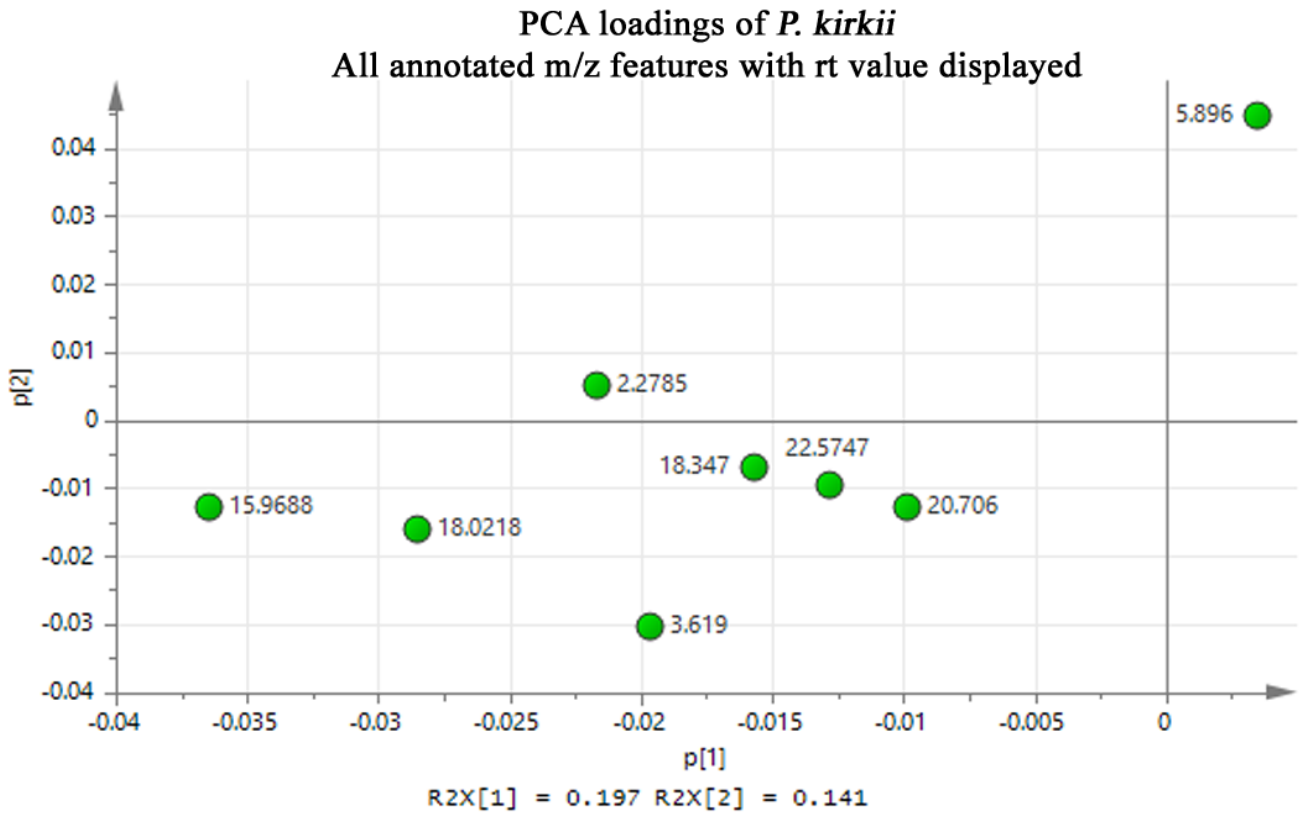

Figure 25. PCA loadings plot of *P. kirkii* tissues selectively displaying the annotated *m/z* features with their rt values.

III.2.7. Ion tree fragmentation measurements

To better understand the MS 2 fragmentation patterns of the cyclic-depsipeptides and cyclic-depsipeptide candidates, the MS 2 spectra of the already structure elucidated cyclic-depsipeptides FR900359, AC-1 and AC-SC are compared (see: III.7.4. Appendix D: MS 1 and MS 2 spectra *of m*/z features annotated by manual analysis of the untargeted matching and alignment *data*, Figure 71, Figure 73 and Figure 75. All cyclic-depsipeptides seem to undergo a ring opening with subsequent CO neutral loss to yield a linear fragment $[M+H-CO]^+$, this is consistent with the fragmentation of cyclic-depsipeptides described in the literature (Paizs and Suhai, 2005). Since the structure of AC-1 differs from FR900359 by a sidechain modification with a $\Delta m/z$ of 30 it was possible to identify which fragments must contain the variable region. Similarly, since AC-SC differs from AC-1 and FR900359 by lacking another sidechain it was possible to identify the fragments containing this variable region as well. These results lead to the creation of a possible fragmentation mechanism for the cyclic-depsipeptides (Figure 26).

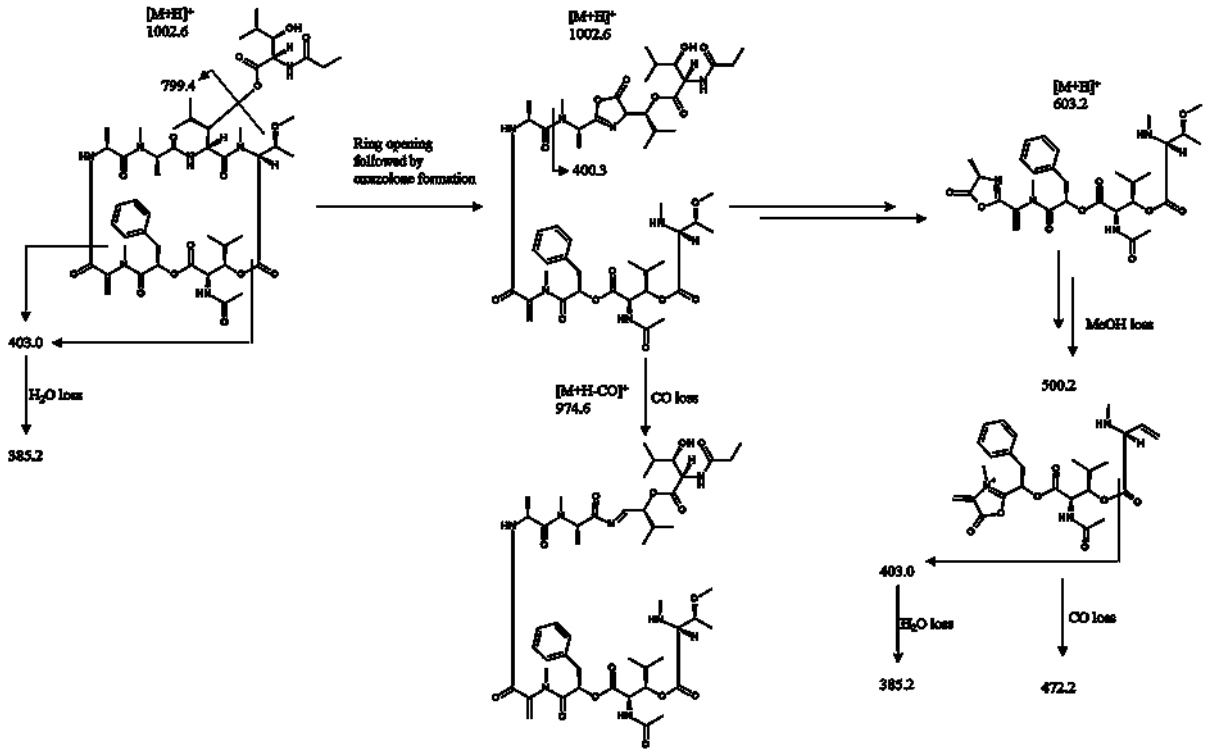

Figure 26. Proposed fragmentation mechanism for FR900359.

Using the derived fragmentation mechanism, it was possible to gather some structural information of the putative cyclic-depsipeptides. All the analytes seem to be derivatives of FR900359. The a putative cyclic-depsipeptides with a *m/z* value of 988.5334 at rt 42.21 min and *m/z* value of 988.5299 at rt 45.72 min seem both to be missing a CH_2 fragment but at different positions. The probable modification sites are illustrated in a figure of FR900359 (Figure 27). These results were also previously found by (Reher et al., 2018). The putative cyclic-depsipeptides with a *m/z* value of 1123.5454 at rt 34.79 min and a *m/z* value of 1123.5459 at rt 37.14 min have very similar fragmentation patterns were mostly only the intensity of different fragments is varying. This suggests that the analytes might be isomers of each other. The Δ*m/z* compared with FR900359 is 121, this indicates that the modification contains an uneven number of nitrogen atoms. The fragmentation pattern also indicates 2 water losses, which indicates the presence of OH groups. The modification likely involves the addition of aminoacids to the core structure of FR900359. The similarity to FR900359 can also be seen by the presence of a fragment with the same mass and fragmentation pattern as FR900359. The probable modification sites are illustrated in a figure of FR900359 (Figure 28). Less information could be gained for the putative cyclic-depsipeptides with a *m/z* value of 1123.5479 at rt 31.75 min, because the low intensity of the parent ion was only sufficient for a MS 2 fragmentation spectrum. The *m/z* feature shares the same Δ*m/z* value of 121 compared to FR900359, which indicates that the modification contains an uneven number of nitrogen atoms. The fragmentation pattern also indicates at least one water loss, which indicates the presence of at least one OH group. Surprisingly the fragment with the same mass and fragmentation pattern as FR900359 seems to be absent. The structure of this *m/z* feature may however still be similar to the *m/z* features with a *m/z* value of 1123.5454 at rt 34.79 min and a *m/z* value of 1123.5459 at rt 37.14 min. To confirm these results a natural product isolation with subsequent structure elucidation by NMR should be attempted. The iontree fragmentation spectra are displayed in the appendix (see: *III.7.9. Appendix I: Spectra of the ion tree fragmentation measurements*, Figure 103, Figure 104, Figure 105, Figure 106, Figure 107, Figure 108, Figure 109, Figure 110, Figure 111, Figure 112, Figure 113, Figure 114, Figure 115, Figure 116, Figure 117, Figure 118, Figure 119, Figure 120, Figure 121, Figure 122, Figure 123, Figure 124, Figure 125, Figure 126, Figure 127, Figure 128, Figure 129, Figure 130, Figure 131, Figure 132, Figure 133, Figure 134, Figure 135, Figure 136, Figure 137, Figure 138, Figure 139, Figure 140, Figure 141, Figure 142, Figure 143, Figure 144, Figure 145, Figure 146 and Figure 147).

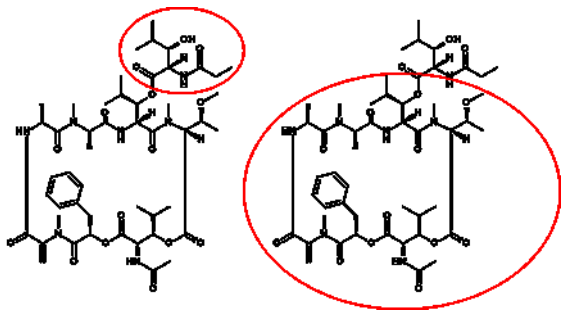

Figure 27. Likely modification sites for the cyclic-depsipeptides with a *m/z* value of 988.5334 at rt 42.21 min (right) and *m/z* value of 988.5299 at rt 45.72 min (left).

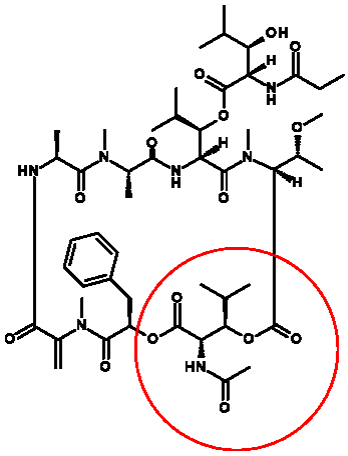

Figure 28. Likely modification sites for the cyclic-depsipeptides with a *m/z* value of 1123.5454 at rt 34.79 min and a *m/z* value of 1123.5459 at rt 37.14 min.

III.3. Conclusion

The results indicate that the metabolite composition of the investigated species differ greatly from each other. This is likely attributed for by the different evolutionary lineages of the species and their variation in natural habitat with resulting characteristic adaptations. A distinct metabolome can be seen for each different tissue type within a species.

For all species the difference in the metabolic composition between tissue types seem to increase with age. This is likely attributed by tissue differentiation and development.

For *A. crenata* and *P. kirkii* the difference in the metabolic composition between nodulated and non-nodulated tissue types seem to increase with age. This effect seems to be stronger pronounced in *A. crenata* compared to *P. kirkii*. For *A. crenata* an additional stage of leaf development was included in the experiment, interestingly the metabolome of these very old tissues seems to be almost identical to the old tissue types. These results indicate that the bacterial endosymbionts start producing secondary metabolites early on in leaf development, but the full capacity of secondary metabolite production is only reached later on in leaf development. For *A crenata* it can also be seen that at a certain stage of leaf development of the secondary metabolome seems to be established and persists probably until leaf senescence.

For *D. bulbifera* the results show a clear difference in the metabolic composition between leaf acumen and leaf lamina tissue types and smaller differences between the leaf lamina tissue types at different leaf developmental stages. Interestingly the metabolome of the leaf acumen tissue types at different leaf developmental stages seem to be almost identical to each other. This indicates that while the leaf lamina tissues seem to differentiate and develop with age, this process probably happens very early on in the development of the leaf acumen tissue. This could be since the leaf acumen is already present at a very early stage of leaf development and the present extrafloral nectaries already start secreting before the main leaf is even present.

Within this experiment 17 compounds could be annotated at various levels of confidence. Caffeoylquinic acid, catechin, epicatechin, naringenin and quercetin-3-glucoside were annotated based on the targeted matching of the in-house developed software mzFun using a database of locally measured standard compounds. These results were confirmed by manual reevaluation of the MS spectra and comparison with an external database (mzCloud). Catechin, epicatechin and epicatechin-3-hydroxy-2-methyl-propanoate could later be isolated from *A. crenata* leaves and their structure was elucidated by NMR (see: IV. Isolation of natural products from nodulated *Ardisia crenata* Sims (Primulaceae) leaf tissue, *IV.7.2. Appendix B: NMR data of the isolated natural products*, Table 23, Table 24 and Table 25; IV.7.3. Appendix C: NMR spectra of the isolated natural *products*, Figure 198, Figure 199, Figure 200, Figure 201, Figure 202, Figure 203, Figure 204, Figure 205, Figure 206, Figure 207, Figure 208, Figure 209, Figure 210, Figure 211, Figure 212, Figure 213, Figure 214, Figure 215, Figure 216, Figure 217 and Figure 218).

Glutathione and glutathione disulfide were confirmed by manual reevaluation of the MS spectra and comparison with an external database (mzCloud). The compounds annotated as cyclic-depsipeptides and pavettamine were confirmed by manual reevaluation of the MS spectra unfortunately comparison with an external database wasn't possible due to the lack of MS spectra measured with similar MS settings.

For *A. crenata* the compounds annotated as cyclic-depsipeptides seem to be characteristic for developed nodulated tissue while catechin and epicatechin seem to be characteristic for developed non-nodulated tissue. The compounds annotated as epicatechin-3-hydroxy-2-methyl-propanoate, glutathione and quercetin-3-glucoside seem to be characteristic for tissues still in development. Interestingly a *m/z* feature annotated as quercetin-3-glucoside also seems to be characteristic for the developed nodulated tissues.

This could indicate that the cyclic-depsipeptides are either produced at a high rate within the developed nodules and/or lack a transporter or diffuse slowly through the leaf tissue. Glutathione within the developing tissue could be responsible for coping with oxidative stress while epicatechin-3-hydroxy-2-methyl-propanoate might be a signaling-compound for the interaction between plant and bacteria.

For *D. bulbifera* the compounds annotated as catechin, glutathione, glutathione disulfide and one of the *m/z* features annotated as naringenin seem to be characteristic for the leaf acumen tissue types, while the compounds annotated as caffeoylquinic acid, one of the *m/z* features annotated as naringenin and quercetin-3-glucoside seem to be characteristic for the leaf lamina tissue types. This could indicate that the bacterial endosymbionts require glutathione to cope with increased oxidative stress within the leaf or that glutathione and glutathione disulfide are enriched by the increased number of bacterial cells within the tissue. The flavonoids present might be used for signaling between plant and bacteria.

For *P. kirkii* the compound annotated as glutathione disulfide seems to be characteristic for the old nodulated tissue, while the compounds annotated as caffeoylquinic acid, glutathione, pavettamine and quercetin-3-glucoside seem to be characteristic for the old non-nodulated tissue. This could indicate that the bacterial endosymbionts cope with increased oxidative stress within the developed leaf by oxidation of glutathione, while pavettamine either diffuses or is transported from the nodulated tissue into the surrounding non-nodulated tissue.

Since the full capacity of secondary metabolite production by the bacterial endosymbionts is only reached at a later developmental stage it would be interesting if the potency of the produced substances is high enough to already deter herbivory at the lower concentrations found in younger leaves or if at this stage other compounds can be found that fulfill a similar role.

It seems that leaf-nodulated plants contain a vast amount of different secondary metabolites within their endosymbiont harboring glands. Most of these substances are probably not yet characterized. Natural product isolation and structure elucidation by NMR could help to further increase the insight into this kind of symbiosis. Especially the potential secondary metabolites

produced by the bacteria through the PKS pathway could be a potential target for further research.

Although 17 compounds could be annotated within this experiment still thousands of unknowns remain. It is likely that some of these *m/z* features were already characterized and are present in other databases. Therefore, even more compounds could probably be annotated by using these resources. Although other databases for secondary metabolites are established the lack of a universal LC-MS based metabolomics protocol still remains as great bottleneck for the technique. This indicates that although steadily improving there is still great room for improvement for secondary metabolite analysis using LC-MS techniques coupled with statistical analysis and database matching. Especially the need for laborious and expensive manual reevaluation of the generated data should be reduced by method improvements to make the technique more accurate, reliable and accessible.

III.4. Experimental

In this experiment 4 different conditions of each species, as well as 2 additional conditions for the species *A. crenata* were compared in a metabolomics approach and subjected to multivariate statistical analysis. The conditions were chosen based on the developmental stage of the leaf and whether the leaf tissue was nodulated or not. Five replicates were taken for each condition, additionally nine blanks were also included into the experiment. To account for biological variability, samples from four different individuals of the same species were pooled to create a replicate. The different conditions were old nodulated leaf tissue, old non-nodulated leaf tissue, young nodulated leaf tissue and young non-nodulated leaf tissue. For the species *A. crenata* the two additional conditions were very old nodulated leaf tissue and very old non-nodulated leaf tissue (Figure 5, Figure 6, Figure 7 and Figure 8). All species were cultivated in a climate and light controlled glasshouse.

III.4.1. General experimental procedures

The plant material was collected in Safe-Lock Tubes 2.0 mL EPPENDORF TUBES®. Homogenisation was carried out using a Retsch® mill MM 400. The plant material and reagents were weighed using a sartorius Entris® 224I-1S Max 220 g, d=0.1 mg analytical balance. The metabolites were extracted with Methanol HiPerSolv CHROMANORM Reag. PH. Eur. For HPLC – GRADIENT GRADE – suitable for UPLC/UHPLC instruments VWR CHEMICALS BDH PROLABO® and sonicated in a TRANSSONIC 700/H Elma® ultrasonic bath. Centrifugation was carried out using a HERAEUS FRESCO 21 Centrifuge Thermo SCIENTIFIC. The extract was collected in 2 mL glass vial, Amber 100/PK Agilent Technologies. The extract was dried using a REACTI-VAP III #TS-18826 Evaporation Unit Thermo SCIENTIFIC apparatus supplied with Nitrogen ≥ 99,999 % H2O ≤ 3.0 ppm-mol O2 2.0 ppm-mol CnHm 0.5 ppm-mol. The extract was aliquoted into Safe-Lock Tubes 1.5 mL EPPENDORF TUBES® and dried using a ScanSpeed 40 SCANVAC connected to a CoolSafe SCANVAC and VACUUM PUMP RZ 2.5 vacuubrand®. For the metabolite measurements the extract was dissolved in a mixture of Milli-Q 18.2 MΩcm TC 27.2 °C TOC 3 ppb H_2O supplied by a Millipore Elix 15.0 MΩcm TC 16.8 °C unit, Acetonitrile HiPerSolv CHROMANORM HPLC LC-MS grade VWR CHEMICALS BDH PROLABO® and Formic acid Optima LC/MS containing the standards Ampicillin trihydrate Analytical standard VETRANAL® Fluka®, Chloramphenicol ≥ 98 % (TLC) SIGMA® Life Science and Reserpine R0875-1 G SIGMA® Life Science. RP-HPLC separation was carried out using an Ultimate 3000 XRS Pump system connected to a RS Autosampler, Column Compartment and SR-3000 Solvent Rack DIONEX equipped with a Accucore 150 –C18 10x2.1 mm, 2.5 µm Defender guards pk4 Thermo SCIENTIFIC Guard Column and Accucore Vanquish C18+ Length (mm): 100, I.D. (mm): 2.1, Particle Size (µm): 1.5 Thermo SCIENTIFIC Column. HRESIMS measurements were conducted using a HESI2 ionisation source in positive ion mode connected to a VELOS PRO, leading into an ORBITRAP ELITE Thermo SCIENTIFIC instrument equipped with Xcalibur software Thermo SCIENTIFIC. Xcalibur RAW file conversion to mzXML data format was performed by using MSConvert included in the ProteoWizard 3.0.6585 open-source software. Peak picking, alignment and analyte annotation on MS 2 level, using a standard database, was performed by the in-house developed software mzFun. The PCA was performed by using SIMCA 13.0.3. software by MKS Umetrics AB. The ANOVA was performed by using Statgraphics Centurion XVII.I software by Statpoint Technologies, Inc..

III.4.2. Harvest of the plant material

For *A. crenata* the nodules on the leaf margin were taken as the nodulated leaf tissue and the tissue near the main leaf vein as the non-nodulated leaf tissue. Care was taken not to include too many bigger veins into the samples. For the developmental stages, the first fully unfolded leaves were chosen as the young leaf tissue, the lowest non-senescent leaves on the branches were chosen as the old leaf tissue and the lowest non-senescent leaves on the main stem were chosen as the very old leaf tissue.

For *D. bulbi*fera the glandular tissue on the leaf acumen was taken as the nodulated leaf tissue and a section near the petiole as the non-nodulated leaf tissue. Care was taken not to include too many bigger veins into the samples. For the developmental stages, hand sized unfolded leaves, that were still red in colour, located near the end of the branches, were chosen as the young leaf tissue and non-senescent leaves on the beginning of the branches were chosen as the old leaf tissue.

For *P. kirkii* the dark green nodules on the leaves were taken as the nodulated leaf tissue and a section were the nodules had been removed as the non-nodulated leaf tissue. Care was taken not to include too many bigger veins into the samples. For the developmental stages, the first fully unfolded leaves were chosen as the young leaf tissue and the lowest non-senescent leaves on the branches or main stem were chosen as the old leaf tissue.

In addition, pooled samples of all conditions were collected for each species to be used in method development and method evaluation.

To account for time dependent metabolic variability each species was harvested on a separate day between 9 and 19 o'clock, in which the different conditions were harvested in a pseudo-randomized order. The harvested plant material was put into 2 mL Eppendorf® Safe-Lock Tubes for storage and immediately preserved in liquid nitrogen. The samples were stored at – 80 °C.

III.4.3. Development and validation of the extraction procedure

To verify if a consistent extraction of methanol soluble metabolites was achieved by the extraction procedure, samples pooled from all tissue types of one species where extracted. Combined samples of *A. crenata*, *D. bulbifera* and *P. kirkii* were extracted. The frozen plant material was cooled down to -196 °C with liquid nitrogen. Homogenization was carried out at liquid nitrogen temperature with a mortar and pestle. (At this point the samples can be stored at – 80 °C.) 26.7-111.1 mg of the homogenized plant material at -196 °C was weighed into pre-chilled 2 mL Eppendorf® Safe-Lock Tubes. For the metabolite extraction the samples were placed on ice and 1 mL of ice-cold methanol was added. The samples were vortexed. To increase extraction efficiency, as well as possibly rupturing intact endophytes the samples were sonicated for 20 min at 0 °C. The extraction mixture was vortexed and centrifuged at 14800 rpm (21.1·g) at 4 °C for 4 minutes. The supernatant was transferred

into an amber glass vial and placed under a stream of dry nitrogen for desiccation. 1 mL of ice-cold methanol was added to the pellet and the extraction procedure was carried out again for a total of 4 times. After the last extraction the colour of the supernatant was observed. The extracts were dried until weight consistency was achieved. (The vials containing the dry extracts were sealed by a non-perforated crimp cap and stored at -20 °C.)

The weights of the dried methanolic extracts was plotted against the weight of the frozen plant material previous to extraction (Figure 29). It was observed at how much plant material the supernatant was still colored after the final extraction and how omittance of sonication would affect the result. In the range of extracted plant material tested, a high linear correlation can be observed for all species and samples. This suggests a consistent extraction method was achieved. It should however be noted that the last extract was beginning to be colored green when more than 60 mg of frozen plant material was used. The last supernatant of samples extracted without sonication also were colored slightly green even though less than 60 mg were extracted, and the samples seem to follow the linear trend. This suggests that chlorophyll concentration can be an even more sensitive method for testing the saturation limit of the extraction method, but it would also require additional spectroscopic measurements. The difference in slopes indicates that each species has a different amount of extractable metabolites per freshweight. *A. crenata* yields the highest amount of extractable material, followed by *P. kirkii* and *D. bulbifera* with the lowest amount. The higher ordinate intercepts and lower R^2 values of *P. kirkii* and *D. bulbifera* likely is a result of the lower sample size compared to *A. crenata*. It can be concluded that not more than 60 mg of frozen plant material should be extracted with this method, also in order to minimize the error of the extraction, an amount close to the 60 mg of frozen plant material limit should be extracted.

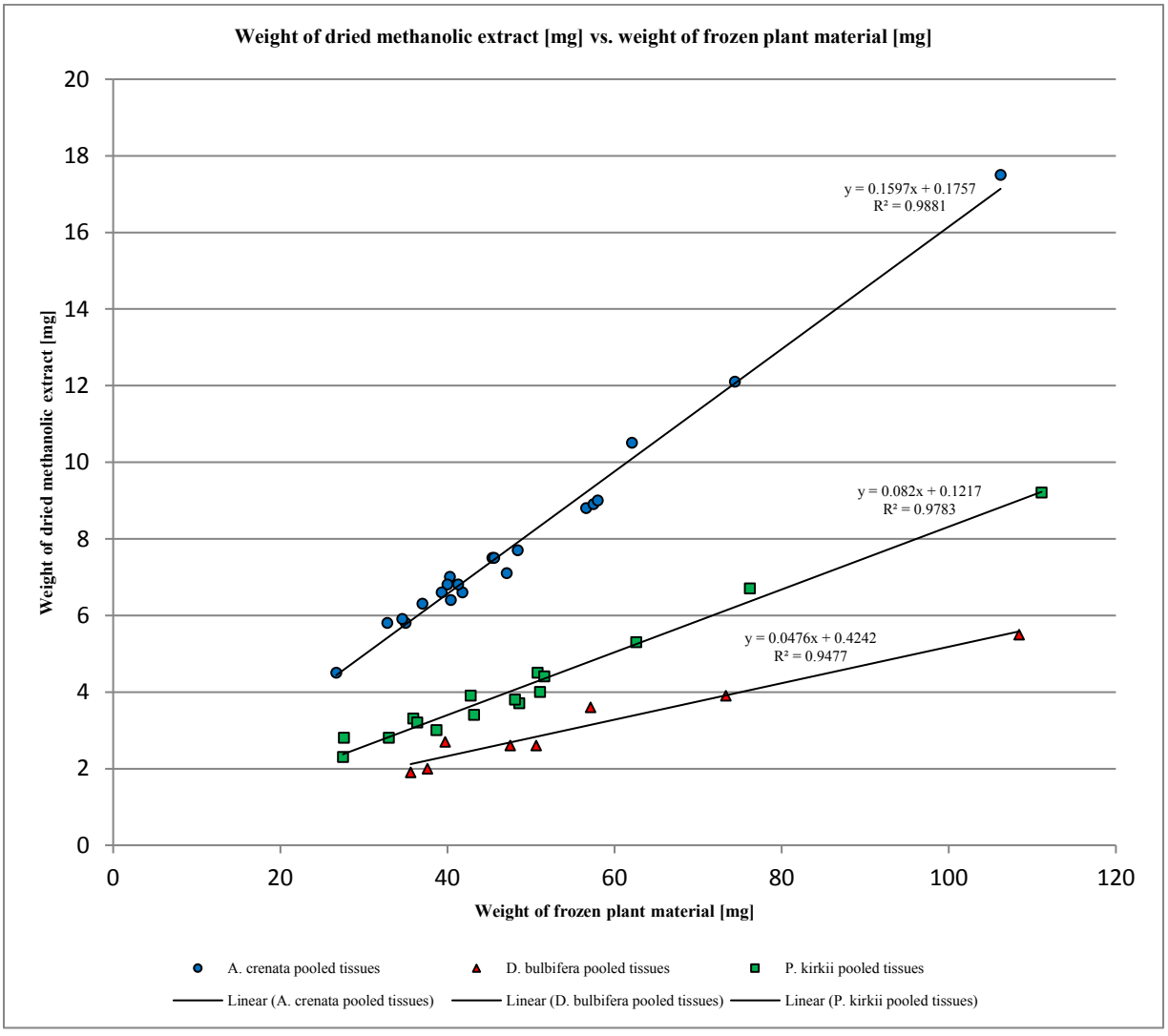

Figure 29. Graph of pool sample extracts, weight of dried methanolic extract [mg] vs. weight of frozen plant material [mg].

III.4.4. Metabolite extraction

The frozen plant material was cooled down to -196 °C with liquid nitrogen. A singular stainless-steel ball bearing, with a diameter of 5 mm, was pre-chilled in liquid nitrogen and added to the samples. Homogenization was carried out at liquid nitrogen temperature with a frequency of 27 Hz for duration of 2 min. The ball bearing was removed with a magnet. (At this point the samples can be stored at – 80 °C.) About 30-50 mg of the homogenized plant material at -196 °C was weighed into pre-chilled 2 mL Eppendorf® Safe-Lock Tubes. For the metabolite extraction the samples were placed on ice and 1 mL of ice-cold methanol was added. The samples were vortexed. To increase extraction efficiency, as well as possibly rupturing intact endophytes the samples were sonicated for 20 min at 0 °C. The extraction mixture was vortexed and centrifuged at 14800 rpm (21.1·g) at 4 °C for 4 minutes. The supernatant was transferred into an amber glass vial and placed under a stream of dry nitrogen for desiccation. 1 mL of ice-cold methanol was added to the pellet and the extraction procedure was carried out again for a total of 4 times. After the last extraction the supernatant was colourless. The extracts were dried until weight consistency was achieved. (The vials containing the dry extracts were sealed by a non-perforated crimp cap and stored at -20 °C.) For aliquotation the extracts were dissolved in 1 mL of ice-cold methanol, transferred into 1.5 mL Eppendorf Tubes® and placed into a vacuum centrifuge. (For one aliquot 450 µL each were transferred into two 1.5 mL Eppendorf Tubes®.) The dried extracts were weighed

III.4.5. RP-HPLC-HRESIMS analysis

. For the RP-HPLC-HRESIMS measurements the plant extracts were dissolved in a concentration of 10 mg/L in a solvent consisting of (98 % H_2O, 2 % ACN) + 0.1 % FA containing the standards ampicillin, chloramphenicol and reserpine each in a concentration of $1 \cdot 10^{-5}$ mol/L. After the solvent was added the samples were vortexed and sonicated to aid solvation. The samples were centrifuged at 14800 rpm (21.1·g) at 4 °C for 10 min. 100 µL of the supernatant were transferred into a glass insert for analysis. The pellet was discarded. The samples were placed into an autosampler at 4 °C. The stationary phase consisted of an Accucore™ Vanquish™ C-18+ UHPLC column (100·2.1 mm; 1.5 µm particle size). The mobile phase system consisted of a mixture of solvent A, an aqueous solution of 0.1 % formic acid (FA) and solvent B, acetonitrile containing 0.1 % FA. A gradient elution method was used for the analysis (Table 6). 10 µL of sample were injected with a flowrate of 0.1 mL/min. A 25 µL loop was used. The column compartment was kept at 30 °C. Between each measurement a column washing step was performed by injecting a solution composed of (99 % H_2O, 1 % ACN) + 0.1 % FA using the following gradient (Table 7).

Table 6
HPLC Gradient used for sample analysis.

Time [min]	Solvent A [%]	Solvent B [%]
0	99	1
5	99	1
60	1	99
89	1	99
110	99	1
120	99	1

Table 7
HPLC Gradient used for column washing.

Time [min]	Solvent A [%]	Solvent B [%]
0	99	1
1	99	1
2	1	99
47	1	99
48	99	1
68	99	1

MS-analysis was performed in positive ion mode using a Velos PRO Iontrap leading into an Orbitrap Elite Instrument. Resolution was set at 120000, a spray voltage of 3.8 kV was used, and the capillary temperature was set at 350 °C. The mass scanning range of the MS 1 fullscan was set at 100-1800 *m/z*. Nitrogen sheath gas and nitrogen auxiliary gas were set at a flow rate of 5 [a.u.] and 0 [a.u.], respectively. Cyclomethicone_N5 was used as lock mass with a *m/z* value of 371.101230. Each MS 1 fullscan was followed up by a maximum of 10 data dependent MS 2 fragmentation spectra, of the most abundant ion species. The time for dynamic exclusion duration of previously measured analytes was set at 30 s. The collision energy for CID was set at 35 eV. To reduce bias from measurement conditions, the samples were measured in sets that contained samples from each species and a blank arranged in a pseudo-randomized order. Before the samples were measured, two measurements, each followed by a column washing step were performed to ensure system equilibrium. A solution composed of (99 % H_2O, 1 % ACN) + 0.1 % FA was injected for all non-sample-type measurements. The standards were measured individually, as well as combined to gain accurate retention times, mass spectra and fragmentation spectra. The pool samples were measured with and without added standards.

III.4.6. Data extraction and analysis

The obtained Xcalibur RAW files where converted to the mzXML data format using MSConvert included in the ProteoWizard 3.0.6585 open-source software. For the conversion mzXML was chosen as the output format with 32 bit as the binary encoding precision. The write index and TPP compatibility boxes were ticked. In the filters section peak picking with Vendor algorithm was chosen for MS level 1-3 (Figure 30). Peak picking, alignment and analyte annotation on MS 1 and MS 2 level, using a standard database, was performed by the in-house developed software mzFun. The minimum peak height was set at 1000 for MS 1 level. The minimum scan number was set at 5 and the signal to noise ratio, which is calculated for each peak by dividing 95 % of the maximum peak height by 5 % of the maximum peak height, was set at 3 for the untargeted searching and alignment. Targeted matching is based on an internal score calculated by mass accuracy on MS 1 level and spectral match on MS 2 level, with the spectral match being weighted more than mass accuracy. The score ranges from 0 to 100 and the desired score threshold was set at 70. The database used within this experiment consists of locally measured standard compounds. However, the database used for *m/z* feature annotation can be tailored for individual needs. Other than these changes, the standard settings were used (Figure 31).

The resulting targeted matching results were subjected to manual reevaluation. The initial data output was reduced by only taking into account *m/z* features which were present in at least 4 out of 5 replicates per condition. Then the MS 1 and MS 2 spectra of the annotated *m/z* features were checked within the original MS spectra and if possible confirmed by comparison with an external database (e.g. mzCloud).

The data matrix obtained for the untargeted matching and alignment was reduced manually. Only features in the rt interval of [1.5 min, 90.0 min] were selected. All features that were only found in less than 4 out of 5 replicates per condition and all features found in 4 or more out of 9 blanks were removed. Missing values were replaced with the lowest area value of the remaining features. Finally, the data matrix was normalized by dividing the area of each feature by the sum of areas of all features of the corresponding measurement.

The obtained dataset was subjected to multivariate statistical analysis (PCA) (ANOVA). The PCA was performed by using SIMCA 13.0.3. software by MKS Umetrics AB. PCA-X was chosen. For the ANOVA the centered and scaled (x, y) coordinates of the PCA scores were taken, the centering was reversed, and the values were normalized to 100. The ANOVA was performed by using Statgraphics Centurion XVII.I software by Statpoint

Technologies, Inc.. A 95 % confidence interval was chosen for the box and whisker plots of the first two principal components.

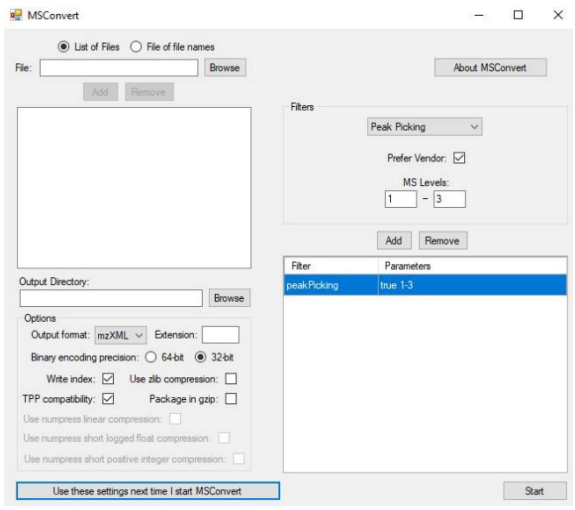

Figure 30. MSConvert settings used to convert Xcalibur .raw files into mzXML format.

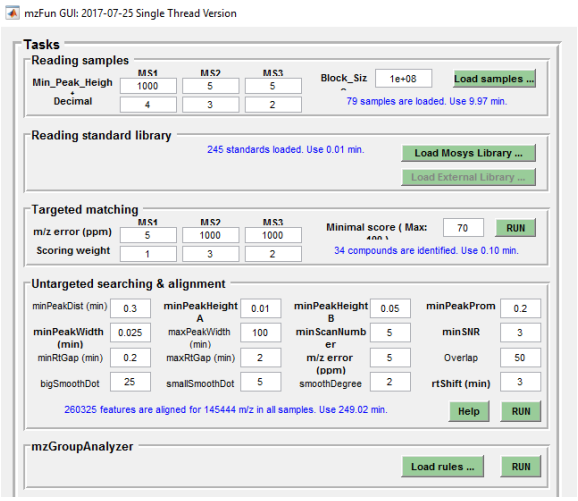

Figure 31. mzFun settings used for peak picking, alignment and analyte annotation on MS 2 level, using a standard database.

III.4.7. Ion tree fragmentation measurements

Ion tree fragmentation measurements were performed in order to gain deeper structural information on some *A. crenata* constituents. The analytes are suspected to be the depsipeptides FR900359, AC-1, as well as further derivatives and novel putative depsipeptide candidates. Since some target analytes had very similar *m/z* values, fragmentation by direct injection was not suitable. Therefore, a method was developed to perform the iontree fragmentation during a HPLC run, since the analytes differed in their retention behavior. The measurements were done with methanolic extracts of combined tissue samples of *A. crenata*. The metabolite extraction procedure was the same as described earlier. For the measurement the plant extracts were dissolved in a concentration of 20 mg/L in a solvent consisting of (98 % H_2O, 2 % ACN) + 0.1 % FA. After the solvent was added the samples were vortexed and sonicated to aid solvation. The sample was centrifuged at 14800 rpm (21.1·g) at 4 °C for 10 min. 100 µL of the supernatant were transferred into a glass insert for analysis. The pellet was discarded. The samples were placed into an autosampler at 4 °C. The stationary phase consisted of an Accucore™ Vanquish™ C-18+ UHPLC column (100·2.1 mm; 1.5 µm particle size). The mobile phase system consisted of a mixture of solvent A, an aqueous solution of 0.1 % formic acid (FA) and solvent B, acetonitrile containing 0.1 % FA. A multistep gradient elution method was used for the analysis (Table 8). 10 µL of sample were injected with a flowrate of 0.1 mL/min. A 25 µL loop was used. The column compartment was kept at 30 °C.

Table 8
HPLC multistep gradient used for sample analysis.

Time [min]	Solvent A [%]	Solvent B [%]
0	99	1
3	99	1
8	60	40
45	1	99
46	99	1
67	99	1

Between each measurement a column washing step was performed by injecting a solution composed of (99 % H_2O, 1 % ACN) + 0.1 % FA using the same multistep gradient used for the measurement. MS-analysis was performed in positive ion mode using a Velos PRO Iontrap Instrument. A spray voltage of 3.8 kV was used, and the capillary temperature was set at 250 °C. The mass scanning range of the MS 1 fullscan was set at 900-1200 *m/z*. Nitrogen sheath gas and nitrogen auxiliary gas were set at a flow rate of 15 [a.u.] and 5 [a.u.], respectively. Each MS 1 fullscan was followed up by data dependent MS 2 fragmentation spectra, of the most abundant ion species. Depth was chosen as the iontree type, with maximum breadth set at 5 and maximum depth set at 4. The minimum MS signal threshold was set at 100 counts. The collision energy for CID was set at 35 eV. Before the samples were measured, two measurements, each followed by a column washing step were performed to ensure system equilibrium. A solution composed of (99 % H_2O, 1 % ACN) + 0.1 % FA was injected for all non-sample-type measurements.

III.5. Acknowledgements

The authors thank Wolfram Weckwerth, head of the Department of Molecular Systems Biology (*mosys*), Lena Fragner (*mosys*) for additional supervision and support. Johannes Herpell (*mosys*) for productive discussions. Further we like to thank Martin Brenner (*mosys*) and Sonja Tischler (*mosys*) for their technical advice with the HPLC and MS instruments. Gert Bachman (*mosys*) for support concerning the statistical evaluation. Finally, special thanks to. Xiaoliang Sun for the development of mzFun and the instruction for the software. We thank the gardeners for caring for the research plants.

III.6. References

Becking, J., 1971. The physiological significance of the leaf nodules of Psychotria. Plant and soil 35, 361-374. https://dx.doi.org/10.1007/BF02661864.

Carlier, A., Fehr, L., Pinto-Carbó, M., Schäberle, T., Reher, R., Dessein, S., König, G., Eberl, L., 2016. The genome analysis of Candidatus Burkholderia crenata reveals that secondary metabolism may be a key function of the Ardisia crenata leaf nodule symbiosis. Environmental microbiology. https://dx.doi.org/10.1111/1462-2920.13184.

Carlier, A. L., Eberl, L., 2012. The eroded genome of a Psychotria leaf symbiont: hypotheses about lifestyle and interactions with its plant host. Environmental microbiology 14, 2757-2769. https://dx.doi.org/10.1111/j.1462-2920.2012.02763.x.

Challinor, V. L., Bode, H. B., 2015. Bioactive natural products from novel microbial sources. Annals of the New York Academy of Sciences 1354, 82-97. https://dx.doi.org/10.1111/nyas.12954.

Crüsemann, M., Reher, R., Schamari, I., Brachmann, A. O., Ohbayashi, T., Kuschak, M., Malfacini, D., Seidinger, A., Pinto-Carbó, M., Richarz, R., 2018. Heterologous Expression, Biosynthetic Studies, and Ecological Function of the Selective Gq-Signaling Inhibitor FR900359. Angewandte Chemie International Edition 57, 836-840. https://dx.doi.org/10.1002/anie.201707996.

HORNER JR, H. T., LERSTEN, N. R., 1972. Nomenclature of bacteria in leaf nodules of the families Myrsinaceae and Rubiaceae. International Journal of Systematic and Evolutionary Microbiology 22, 117-122. https://dx.doi.org/10.1099/00207713-22-2-117.

Kitajima, K., Fox, A. M., Sato, T., Nagamatsu, D., 2006. Cultivar selection prior to introduction may increase invasiveness: evidence from Ardisia crenata. Biological Invasions 8, 1471. https://dx.doi.org/10.1007/s10530-005-5839-9.

Kobayashi, H., de Mejía, E., 2005. The genus Ardisia: a novel source of health-promoting compounds and phytopharmaceuticals. Journal of Ethnopharmacology 96, 347-354. https://dx.doi.org/10.1016/j.jep.2004.09.037.

Li, Y., Gan, L., Li, Y., Deng, L., 2015. The HPLC–MS/MS Method for Determination of Diosbulbin B in the Plasma of Rats Administered with Rhizoma Dioscoreae Bulbiferae Combinations: Application to Comparative Pharmacokinetic Study. Journal of Liquid Chromatography & Related Technologies 38, 847-854. https://dx.doi.org/10.1080/10826076.2014.976711.

Ludwig-Müller, J., 2015. Plants and endophytes: equal partners in secondary metabolite production? Biotechnology letters 37, 1325-1334. https://dx.doi.org/10.1007/s10529-015-1814-4.

Miller, I., Reporter, M., 1987. Bacterial leaf symbiosis in Dioscorea sansibarensis: morphology and ultrastructure of the acuminate leaf glands. Plant, Cell & Environment 10, 413-424. https://dx.doi.org/10.1111/1365-3040.ep11603654.

Neuwinger, H. D., 2004. Plants used for poison fishing in tropical Africa. Toxicon 44, 417-430. https://dx.doi.org/10.1016/j.toxicon.2004.05.014.

Ogbuagu, M., 2008. Nutritive and antinutritive composition of the wild (in-edible) species of Dioscorea bulbifera (Potato Yam) and Dioscorea dumentorum (Bitter Yam). J Food Technol 6, 224-226.

Paizs, B., Suhai, S., 2005. Fragmentation pathways of protonated peptides. Mass spectrometry reviews 24, 508-548. https://dx.doi.org/10.1002/mas.20024.

Pinto-Carbó, M., Gademann, K., Eberl, L., Carlier, A., 2018. Leaf nodule symbiosis: function and transmission of obligate bacterial endophytes. Current opinion in plant biology 44, 23-31. https://dx.doi.org/10.1016/j.pbi.2018.01.001.

Reher, R., Kuschak, M., Heycke, N., Annala, S., Kehraus, S., Dai, H.-F., Müller, C. E., Kostenis, E., König, G. M., Crüsemann, M., 2018. Applying Molecular Networking for the Detection of Natural Sources and Analogues of the Selective Gq Protein Inhibitor FR900359. Journal of natural products 81, 1628-1635. https://dx.doi.org/10.1021/acs.jnatprod.8b00222.

Sieber, S., Carlier, A., Neuburger, M., Grabenweger, G., Eberl, L., Gademann, K., 2015. Isolation and total synthesis of kirkamide, an aminocyclitol from an obligate leaf nodule symbiont. Angewandte Chemie International Edition 54, 7968-7970. https://dx.doi.org/10.1002/anie.201502696.

Silver, W., Centifanto, Y. M., Nicholas, D., 1963. Nitrogen fixation by the leaf-nodule endophyte of Psychotria bacteriophila. Nature 199, 396. https://dx.doi.org/10.1038/199396b0.

Van Elst, D., Nuyens, S., Van Wyk, B., Verstraete, B., Dessein, S., Prinsen, E., 2013. Distribution of the cardiotoxin pavettamine in the coffee family (Rubiaceae) and its significance for gousiekte, a fatal poisoning of ruminants. Plant physiology and biochemistry 67, 15-19. https://dx.doi.org/10.1016/j.plaphy.2013.02.022.

Yang, C.-J., Hu, J.-M., 2018. Bacterial Leaf Nodule Symbiosis in Flowering Plants. Symbiosis. IntechOpen. http://dx.doi.org/10.5772/intechopen.73078.

III.7. Appendix

III.7.1. Appendix A: PCA summary of fit graphs

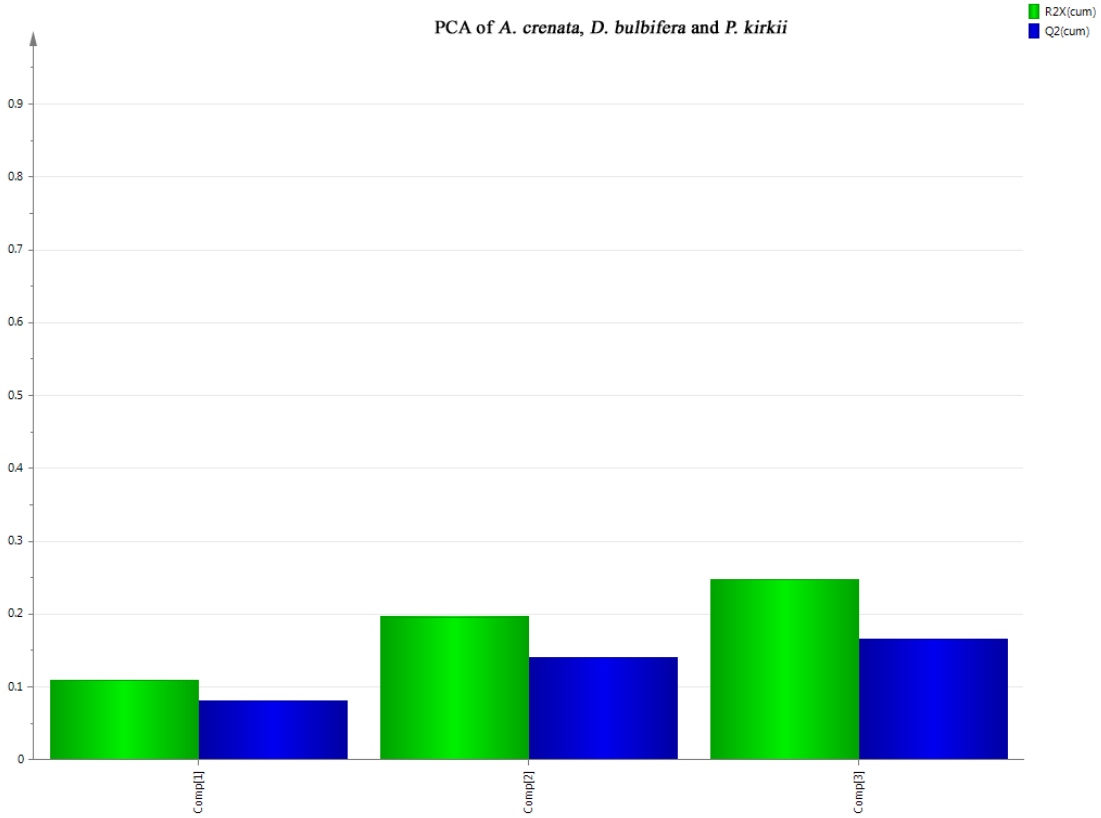

Figure 32. PCA summary of fit plot of *A. crenata* tissues, *D. bulbifera* tissues and *P. kirkii* tissues.

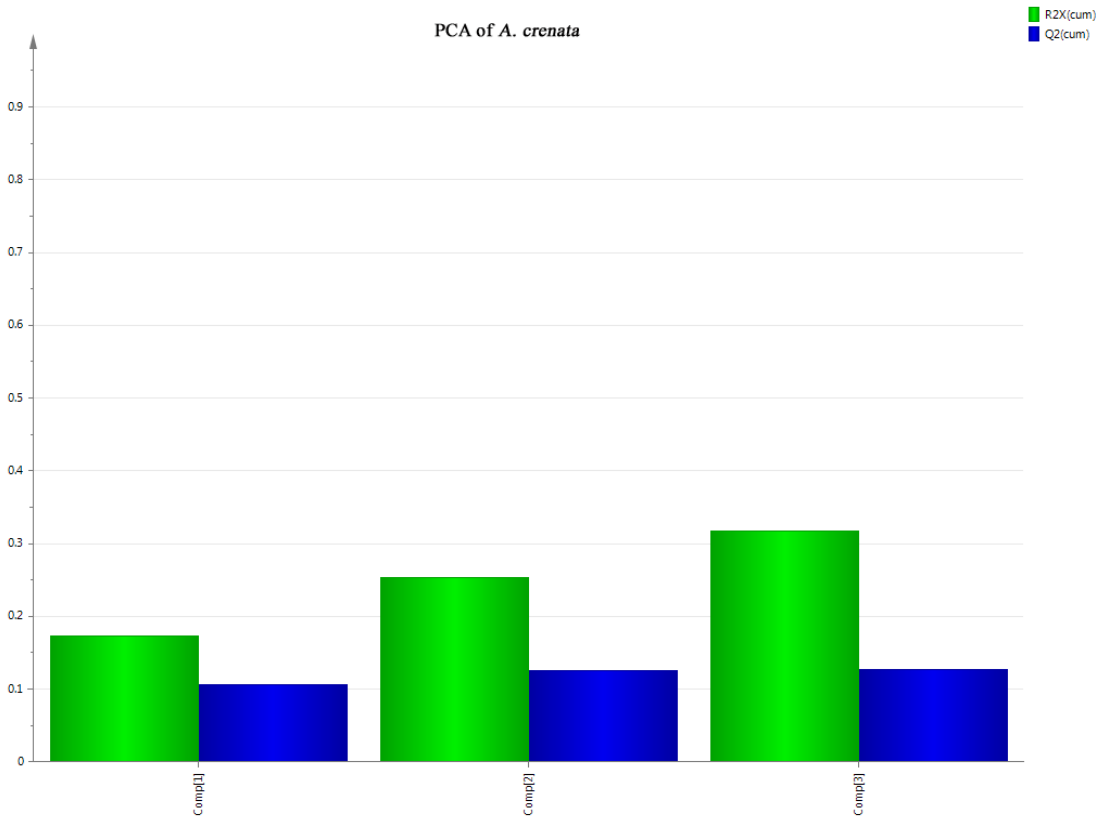

Figure 33. PCA summary of fit plot of *A. crenata* tissues.

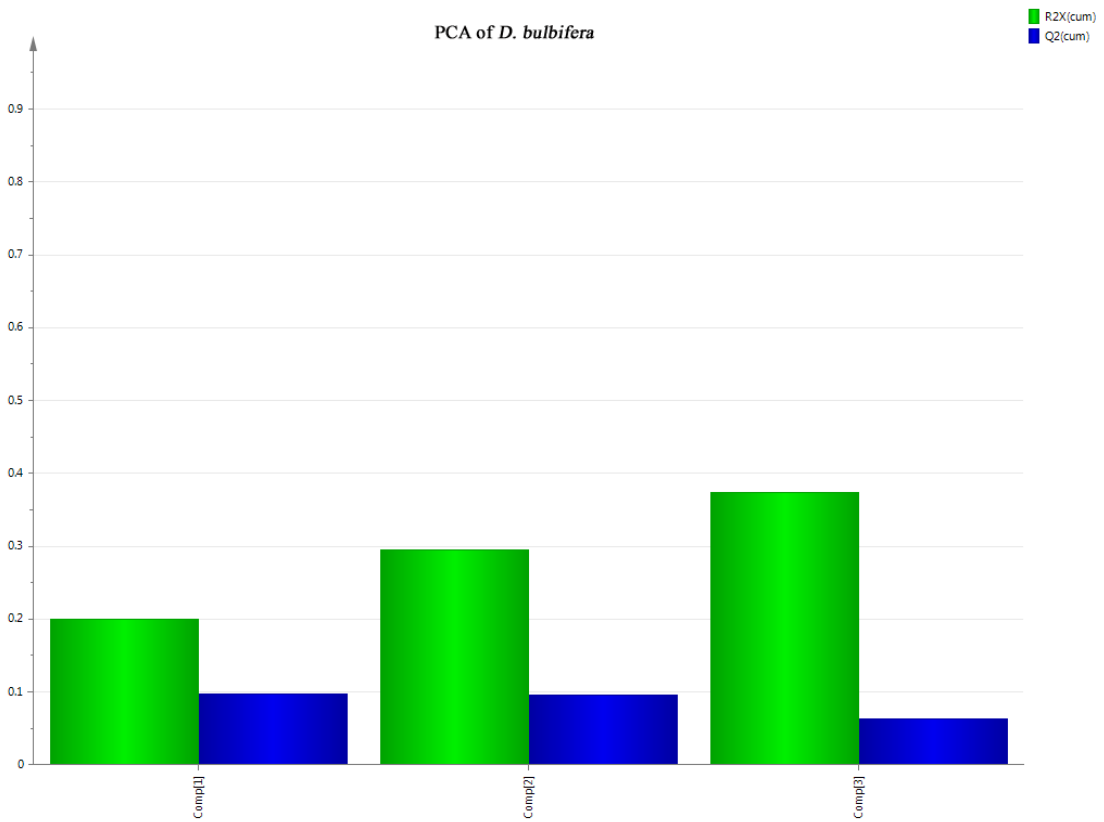

Figure 34. PCA summary of fit plot of *D. bulbifera* tissues.

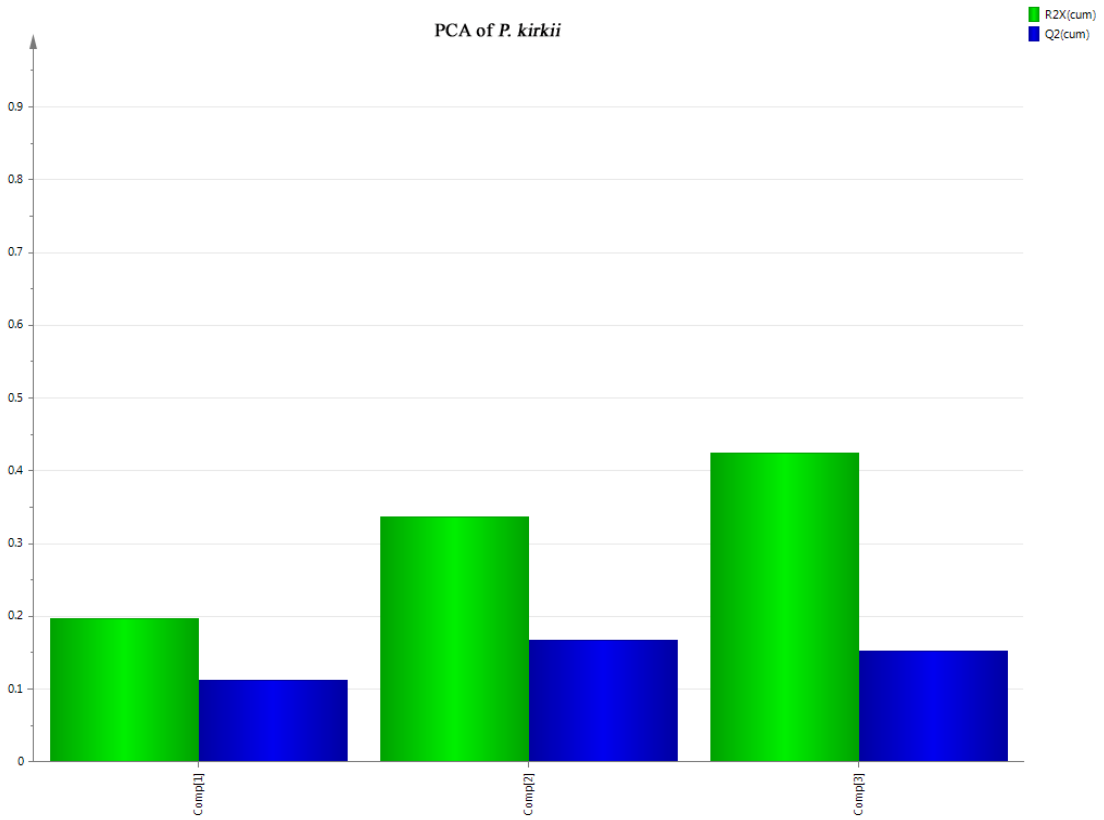

Figure 35. PCA summary of fit plot of *P. kirkii* tissues.

III.7.2. Appendix B: ANOVA graphs

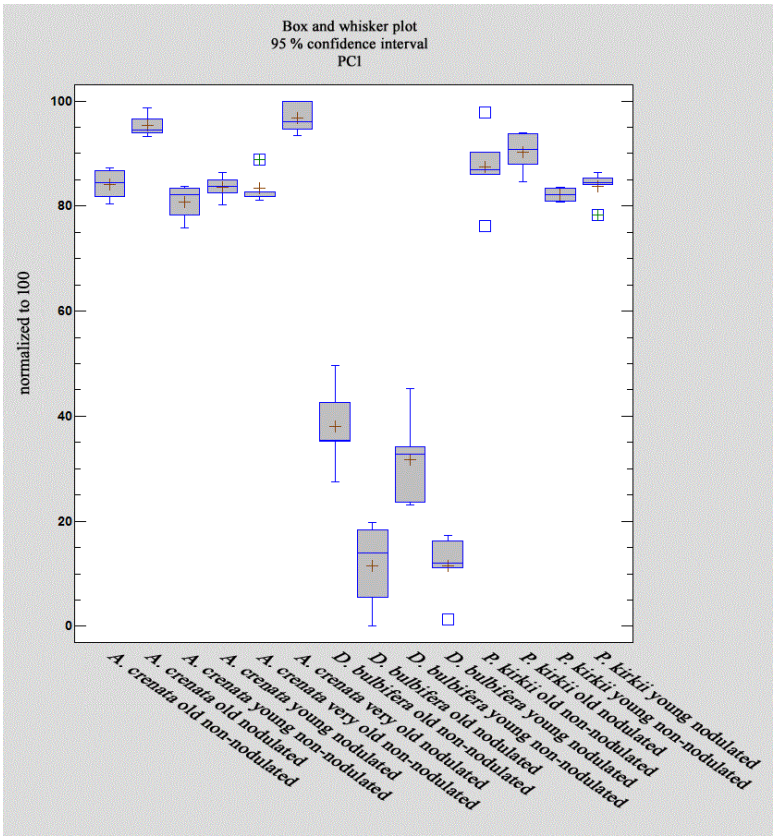

Figure 36. Box and whisker plot of PC1 within a 95 % confidence interval of *A. crenata* tissues, *D. bulbifera* tissues and *P. kirkii* tissues.

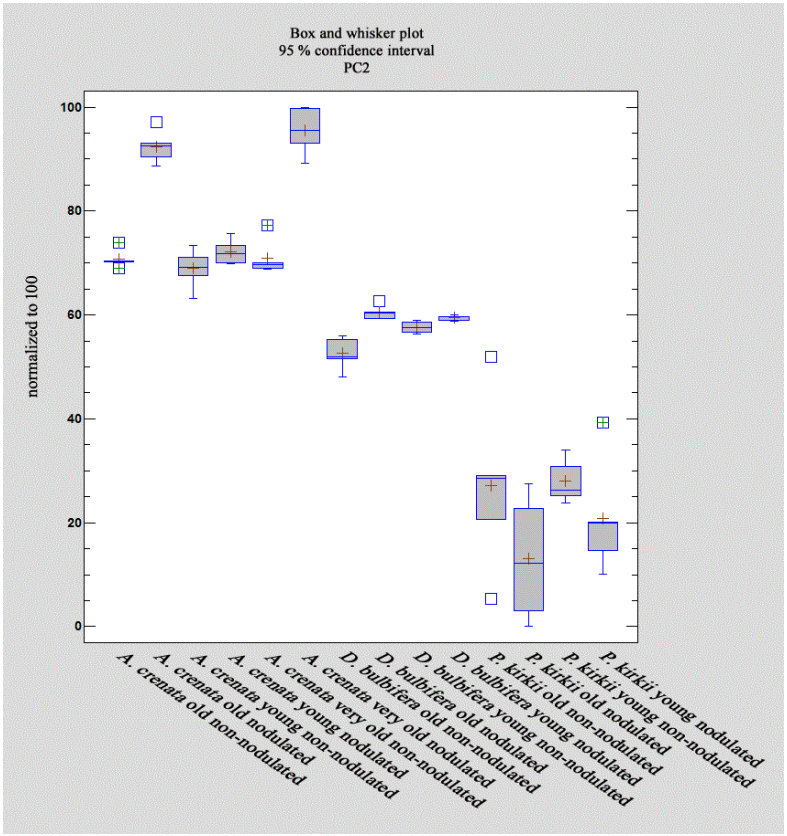

Figure 37. Box and whisker plot of PC2 within a 95 % confidence interval of *A. crenata* tissues, *D. bulbifera* tissues and *P. kirkii* tissues.

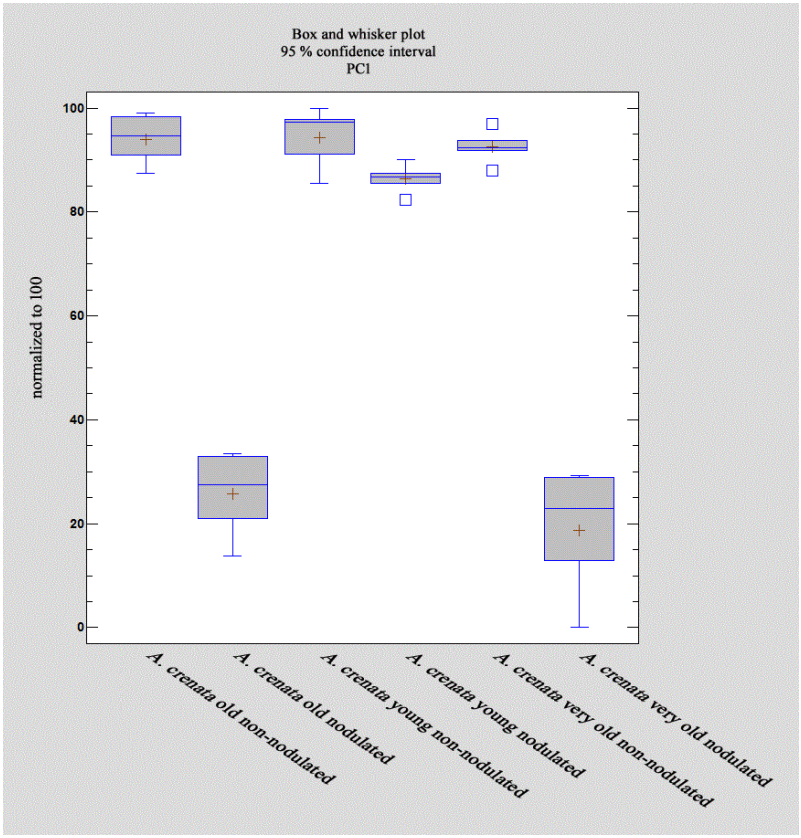

Figure 38. Box and whisker plot of PC1 within a 95 % confidence interval of *A. crenata* tissues.

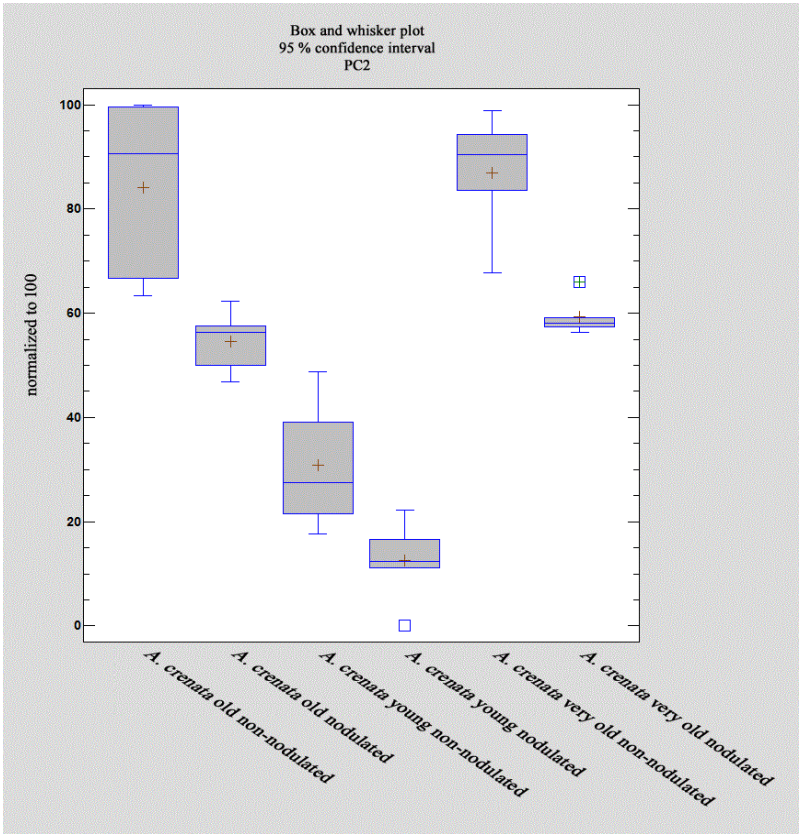

Figure 39. Box and whisker plot of PC2 within a 95 % confidence interval of *A. crenata* tissues.

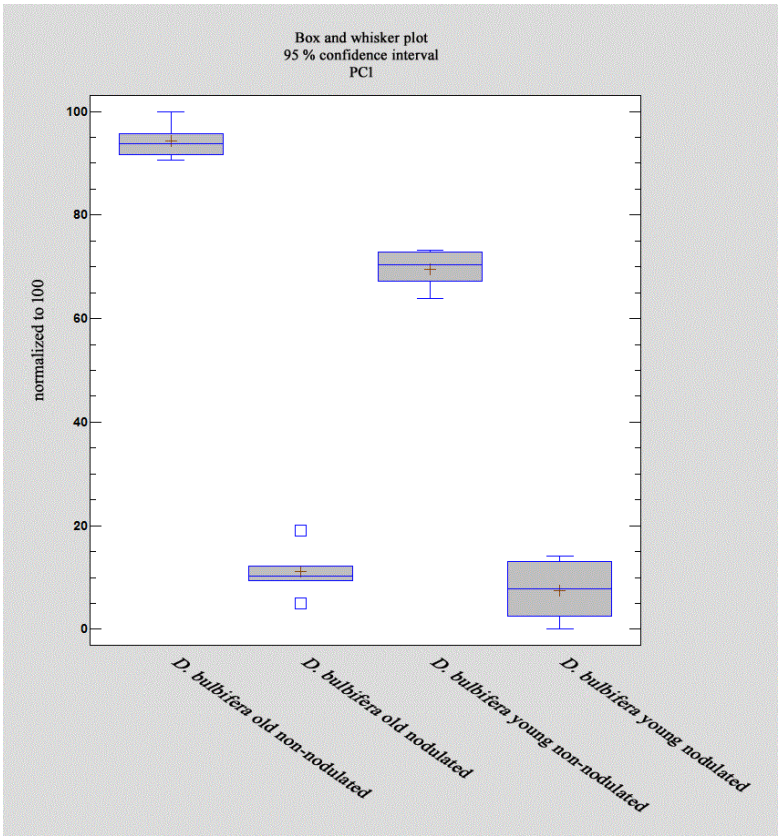

Figure 40. Box and whisker plot of PC1 within a 95 % confidence interval of *D. bulbifera* tissues.

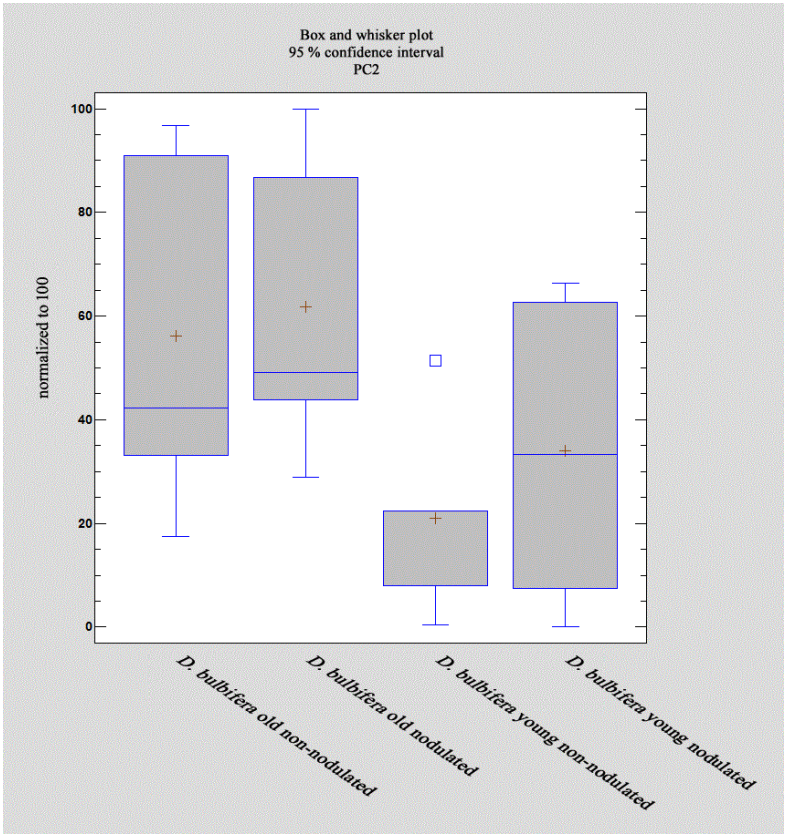

Figure 41. Box and whisker plot of PC2 within a 95 % confidence interval of *D. bulbifera* tissues.

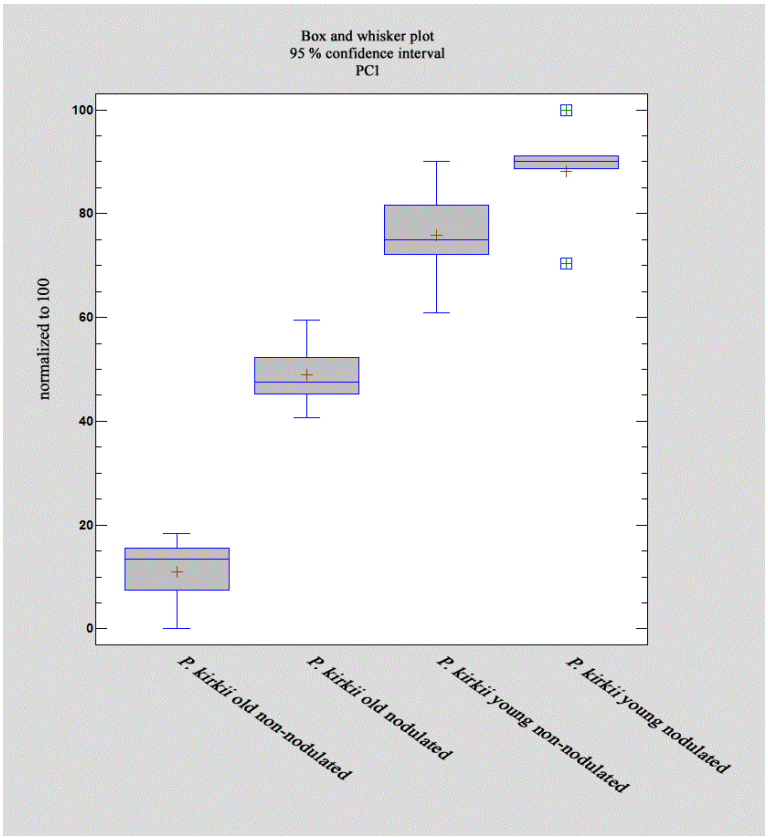

Figure 42. Box and whisker plot of PC1 within a 95 % confidence interval of *P. kirkii* tissues.

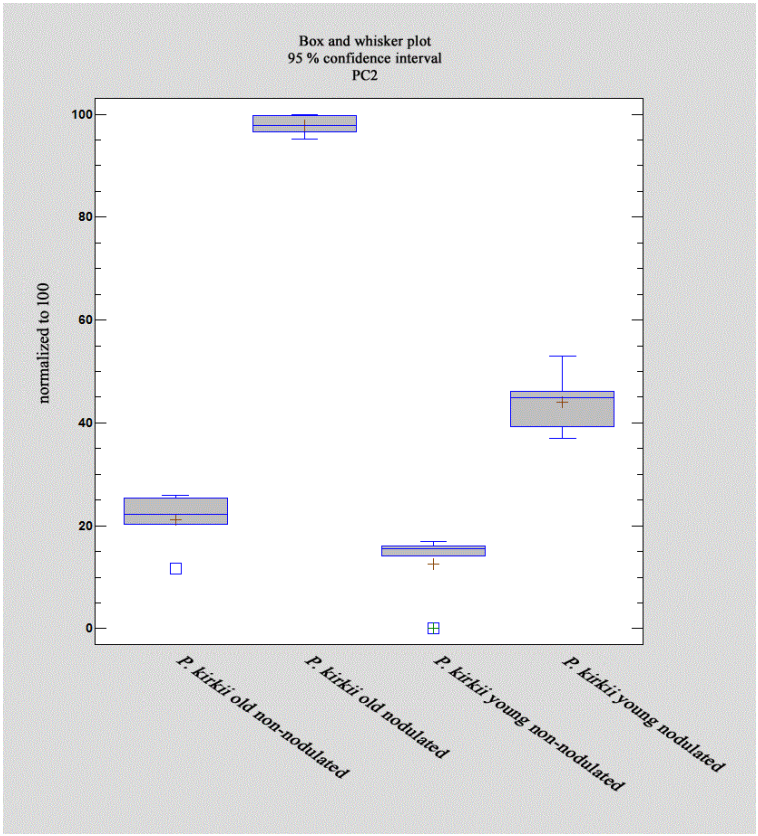

Figure 43. Box and whisker plot of PC2 within a 95 % confidence interval of *P. kirkii* tissues.

III.7.3. Appendix C: MS 1 and MS 2 spectra of m/z features annotated by targeted matching

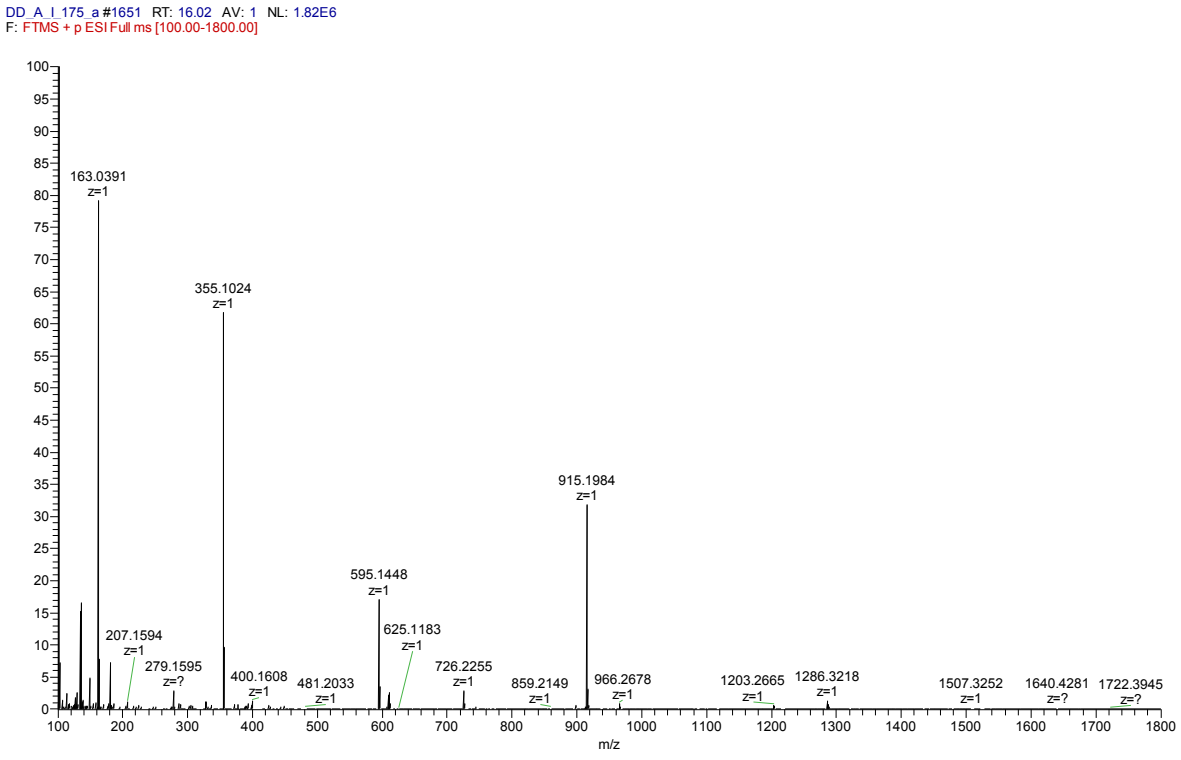

Figure 44. MS 1 spectrum of the *m/z* feature annotated as caffeoylquinic acid with a *m/z* value of 355.1024 at rt 16.02 min. The *m/z* value lies within 5 ppm of the theoretical *m/z* value.

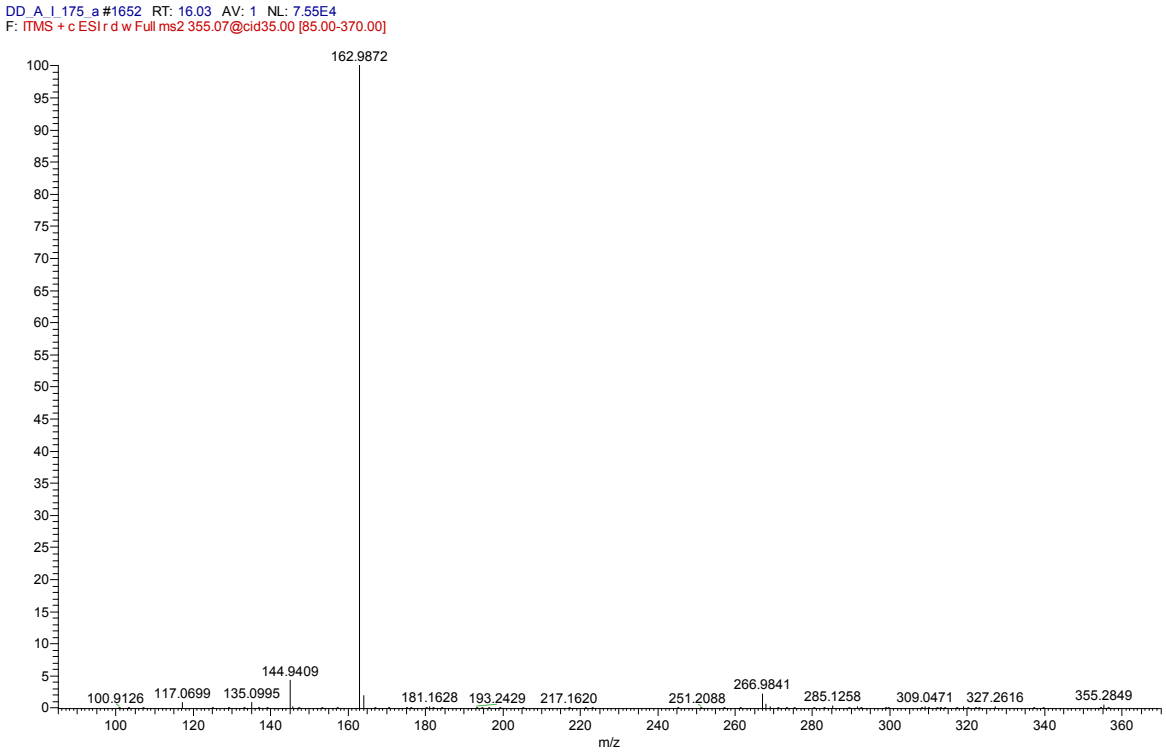

Figure 45. MS 2 spectrum of the *m/z* feature annotated as caffeoylquinic acid with a *m/z* value of 355.1024 at rt 16.03 min.

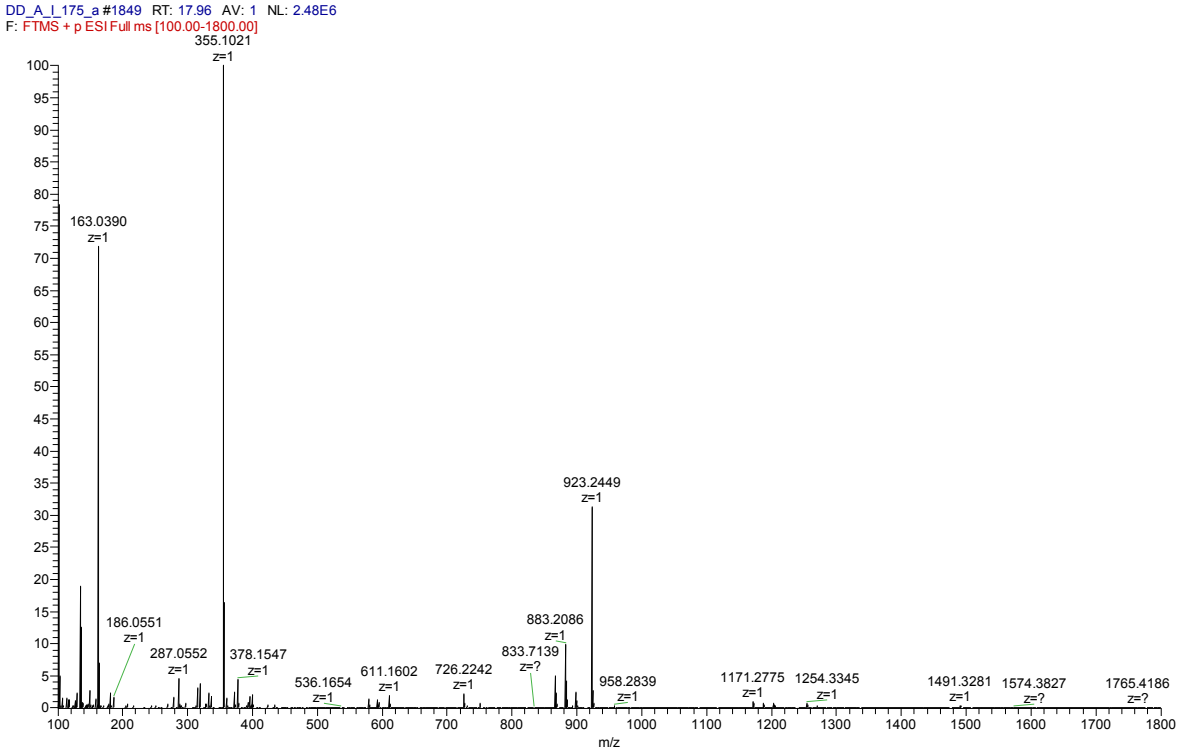

Figure 46. MS 1 spectrum of the *m/z* feature annotated as caffeoylquinic acid with a *m/z* value of 355.1021 at rt 17.96 min. The *m/z* value lies within 5 ppm of the theoretical *m/z* value.

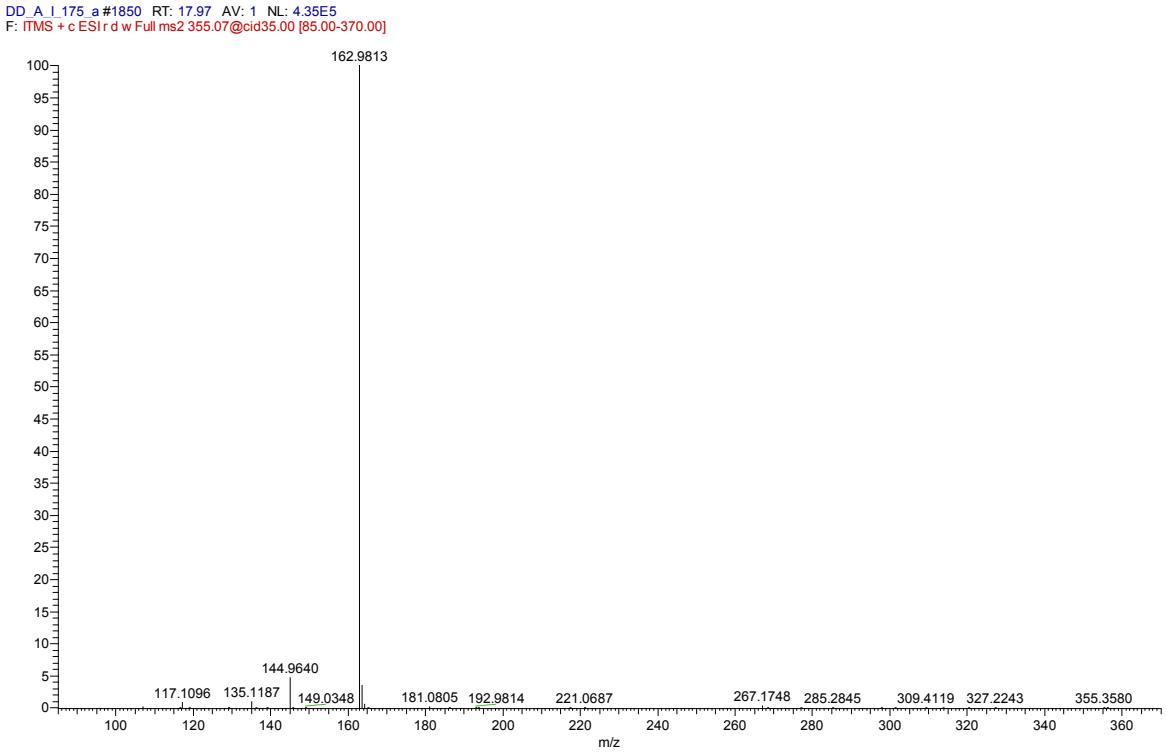

Figure 47. MS 2 spectrum of the *m/z* feature annotated as caffeoylquinic acid with a *m/z* value of 355.1021 at rt 17.97 min.

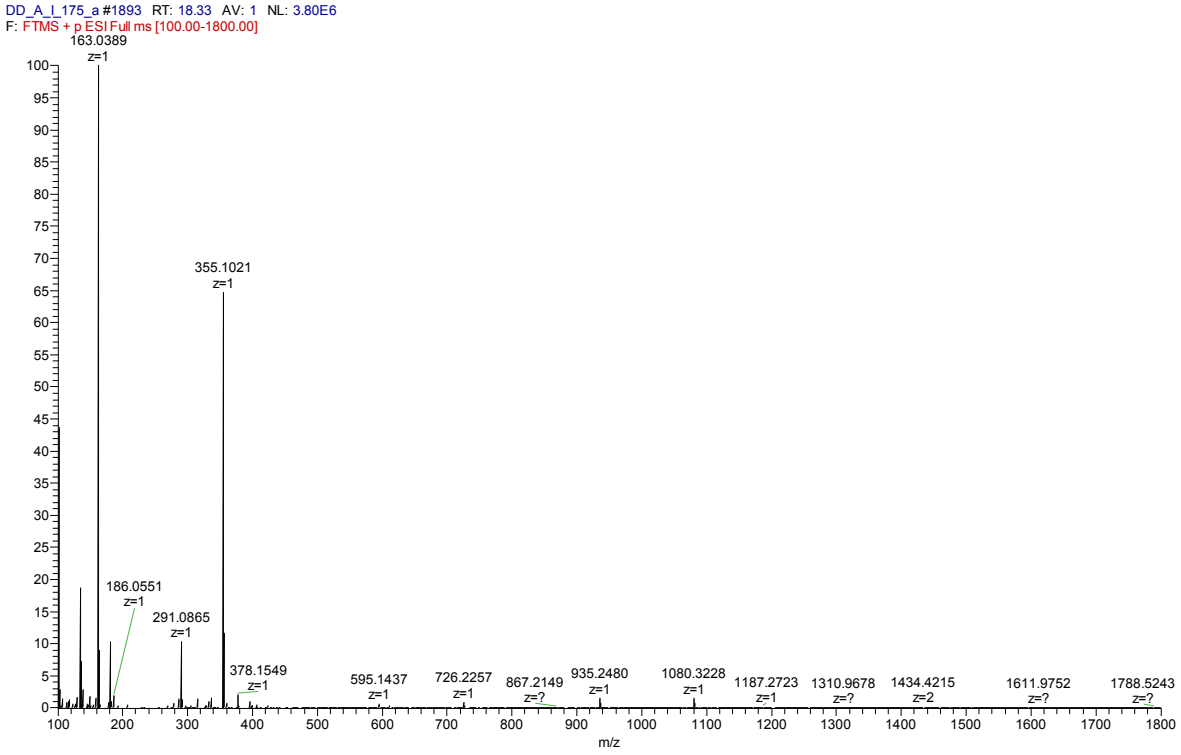

Figure 48. MS 1 spectrum of the *m/z* feature annotated as caffeoylquinic acid with a *m/z* value of 355.1021 at rt 18.33 min. The *m/z* value lies within 5 ppm of the theoretical *m/z* value.

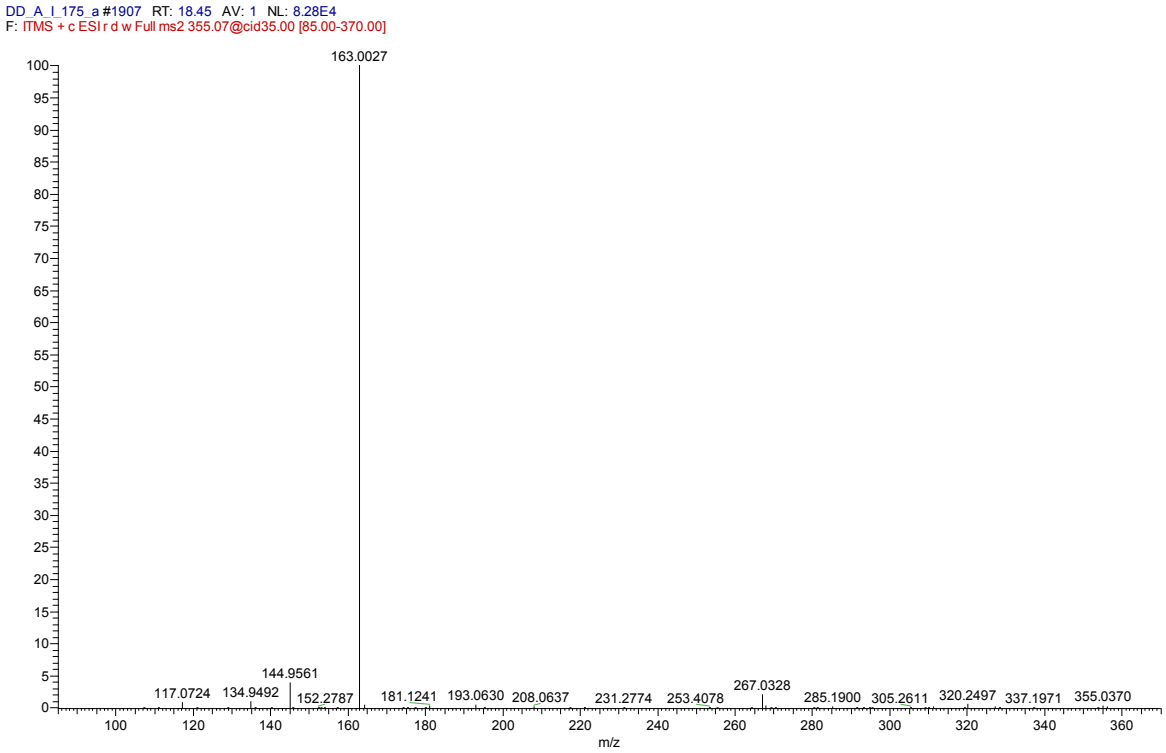

Figure 49. MS 2 spectrum of the *m/z* feature annotated as caffeoylquinic acid with a *m/z* value of 355.1021 at rt 18.45 min.

Reference spectra can be found at: https://www.mzcloud.org/DataViewer#Creference962#T1640#c#351996

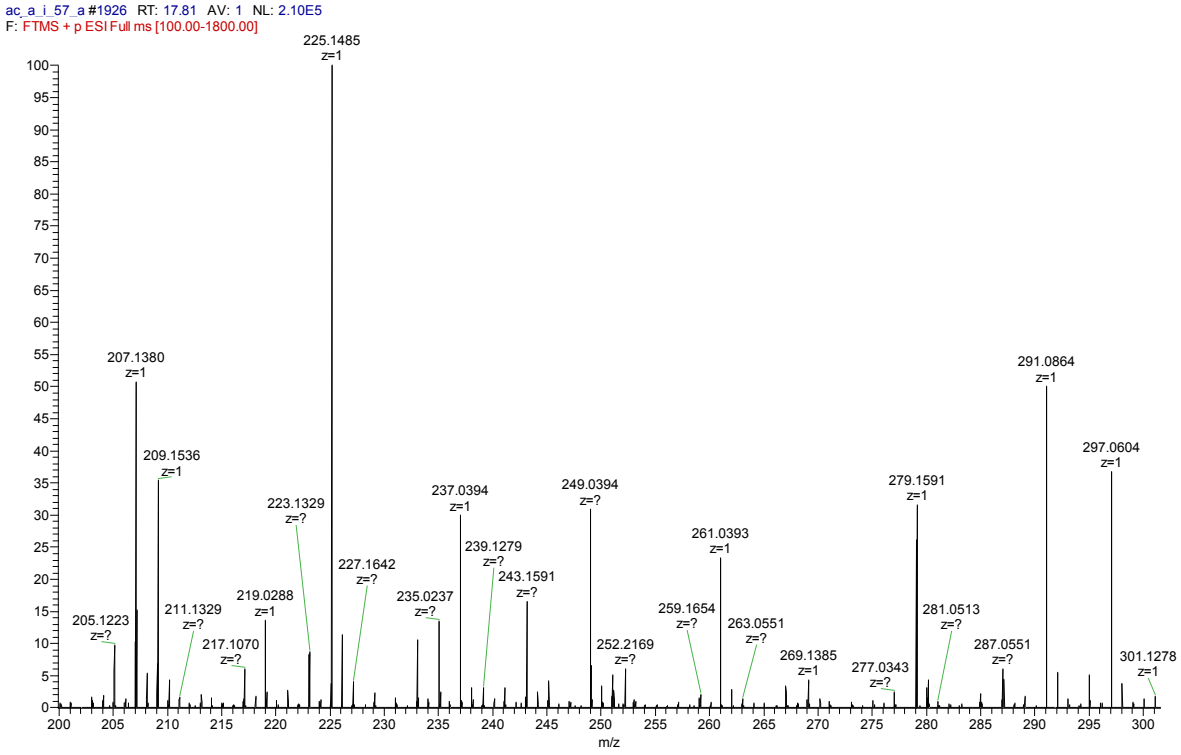

Figure 50. MS 1 spectrum of the *m/z* feature annotated as catechin with a *m/z* value of 291.0864 at rt 17.81 min. The *m/z* value lies within 5 ppm of the theoretical *m/z* value.

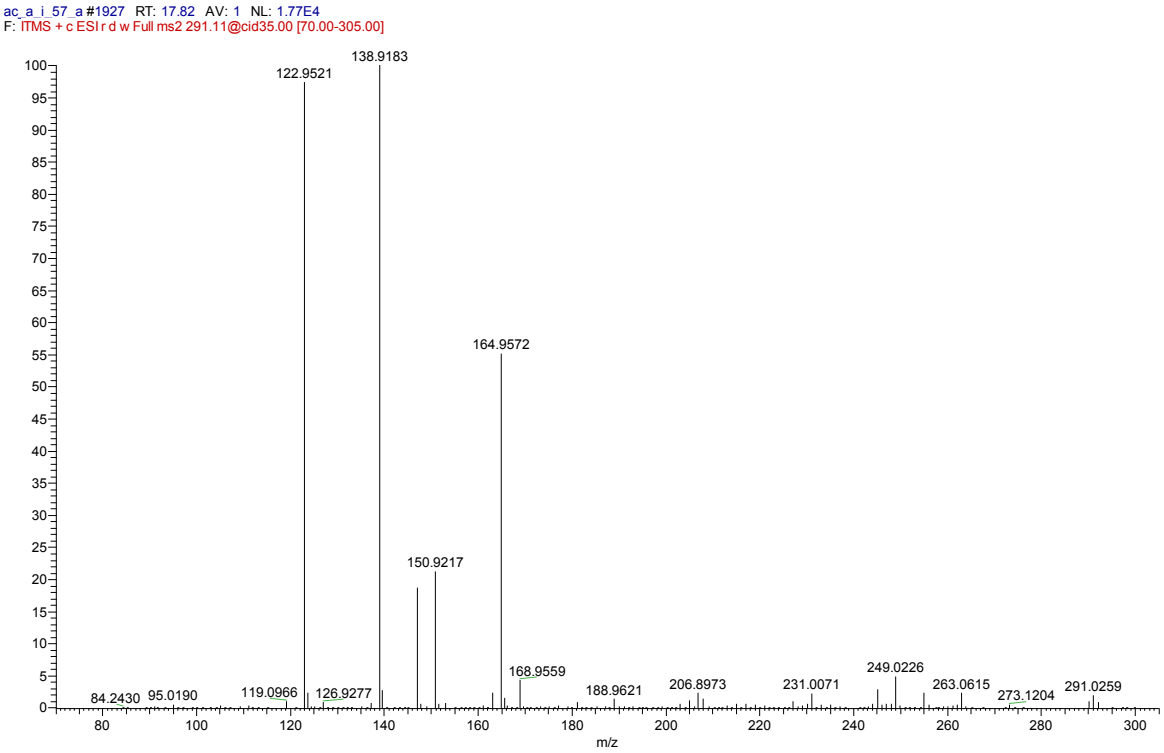

Figure 51. MS 2 spectrum of the *m/z* feature annotated as catechin with a *m/z* value of 291.0864 at rt 17.82 min.

Reference spectra can be found at: https://www.mzcloud.org/DataViewer#Creference1524#T2372#c#270825

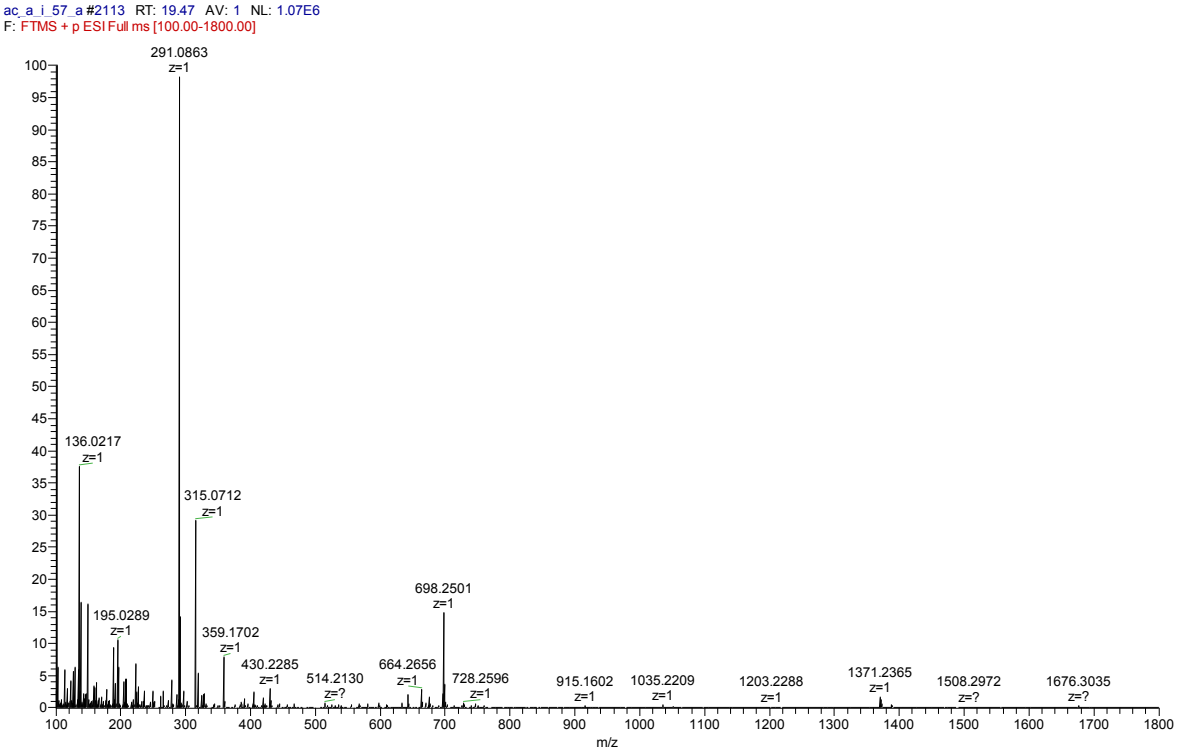

Figure 52. MS 1 spectrum of the *m/z* feature annotated as epicatechin with a *m/z* value of 291.0863 at rt 19.47 min. The *m/z* value lies within 5 ppm of the theoretical *m/z* value.

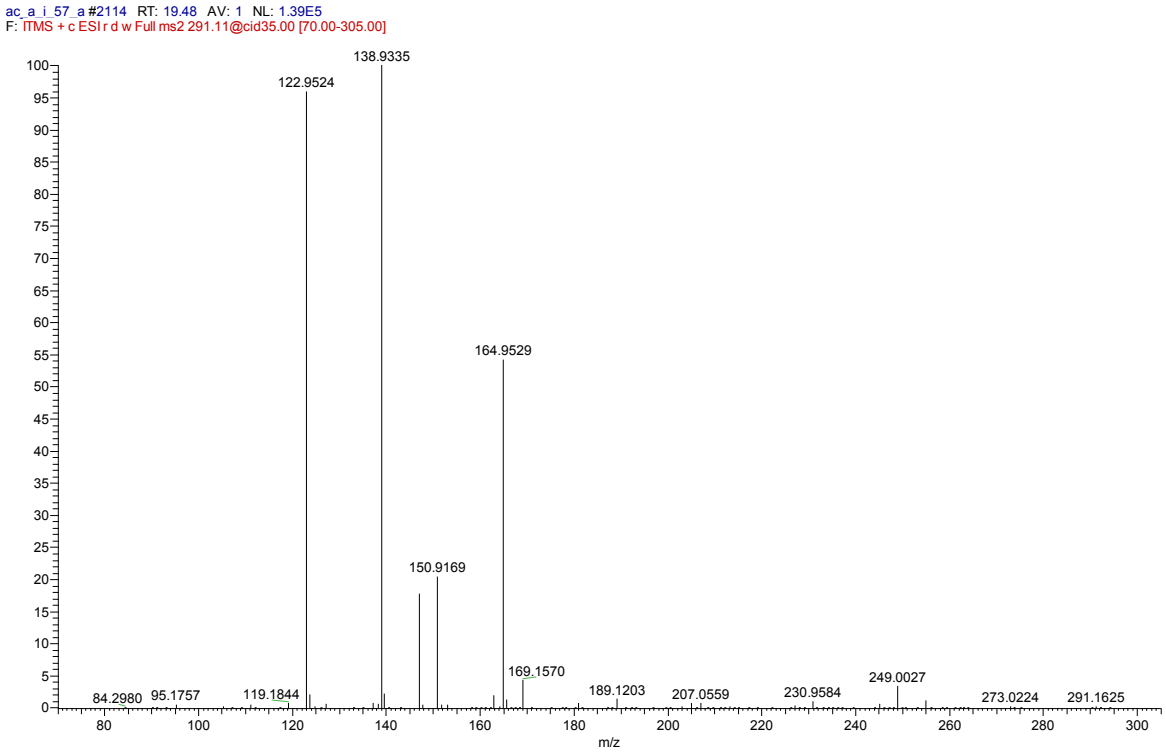

Figure 53. MS 2 spectrum of the *m/z* feature annotated as epicatechin with a *m/z* value of 291.0863 at rt 19.48 min.

Reference spectra can be found at: https://www.mzcloud.org/DataViewer#Creference7790#T12070#c#2776785

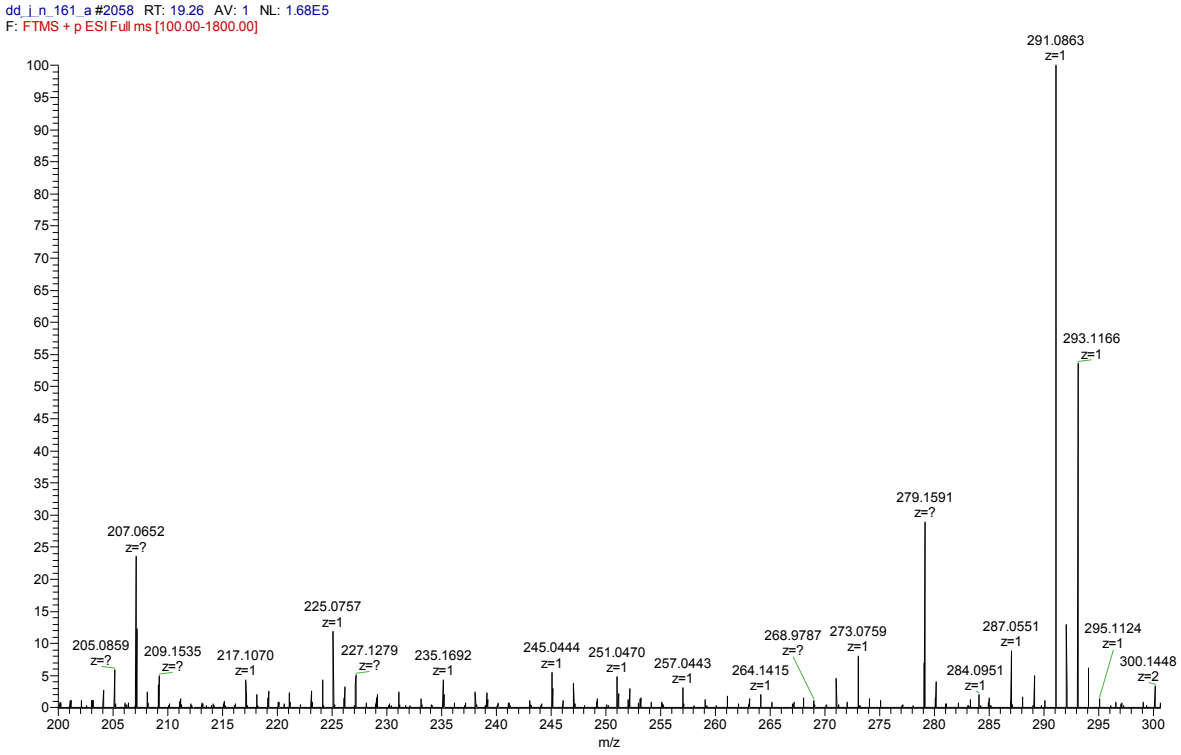

Figure 54. MS 1 spectrum of the *m/z* feature annotated as naringenin with a *m/z* value of 273.0759 at rt 19.20 min. The *m/z* value lies within 5 ppm of the theoretical *m/z* value.

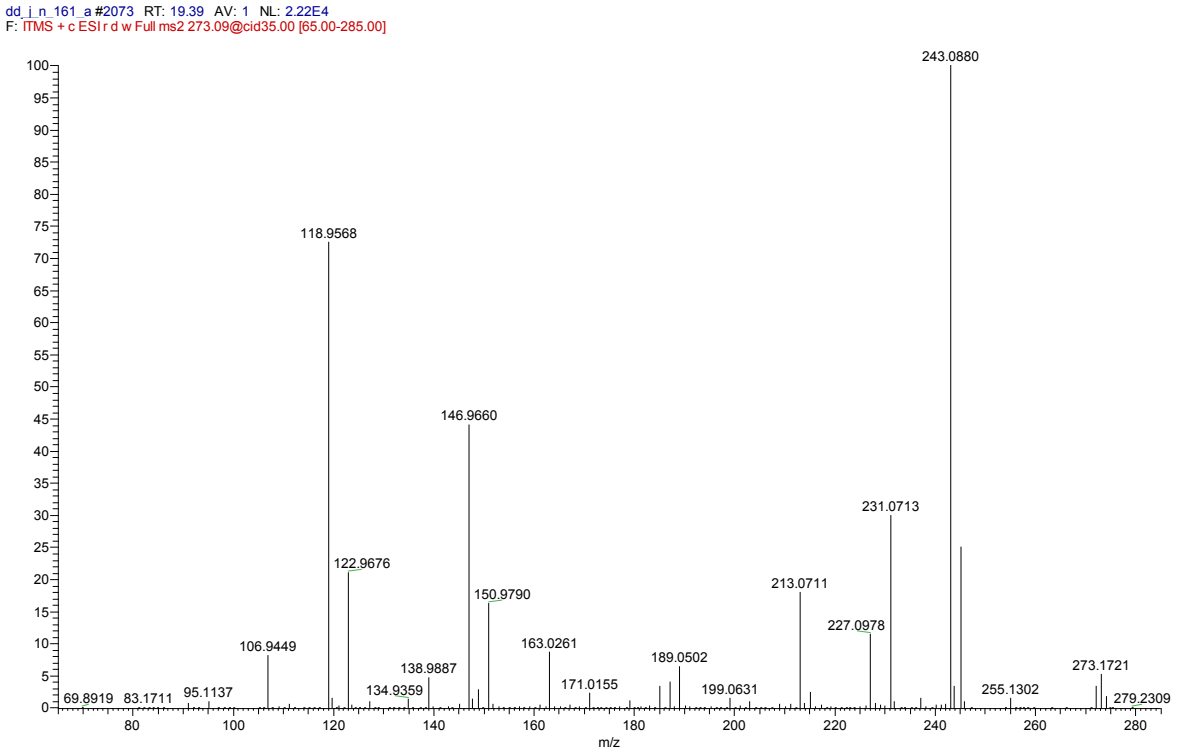

Figure 55. MS 2 spectrum of the *m/z* feature annotated as naringenin with a *m/z* value of 273.0759 at rt 19.39 min.

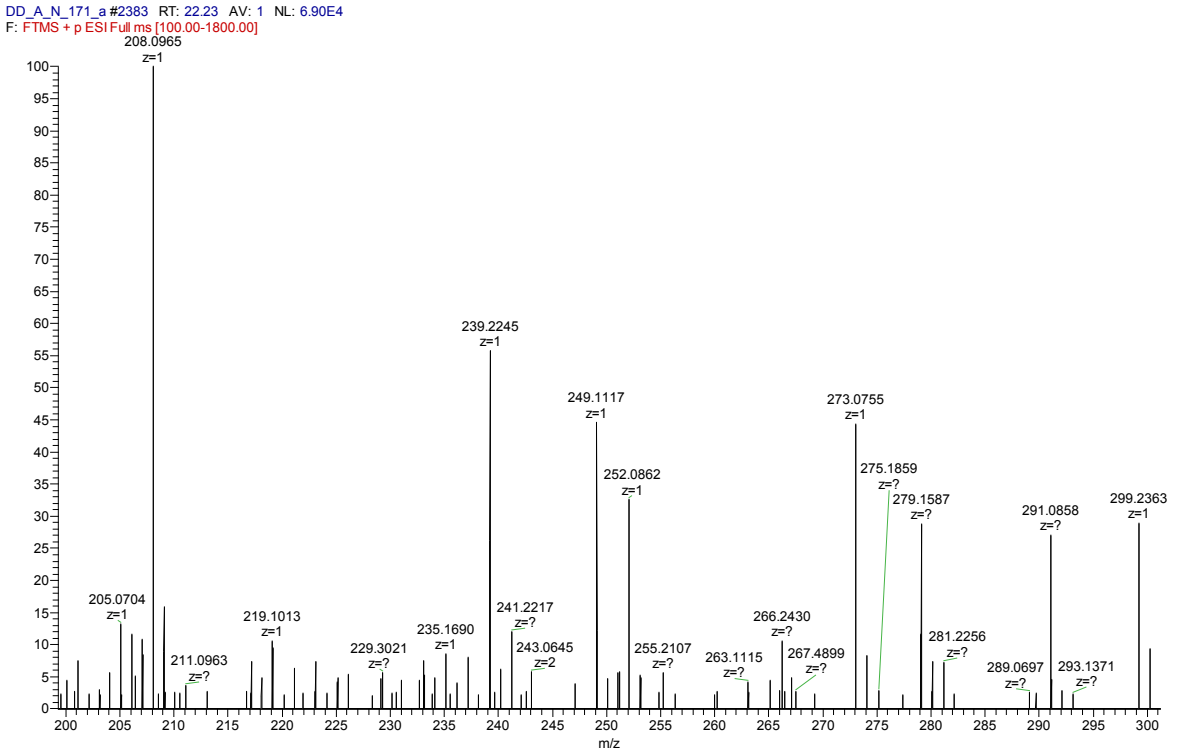

Figure 56. MS 1 spectrum of the *m/z* feature annotated as naringenin with a *m/z* value of 273.0755 at rt 22.27 min. The *m/z* value lies within 5 ppm of the theoretical *m/z* value.

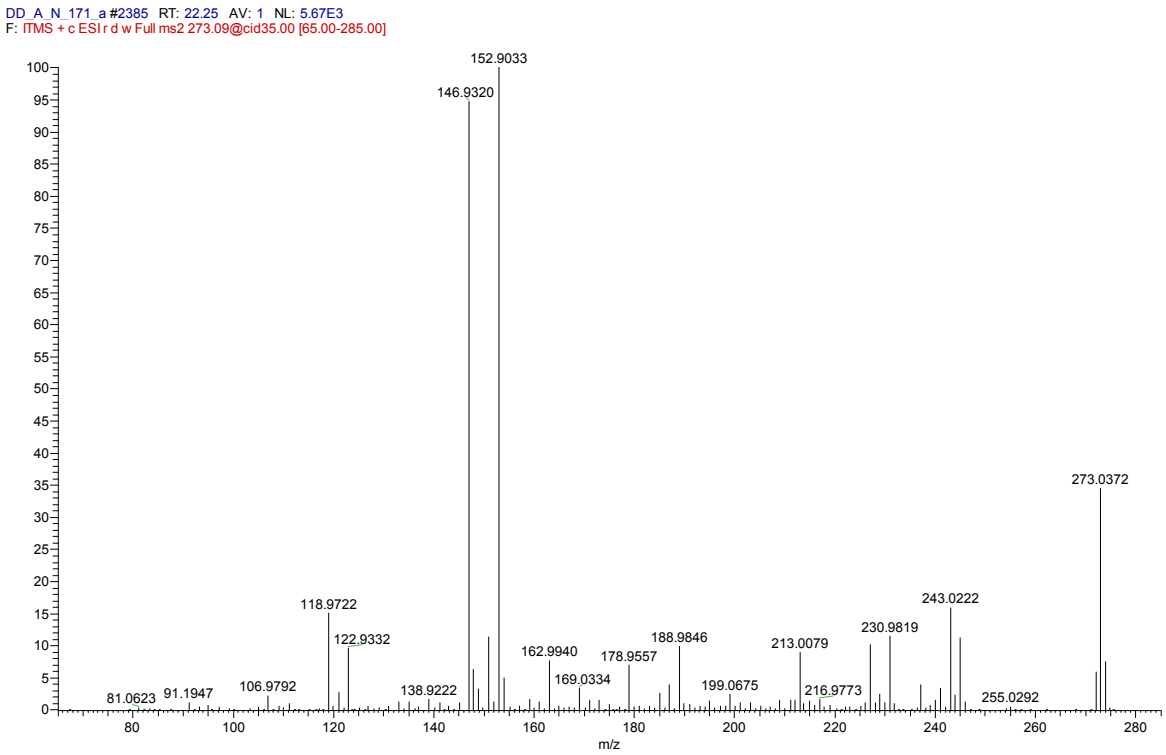

Figure 57. MS 2 spectrum of the *m/z* feature annotated as naringenin with a *m/z* value of 273.0755 at rt 22.25 min.

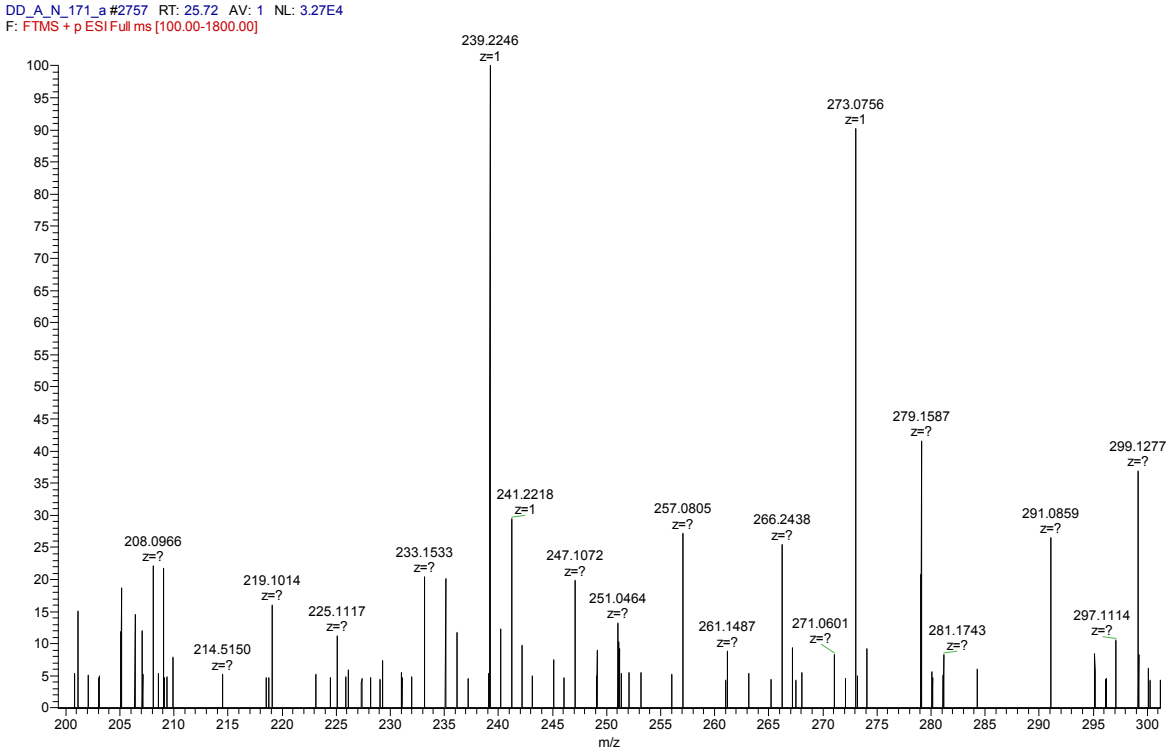

Figure 58. MS 1 spectrum of the *m/z* feature annotated as naringenin with a *m/z* value of 273.0756 at rt 25.71 min. The *m/z* value lies within 5 ppm of the theoretical *m/z* value.

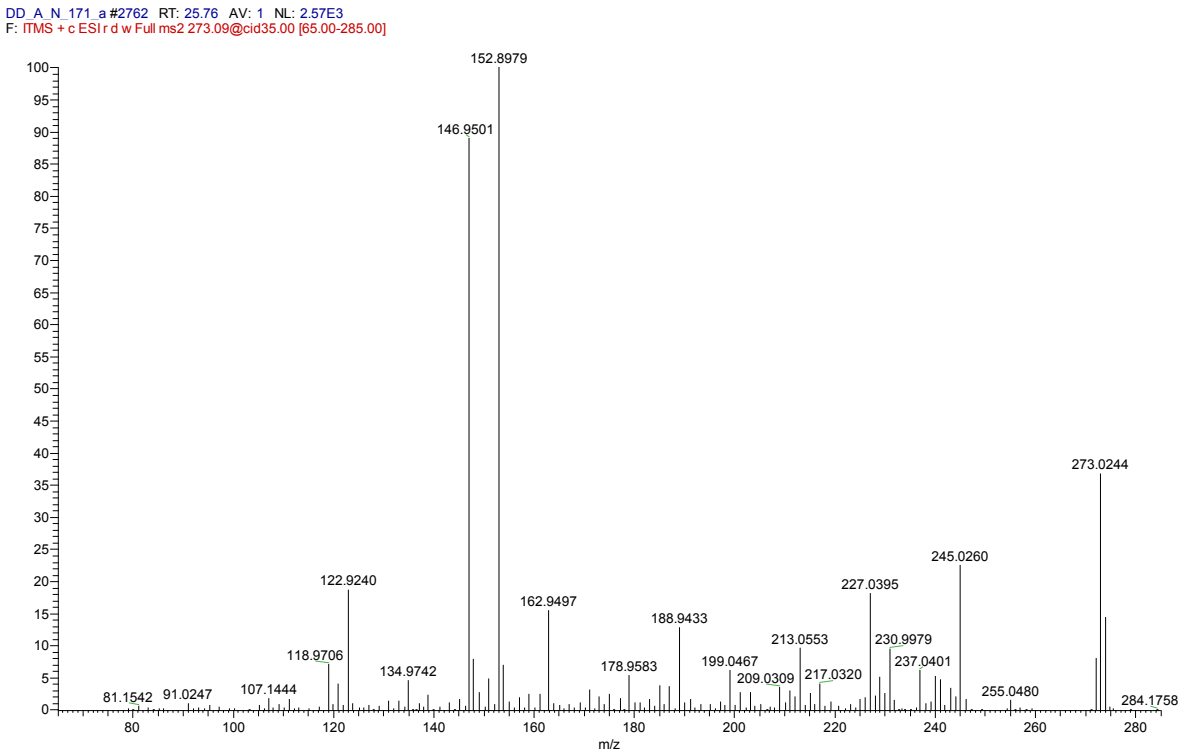

Figure 59. MS 2 spectrum of the *m/z* feature annotated as naringenin with a *m/z* value of 273.0756 at rt 25.76 min.

Reference spectra can be found at: https://www.mzcloud.org/DataViewer#Creference18#T45#c#8420

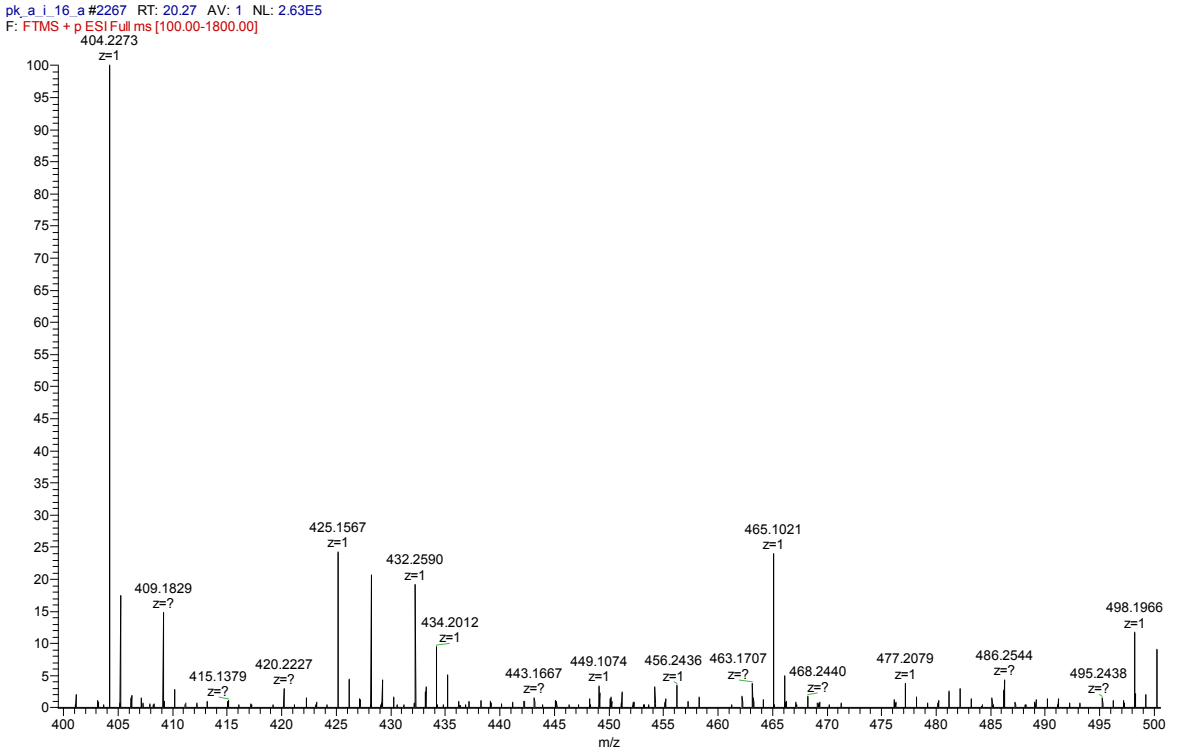

Figure 60. MS 1 spectrum of the *m/z* feature annotated as quercetin 3 glucoside with a *m/z* value of 465.1021 at rt 20.70 min. The *m/z* value lies within 5 ppm of the theoretical *m/z* value.

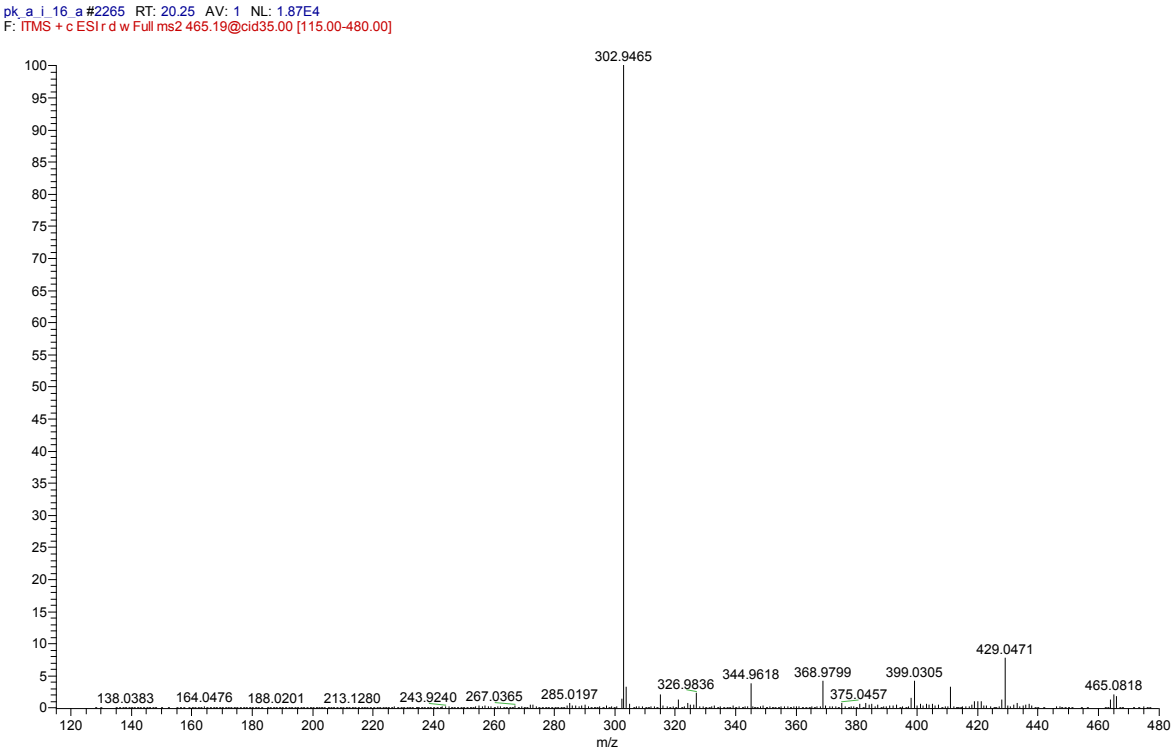

Figure 61. MS 2 spectrum of the *m/z* feature annotated as quercetin 3 glucoside with a *m/z* value of 465.1021 at rt 20.25 min.

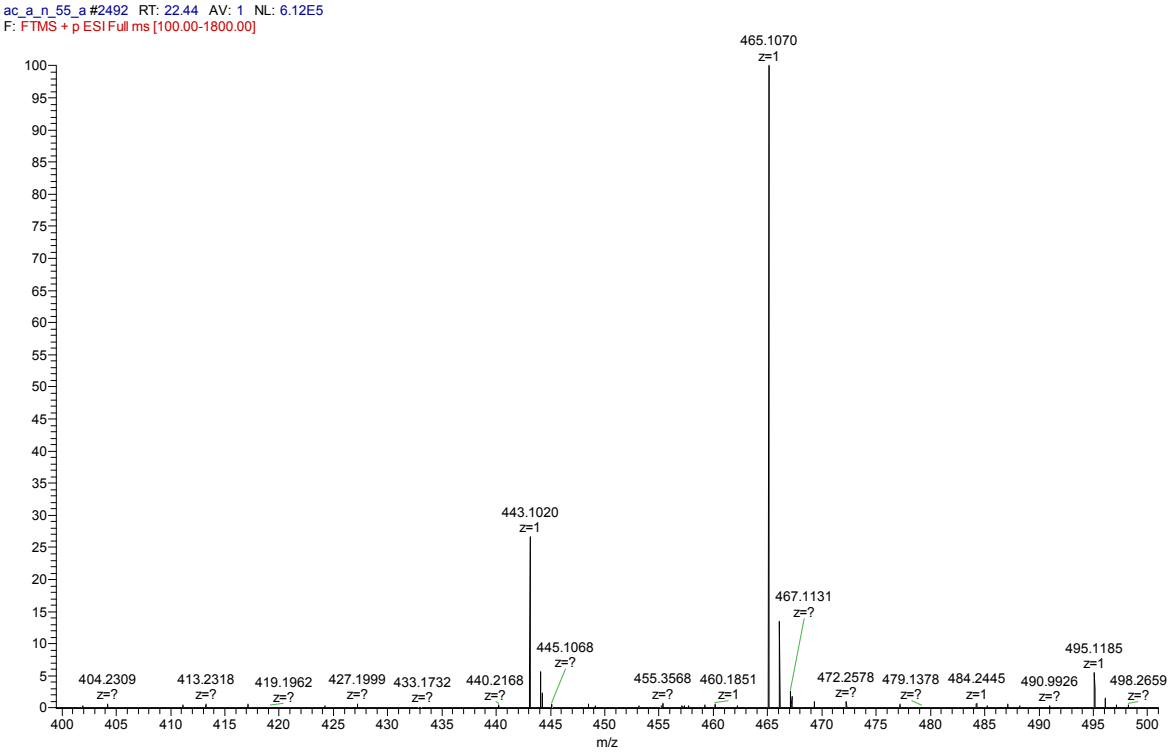

Figure 62. MS 1 spectrum of the *m/z* feature annotated as quercetin 3 glucoside with a *m/z* value of 465.1070 at rt 22.58 min.

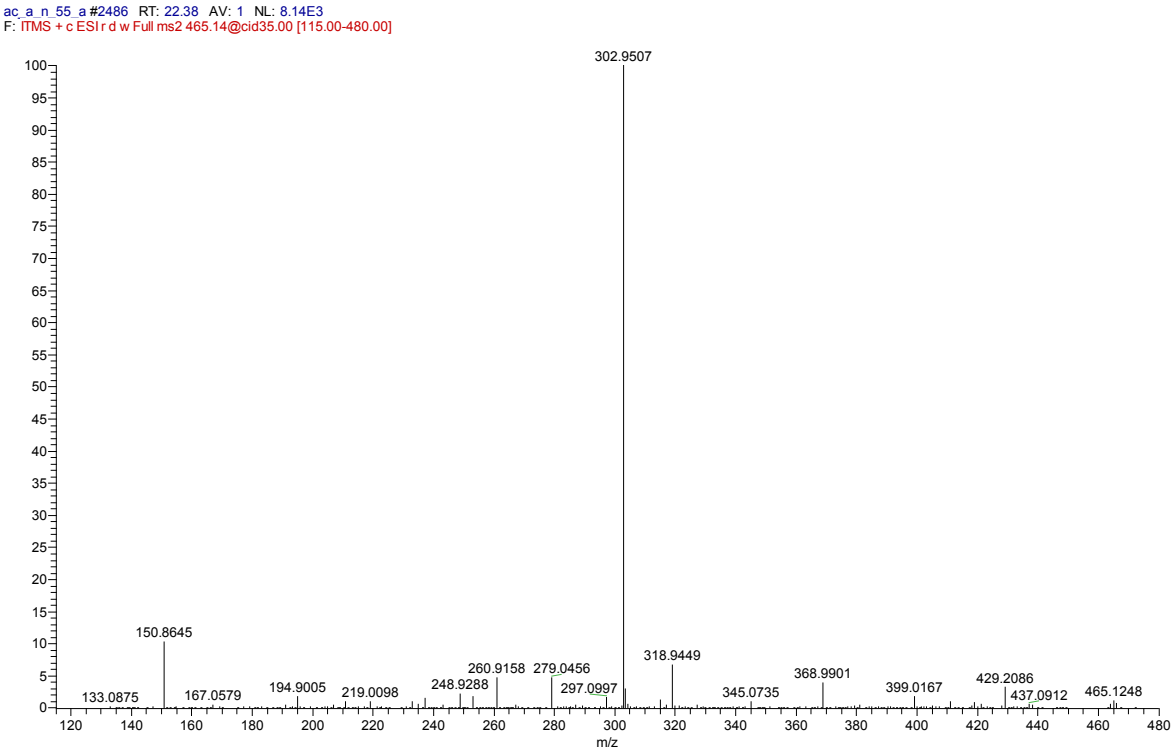

Figure 63. MS 2 spectrum of the *m/z* feature annotated as quercetin 3 glucoside with a *m/z* value of 465.1070 at rt 22.38 min.

Reference spectra can be found at: https://www.mzcloud.org/DataViewer#Creference1472#T11659#c#2702088

III.7.4. Appendix D: MS 1 and MS 2 spectra of m/z features annotated by manual analysis of the untargeted matching and alignment data

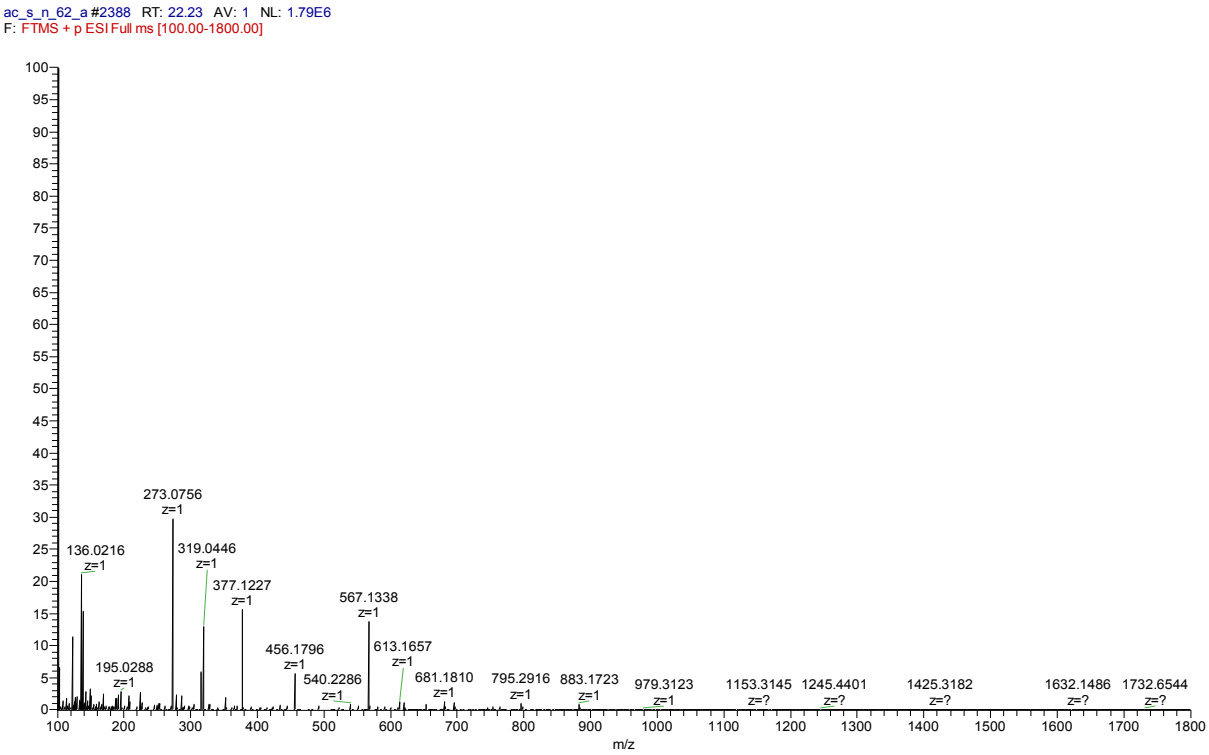

Figure 64. MS 1 spectrum of the *m/z* feature annotated as epicatechin-3-hydroxy-2-methyl-propanoate with a *m/z* value of 377.1227 at rt 22.23 min. The *m/z* value lies within 5 ppm of the theoretical *m/z* value.

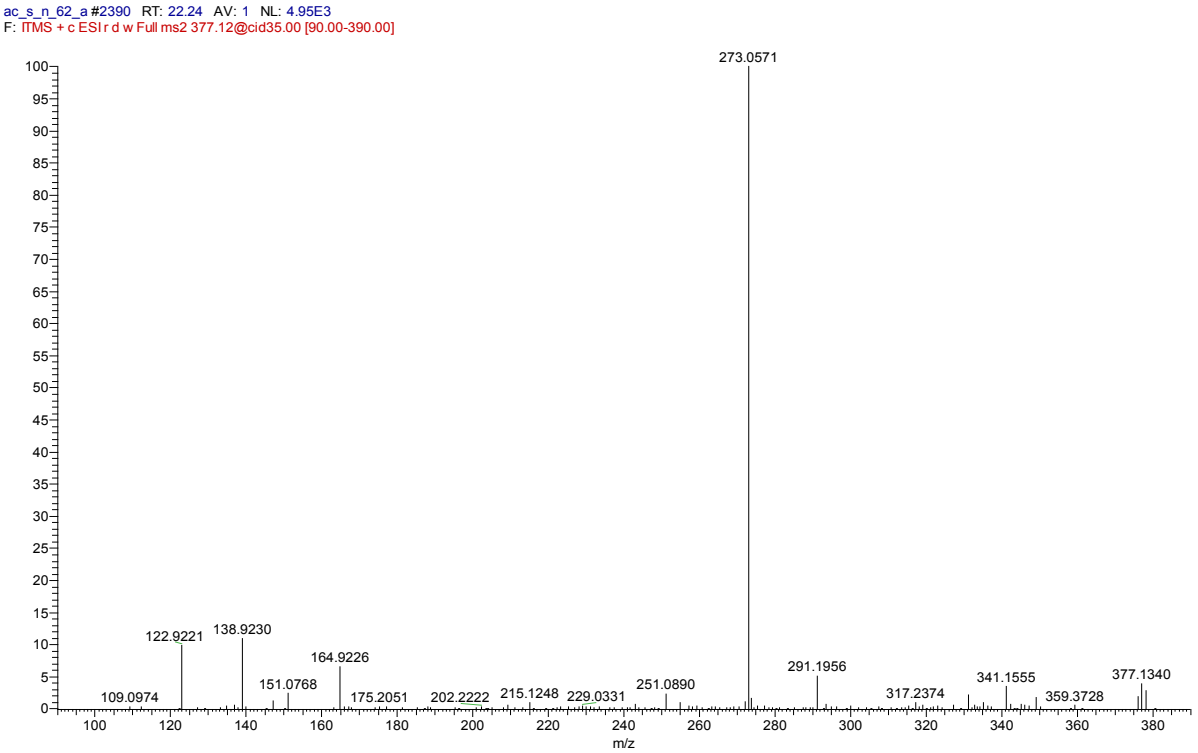

Figure 65. MS 2 spectrum of the *m/z* feature annotated as epicatechin-3-hydroxy-2-methyl-propanoate with a *m/z* value of 377.1227 at rt 22.24 min.

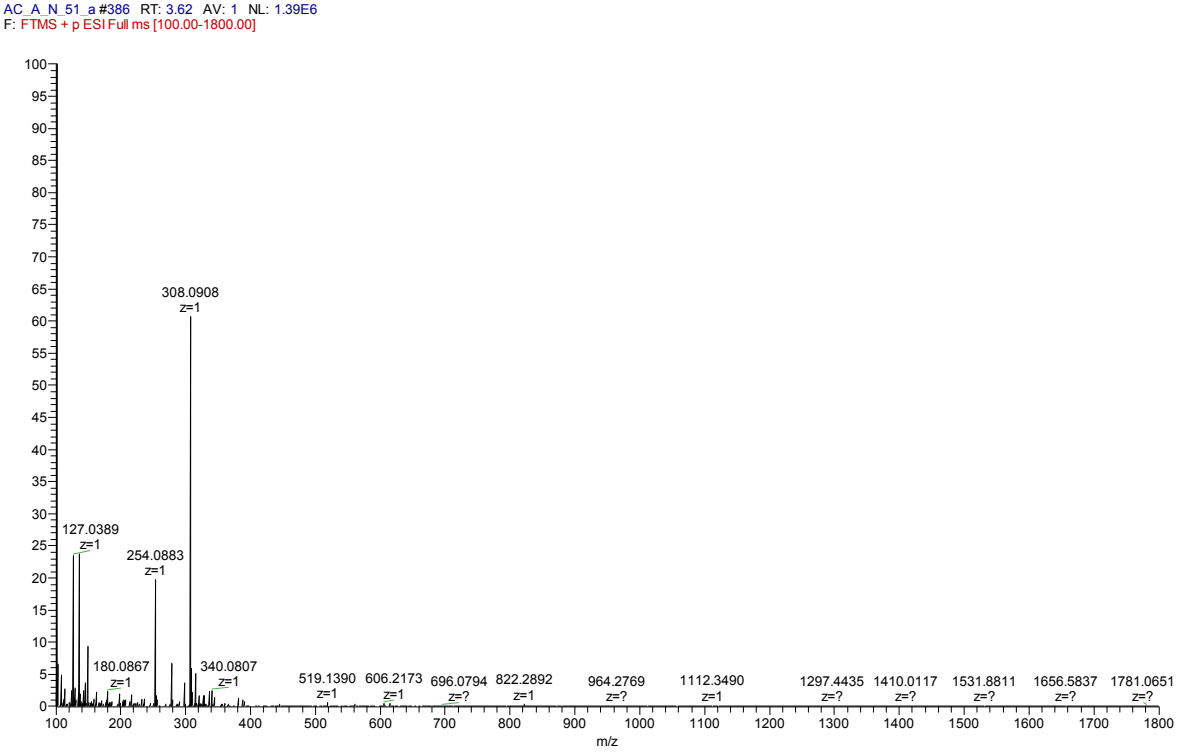

Figure 66. MS 1 spectrum of the *m/z* feature annotated as glutathione with a *m/z* value of 308.0908 at rt 3.62 min. The *m/z* value lies within 5 ppm of the theoretical *m/z* value.

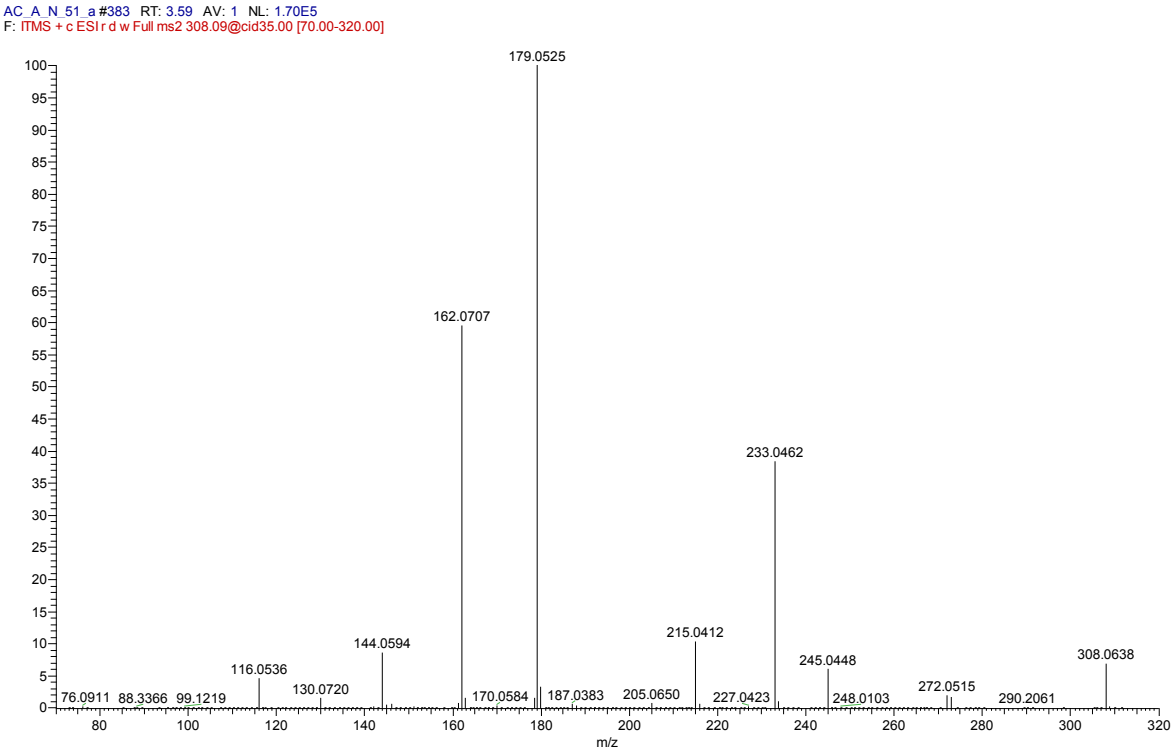

Figure 67. MS 2 spectrum of the *m/z* feature annotated as glutathione with a *m/z* value of 308.0908 at rt 3.59 min.

Reference spectra can be found at: https://www.mzcloud.org/DataViewer#Creference472#T858#c#113687

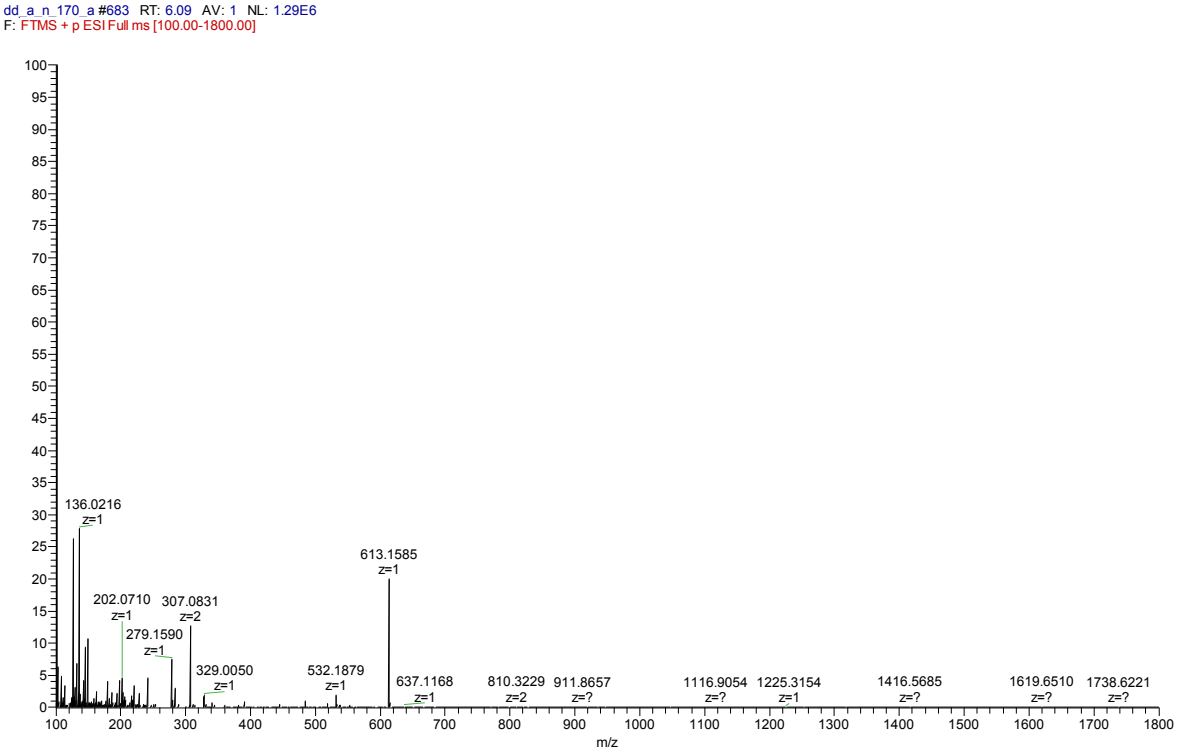

Figure 68. MS 1 spectrum of the *m/z* feature annotated as glutathione disulfide with a *m/z* value of 613.1585 at rt 6.09 min. The *m/z* value lies within 5 ppm of the theoretical *m/z* value.

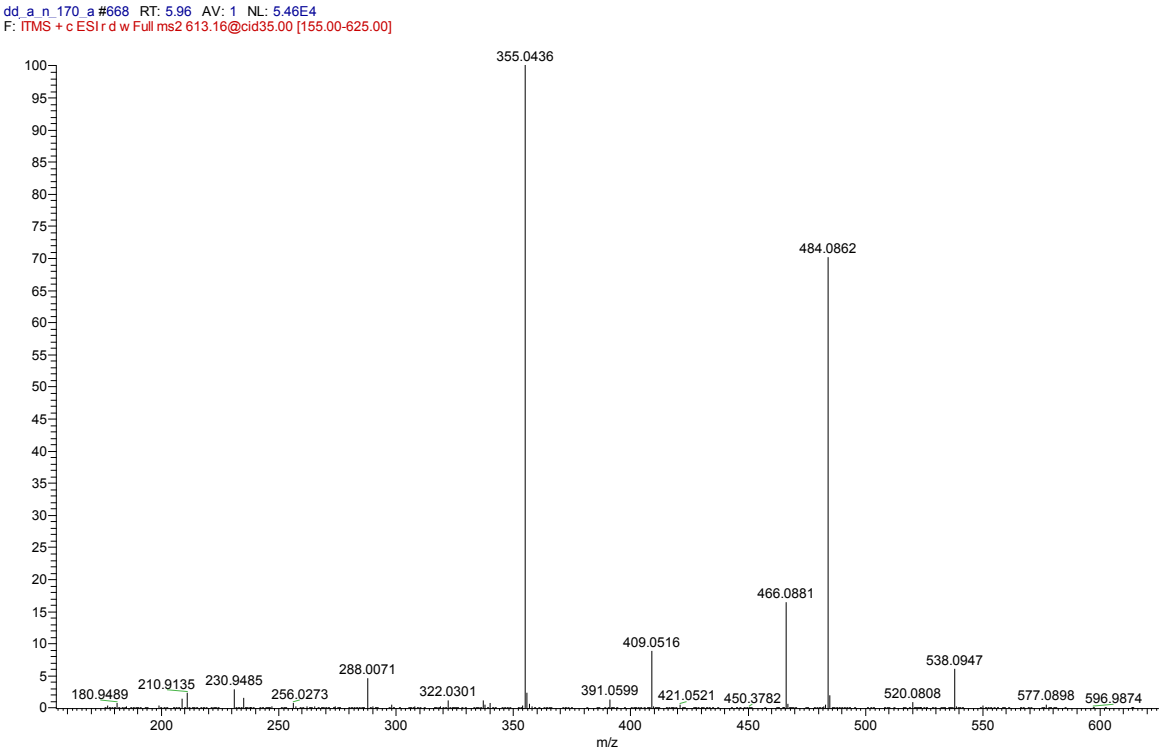

Figure 69. MS 2 spectrum of the *m/z* feature annotated as glutathione disulfide with a *m/z* value of 613.1585 at rt 5.96 min.

Reference spectra can be found at: https://www.mzcloud.org/DataViewer#Creference471#T856#c#113319

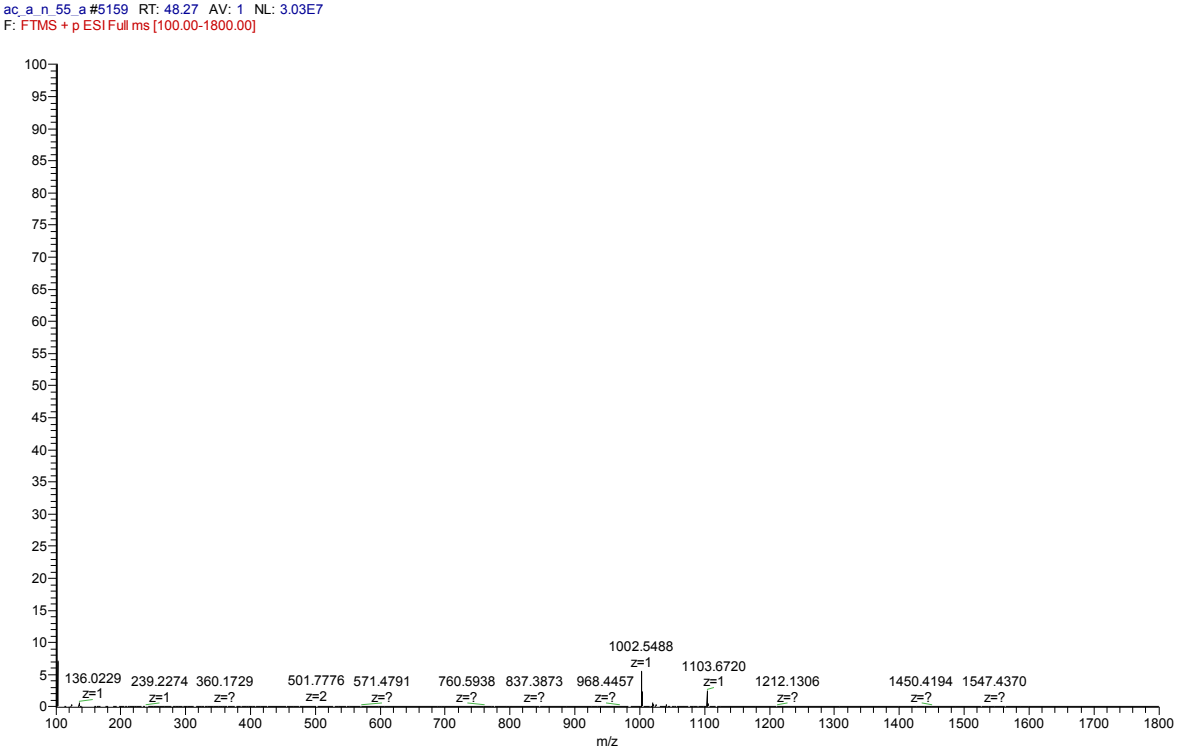

Figure 70. MS 1 spectrum of the *m/z* feature annotated as FR900359 with a *m/z* value of 1002.5488 at rt 48.27 min.

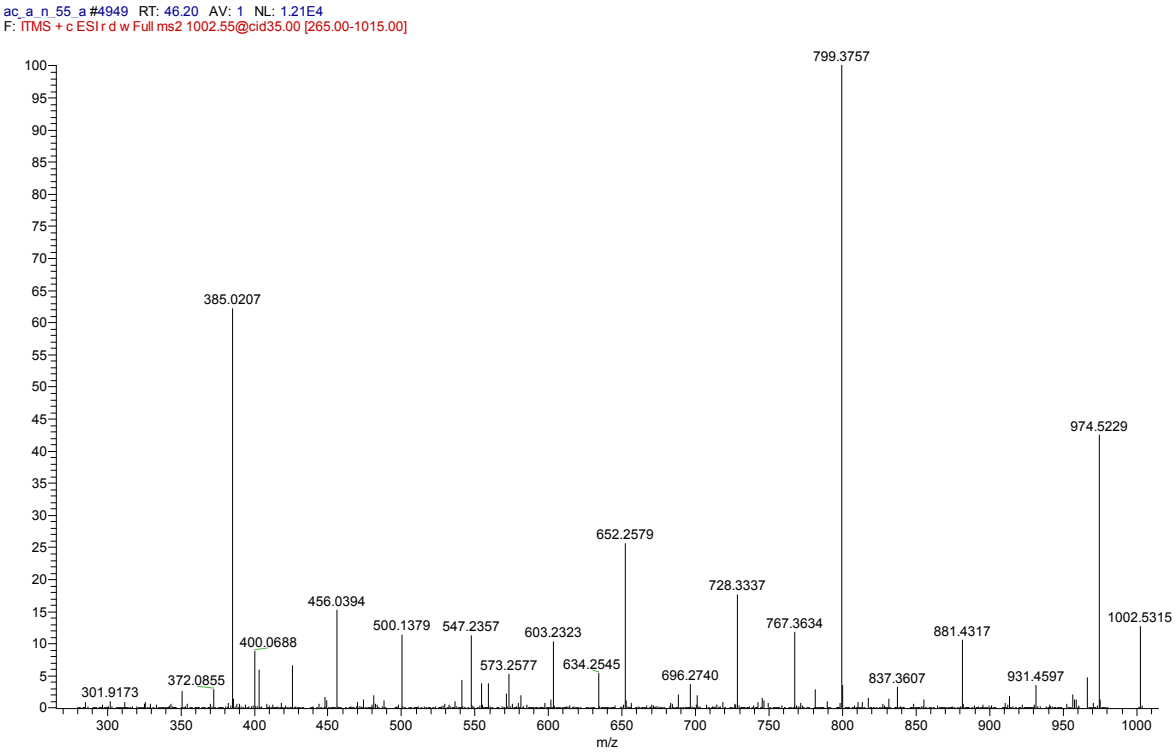

Figure 71. MS 2 spectrum of the *m/z* feature annotated as FR900359 with a *m/z* value of 1002.5488 at rt 46.20 min.

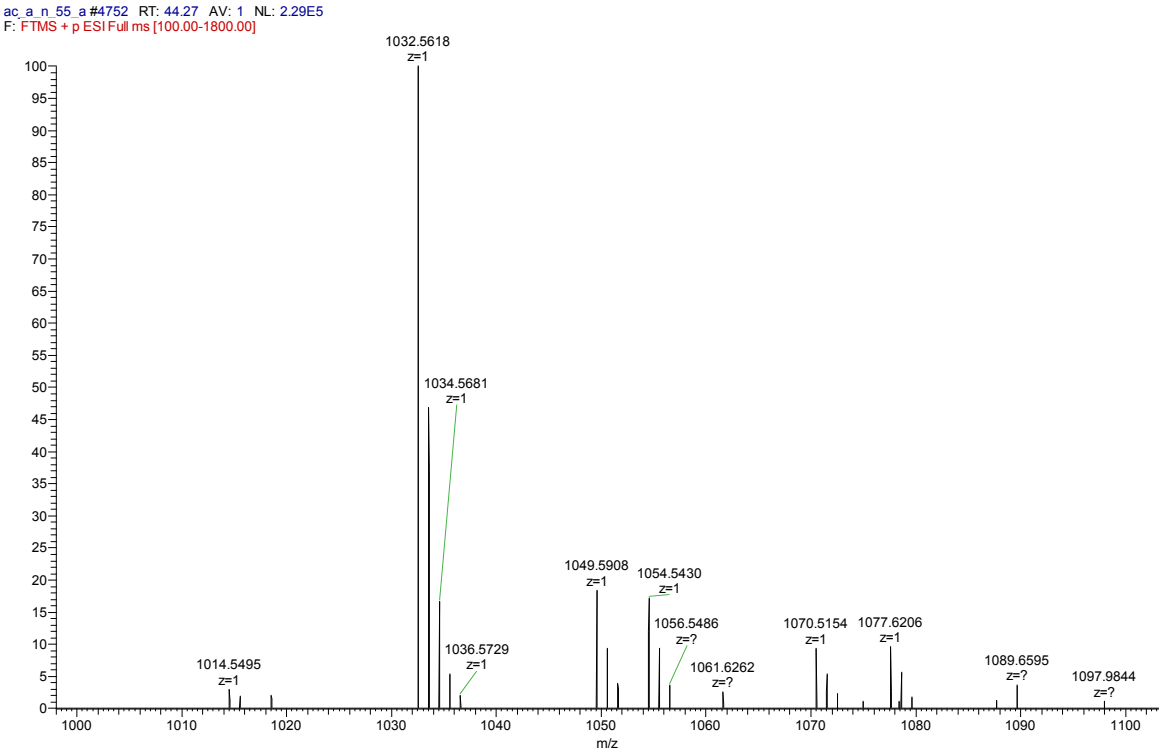

Figure 72. MS 1 spectrum of the *m/z* feature annotated as AC-1 with a *m/z* value of 1032.5618 at rt 44.27 min.

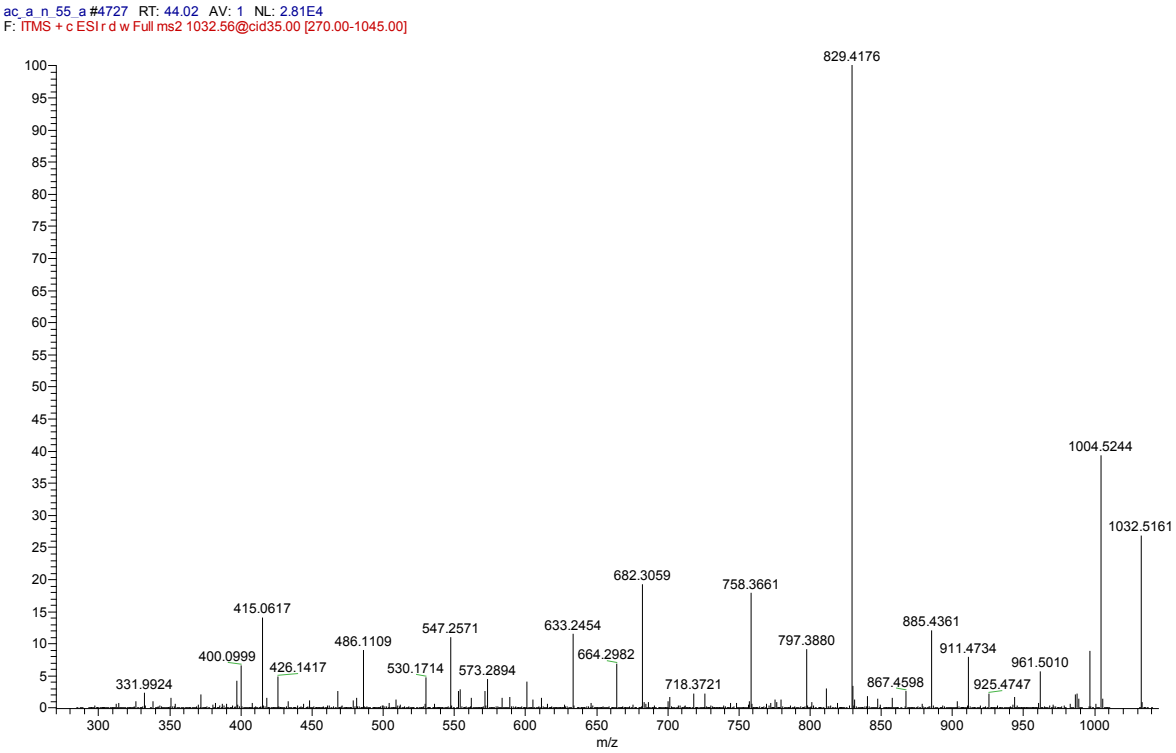

Figure 73. MS 2 spectrum of the *m/z* feature annotated as AC-1 with a *m/z* value of 1032.5618 at rt 44.02 min.

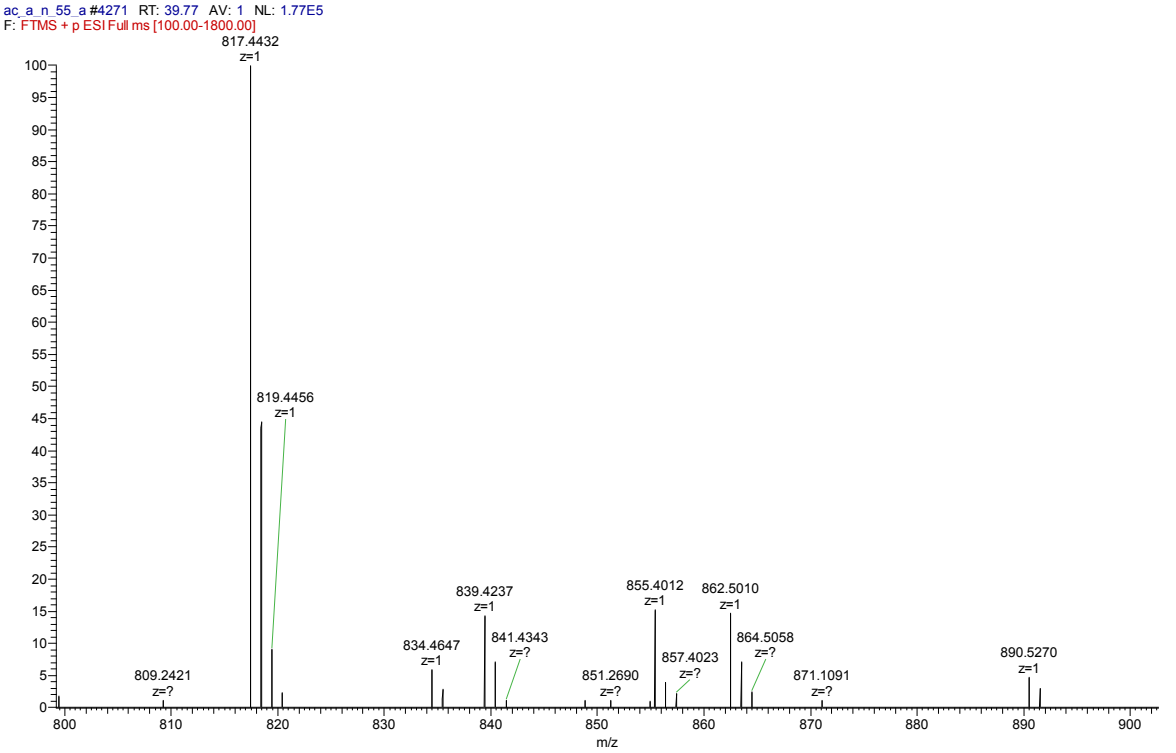

Figure 74. MS 1 spectrum of the *m/z* feature annotated as AC-SC with a *m/z* value of 817.4432 at rt 39.77 min.

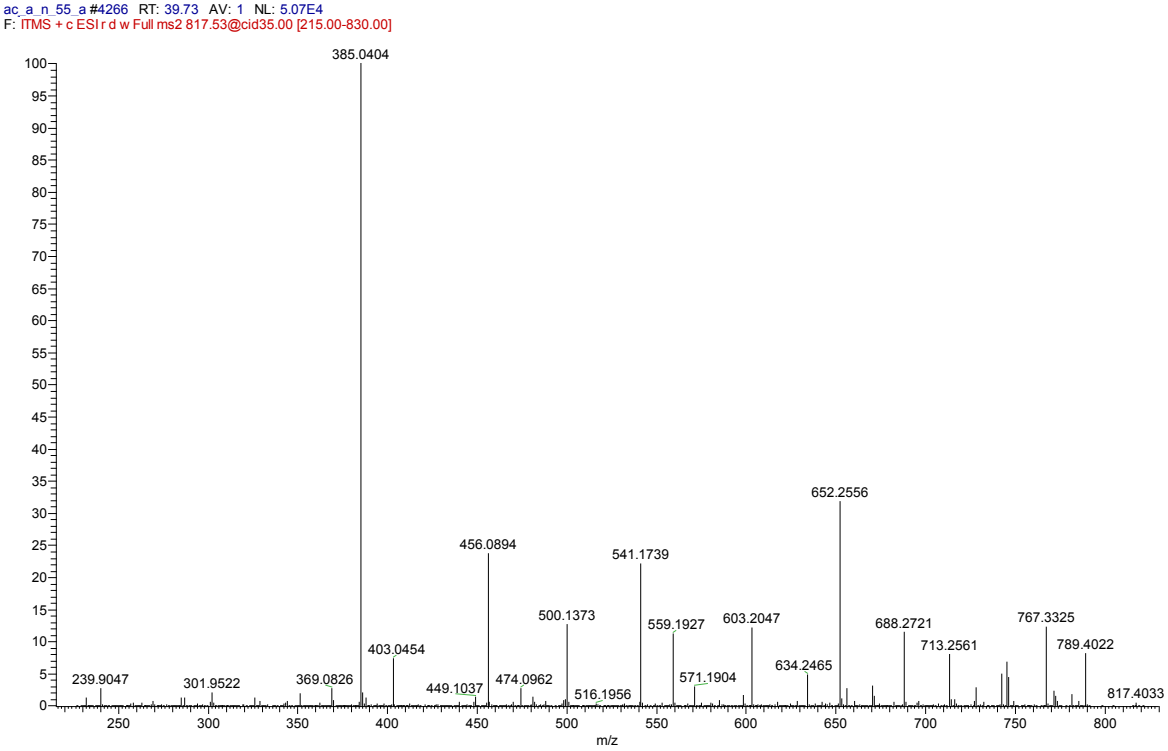

Figure 75. MS 2 spectrum of the *m/z* feature annotated as AC-SC with a *m/z* value of 817.4432 at rt 39.73 min.

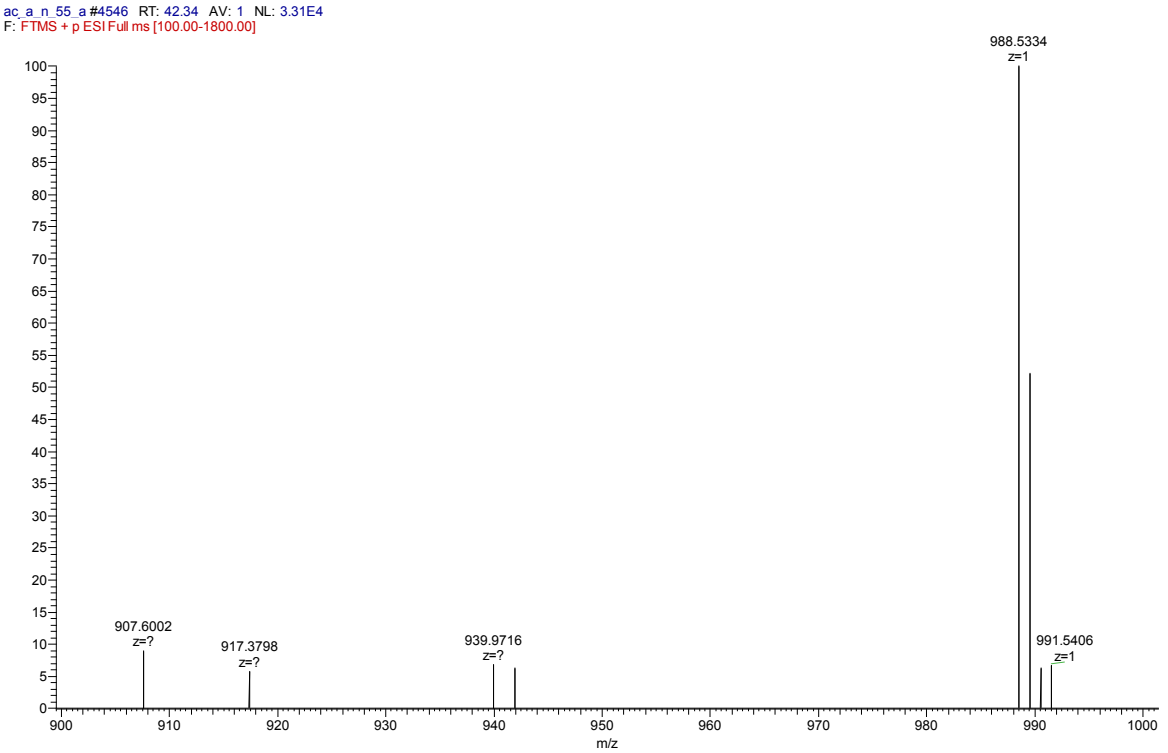

Figure 76. MS 1 spectrum of the *m/z* feature annotated as a putative cyclic-depsipeptide with a *m/z* value of 988.5334 at rt 42.34 min.

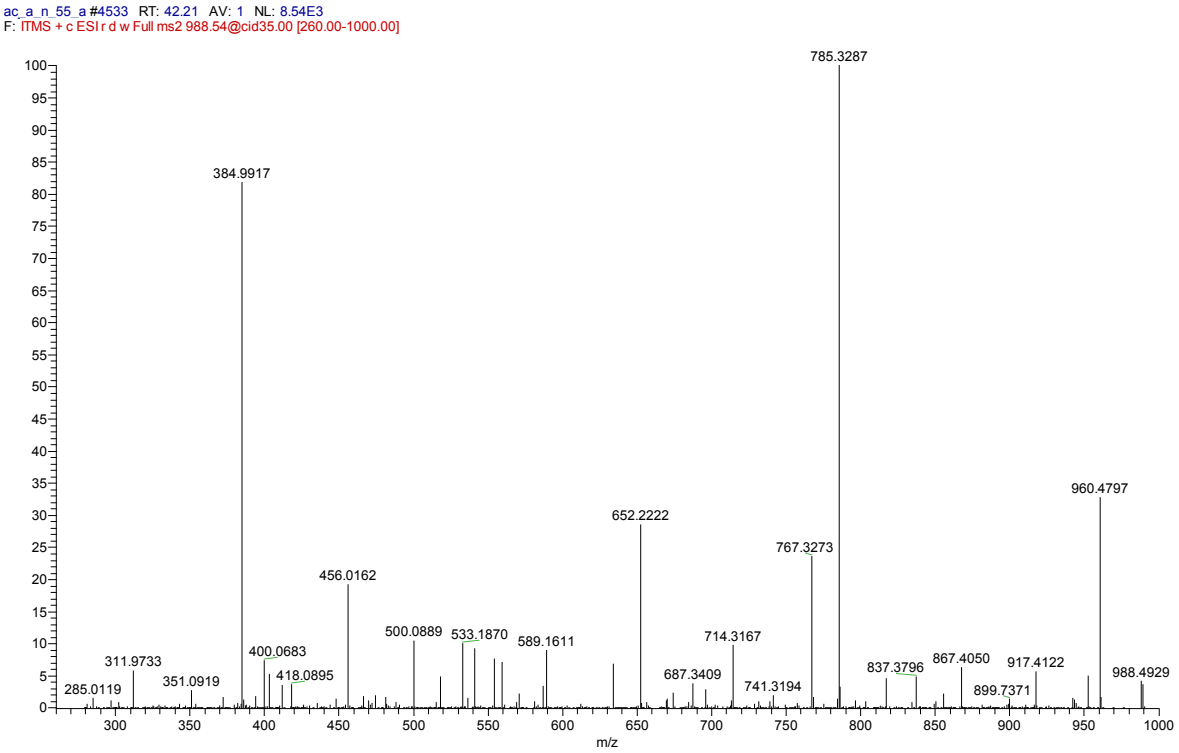

Figure 77. MS 2 spectrum of the *m/z* feature annotated as a putative cyclic-depsipeptide with a *m/z* value of 988.5334 at rt 42.21 min.

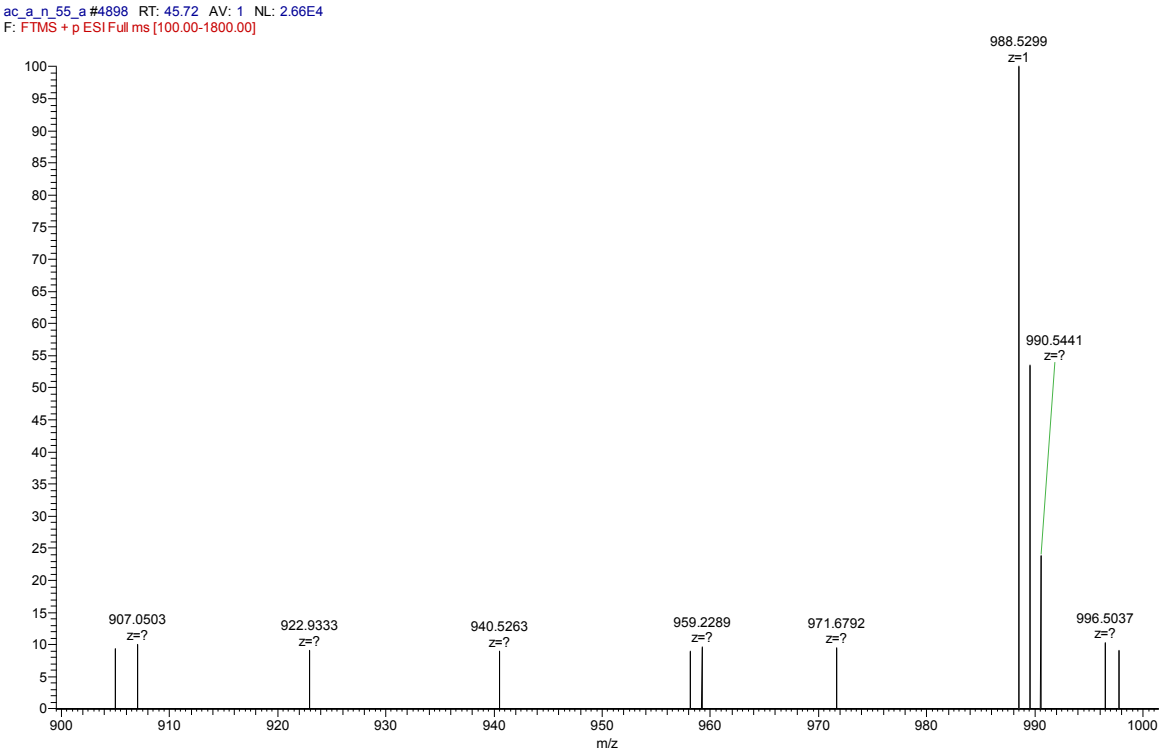

Figure 78. MS 1 spectrum of the *m/z* feature annotated as a putative cyclic-depsipeptide with a *m/z* value of 988.5299 at rt 45.72 min.

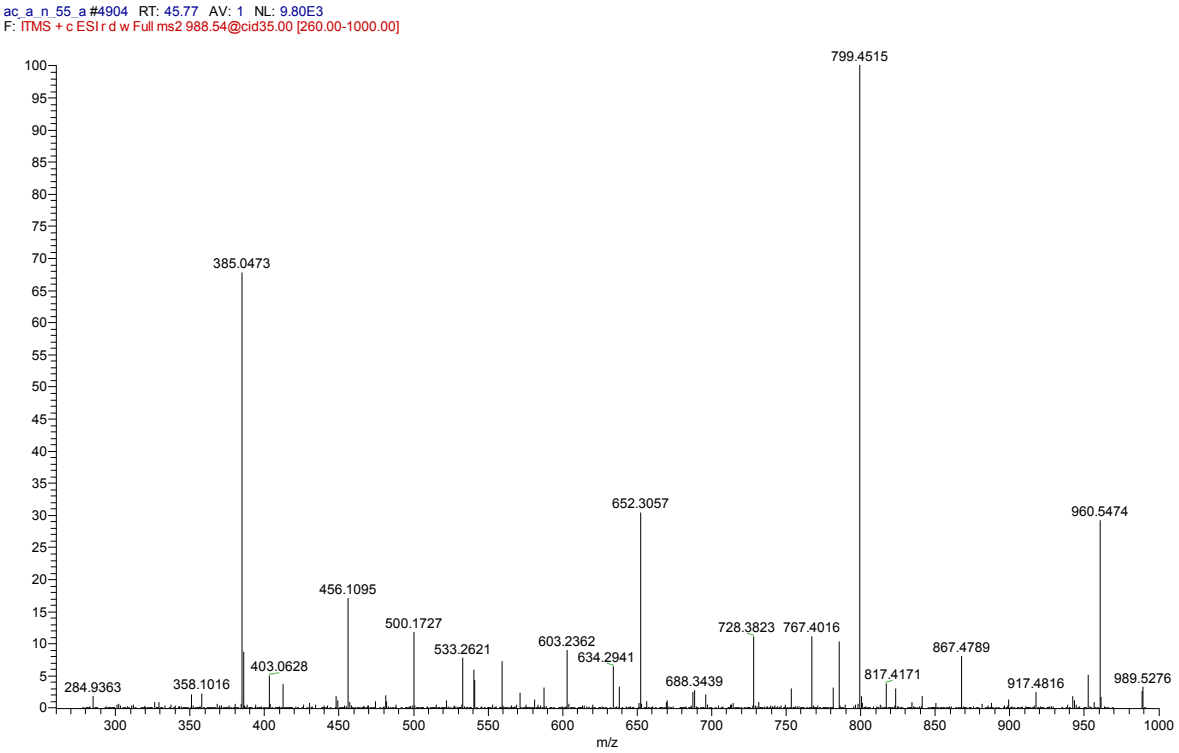

Figure 79. MS 2 spectrum of the *m/z* feature annotated as a putative cyclic-depsipeptide with a *m/z* value of 988.5299 at rt 45.77 min.

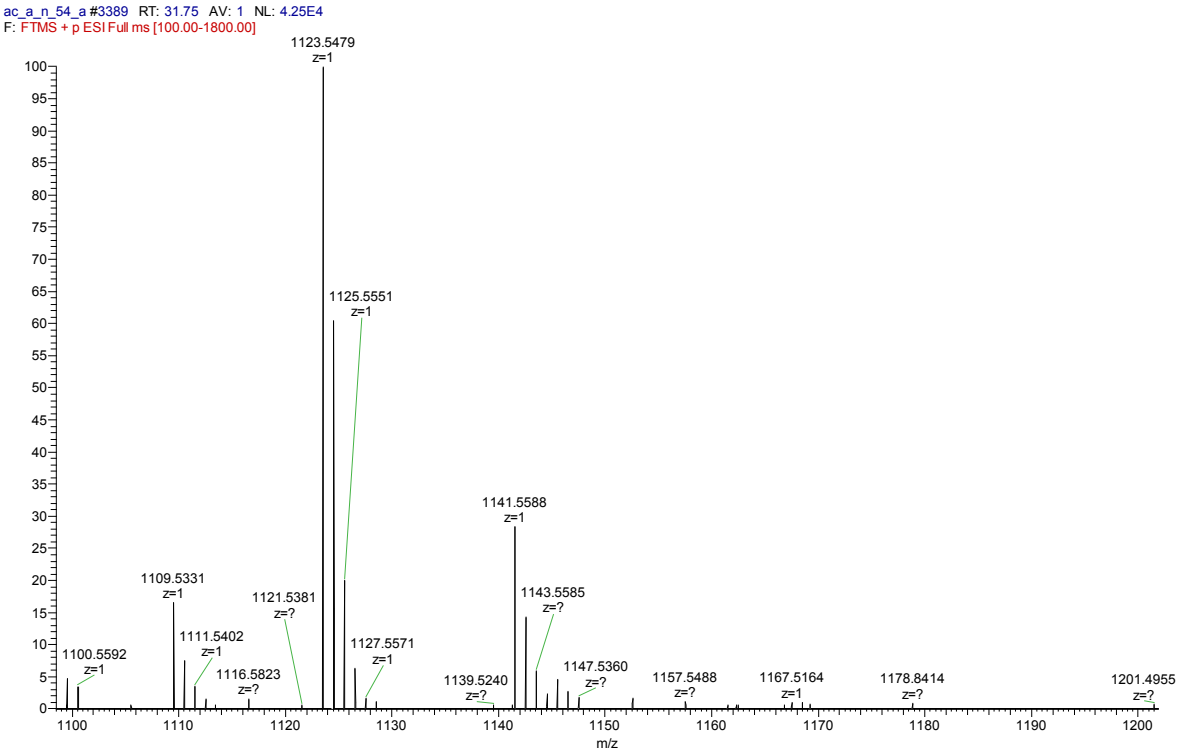

Figure 80. MS 1 spectrum of the *m/z* feature annotated as a putative cyclic-depsipeptide with a *m/z* value of 1123.5479 at rt 31.75 min.

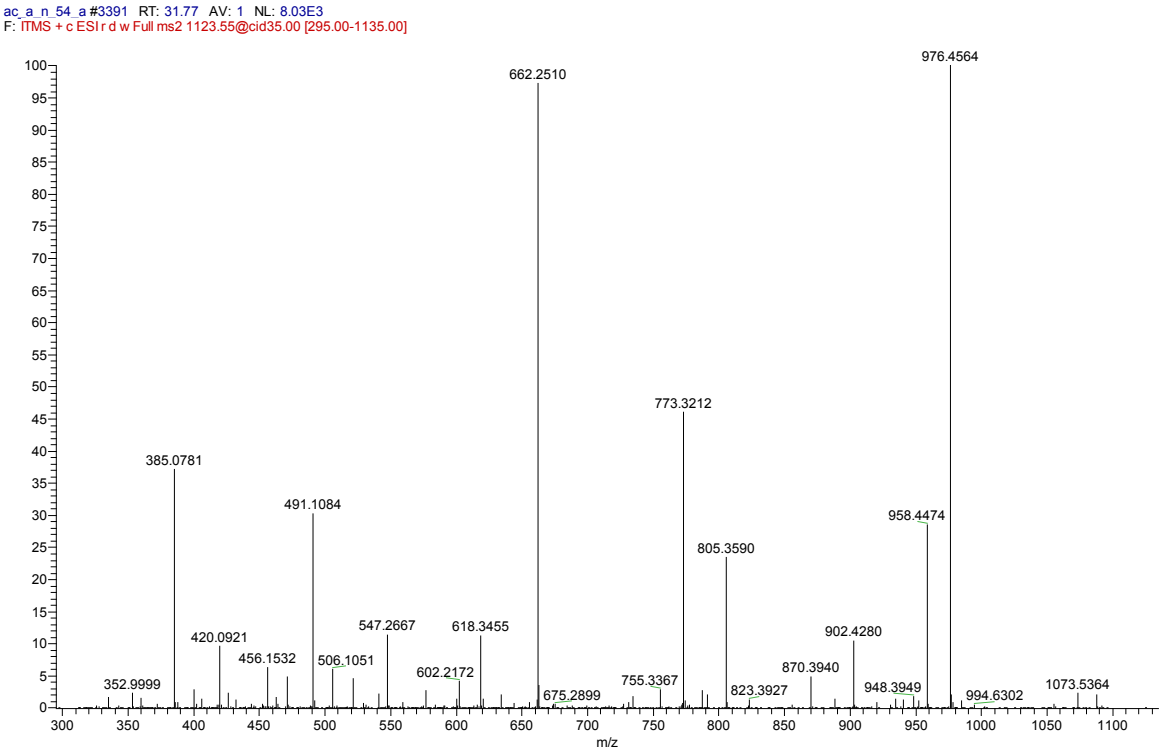

Figure 81. MS 2 spectrum of the *m/z* feature annotated as a putative cyclic-depsipeptide with a *m/z* value of 1123.5479 at rt 31.77 min.

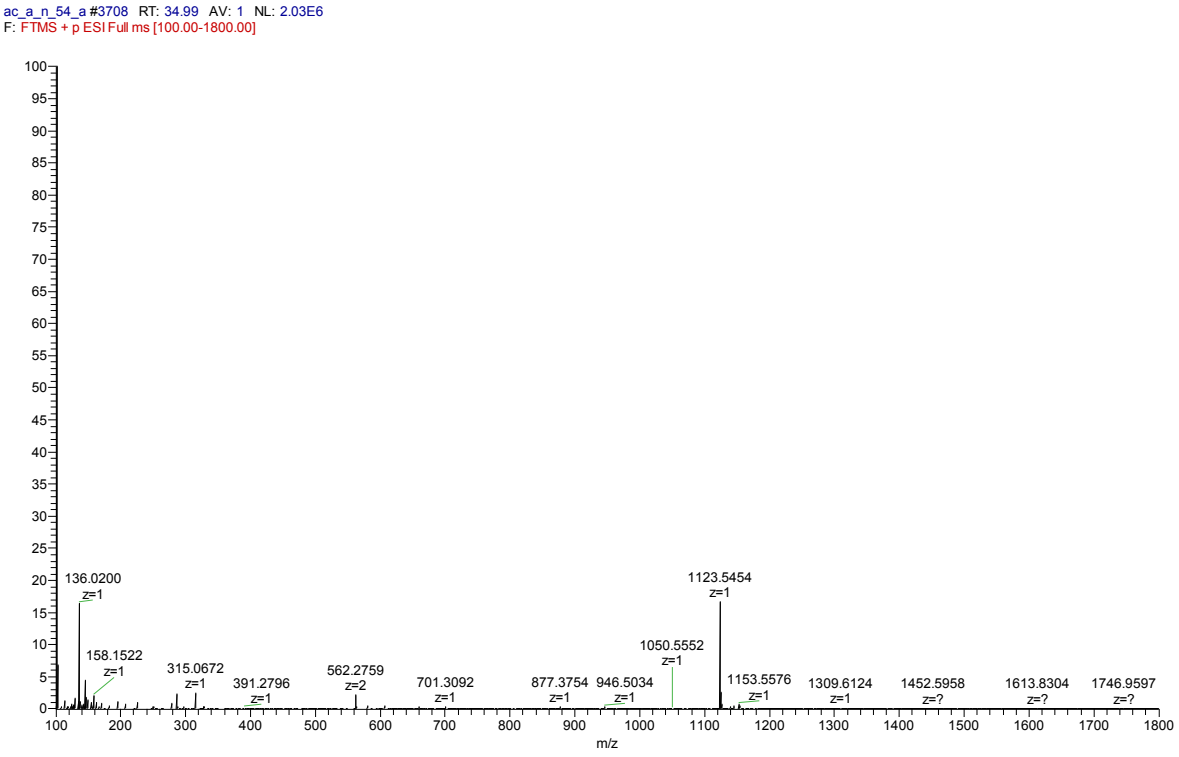

Figure 82. MS 1 spectrum of the *m/z* feature annotated as a putative cyclic-depsipeptide with a *m/z* value of 1123.5454 at rt 34.99 min.

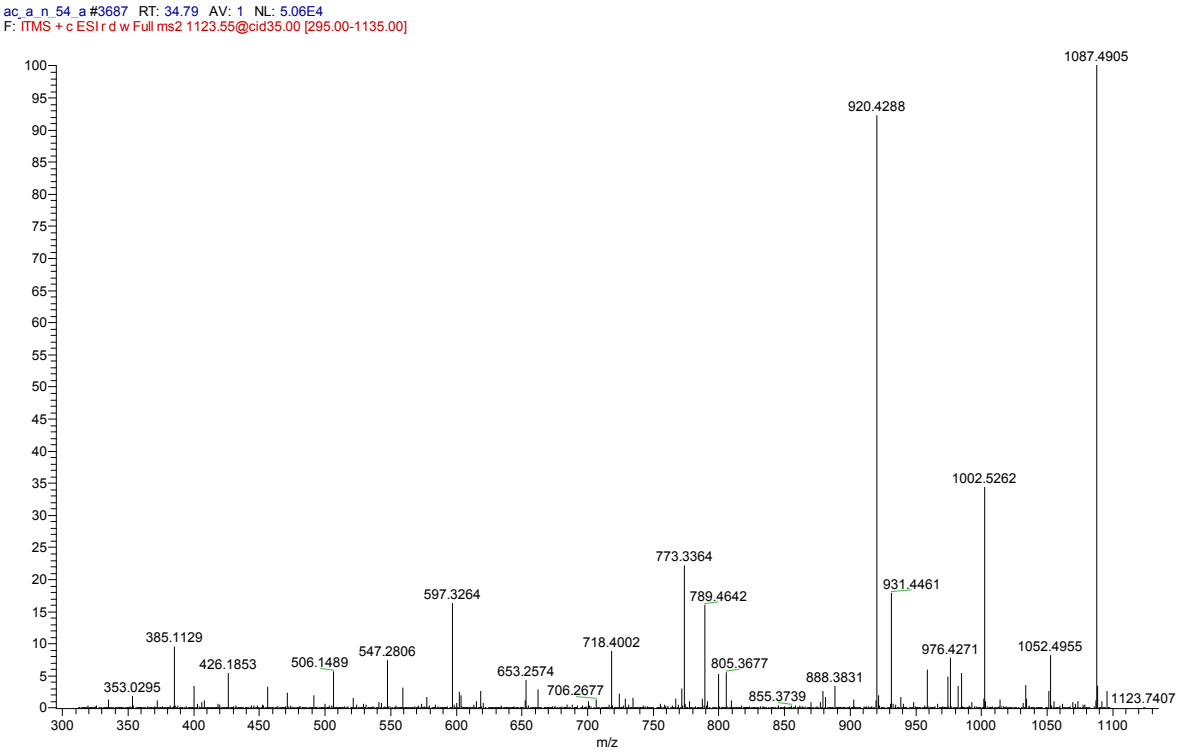

Figure 83. MS 2 spectrum of the *m/z* feature annotated as a putative cyclic-depsipeptide with a *m/z* value of 1123.5454 at rt 34.79 min.

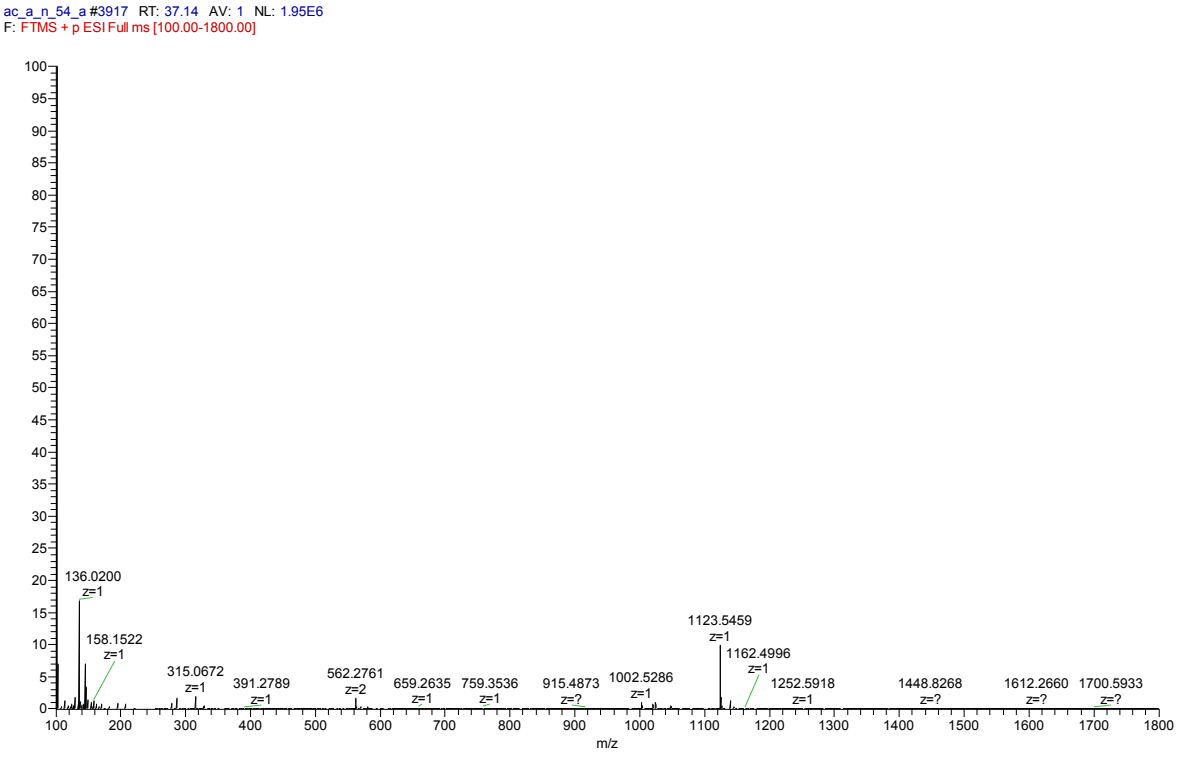

Figure 84. MS 1 spectrum of the *m/z* feature annotated as a putative cyclic-depsipeptide with a *m/z* value of 1123.5459 at rt 37.14 min.

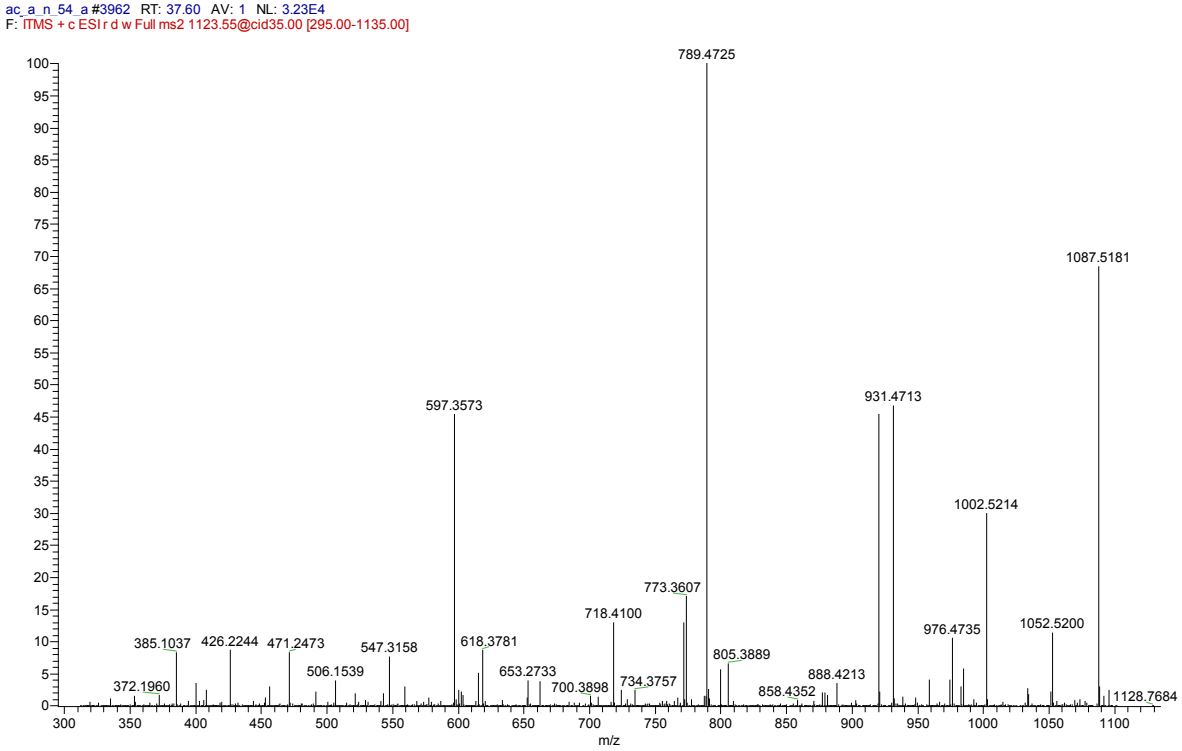

Figure 85. MS 2 spectrum of the *m/z* feature annotated as a putative cyclic-depsipeptide with a *m/z* value of 1123.5459 at rt 37.60 min.

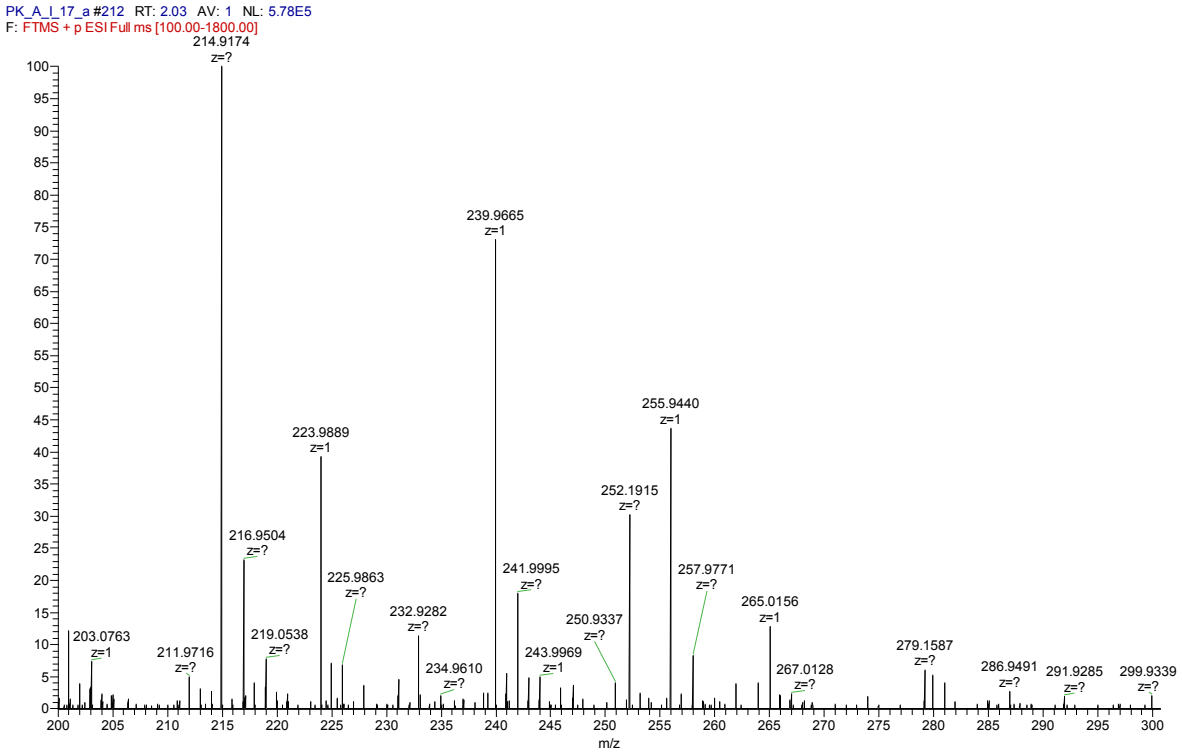

Figure 86. MS 1 spectrum of the *m/z* feature annotated as pavettamine with a *m/z* value of 252.1915 at rt 2.03 min. The *m/z* value lies within 5 ppm of the theoretical *m/z* value.

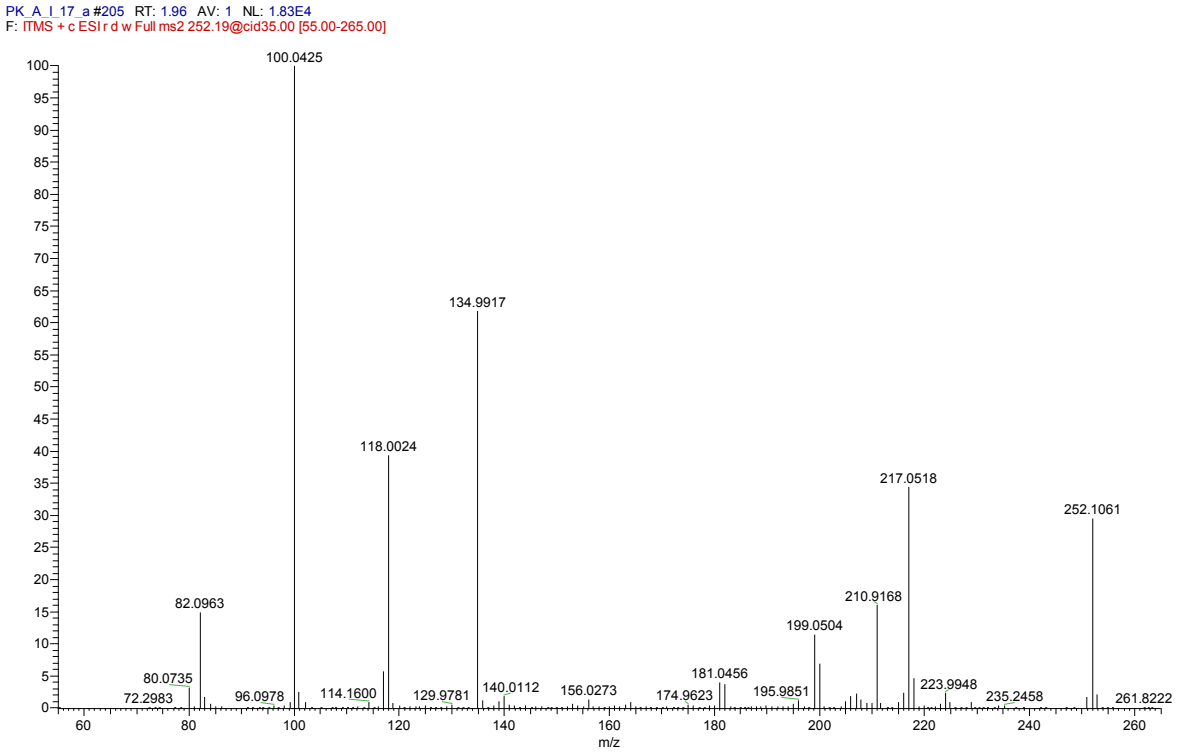

Figure 87. MS 2 spectrum of the *m/z* feature annotated as pavettamine with a *m/z* value of 252.1915 at rt 1.96 min.

III.7.5. Appendix E: MS 1 and MS 2 spectra of the m/z features annotated as putative peptides found in the MS spectra of P. kirkii by manual analysis

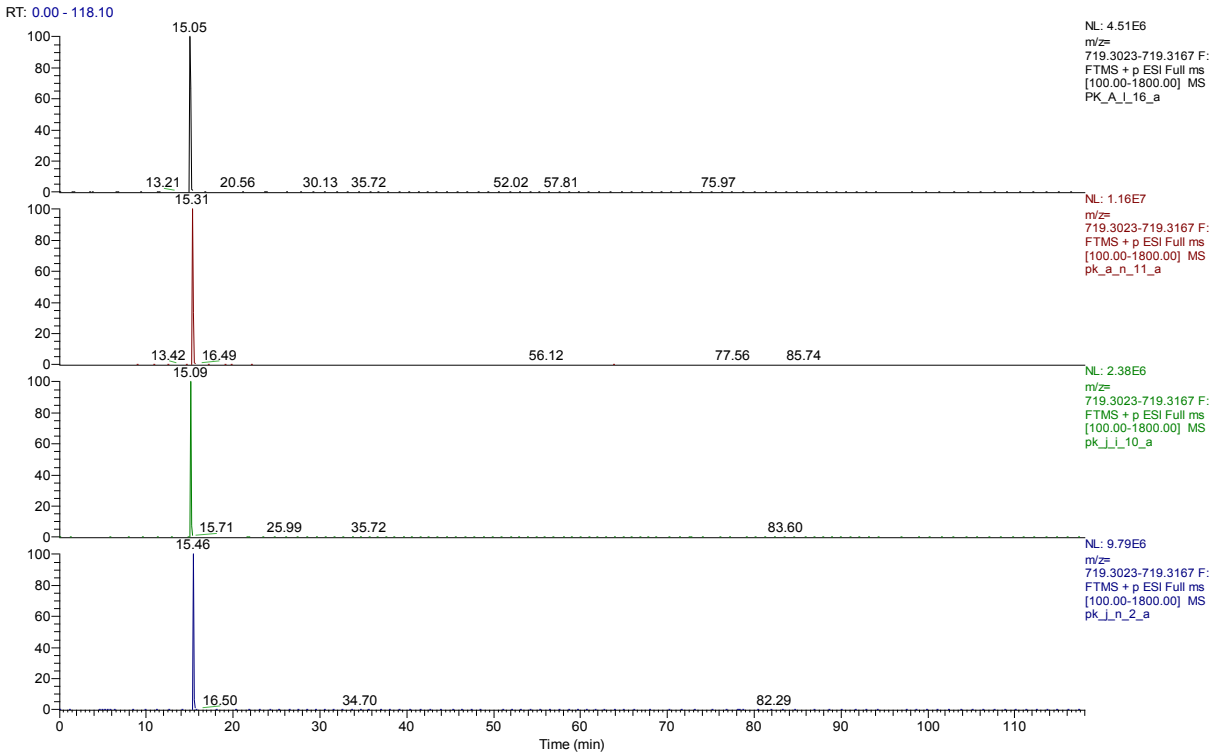

Figure 88. XICs of following *m/z* value for, top to bottom: *P. kirkii* old non-nodulated tissue, *P. kirkii* old nodulated tissue, *P. kirkii* young non-nodulated tissue, *P. kirkii* young nodulated tissue, selected *m/z* value is: 719.3095, rt 15.05 min.

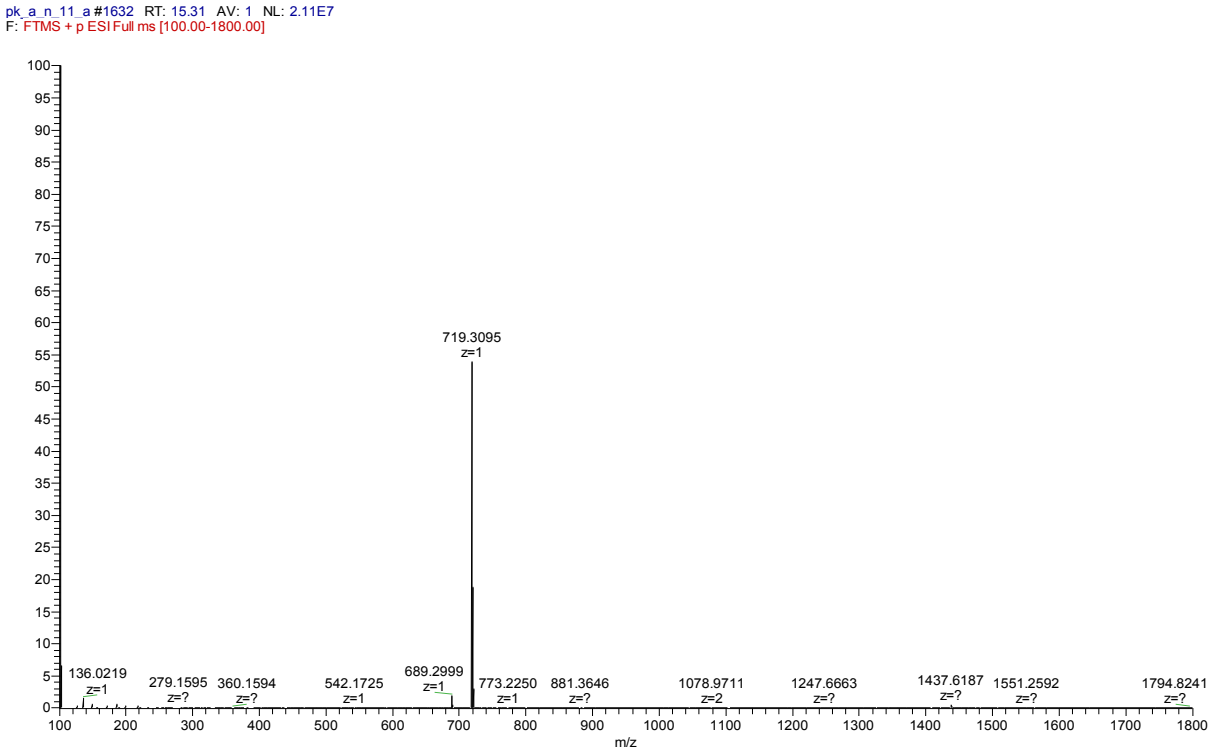

Figure 89. MS 1 fullscan of *P. kirkii* old nodulated tissue at rt 15.31 min showing the *m/z* feature with a *m/z* value of 719.3095.

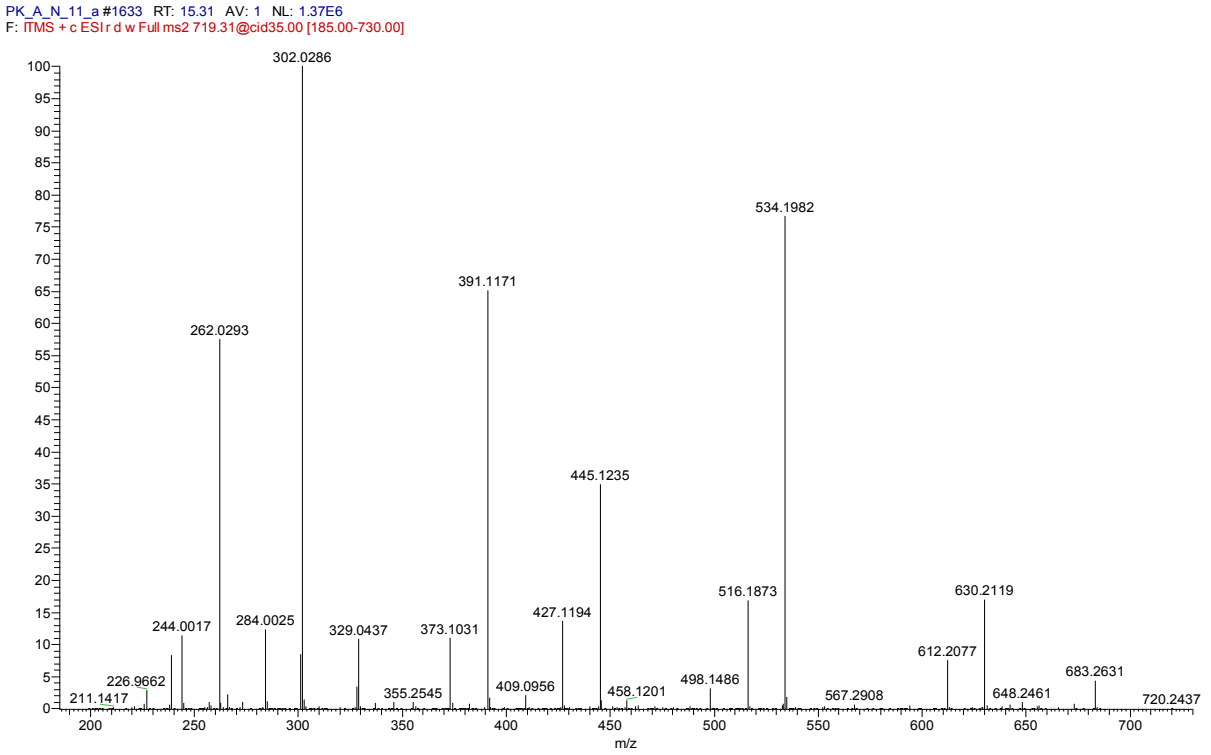

Figure 90. MS 2 of *P. kirkii* old nodulated tissue at *m/z* 719.31 (rt 15.31 min).

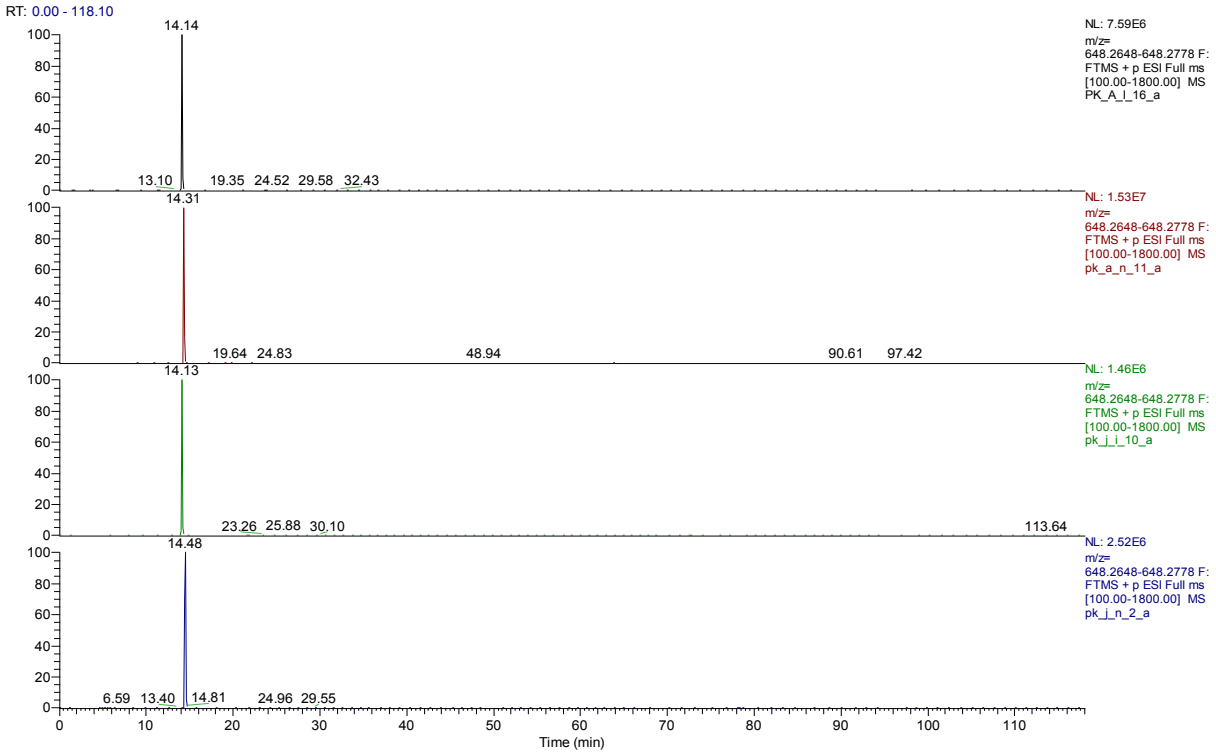

Figure 91. XICs of following *m/z* value for, top to bottom: *P. kirkii* old non-nodulated tissue, *P. kirkii* old nodulated tissue, *P. kirkii* young non-nodulated tissue, *P. kirkii* young nodulated tissue, selected *m/z* value is: 648.2713, rt 14.14 min.

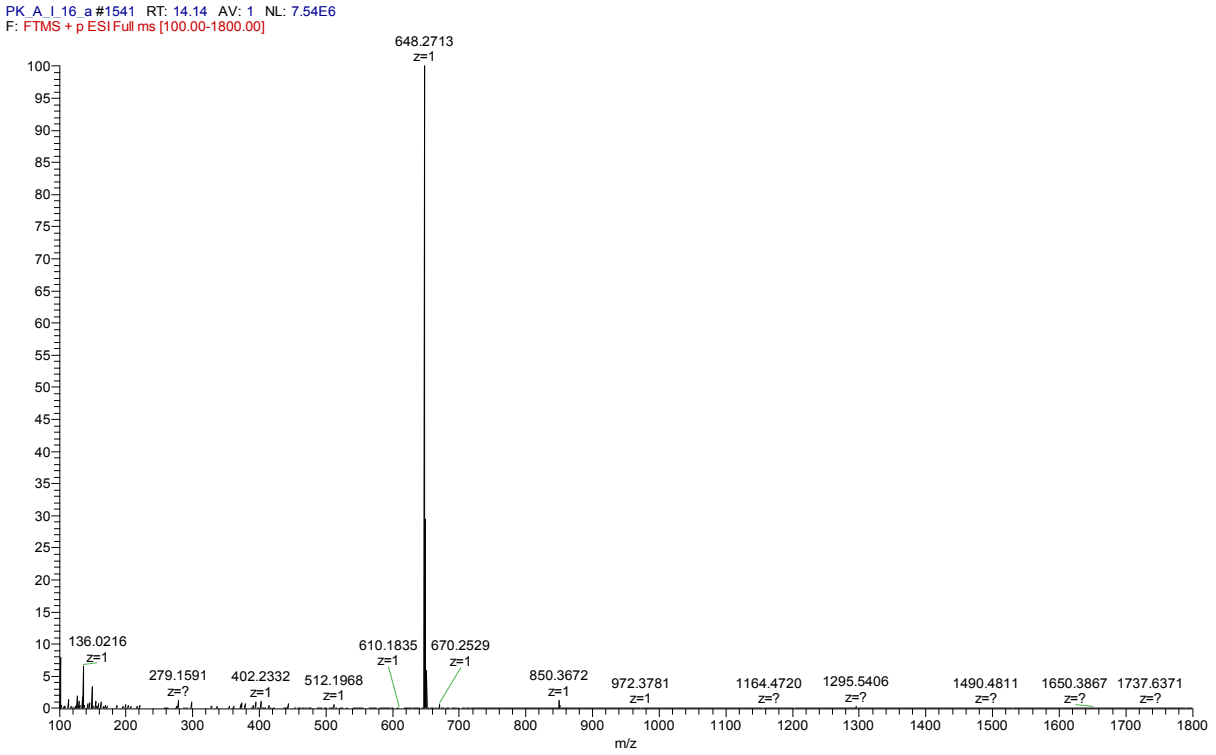

Figure 92. MS 1 fullscan of *P. kirkii* old non-nodulated tissue at rt 14.14 min showing the *m/z* feature with a *m/z* value of 648.2713.

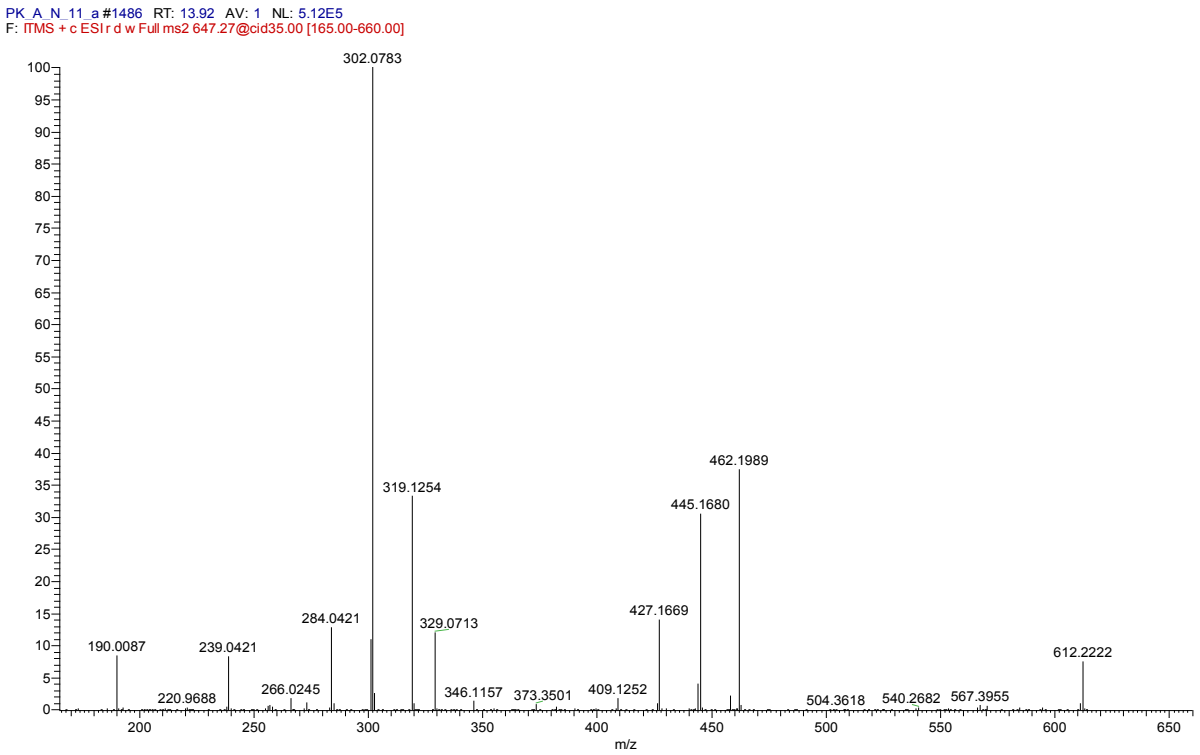

Figure 93. MS 2 of *P. kirkii* old nodulated tissue at *m/z* 647.27 (rt 13.92 min).

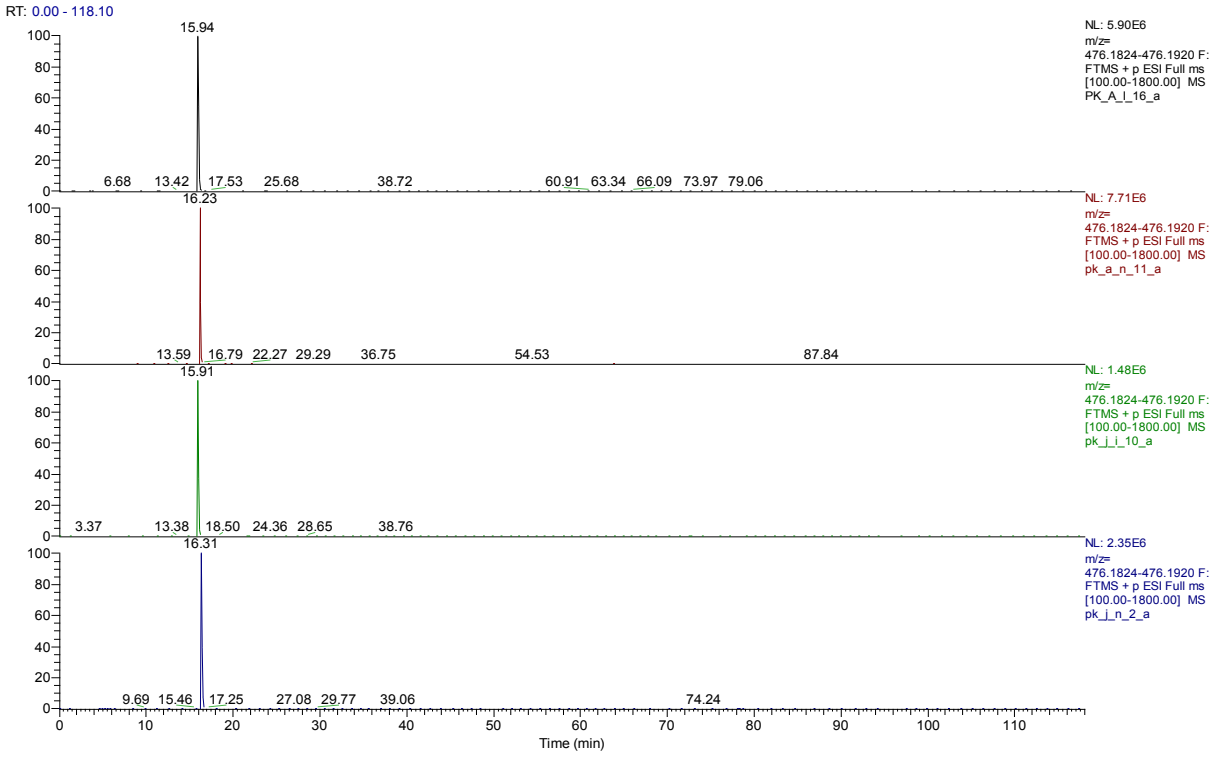

Figure 94. XICs of following *m/z* value for, top to bottom: *P. kirkii* old non-nodulated tissue, *P. kirkii* old nodulated tissue, *P. kirkii* young non-nodulated tissue, *P. kirkii* young nodulated tissue, selected *m/z* value is: 476.1871, rt 15.94 min.

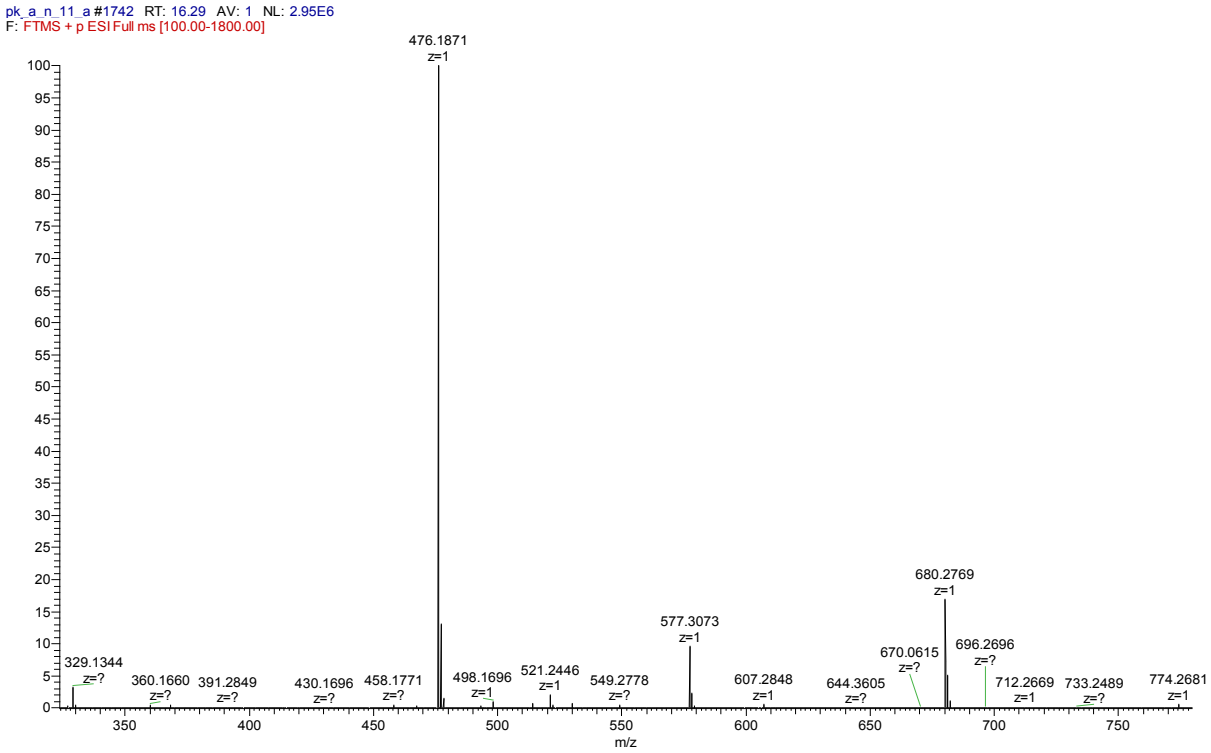

Figure 95. MS 1 fullscan of *P. kirkii* old nodulated tissue at rt 16.29 min showing the *m/z* feature with a *m/z* value of 476.1871.

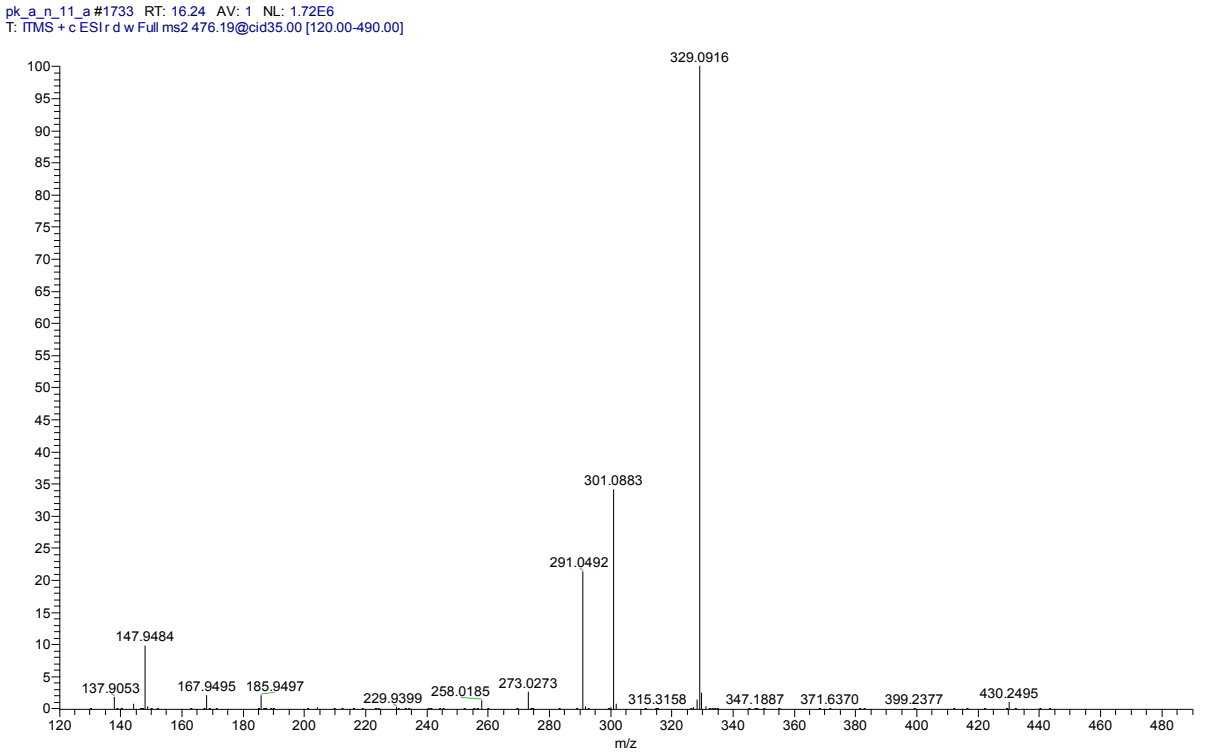

Figure 96. MS 2 of *P. kirkii* old nodulated tissue at *m/z* 476.19 (rt 16.24 min).

III.7.6. Appendix F: Area of the m/z features annotated as putative peptides found in the MS spectra of P. kirkii by manual analysis

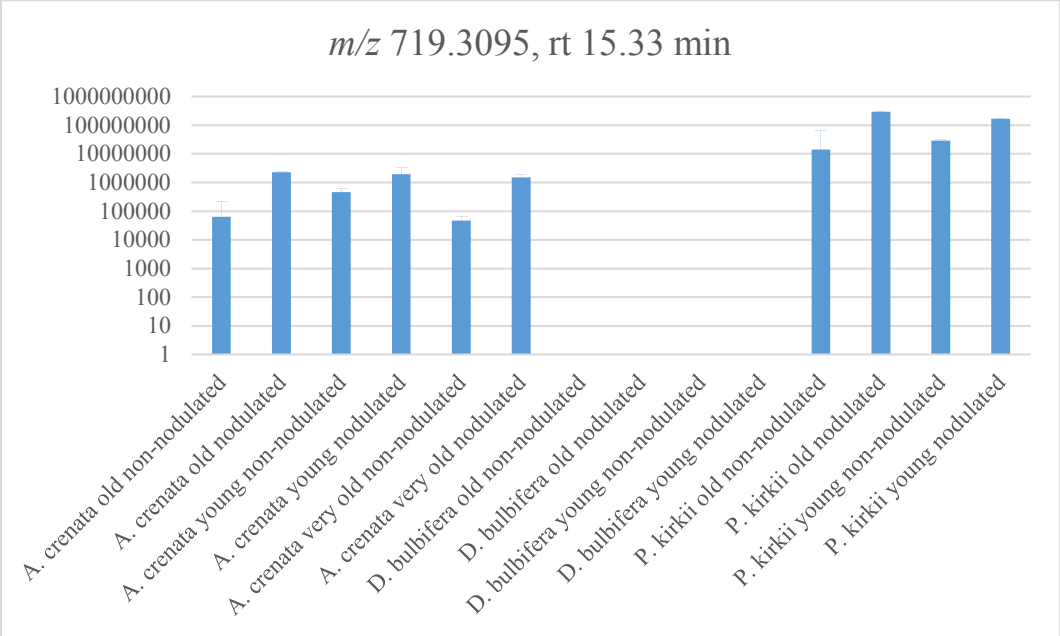

Figure 97. Area of the *m/z* features with a *m/z* value of 719.3095 and rt of 15.33 min annotated as putative peptides found in the MS spectra of *P. kirkii* by manual analysis.

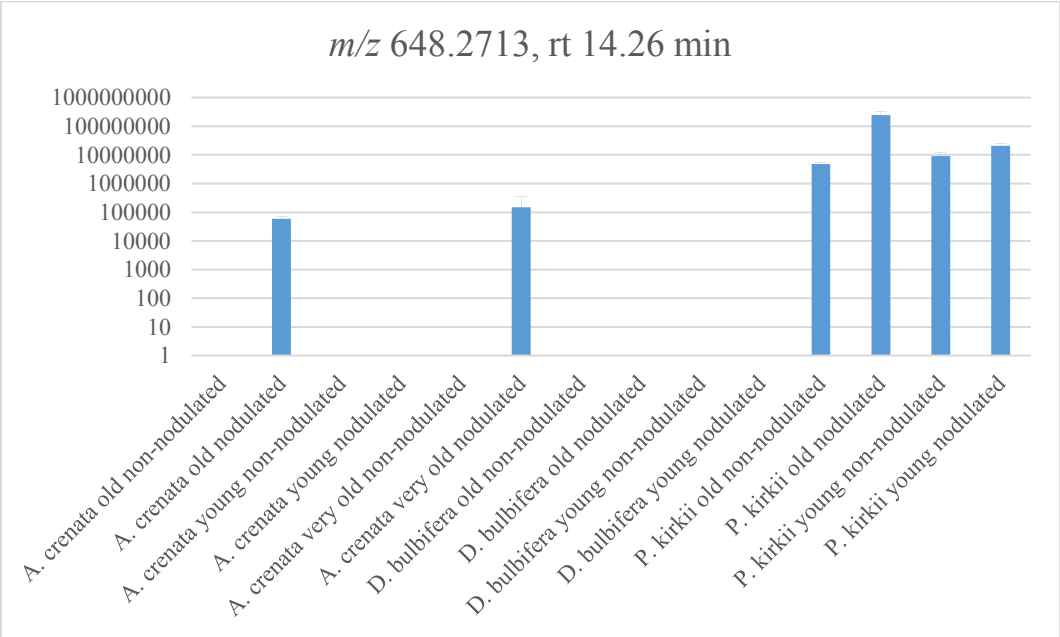

Figure 98. Area of the *m/z* features with a *m/z* value of 648.2713 and rt of 14.26 min annotated as putative peptides found in the MS spectra of *P. kirkii* by manual analysis.

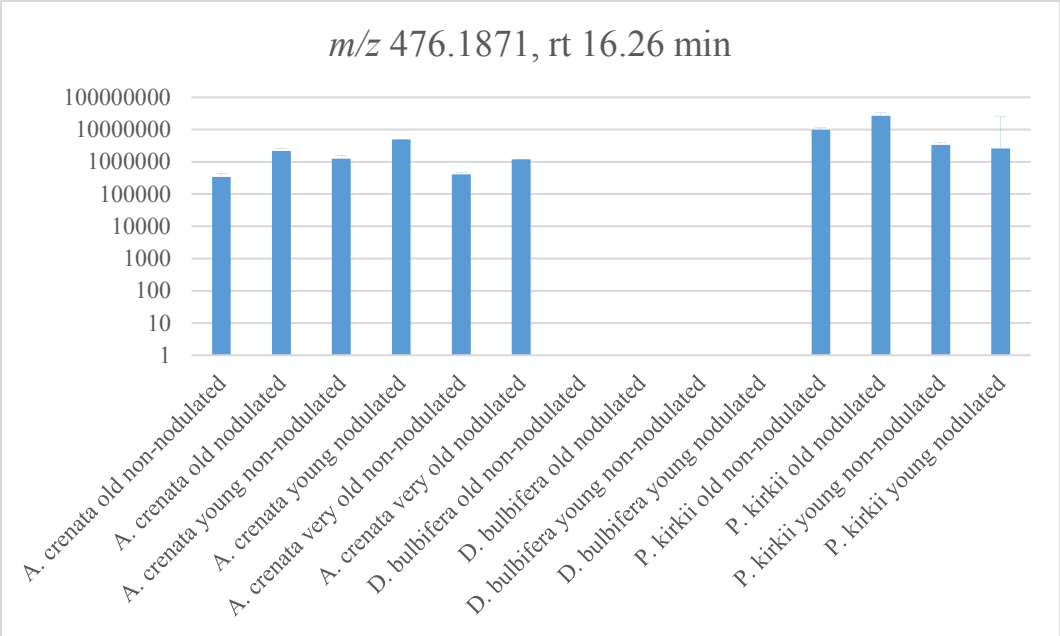

Figure 99. Area of the *m/z* features with a *m/z* value of 476.1871 and rt of 16.26 min annotated as putative peptides found in the MS spectra of *P. kirkii* by manual analysis.

III.7.7. Appendix G: Selected loadings plots of A. crenata of all m/z features corresponding to annotated cyclic-depsipeptides and putative cyclic-depsipeptides including doubly protonated molecular ions and isotope peaks

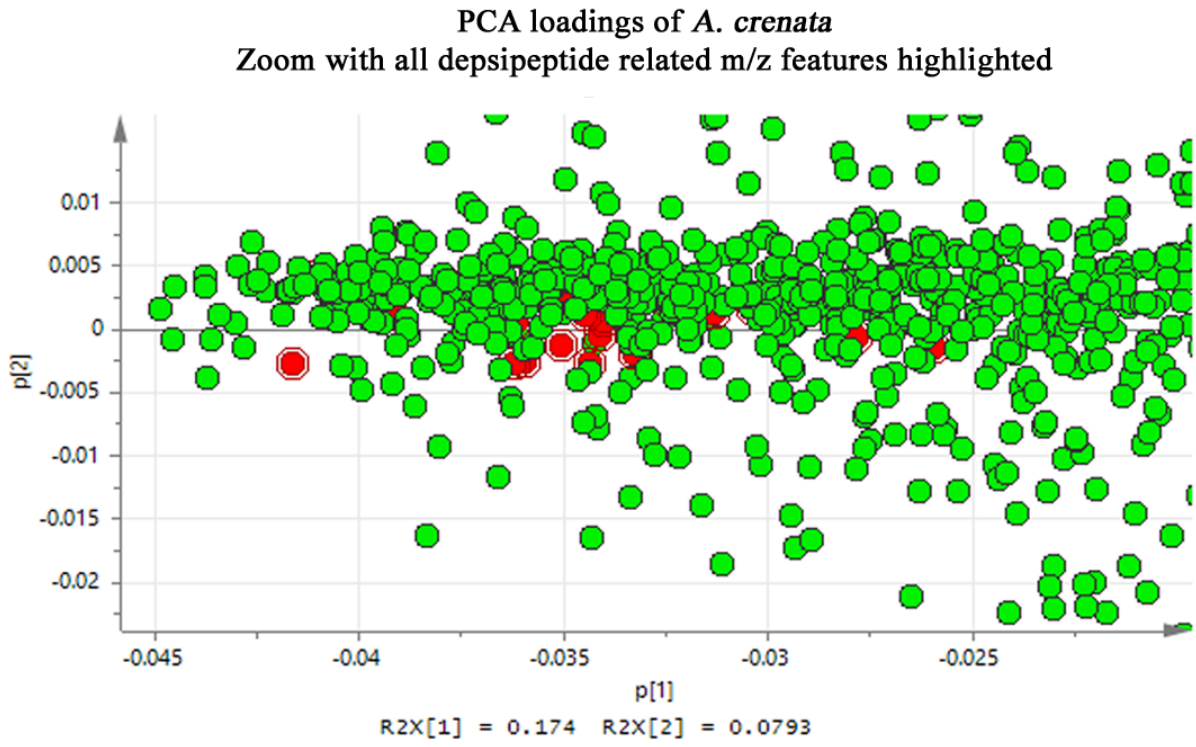

Figure 100. Zoom of the PCA loadings plot of *A. crenata* tissues, the *m/z* features annotated as cyclic-depsipeptides including doubly protonated molecular ions and isotope peaks are highlighted in red.

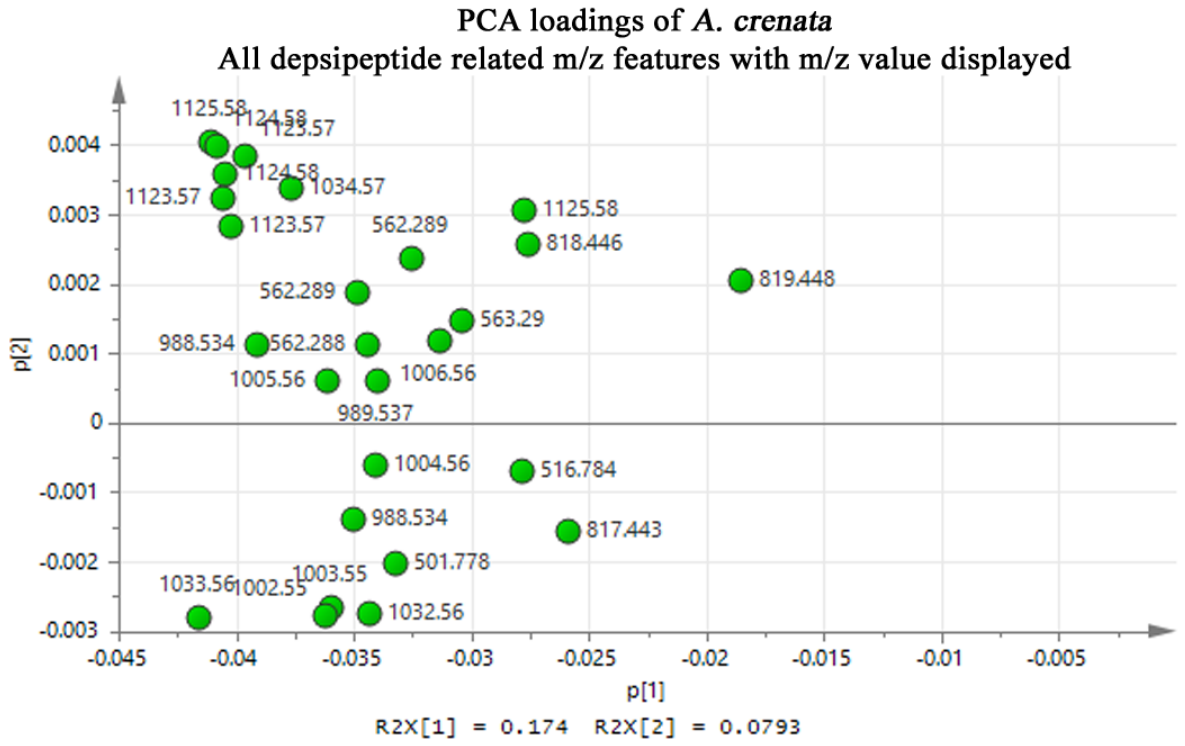

Figure 101. PCA loadings plot of *A. crenata* tissues selectively displaying the *m/z* features annotated as cyclic-depsipeptides including doubly protonated molecular ions and isotope peaks with their *m/z* values.

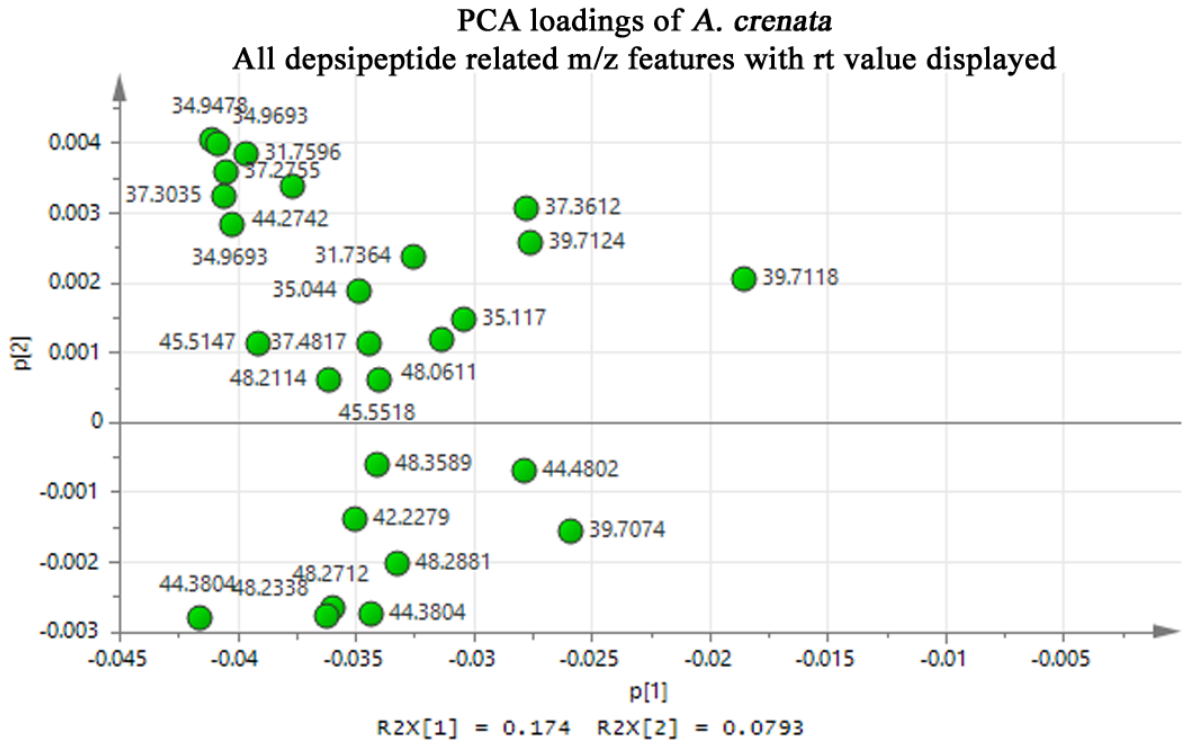

Figure 102. PCA loadings plot of *A. crenata* tissues selectively displaying the *m/z* features annotated as cyclic-depsipeptides including doubly protonated molecular ions and isotope peaks with their rt values.

III.7.8. Appendix H: Table of the highest 25 and lowest 25 PCA loadings for PC1 and PC2 for each species

Table 9
Table of the highest 25 and lowest 25 PCA loadings for PC1 for *A. crenata*, *D. bulbifera* and *P. kirkii*.

Var ID (Primary)	Var ID (Var. Sec. ID:1) *m/z*	Var ID (Var. Sec. ID:2) rt [min]	M1.p[1]	M1.p[2]
4072	318.142	29.1641	-0.0350518	0.00157927
3758	346.137	29.1721	-0.0349176	0.0015715
5457	203.107	29.1947	-0.0348755	0.00145189
4050	319.145	29.1721	-0.0348428	0.00151295
4101	317.139	29.1682	-0.0348154	0.00151559
3767	345.134	29.1721	-0.0347348	0.00158981
5759	185.097	29.1824	-0.0346995	0.00152413
5686	189.07	29.1675	-0.0346252	0.00145376
5480	202.078	29.1588	-0.0345828	0.00146406
4866	249.113	29.1675	-0.0343902	0.00141441
6555	133.102	29.152	-0.0343743	0.00152453
5915	176.063	29.1634	-0.034278	0.00141904
4357	299.129	29.1588	-0.0342173	0.001572
6060	167.086	29.1721	-0.0342032	0.0015115
6442	143.086	29.1588	-0.0341896	0.00142284
1239	706.286	29.16	-0.0340738	0.00126319
6693	121.065	29.152	-0.0338665	0.00135918
1154	734.318	29.1624	-0.0337555	0.00155995
6800	107.086	29.1663	-0.0336636	0.00146582
1754	598.152	15.5604	-0.0334052	0.00121863
4558	281.118	29.1641	-0.0333883	0.00149278
3569	363.164	29.1795	-0.0333405	0.00132284
6344	150.047	29.1588	-0.0333365	0.00132369
6178	159.117	29.1665	-0.0333231	0.00155477
3904	333.133	18.1423	-0.0332545	0.00104181
759	843.33	20.1315	0.0163316	0.000663789
3991	326.116	2.5654	0.0164683	0.0109958
4315	303.05	22.6205	0.01648	0.00649439
4958	242.102	2.4688	0.0165012	0.0170663
4172	314.144	6.1192	0.0165334	0.01777
6262	154.094	5.1172	0.0165536	0.0268458
3613	360.15	2.5674	0.0165971	0.0139094
4593	277.111	12.2885	0.0166281	-0.0132155
5987	171.117	18.976	0.0166394	-0.00597152
6795	109.028	2.6984	0.0166633	0.00622807
3782	343.123	2.574	0.0166753	0.00379099
4510	286.092	2.508	0.016812	0.0256474
6676	123.045	22.6265	0.0168466	0.0259981
3595	361.153	2.5668	0.0171131	0.00493031
6205	158.081	14.0271	0.017449	0.0172067
4201	312.13	6.4913	0.0174881	0.0184738
4169	314.145	3.1218	0.0178378	0.0166522
4355	299.134	2.9868	0.017901	0.00196632
3341	386.165	2.53785	0.0182064	0.000271492
5130	226.152	18.9127	0.0182751	0.00113511
4607	276.108	12.2833	0.0183423	-0.00265014

4660	270.155	9.1148	0.0188014	0.00923827
4317	303.05	20.9235	0.0189464	-0.0172995
3319	388.181	2.5402	0.0196073	0.00469019
3552	365.105	2.4224	0.020305	0.0135915

Table 10
Table of the highest 25 and lowest 25 PCA loadings for PC2 for *A. crenata*, *D. bulbifera* and *P. kirkii*.

Var ID (Primary)	Var ID (Var. Sec. ID:1) *m/z*	Var ID (Var. Sec. ID:2) rt [min]	M1.p[1]	M1.p[2]
5538	198.076	2.8558	0.00860259	-0.0343354
3821	339.107	19.853	0.00536487	-0.0339345
5820	182.081	2.6033	0.0112928	-0.0324323
6667	124.047	2.7474	0.0112195	-0.0320504
6680	123.044	2.7136	0.0122304	-0.0319117
671	874.297	27.159	0.0120264	-0.0318456
5172	224.055	6.5569	0.0122774	-0.0316706
3212	400.218	19.9393	0.0113756	-0.0314182
570	908.302	26.2411	0.0114221	-0.0313934
6241	156.066	2.8577	0.0105154	-0.0313367
4321	302.134	3.2313	0.011208	-0.0309375
6110	164.071	2.724	0.00944444	-0.0306965
2912	432.15	17.508	0.00999108	-0.0306085
5310	212.113	2.8596	0.0113861	-0.0305985
1456	653.205	24.8347	0.0109324	-0.0304393
6647	126.055	2.49295	0.00862491	-0.0303521
3759	346.113	10.7043	0.0117192	-0.0302989
6475	141.055	2.6448	0.00888793	-0.0301877
6621	128.07	2.4007	-0.00353909	-0.0300142
5895	177.076	3.0559	0.00257182	-0.0299804
6193	159.065	2.6026	0.00620209	-0.0296247
618	893.31	26.4045	0.0108095	-0.0295135
668	875.299	25.9212	0.0103725	-0.0293907
4898	247.092	4.4833	0.0109841	-0.0293028
5265	216.05	2.8422	0.0107841	-0.0292607
4009	324.165	16.6191	0.0147253	0.0238479
547	915.198	16.0142	0.00393979	0.0238513
1208	713.276	21.4273	0.0149284	0.0238734
6250	155.081	6.1038	0.0147239	0.0240067
1252	700.356	18.1793	0.013242	0.0240284
5835	181.086	16.3638	0.0133479	0.0240402
2525	481.102	21.1601	0.013632	0.02409
4635	273.079	23.5398	0.01466	0.0242485
4534	284.134	9.77665	0.0155711	0.0243529
6217	157.097	12.6905	0.0136311	0.0244369
1316	686.341	17.8927	0.013835	0.0244683
4112	317.068	24.069	-0.00159599	0.0248217
2465	491.181	17.6817	0.0142003	0.024825
1350	680.197	13.6147	0.0141111	0.0251431
5285	214.107	14.2717	0.0153124	0.0252351

6007	170.118	14.2962	0.0154623	0.0253647
5269	215.111	14.2975	0.0127281	0.0253761
5515	199.116	4.8995	0.0155521	0.0254695
4510	286.092	2.508	0.016812	0.0256474
6676	123.045	22.6265	0.0168466	0.0259981
5536	198.112	4.88175	0.0161758	0.0262118
6249	155.082	9.0137	0.0158697	0.0262877
6262	154.094	5.1172	0.0165536	0.0268458
4763	259.168	17.6987	0.0157784	0.0269532
4637	273.078	22.2728	0.0154477	0.0284368

Table 11
Table of the highest 25 and lowest 25 PCA loadings for PC1 for *A. crenata*.

Var ID (Primary)	Var ID (Var. Sec. ID:1) *m/z*	Var ID (Var. Sec. ID:2) rt [min]	M1.p[1]	M1.p[2]
2122	181.086	16.3638	-0.0448591	0.00157534
417	686.341	17.8927	-0.0445423	-0.000792773
153	956.475	28.7263	-0.0445034	0.00334391
609	571.208	17.6689	-0.0437642	0.0040798
1690	263.091	14.4955	-0.0437172	0.00330151
440	680.197	13.6147	-0.0436886	-0.00393458
391	700.356	18.1793	-0.0436047	-0.000881043
2311	152.092	2.2597	-0.043402	0.000992471
1284	343.139	16.3531	-0.0429765	0.000470378
963	426.201	21.4044	-0.0429635	0.00495869
387	702.336	17.7708	-0.0427782	-0.00143109
2447	126.101	19.8153	-0.0426512	0.00342791
792	491.181	17.6817	-0.0426146	0.0068577
2458	123.081	19.0065	-0.0424628	0.00371202
385	703.34	17.7542	-0.0422298	0.0029815
152	956.475	28.2492	-0.0421965	0.00520466
980	424.185	21.5494	-0.0418456	0.00100589
1394	321.158	18.3623	-0.0417264	0.00299968
2248	161.129	2.98235	-0.0417179	0.0029901
97	1033.56	44.3804	-0.0415957	-0.00279525
1805	233.186	12.541	-0.0415943	0.0028739
2281	156.074	13.2387	-0.041541	0.00326563
2095	186.076	12.2734	-0.0414744	0.00481385
2332	148.098	18.6627	-0.0412911	0.00345321
39	1125.58	34.9478	-0.0411104	0.00403332
1754	249.039	14.3703	0.0246911	-0.0047233
2229	165.055	18.2052	0.0248396	-0.0339428
2038	195.029	14.4325	0.0250782	0.0141821
333	748.271	25.142	0.0251558	-0.019269
1795	237.039	14.3723	0.0252948	-0.00900939
1637	279.05	14.3694	0.0253136	-0.0110776
2288	155.034	2.859	0.0253467	0.000236408
1667	271.063	19.9982	0.0254952	-0.0135366
2300	153.02	17.456	0.0258239	0.0133637

764	498.26	22.8961	0.025958	0.026254
1552	297.061	14.3694	0.0259587	0.00110584
1348	332.098	14.3713	0.0261287	-0.00316078
662	540.245	19.4678	0.0263692	0.0139682
359	720.334	26.3338	0.0265687	0.0346709
266	806.337	26.8877	0.0267826	0.0176946
2395	139.04	20.0268	0.0270022	-0.0119156
2434	130.05	2.3526	0.0276135	0.0210265
1595	288.059	22.39	0.0281152	-0.0103986
1747	249.112	22.34	0.0290022	0.0398164
1654	275.056	17.2095	0.0290198	0.0242573
1437	316.074	14.3669	0.0295244	-0.00662427
264	806.337	27.2526	0.030067	0.0168665
1891	220.107	19.5207	0.0302032	-0.00279626
1442	315.071	14.3669	0.0309991	0.00224083
1895	219.104	19.509	0.0315889	0.00885224

Table 12
Table of the highest 25 and lowest 25 PCA loadings for PC2 for *A. crenata*.

Var ID (Primary)	Var ID (Var. Sec. ID:1) *m/z*	Var ID (Var. Sec. ID:2) rt [min]	M1.p[1]	M1.p[2]
1136	378.139	7.1298	0.0143972	-0.056355
2	1523.3	18.411	0.0191481	-0.0551123
2039	195.029	5.77285	0.0182191	-0.054812
1344	333.081	5.7816	0.0202521	-0.0543992
1443	315.071	5.8314	0.0149675	-0.0533101
25	1219.26	14.1751	-0.00132053	-0.0523175
2093	186.112	2.86955	0.0147031	-0.0513162
1803	235.024	5.8845	0.0179452	-0.0512605
2234	164.107	4.55105	0.00218312	-0.0512056
1796	237.039	5.8014	0.0144747	-0.0509361
2202	170.089	2.9451	0.0190022	-0.050786
23	1220.26	14.1193	-0.00100609	-0.0504252
2111	182.118	2.9939	0.0146985	-0.0499324
2215	168.102	2.8848	0.0196986	-0.0489723
990	422.129	7.15295	0.00420419	-0.0483587
668	536.117	24.7575	0.013723	-0.048254
1899	219.029	5.77285	0.0134413	-0.0481144
1764	246.061	2.5239	0.0132962	-0.0478523
2312	152.079	2.93755	0.0187551	-0.0475422
1755	249.039	5.8014	0.0168108	-0.0472253
2035	196.032	5.8257	0.0136776	-0.0471019
2167	175.039	5.99975	0.0164949	-0.0469956
2335	148.076	2.90345	0.0151129	-0.0467859
1918	214.107	2.8761	0.0201772	-0.0460479
1553	297.06	5.76025	0.0134806	-0.04564
432	681.276	22.935	0.016404	0.0497986
2158	175.148	17.8893	0.0186697	0.0502213
2065	190.131	19.4037	0.0220602	0.0504996

399	697.271	19.374	0.0189028	0.0507124
1072	392.191	14.9534	0.00572989	0.050732
2247	161.133	16.5954	0.0226514	0.0513116
1022	408.263	22.895	-0.000480496	0.0514858
1962	207.138	19.1203	0.0152706	0.0516128
1203	362.145	14.0553	-0.00808221	0.0517158
1787	240.116	4.4295	0.011288	0.0518374
211	859.331	19.3535	0.0159187	0.0520044
1964	207.138	16.5715	0.0193104	0.0522378
2190	171.117	18.976	0.0168244	0.0526576
220	843.33	20.1315	-0.000673572	0.0528305
2057	191.143	14.6297	0.0173351	0.0528509
1121	381.235	22.8749	-0.000809154	0.0531623
2006	200.092	13.8678	0.00979429	0.0532978
430	681.276	22.0907	0.0120595	0.0534983
2056	191.143	15.7453	0.0158177	0.0542483
1519	302.123	16.349	0.0222881	0.0544369
842	468.28	16.5443	0.0219827	0.0546975
447	676.271	19.5068	0.0135844	0.0575902
2069	189.128	19.0123	0.0188772	0.0577691
1746	249.112	19.3556	0.0194563	0.0583796
1947	209.154	15.7358	0.00845216	0.058856

Table 13
Table of the highest 25 and lowest 25 PCA loadings for PC1 for *D. bulbifera*.

Var ID (Primary)	Var ID (Var. Sec. ID:1) *m/z*	Var ID (Var. Sec. ID:2) rt [min]	M1.p[1]	M1.p[2]
395	851.22	20.864	-0.0374273	0.00205612
390	852.223	22.7342	-0.0364874	0.00156677
1999	275.124	2.89235	-0.035771	0.00125699
2007	274.092	3.8441	-0.0356193	-0.00297736
949	547.16	23.6862	-0.0354552	0.00325171
414	835.223	22.2406	-0.0354092	0.0063086
397	851.22	19.2788	-0.0351901	-0.00462096
2306	218.103	19.8912	-0.0349959	-0.00298141
389	852.223	19.5627	-0.0349064	-0.00277628
2085	259.092	2.93145	-0.034581	-0.00960934
410	835.225	23.9869	-0.0345731	0.00379962
1922	292.09	18.084	-0.0344257	-0.00525565
2212	233.077	2.9135	-0.0343785	-0.00660307
2318	216.087	8.1565	-0.0343138	-0.0078391
1927	291.087	18.0868	-0.034285	-0.00431992
2111	255.098	2.8915	-0.0342311	-0.00893246
2369	208.046	10.5887	-0.0342008	-0.0018956
2578	186.076	2.5635	-0.0339012	0.0042393
2174	241.155	5.4478	-0.0336793	-0.0045465
2331	213.112	16.9009	-0.0335986	0.00886414
1688	330.139	2.8719	-0.0334303	0.00208697
373	867.214	21.4395	-0.0333693	-0.0161421

2760	168.066	2.5729	-0.0333508	-0.000534814
2107	256.093	2.7565	-0.0330983	-0.00176658
394	851.221	22.461	-0.0330828	-0.00913118
766	600.413	65.8978	0.032088	0.00484068
554	724.572	83.9163	0.0321148	-0.00666544
2262	224.077	2.6026	0.0322616	-0.00904061
1636	335.259	69.2532	0.0322674	-0.00755091
383	854.578	74.2453	0.0322944	0.000484321
423	819.528	85.0574	0.0322955	0.00345997
66	1204.27	16.4016	0.0323577	0.00231856
91	1187.27	16.3351	0.0323667	-0.0168044
788	597.394	58.0392	0.0323998	-0.00420857
298	902.212	15.1055	0.0325724	0.00549559
736	611.139	13.5692	0.0326298	0.00627136
65	1204.27	17.132	0.0326981	-0.00134619
471	792.563	74.267	0.0328111	-0.0113494
61	1205.27	15.3579	0.0328248	0.00989672
1430	382.082	2.41	0.0331684	-0.0174293
974	534.489	74.6668	0.0332315	-0.0127806
2809	163.039	24.4265	0.0333519	0.00403599
509	762.492	65.4957	0.0334336	0.00707939
778	599.409	66.6245	0.0337453	0.00190934
2173	242.087	2.7931	0.0338253	-0.0144924
1425	383.077	2.4263	0.03427	-0.00367198
468	793.567	74.2629	0.0348652	-0.0104809
1437	381.078	2.4049	0.0351752	-0.00317432
289	915.198	16.0142	0.0352183	-0.00202021
938	552.428	68.843	0.0353094	0.00741526

Table 14
Table of the highest 25 and lowest 25 PCA loadings for PC2 for *D. bulbifera*.

Var ID (Primary)	Var ID (Var. Sec. ID:1) *m/z*	Var ID (Var. Sec. ID:2) rt [min]	M1.p[1]	M1.p[2]
827	593.129	16.4041	0.00559398	-0.0443603
2060	263.087	2.8489	0.00558486	-0.0440986
1497	364.166	29.1665	-0.00801469	-0.0434744
2161	245.044	16.3924	0.00792337	-0.0427246
1503	363.164	29.1795	-0.0128727	-0.0417971
1877	301.138	29.176	-0.00193391	-0.0416934
1105	470.224	22.527	0.00833719	-0.0413139
1511	362.16	29.1646	-0.014848	-0.0398568
2568	187.108	2.55875	-0.0127513	-0.0395865
671	633.203	25.6005	-0.00215943	-0.0391941
1532	360.15	2.5674	-0.0099271	-0.0391935
2220	231.099	2.2513	0.00644099	-0.0388588
1243	424.201	22.886	0.00930734	-0.0384281
2534	190.071	4.5967	0.00778359	-0.0377388
1836	306.101	7.28885	-0.0101742	-0.0373326
1461	377.127	20.6661	-0.00682167	-0.0371058

1459	377.163	30.1983	0.0115762	-0.0367689
1472	375.147	21.3257	-0.00773179	-0.03656
1543	358.135	2.5402	0.00462128	-0.0364482
2813	162.113	2.7801	-0.0187148	-0.0362915
3170	118.065	29.1432	-0.0145394	-0.0360423
1362	396.166	22.8535	-0.0139691	-0.035972
1552	355.106	24.444	0.0162707	-0.0359217
2957	146.165	2.223	-0.0172015	-0.0358284
1250	423.071	15.1542	0.00806857	-0.0355144
2042	266.244	2.3881	0.00771689	0.0409796
2641	181.065	29.154	-0.00455918	0.04126
2922	151.035	2.0462	0.00704623	0.0413939
3086	130.078	29.1682	-0.00765223	0.0414513
2592	185.06	29.176	-0.00459787	0.0415583
2410	203.086	29.1575	-0.00340611	0.0419959
2371	207.117	29.1682	-0.0036527	0.0420085
2535	190.065	29.1888	-0.00392671	0.0425263
2333	213.091	29.16	-0.0120995	0.043292
1128	462.249	25.1175	0.000135925	0.0433828
2667	178.078	29.1682	0.000494317	0.0436411
3022	139.054	29.16	0.00625895	0.0436822
1170	446.255	29.1588	-0.000309768	0.0437746
2759	168.081	29.1645	-0.00465097	0.0439078
1124	464.264	24.4214	0.00126423	0.0439639
2842	159.081	29.1668	-0.0101285	0.0443753
2529	190.078	29.16	0.00276656	0.045195
2530	190.073	29.1575	-0.00750126	0.0453413
2774	166.073	29.16	0.00392943	0.0453583
3118	126.046	29.1648	0.0128704	0.0455378
2863	157.101	29.1648	-0.00495796	0.0458181
2495	193.101	29.1682	-0.00513446	0.0461537
2745	169.101	29.1682	-0.000349551	0.0471212
1125	464.264	21.8514	-0.00949399	0.0484276
2660	179.081	29.1398	0.00256035	0.0488453

Table 15
Table of the highest 25 and lowest 25 PCA loadings for PC1 for *P. kirkii*.

Var ID (Primary)	Var ID (Var. Sec. ID:1) *m/z*	Var ID (Var. Sec. ID:2) rt [min]	M1.p[1]	M1.p[2]
2095	227.091	6.2857	-0.0395518	0.00296276
2204	207.138	19.1203	-0.0390681	-0.0101807
2536	159.117	16.4569	-0.038328	-0.00731937
2693	135.044	15.9045	-0.0377799	-0.016124
2091	227.164	19.8113	-0.0375666	-0.00403601
2120	223.133	15.9092	-0.0374583	-0.00626472
1333	420.224	16.6692	-0.0373635	-0.00334512
959	541.202	15.0671	-0.0373623	0.00268175
2301	191.143	23.2724	-0.0371366	-0.012572
1467	388.205	18.7143	-0.0370092	-0.00718727

1334	420.223	19.7357	-0.0370042	-0.00146855
2224	204.159	10.9121	-0.036954	0.0102026
1287	432.259	19.4263	-0.0368193	-0.0155613
2640	145.086	16.2102	-0.0367913	0.000691554
2312	190.131	19.4037	-0.0366987	-0.00932035
1456	390.176	16.4855	-0.0366867	-0.000672897
2183	210.157	22.7438	-0.0365695	-0.0106094
2523	161.133	19.4383	-0.0365467	-0.0173084
1578	355.102	15.9688	-0.0364722	-0.0127729
2684	137.081	2.90905	-0.0364495	-0.017934
2703	133.101	23.2362	-0.0363543	-0.0159978
2188	209.154	15.7358	-0.0363353	-0.00502574
1967	253.128	12.9577	-0.0363291	-0.0108203
2181	210.157	17.874	-0.0362997	0.00280325
2330	188.128	3.7106	-0.0362856	-0.00503308
820	581.399	58.0216	0.0338916	-0.010091
46	983.598	87.9022	0.0339346	-0.00960532
475	742.582	83.9293	0.0339381	-0.00478524
464	758.529	74.289	0.0340281	-0.0122779
386	791.508	85.8453	0.0340569	-0.00818158
745	599.409	66.6245	0.0341347	-0.00588779
1744	313.274	85.2335	0.0341733	-0.00928353
816	583.414	58.018	0.0343067	-0.00847177
739	599.41	57.997	0.034362	0.00232455
784	592.502	85.8411	0.0347357	-0.00492181
1655	335.258	85.7713	0.0348597	-0.00201057
1654	335.258	78.5469	0.0348773	-0.00776868
661	615.499	73.0298	0.0350509	-0.00606287
840	573.487	78.4781	0.0350679	-0.0123748
811	583.414	57.2265	0.0351667	-0.00893529
669	614.486	74.279	0.0353151	-0.0120095
675	613.483	74.2693	0.0356562	-0.0117595
764	596.476	74.3038	0.0357265	-0.015663
668	614.486	69.2248	0.0363213	-0.0163644
785	592.501	78.4881	0.0363244	-0.0142173
381	792.563	74.267	0.0363413	-0.00846376
787	591.498	85.8655	0.0363619	-0.00607172
674	613.483	69.2227	0.0363779	-0.0124332
1652	335.259	74.2753	0.0365996	-0.00993176
786	591.498	78.4708	0.0366248	-0.0109233

Table 16
Table of the highest 25 and lowest 25 PCA loadings for PC2 for *P. kirkii*.

Var ID (Primary)	Var ID (Var. Sec. ID:1) *m/z*	Var ID (Var. Sec. ID:2) rt [min]	M1.p[1]	M1.p[2]
2093	227.128	18.5798	-0.0010342	-0.0415564
2036	238.092	3.0389	-0.00975915	-0.0413378
1393	406.207	19.3077	-0.00616934	-0.0385737
2520	162.076	2.6108	-0.00691969	-0.0383024

2257	199.101	2.6119	-0.0164526	-0.0377897
2393	180.087	2.5627	-0.00977382	-0.0373856
2589	152.038	2.0438	-0.00628681	-0.0370995
2514	163.06	2.55875	0.00037077	-0.0368768
2584	153.033	2.0462	-0.00403582	-0.0367125
2806	115.039	2.573	-0.0183079	-0.0364576
2495	165.055	18.2052	0.0166374	-0.0356263
2192	209.117	19.3269	-0.000544985	-0.0353557
2428	175.039	18.5445	0.0183236	-0.0353154
2099	226.071	2.8645	-0.00751053	-0.0353077
2168	212.092	2.86205	-0.00932452	-0.0350057
2601	150.063	18.559	0.0135244	-0.0348639
2350	186.055	18.3828	0.0123668	-0.0348557
2425	175.045	2.0438	-0.00289627	-0.0348303
2143	219.026	2.3078	0.0187941	-0.0348141
2662	142.035	2.04515	0.00674908	-0.0343295
2092	227.128	19.1775	0.00280868	-0.0340949
2419	176.042	18.5497	0.0147845	-0.0339295
2288	193.071	2.7502	-0.008483	-0.0334444
833	577.176	15.7523	0.00811006	-0.0332183
2614	148.06	2.3538	-0.00948606	-0.0328726
1995	248.077	4.42325	-0.00595642	0.0440709
1994	248.077	3.7122	-0.00378772	0.0444065
2064	232.07	3.9992	-0.00106115	0.0444417
1126	480.207	15.9309	-0.00587704	0.0444582
234	846.309	2.5255	0.00736379	0.0445985
927	550.196	24.7293	0.00202925	0.0447256
680	613.159	5.896	0.00347212	0.0447541
599	647.288	13.9043	-0.00462617	0.0448535
465	758.297	20.8983	-0.00172057	0.0449046
325	807.309	26.2113	0.00238672	0.0450439
2567	155.053	2.8284	-0.00266082	0.045167
41	991.335	2.46225	0.0051038	0.04527
389	791.314	26.2923	0.00386626	0.0454221
1555	362.145	15.7237	-0.00213414	0.0456529
2068	231.069	3.892	-0.000638955	0.0456606
20	1170.42	2.5876	0.00236852	0.0457103
2078	230.066	3.8638	-0.00208805	0.0458265
2262	198.112	17.1422	0.0040987	0.0458441
2018	243.098	2.8327	-0.00104781	0.0459581
2067	231.069	4.42225	-0.00218622	0.0459929
2358	185.064	3.9139	-0.00223945	0.0459978
2248	201.087	2.7142	-0.00207928	0.0460875
1358	414.197	18.2593	0.00475199	0.0463401
2359	185.064	4.4294	-0.00492034	0.0465102
1667	332.134	5.3018	0.00162656	0.046587

III.7.9. Appendix I: Spectra of the ion tree fragmentation measurements

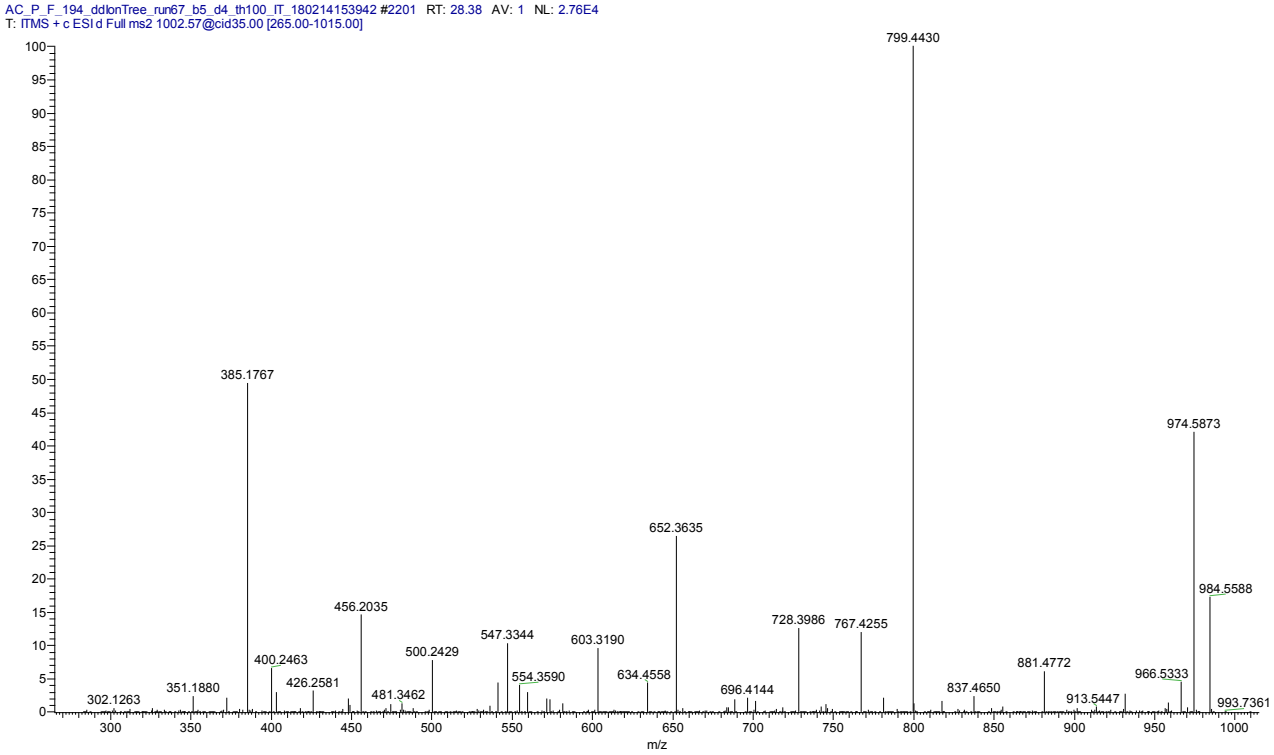

Figure 103. MS 2 spectrum of the *m/z* feature annotated as FR900359 with a *m/z* value of 1002.57 at rt 28.38 min.

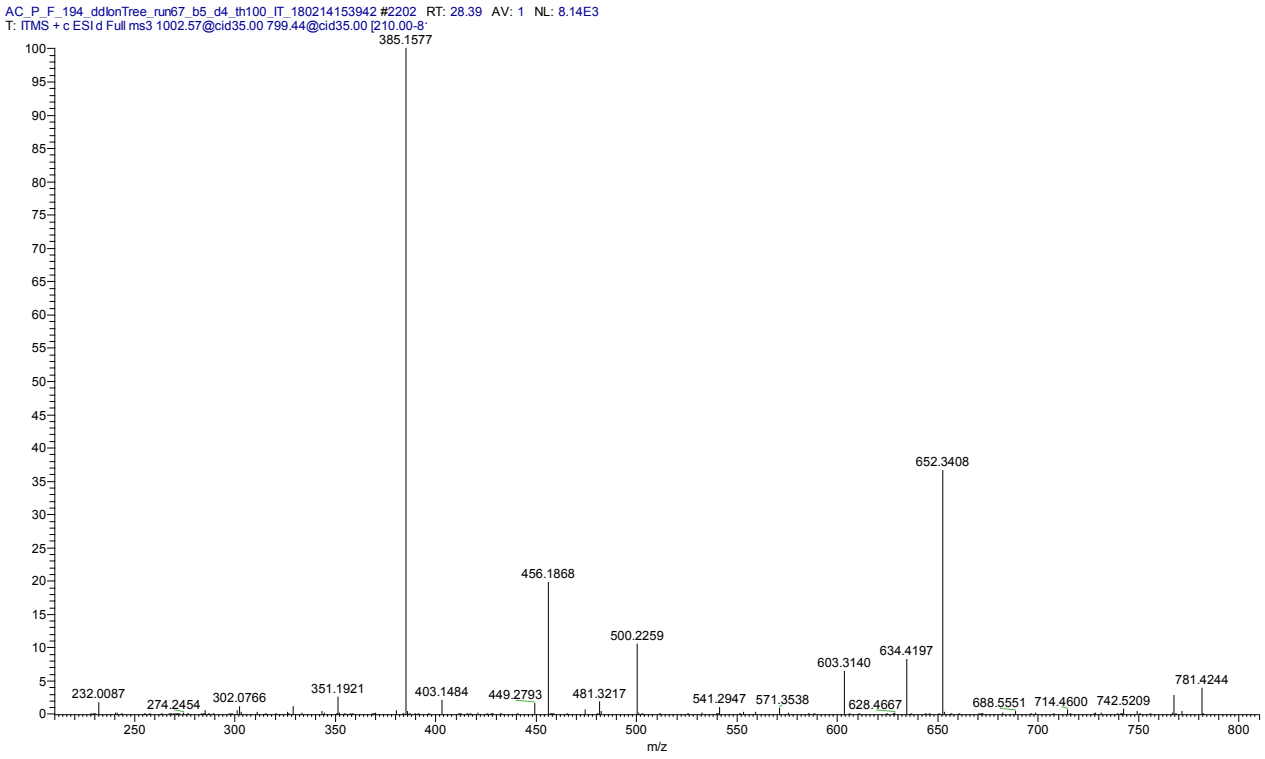

Figure 104. MS 3 spectrum of the fragment with *m/z* value of 799.44 of the *m/z* feature annotated as FR900359 with a *m/z* value of 1002.57 at rt 28.39 min.

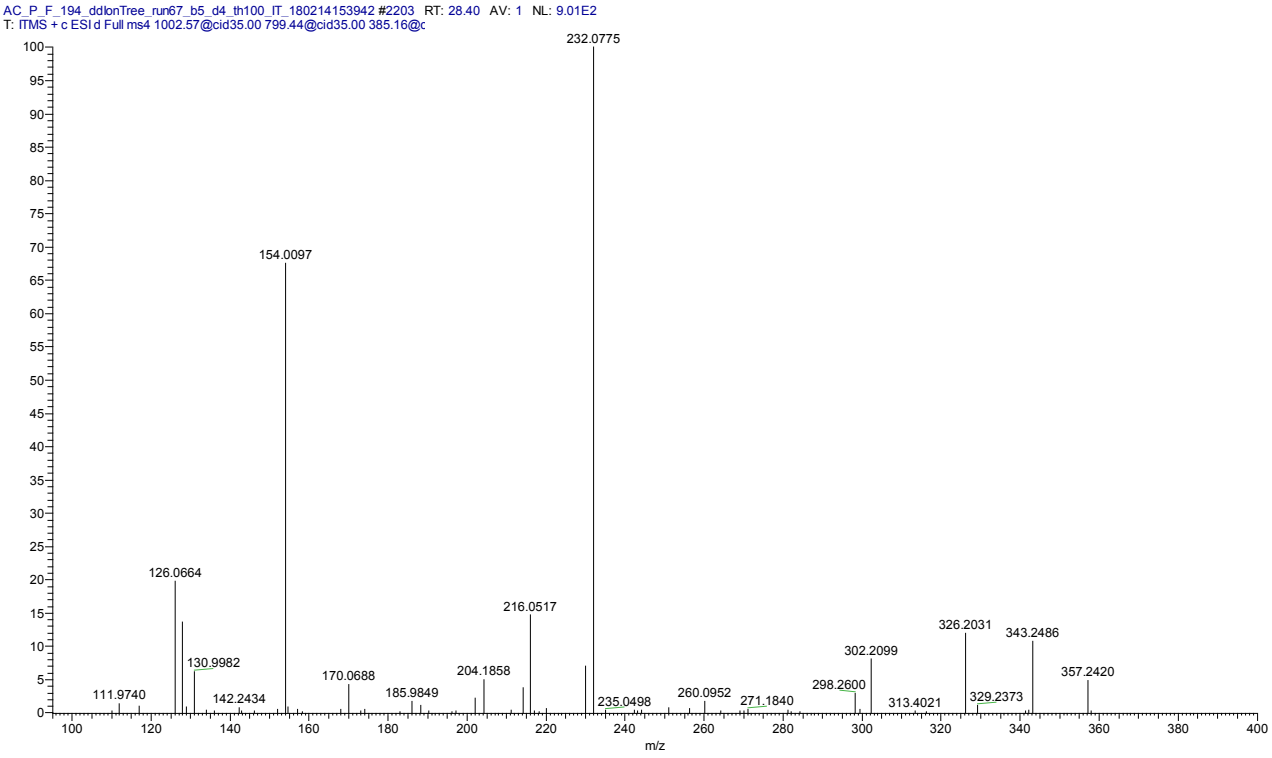

Figure 105. MS 4 spectrum of the fragment with *m/z* value of 385.16 of the fragment with *m/z* value of 799.44 of the *m/z* feature annotated as FR900359 with a *m/z* value of 1002.57 at rt 28.40 min.

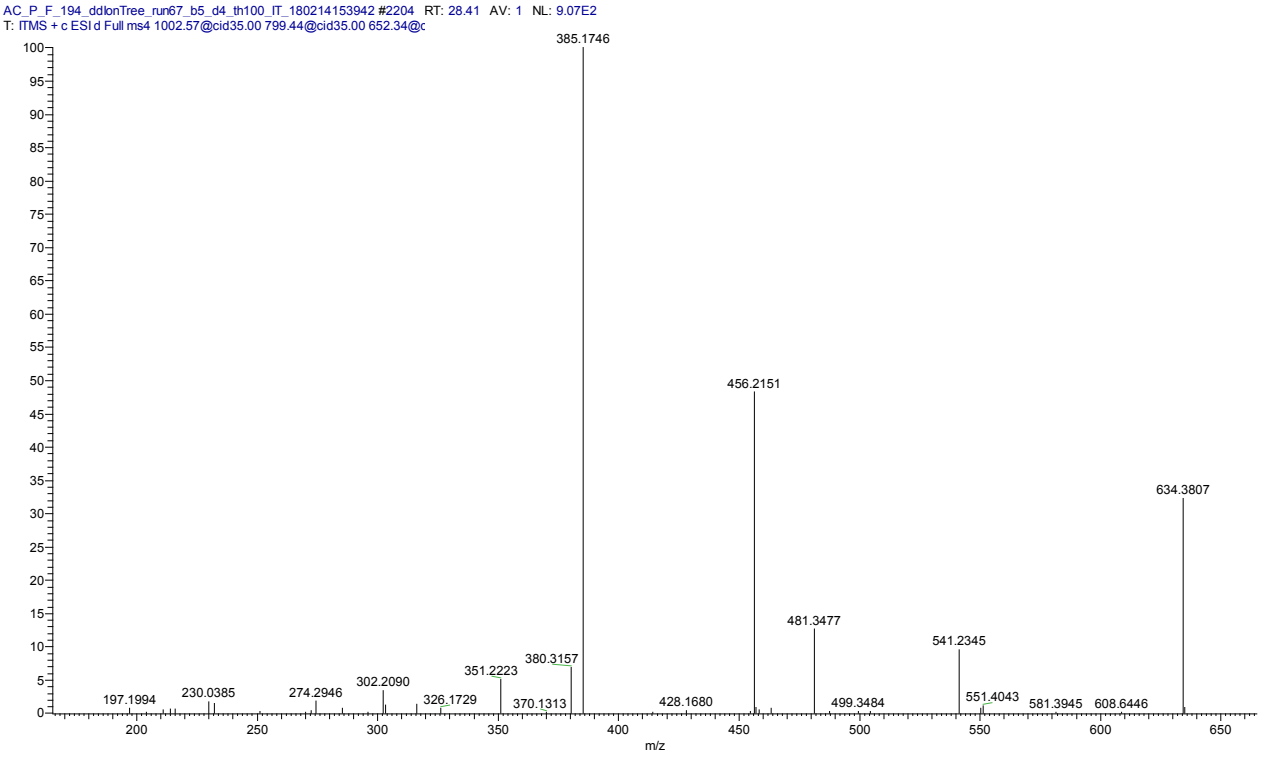

Figure 106. MS 4 spectrum of the fragment with *m/z* value of 652.34 of the fragment with *m/z* value of 799.44 of the *m/z* feature annotated as FR900359 with a *m/z* value of 1002.57 at rt 28.41 min.

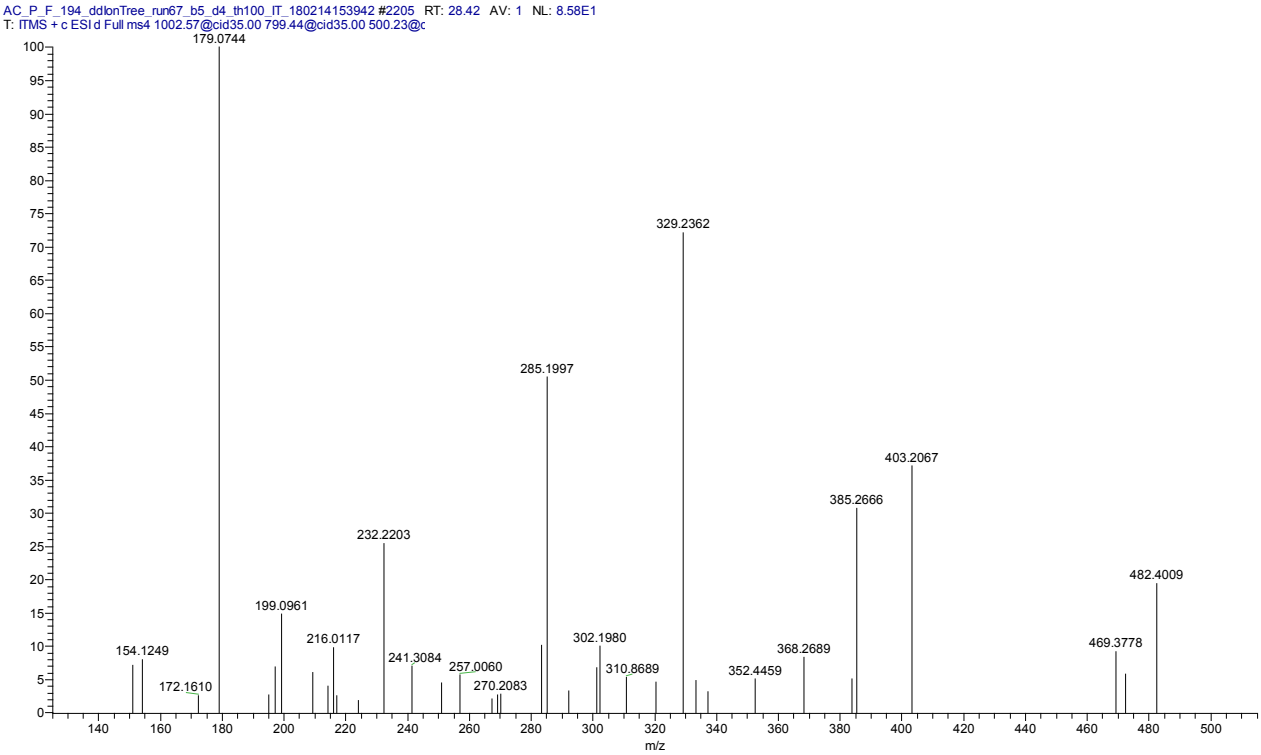

Figure 107. MS 4 spectrum of the fragment with *m/z* value of 500.23 of the fragment with *m/z* value of 799.44 of the *m/z* feature annotated as FR900359 with a *m/z* value of 1002.57 at rt 28.42 min.

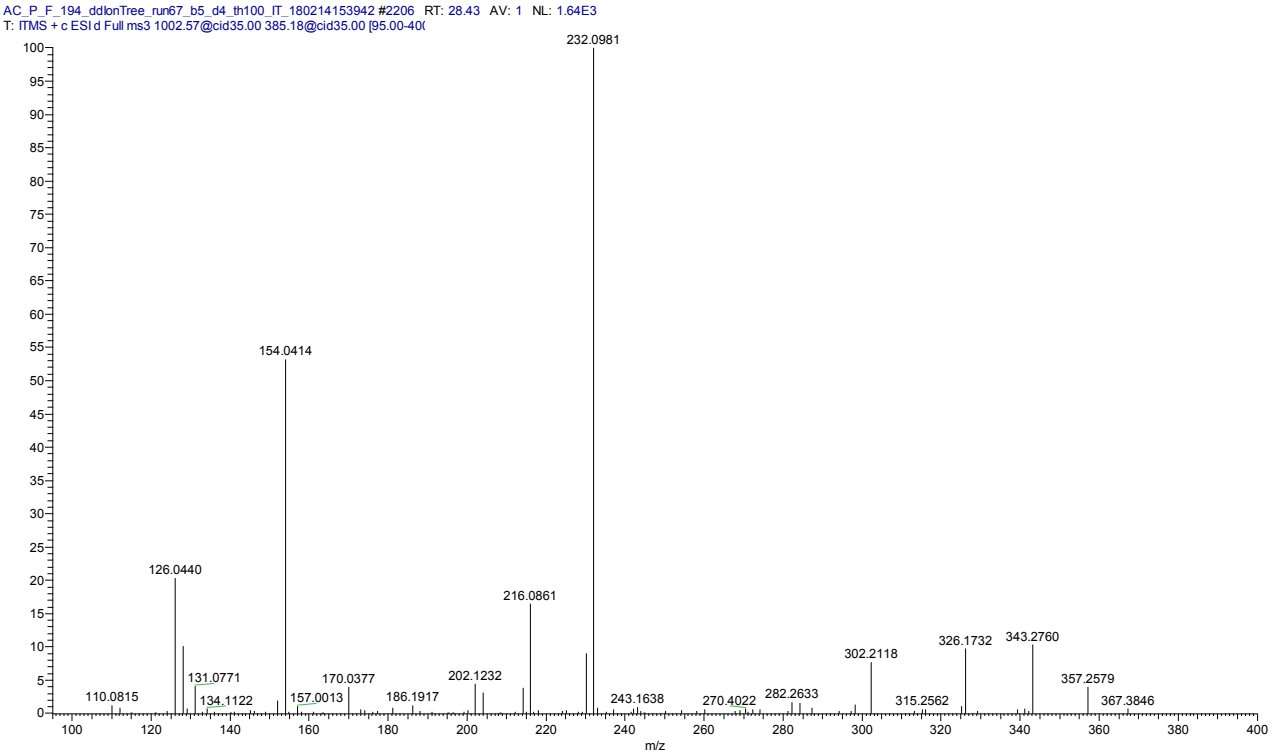

Figure 108. MS 3 spectrum of the fragment with *m/z* value of 385.18 of the *m/z* feature annotated as FR900359 with a *m/z* value of 1002.57 at rt 28.43 min.

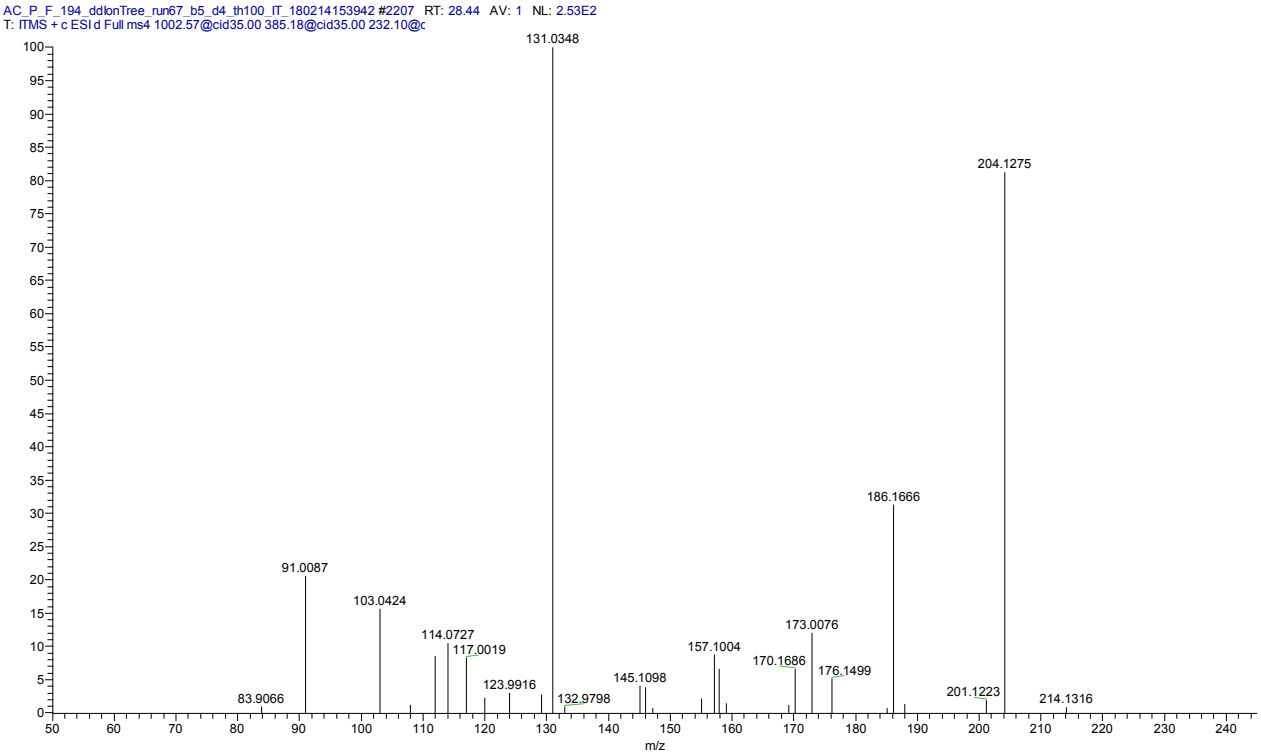

Figure 109. MS 4 spectrum of the fragment with *m/z* value of 232.10 of the fragment with *m/z* value of 385.18 of the *m/z* feature annotated as FR900359 with a *m/z* value of 1002.57 at rt 28.44 min.

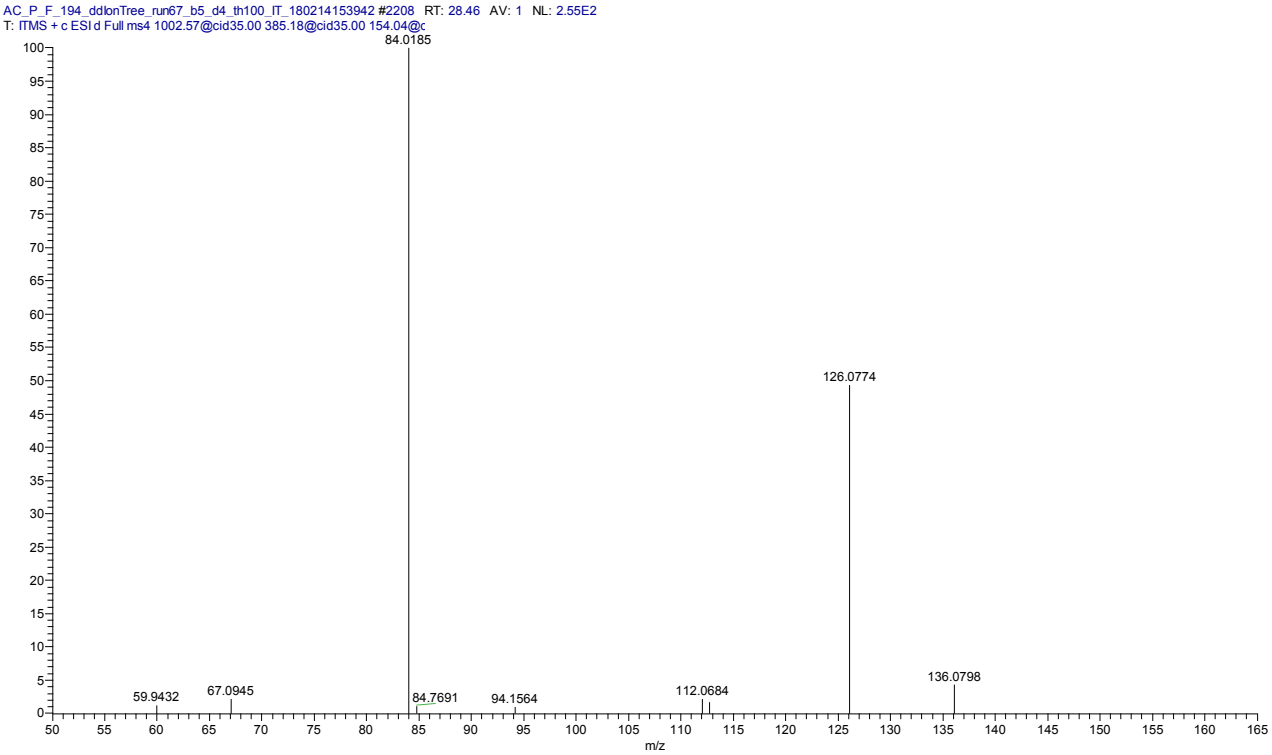

Figure 110. MS 4 spectrum of the fragment with *m/z* value of 154.04 of the fragment with *m/z* value of 385.18 of the *m/z* feature annotated as FR900359 with a *m/z* value of 1002.57 at rt 28.46 min.

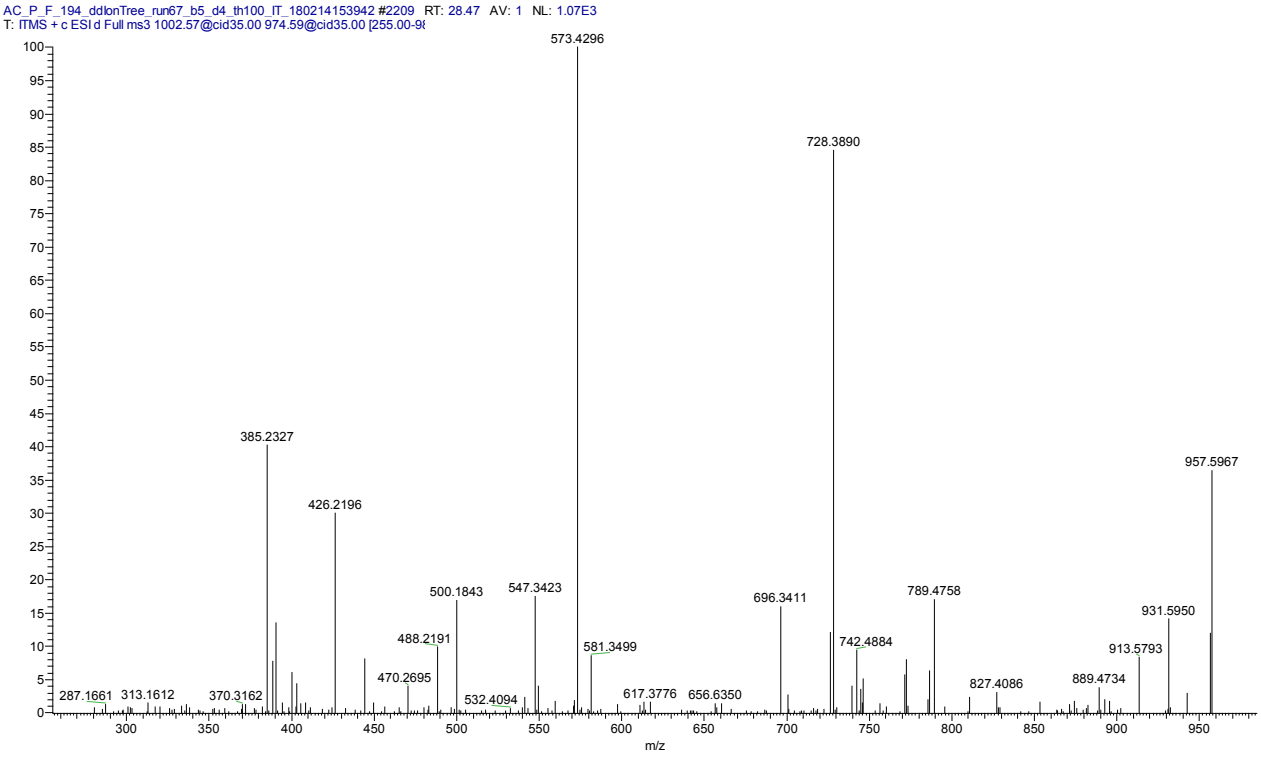

Figure 111. MS 3 spectrum of the fragment with *m/z* value of 974.59 of the *m/z* feature annotated as FR900359 with a *m/z* value of 1002.57 at rt 28.47 min.

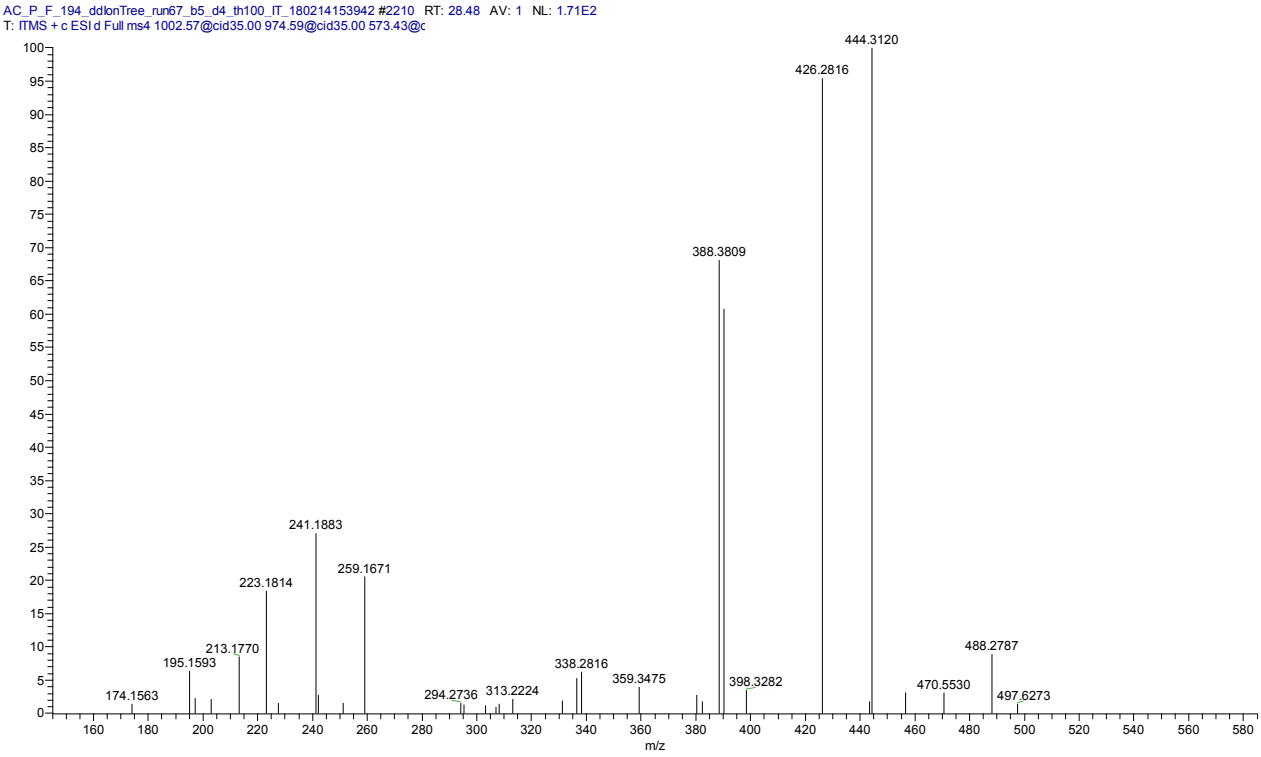

Figure 112. MS 4 spectrum of the fragment with *m/z* value of 573.43 of the fragment with *m/z* value of 974.59 of the *m/z* feature annotated as FR900359 with a *m/z* value of 1002.57 at rt 28.48 min.

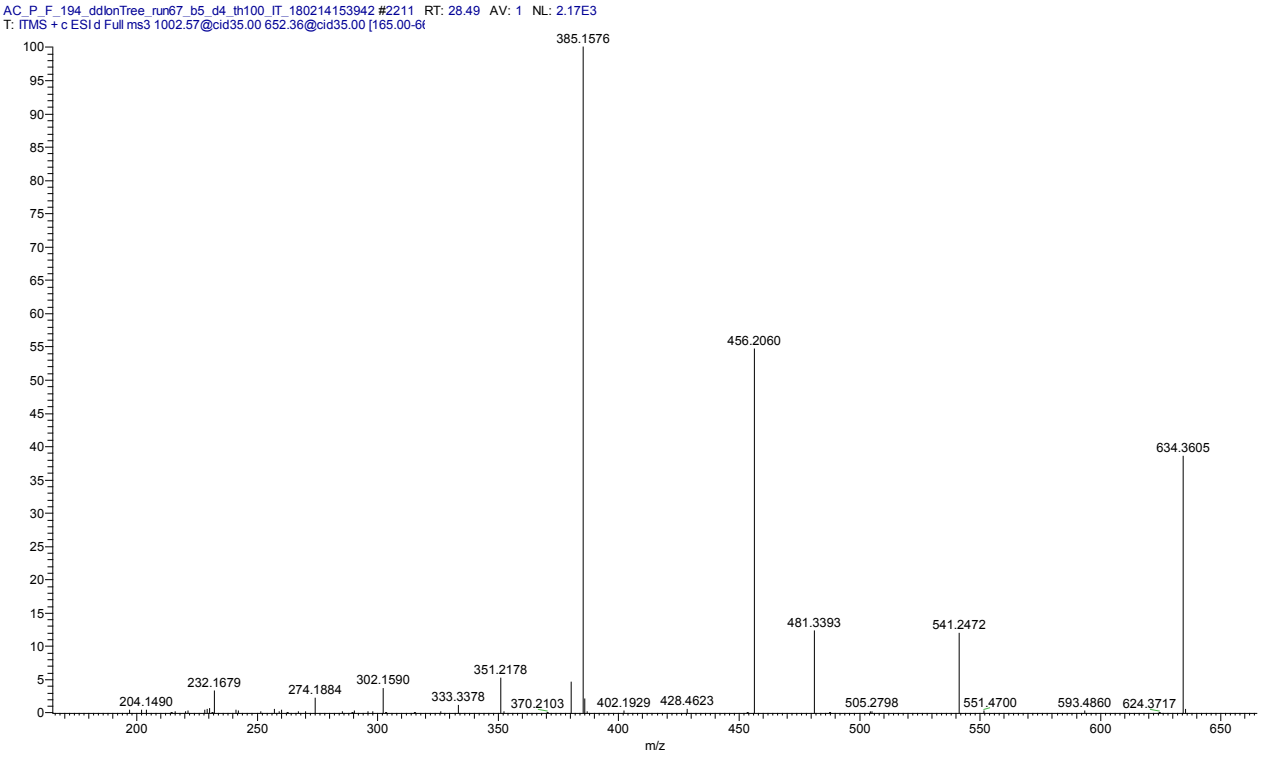

Figure 113. MS 3 spectrum of the fragment with *m/z* value of 652.36 of the *m/z* feature annotated as FR900359 with a *m/z* value of 1002.57 at rt 28.49 min.

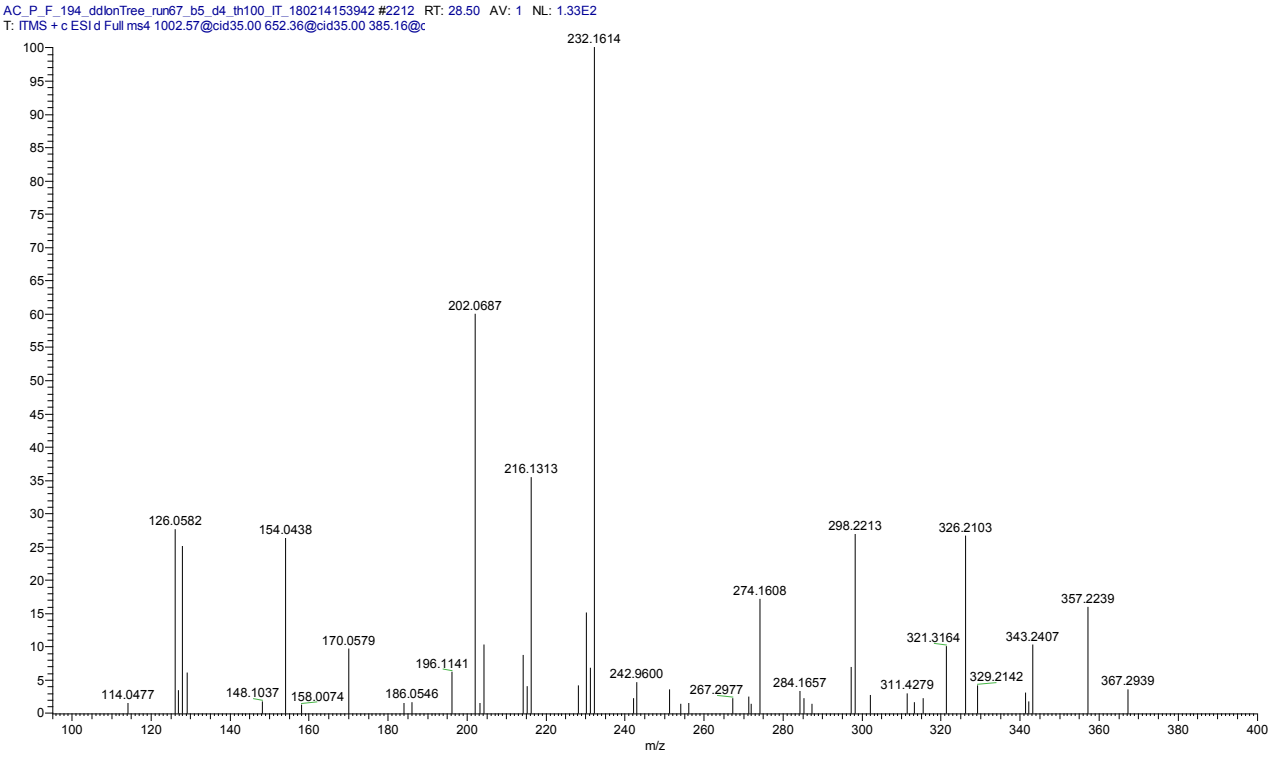

Figure 114. MS 4 spectrum of the fragment with *m/z* value of 385.16 of the fragment with *m/z* value of 652.36 of the *m/z* feature annotated as FR900359 with a *m/z* value of 1002.57 at rt 28.50 min.

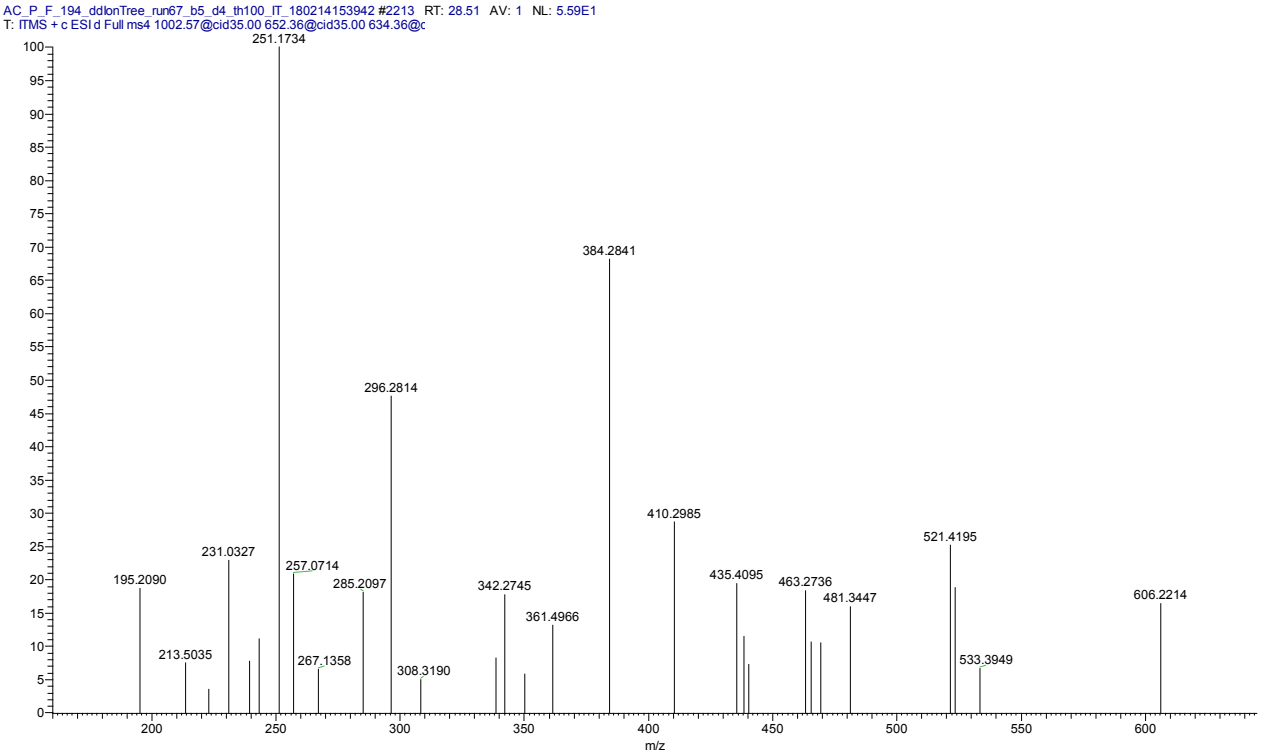

Figure 115. MS 4 spectrum of the fragment with *m/z* value of 634.36 of the fragment with *m/z* value of 652.36 of the *m/z* feature annotated as FR900359 with a *m/z* value of 1002.57 at rt 28.51 min.

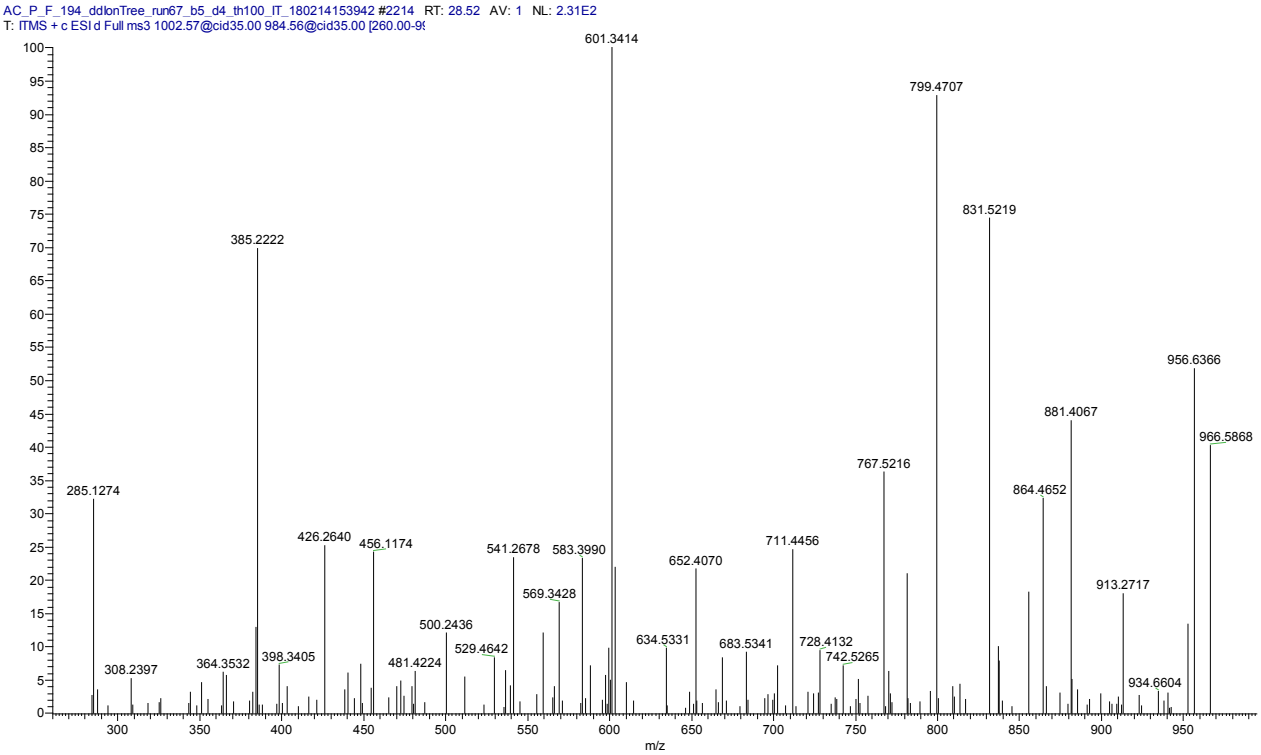

Figure 116. MS 3 spectrum of the fragment with *m/z* value of 984.56 of the *m/z* feature annotated as FR900359 with a *m/z* value of 1002.57 at rt 28.52 min.

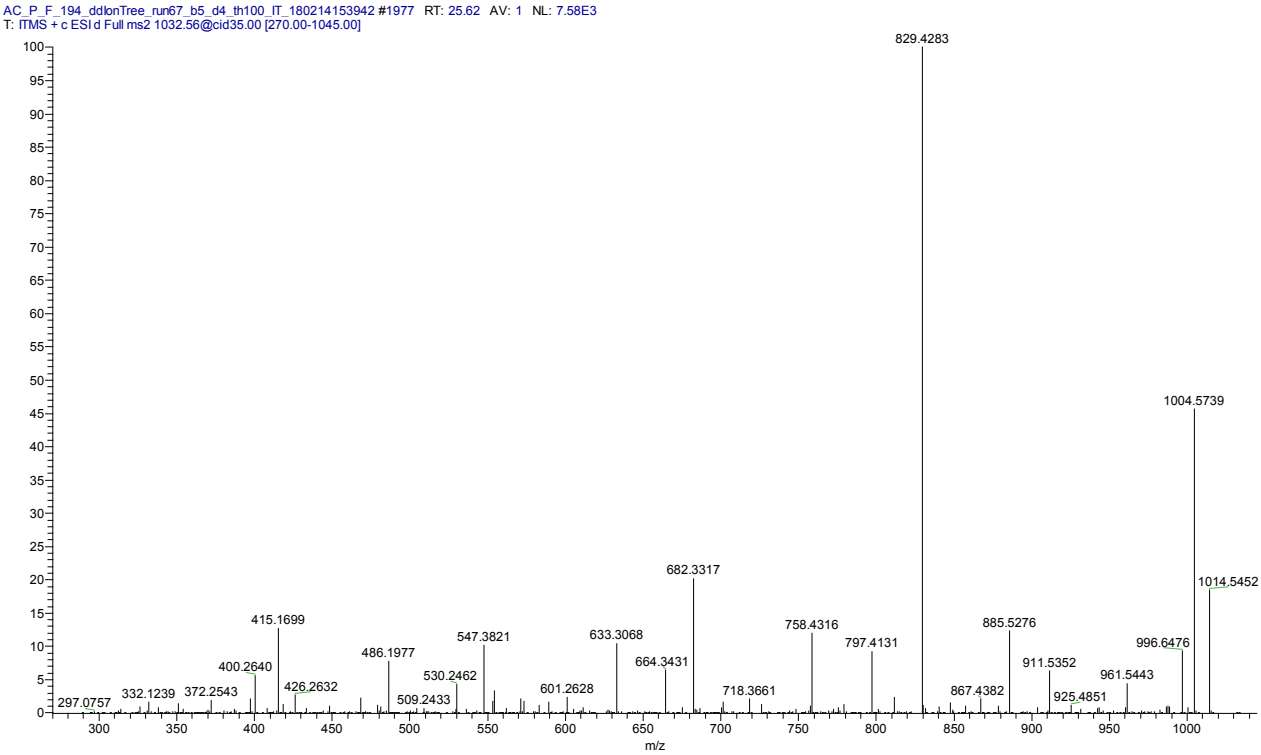

Figure 117. MS 2 spectrum of the *m/z* feature annotated as AC-1 with a *m/z* value of 1032.56 at rt 25.62 min.

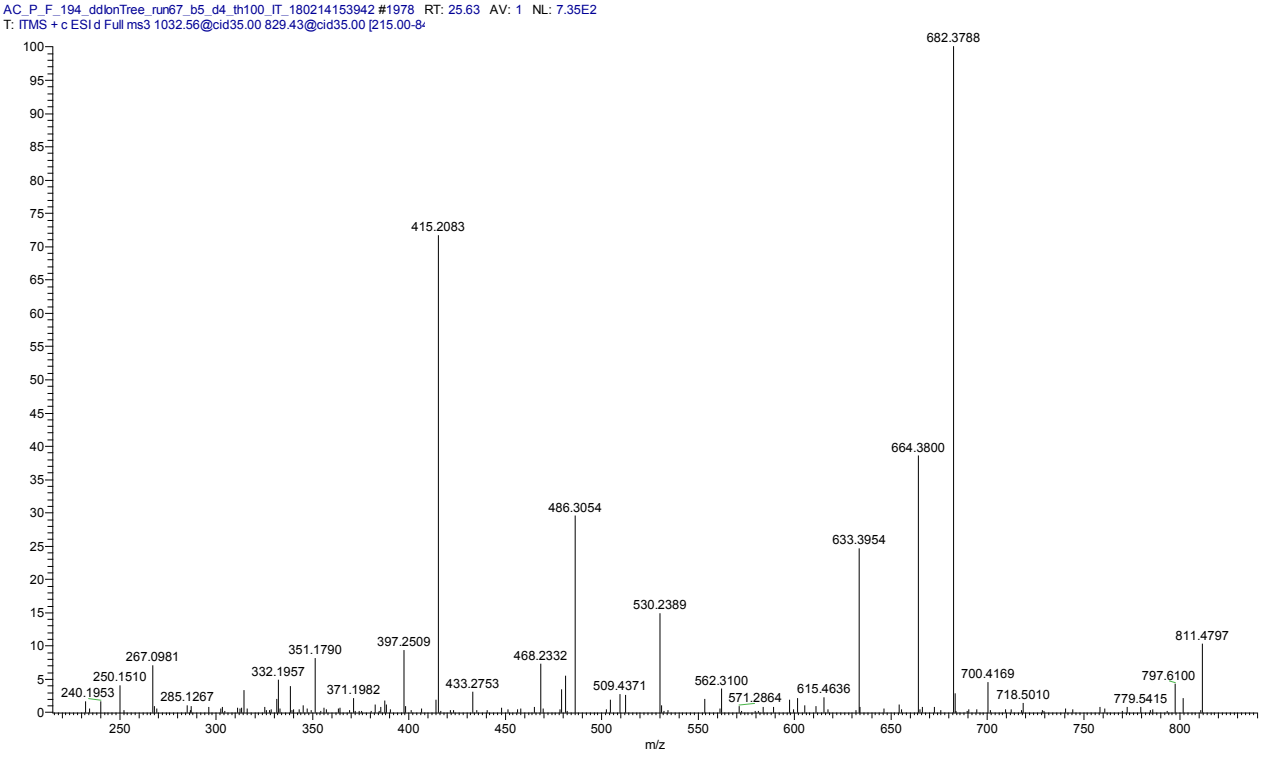

Figure 118. MS 3 spectrum of the fragment with *m/z* value of 829.43 of the *m/z* feature annotated as AC-1 with a *m/z* value of 1032.56 at rt 25.63 min.

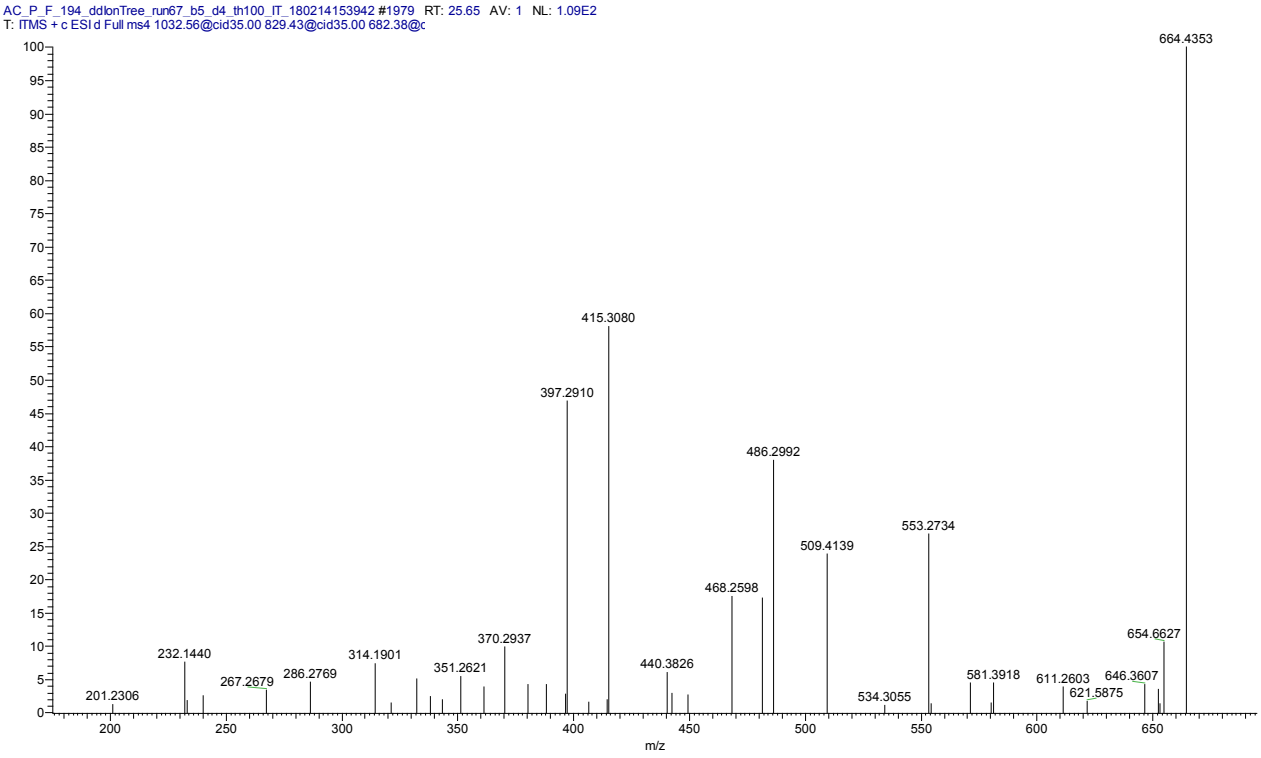

Figure 119. MS 4 spectrum of the fragment with *m/z* value of 682.38 of the fragment with *m/z* value of 829.43 of the *m/z* feature annotated as AC-1 with a *m/z* value of 1032.56 at rt 25.65 min.

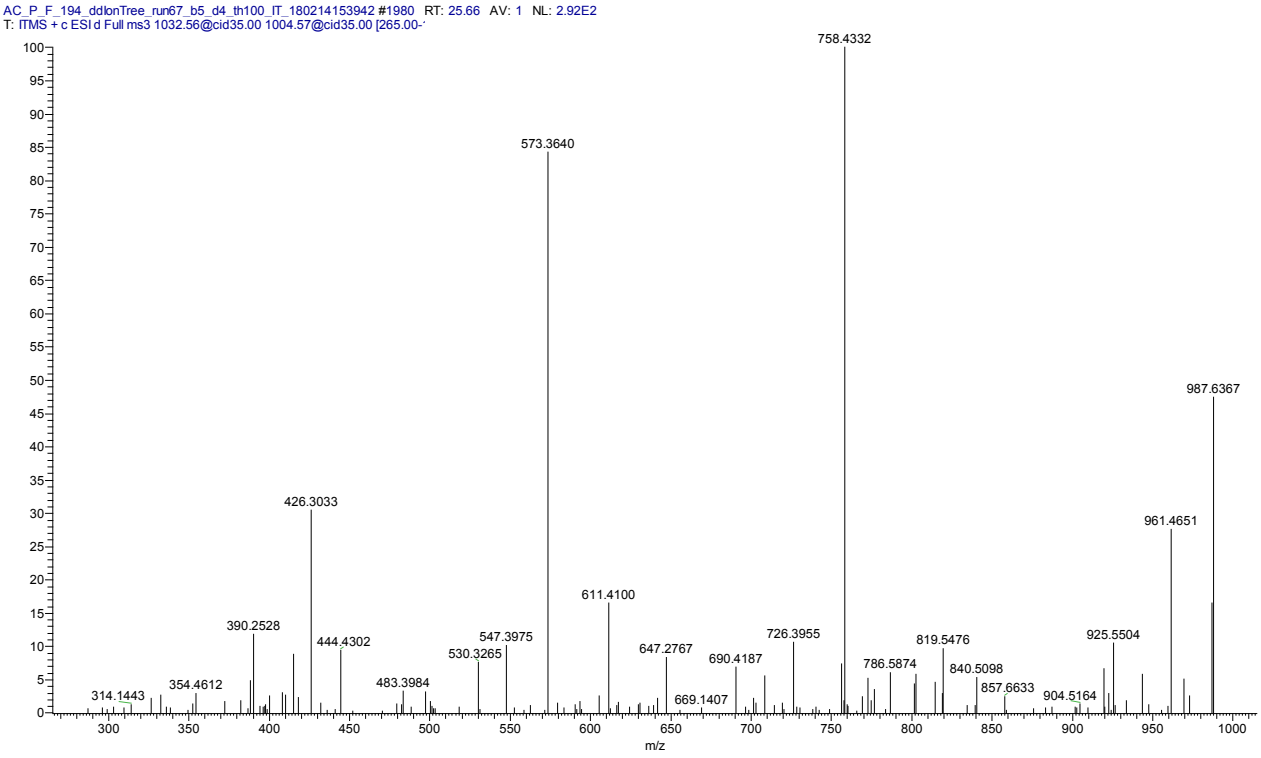

Figure 120. MS 3 spectrum of the fragment with *m/z* value of 1004.57 of the *m/z* feature annotated as AC-1 with a *m/z* value of 1032.56 at rt 25.66 min.

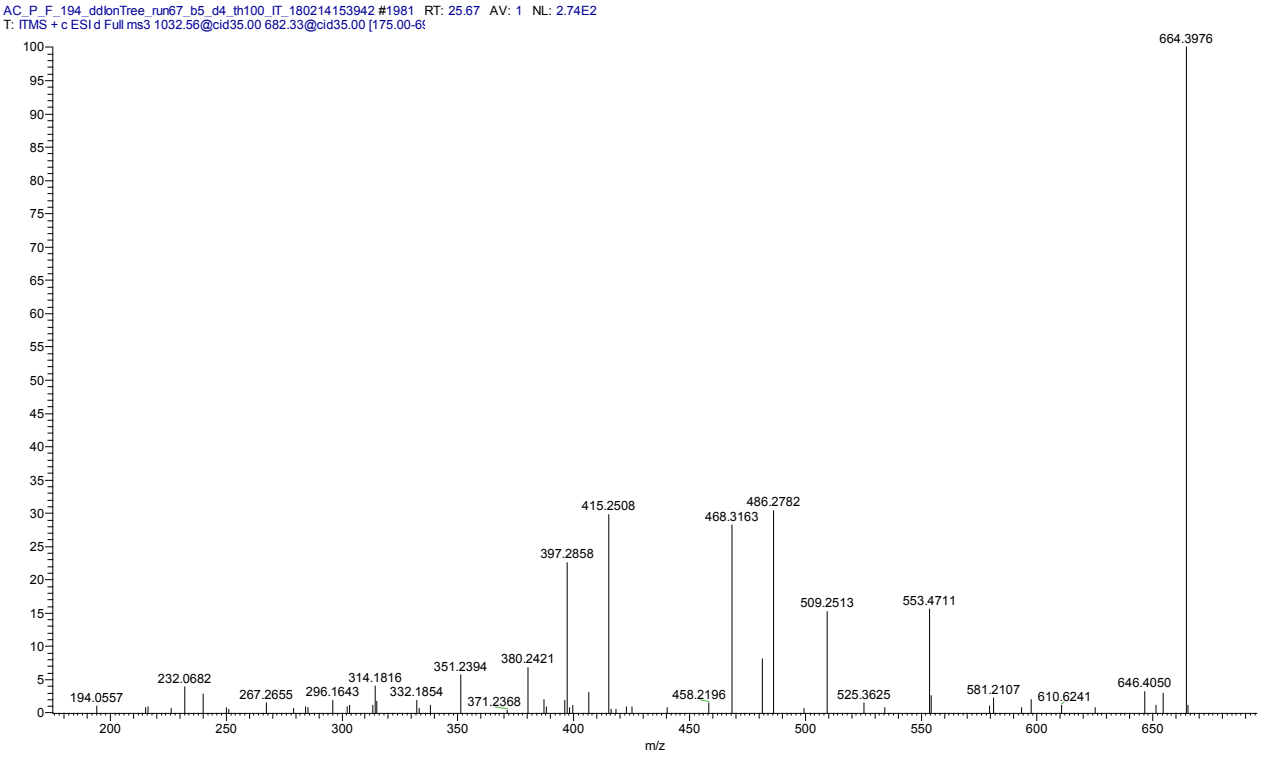

Figure 121. MS 3 spectrum of the fragment with *m/z* value of 682.33 of the *m/z* feature annotated as AC-1 with a *m/z* value of 1032.56 at rt 25.67 min.

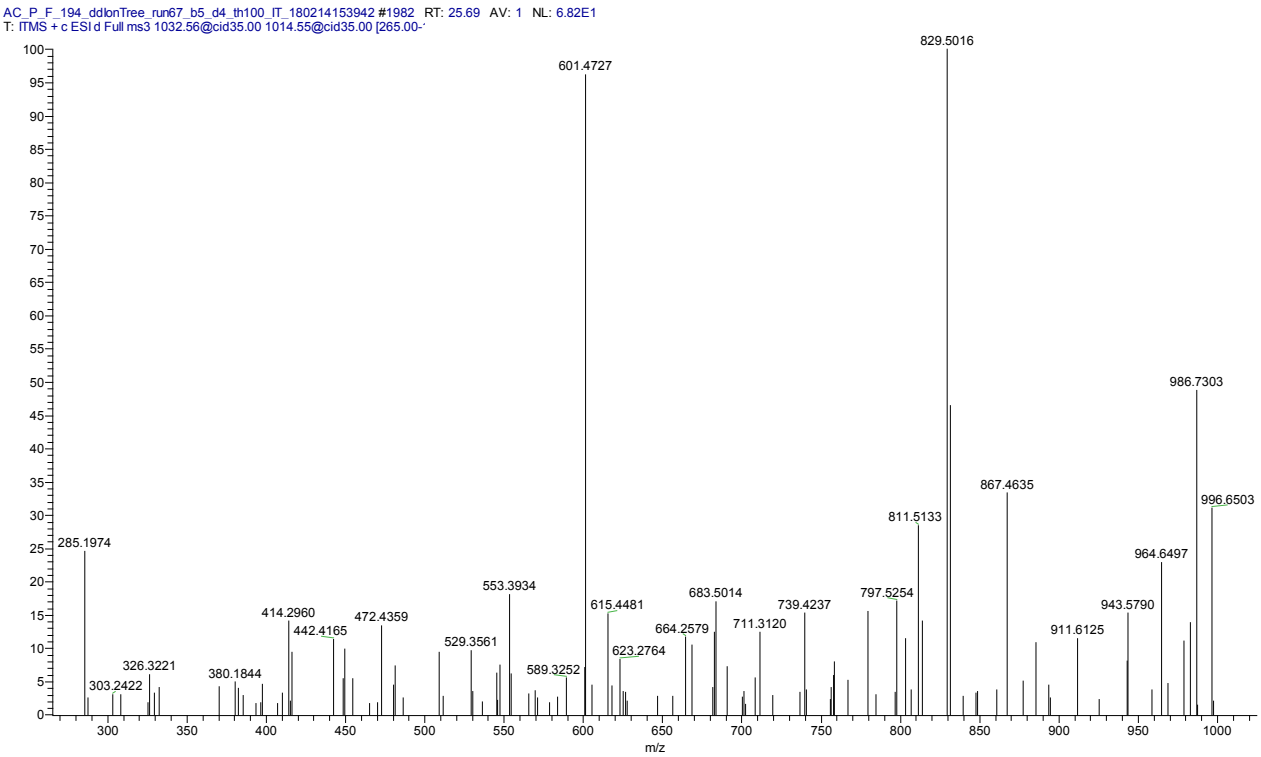

Figure 122. MS 3 spectrum of the fragment with *m/z* value of 1014.55 of the *m/z* feature annotated as AC-1 with a *m/z* value of 1032.56 at rt 25.69 min.

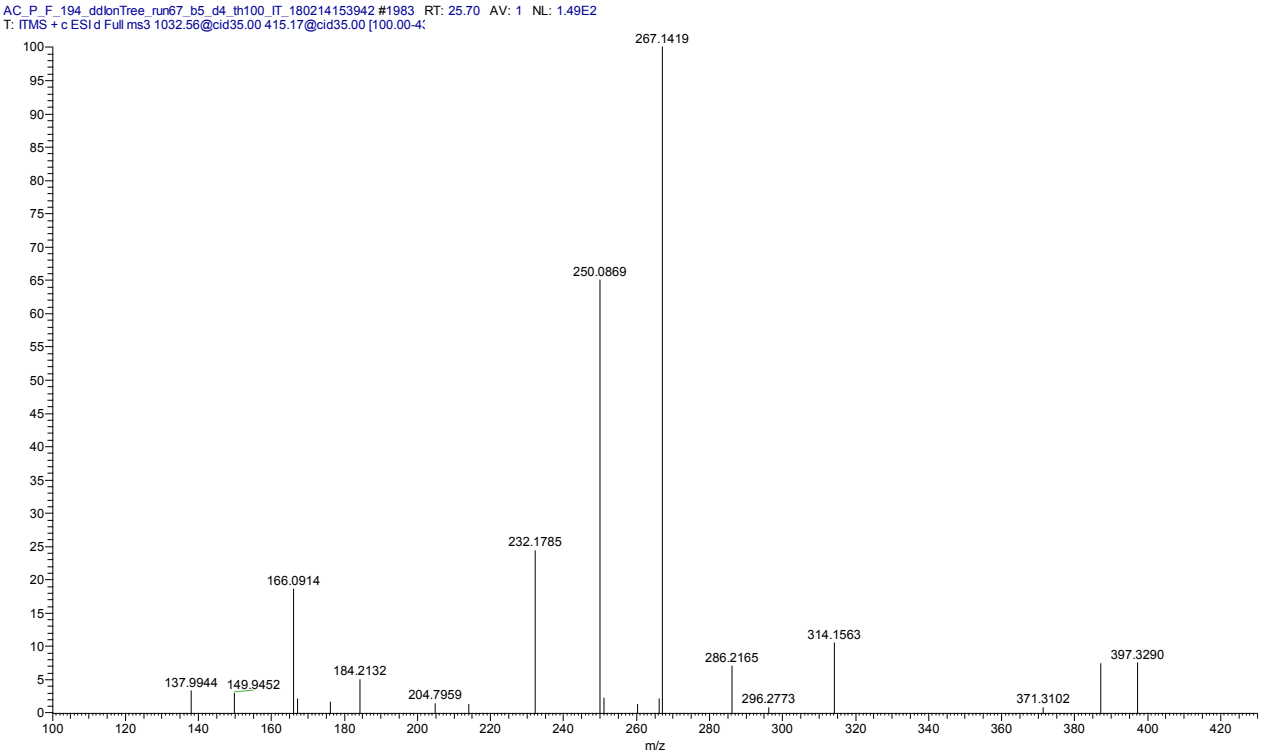

Figure 123. MS 3 spectrum of the fragment with *m/z* value of 415.17 of the *m/z* feature annotated as AC-1 with a *m/z* value of 1032.56 at rt 25.63 min.

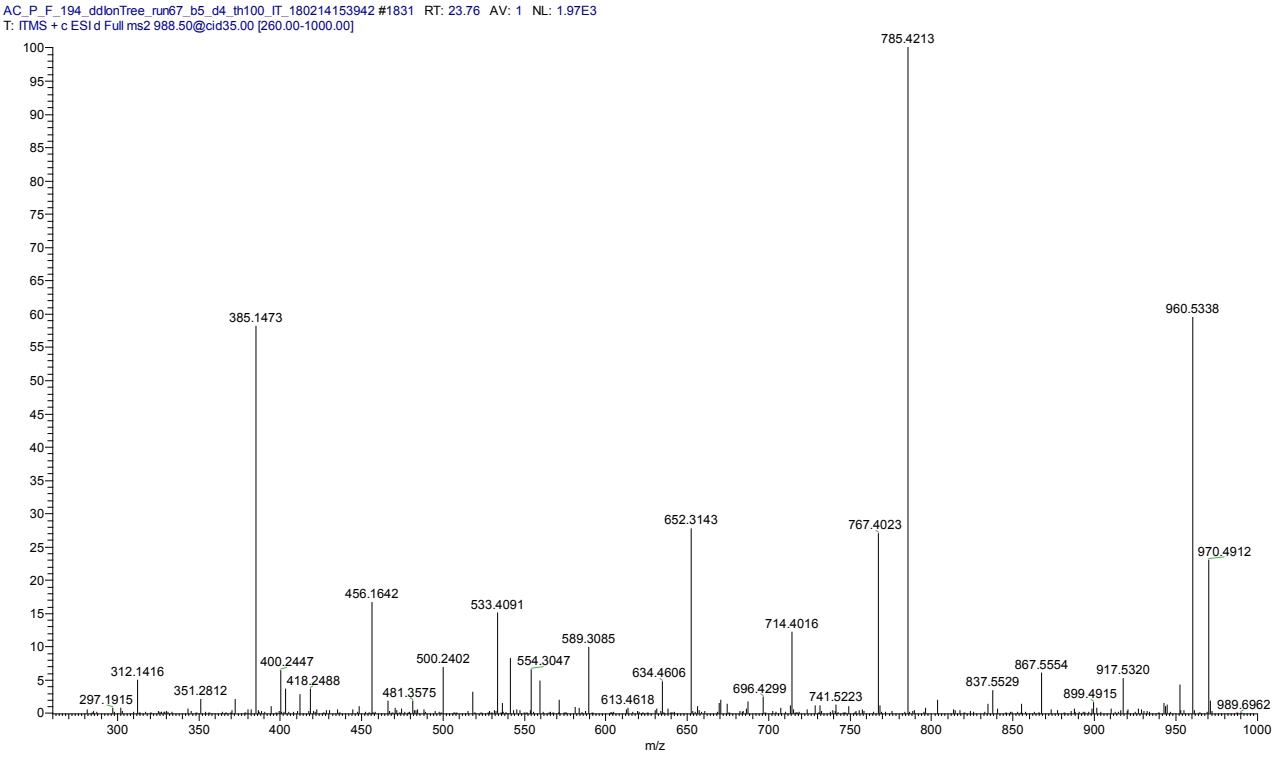

Figure 124. MS 2 spectrum of the *m/z* feature annotated as putative cyclic-depsipeptide with a *m/z* value of 988.50 at rt 23.76 min.

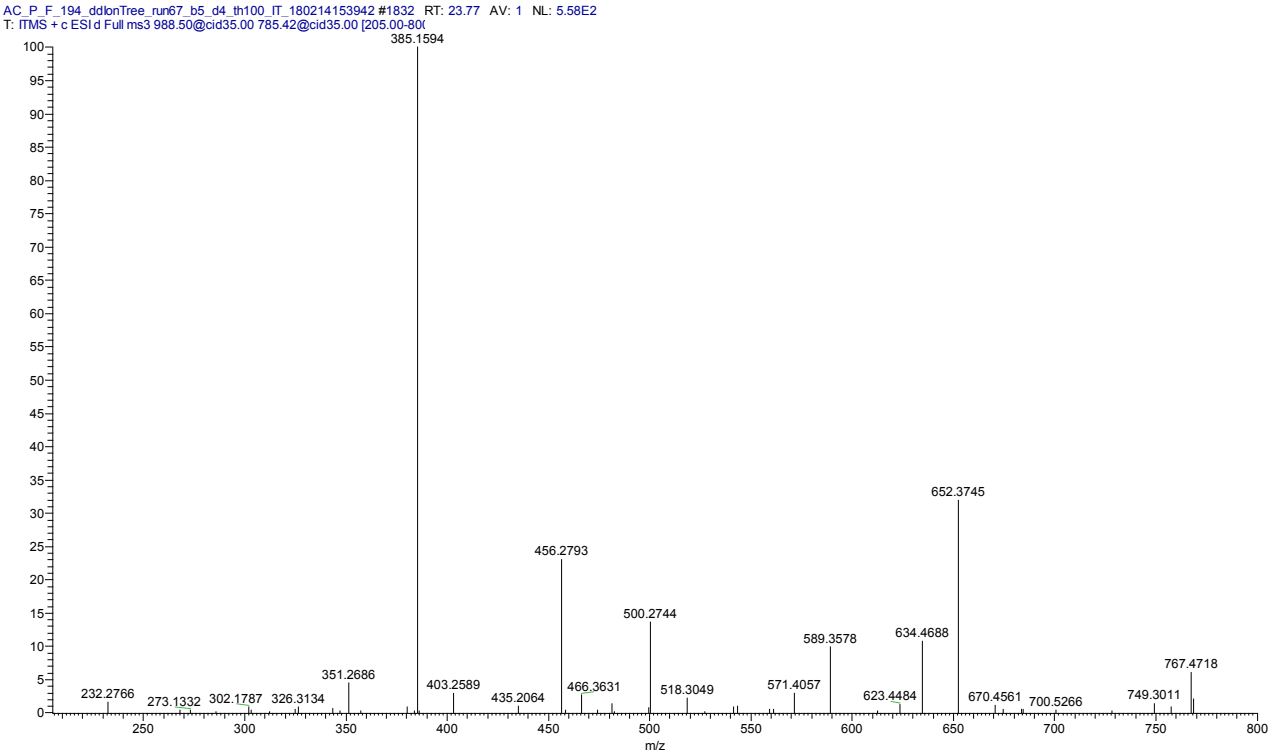

Figure 125. MS 3 spectrum of the fragment with *m/z* value of 785.42 of the *m/z* feature annotated as putative cyclic-depsipeptide with a *m/z* value of 988.50 at rt 23.77 min.

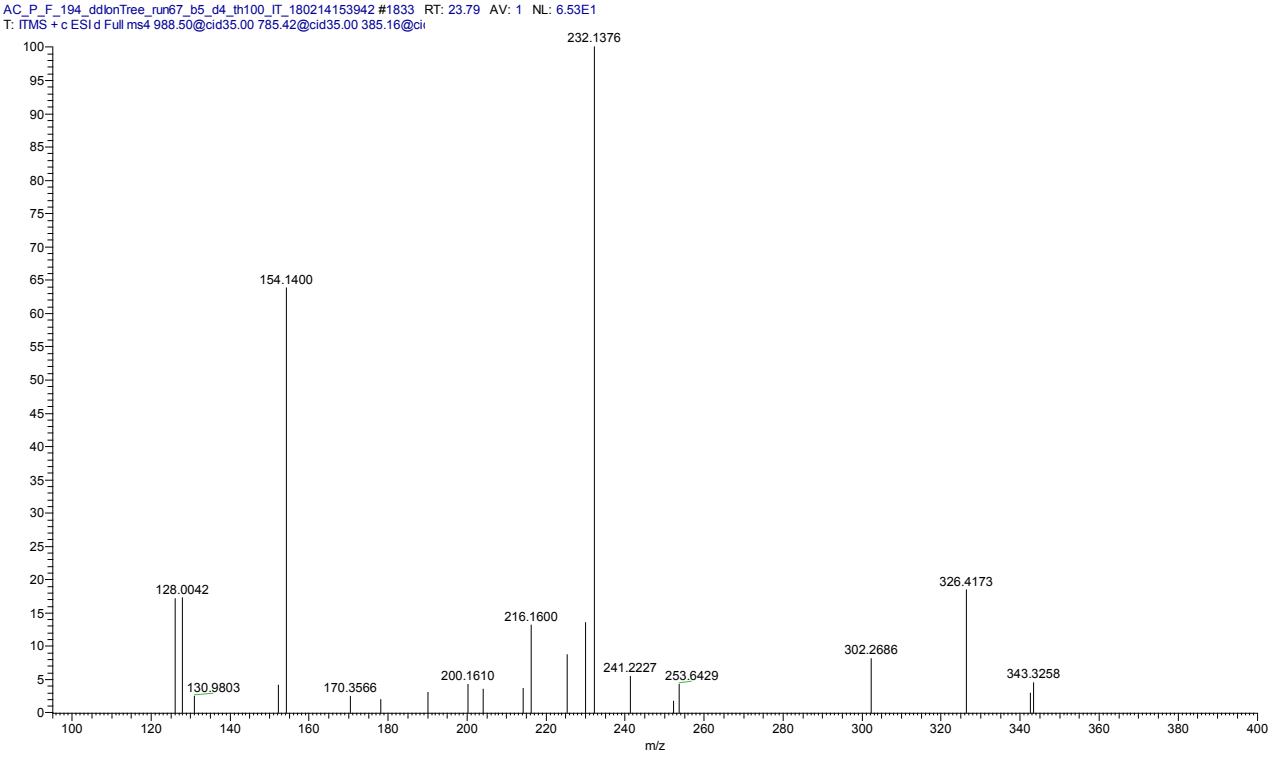

Figure 126. MS 4 spectrum of the fragment with *m/z* value of 385.16 of the fragment with *m/z* value of 785.42 of the *m/z* feature annotated as putative cyclic-depsipeptide with a *m/z* value of 988.50 at rt 23.79 min.

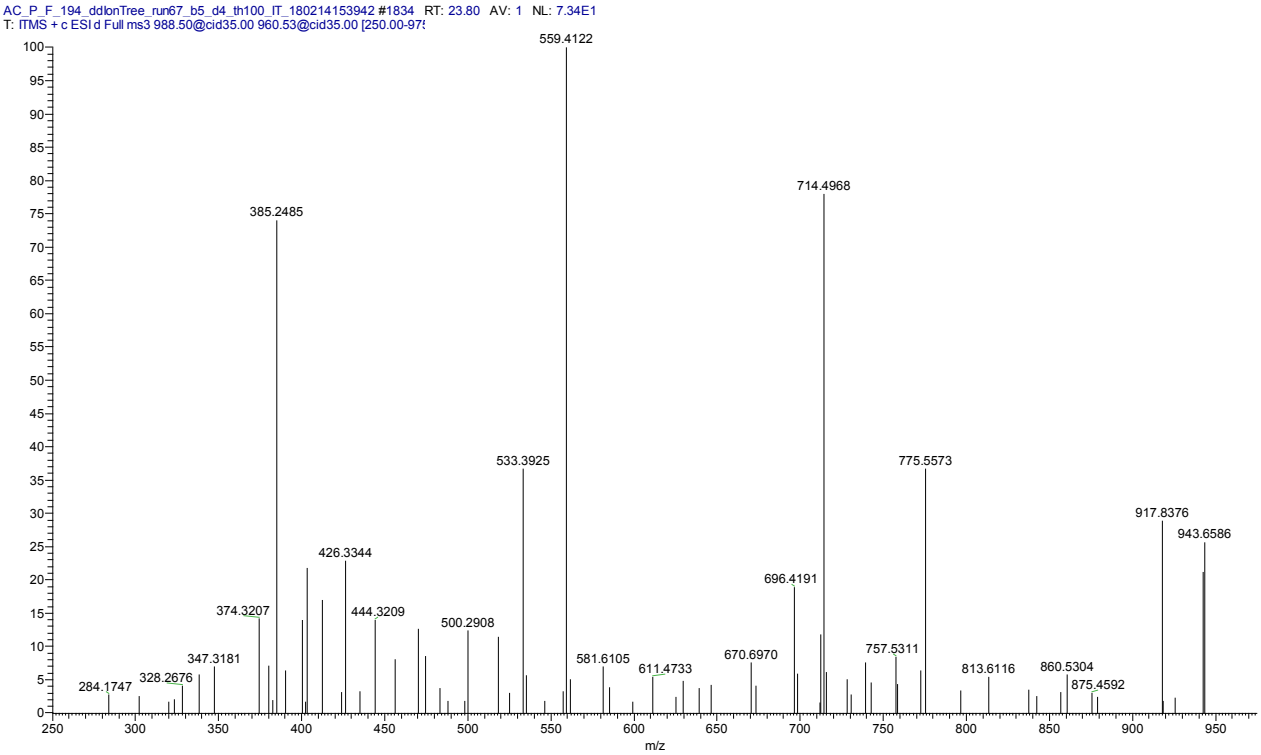

Figure 127. MS 3 spectrum of the fragment with *m/z* value of 960.53 of the *m/z* feature annotated as putative cyclic-depsipeptide with a *m/z* value of 988.50 at rt 23.80 min.

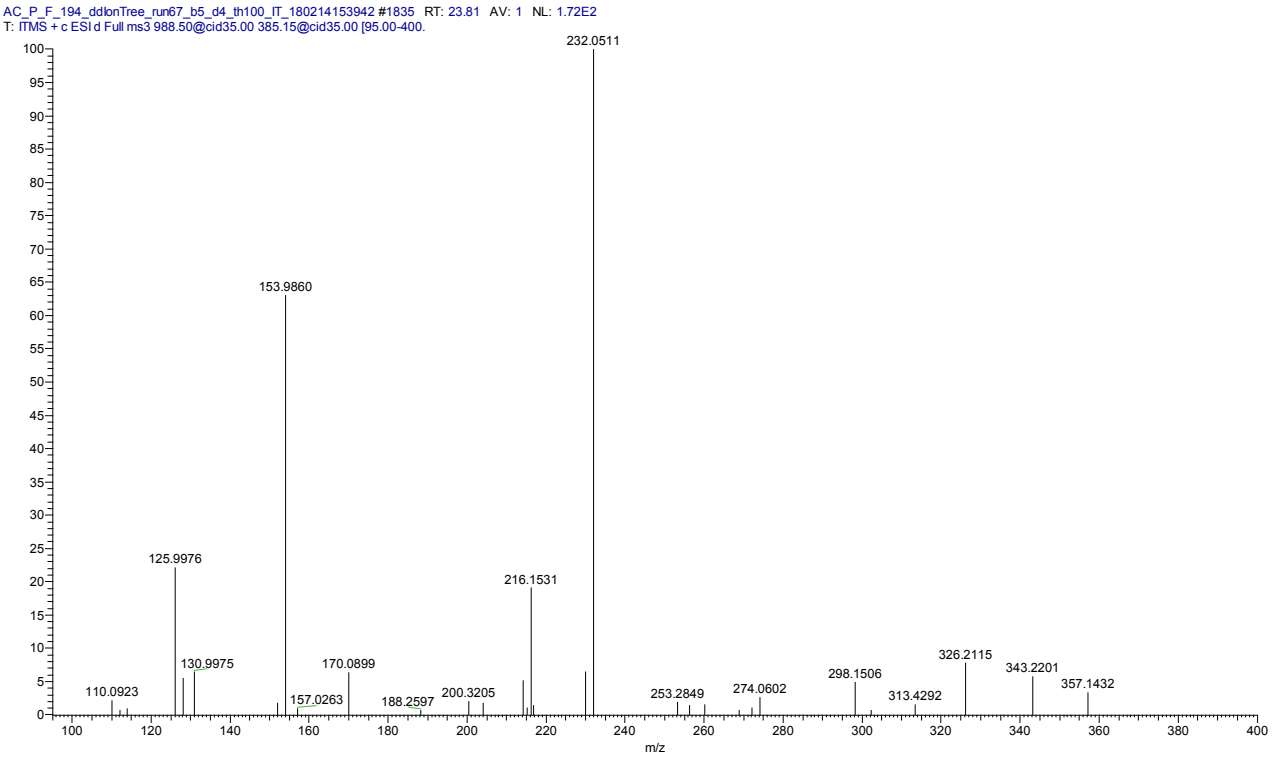

Figure 128. MS 3 spectrum of the fragment with *m/z* value of 385.15 of the *m/z* feature annotated as putative cyclic-depsipeptide with a *m/z* value of 988.50 at rt 23.81 min.

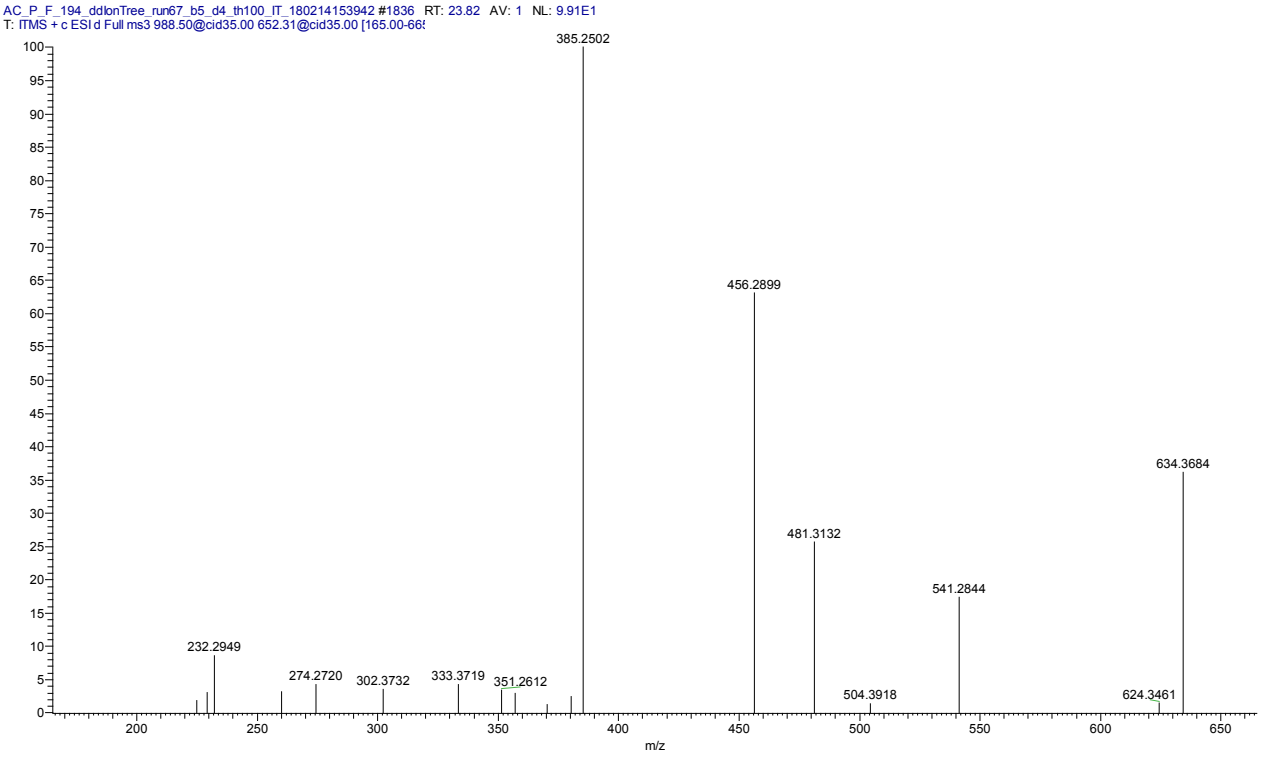

Figure 129. MS 3 spectrum of the fragment with *m/z* value of 652.31 of the *m/z* feature annotated as putative cyclic-depsipeptide with a *m/z* value of 988.50 at rt 23.82 min.

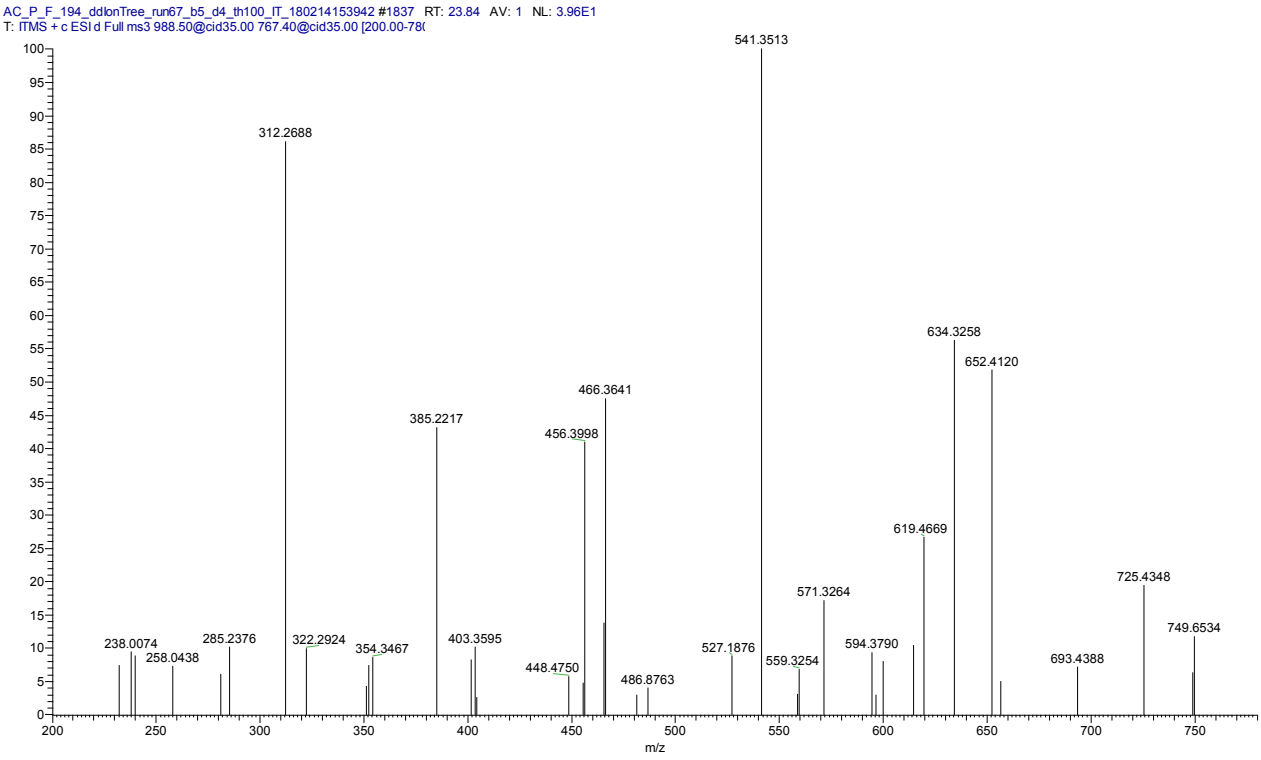

Figure 130. MS 3 spectrum of the fragment with *m/z* value of 988.50 of the *m/z* feature annotated as putative cyclic-depsipeptide with a *m/z* value of 988.50 at rt 23.84 min.

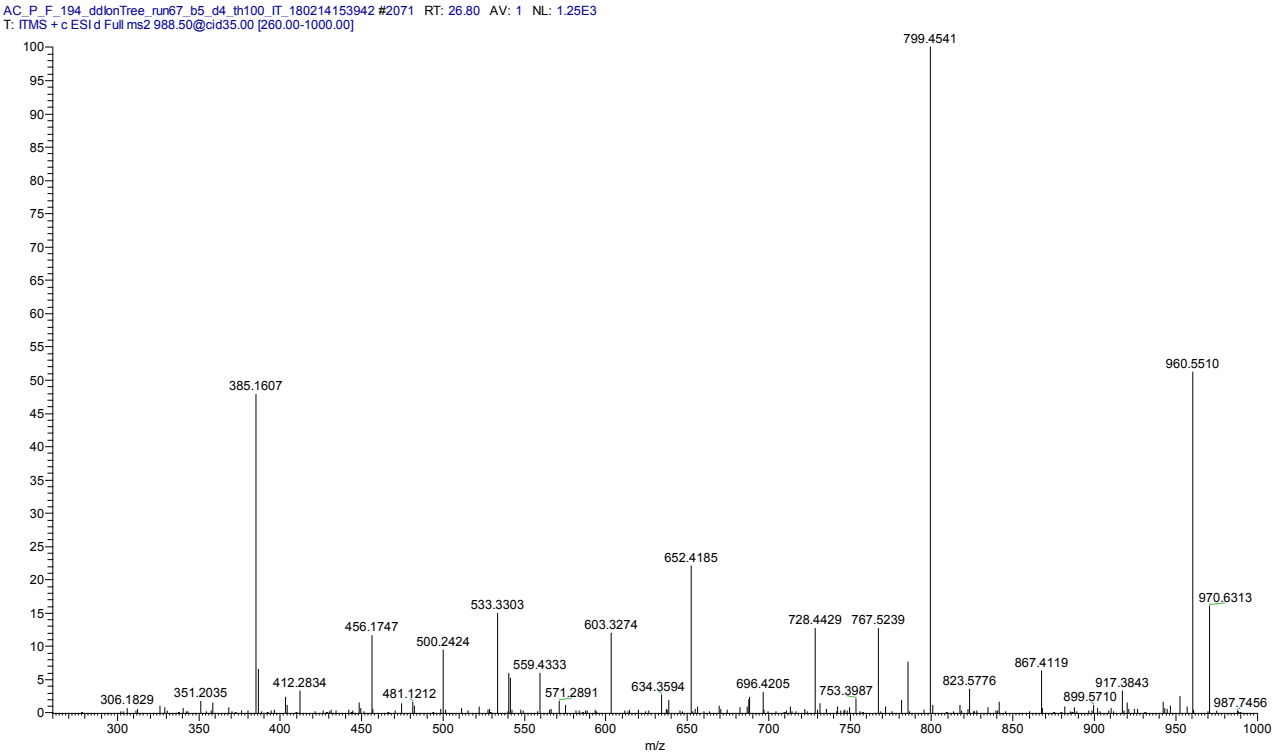

Figure 131. MS 2 spectrum of the *m/z* feature annotated as putative cyclic-depsipeptide with a *m/z* value of 988.50 at rt 26.80 min.

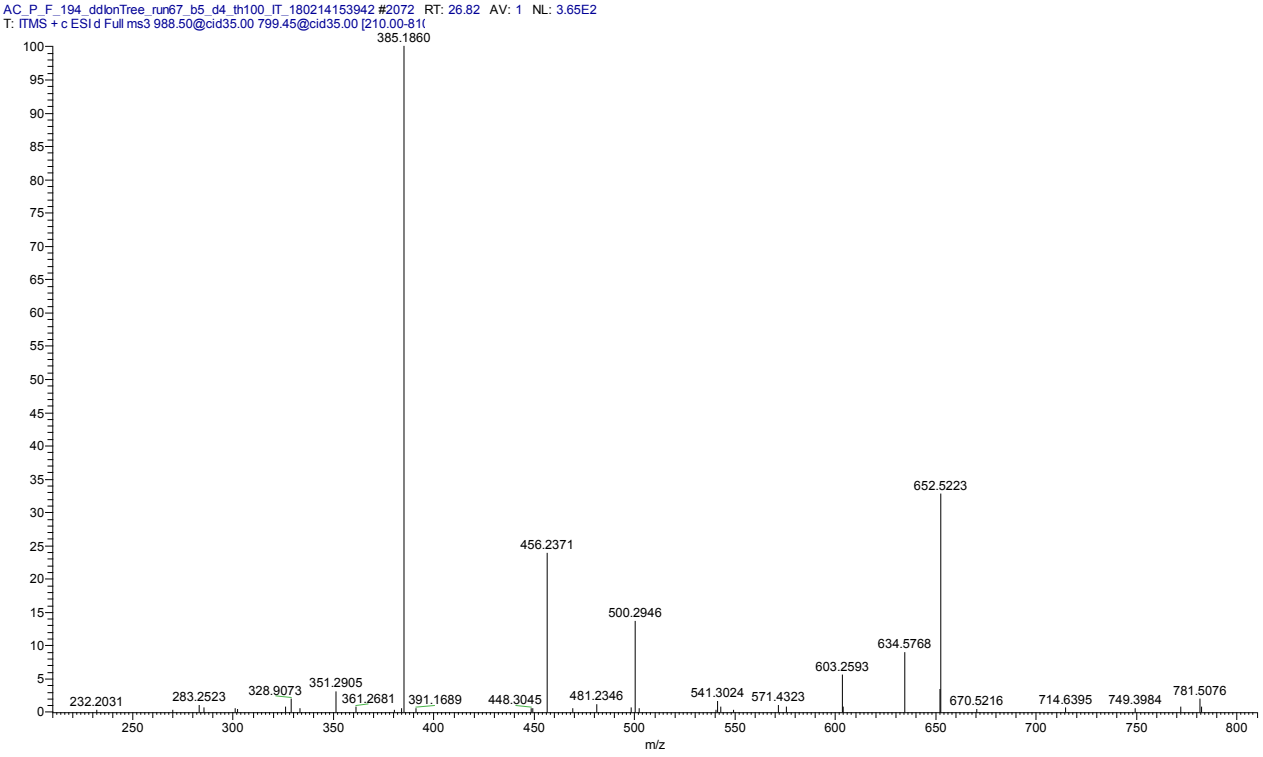

Figure 132. MS 3 spectrum of the fragment with *m/z* value of 799.45 of the *m/z* feature annotated as putative cyclic-depsipeptide with a *m/z* value of 988.50 at rt 26.82 min.

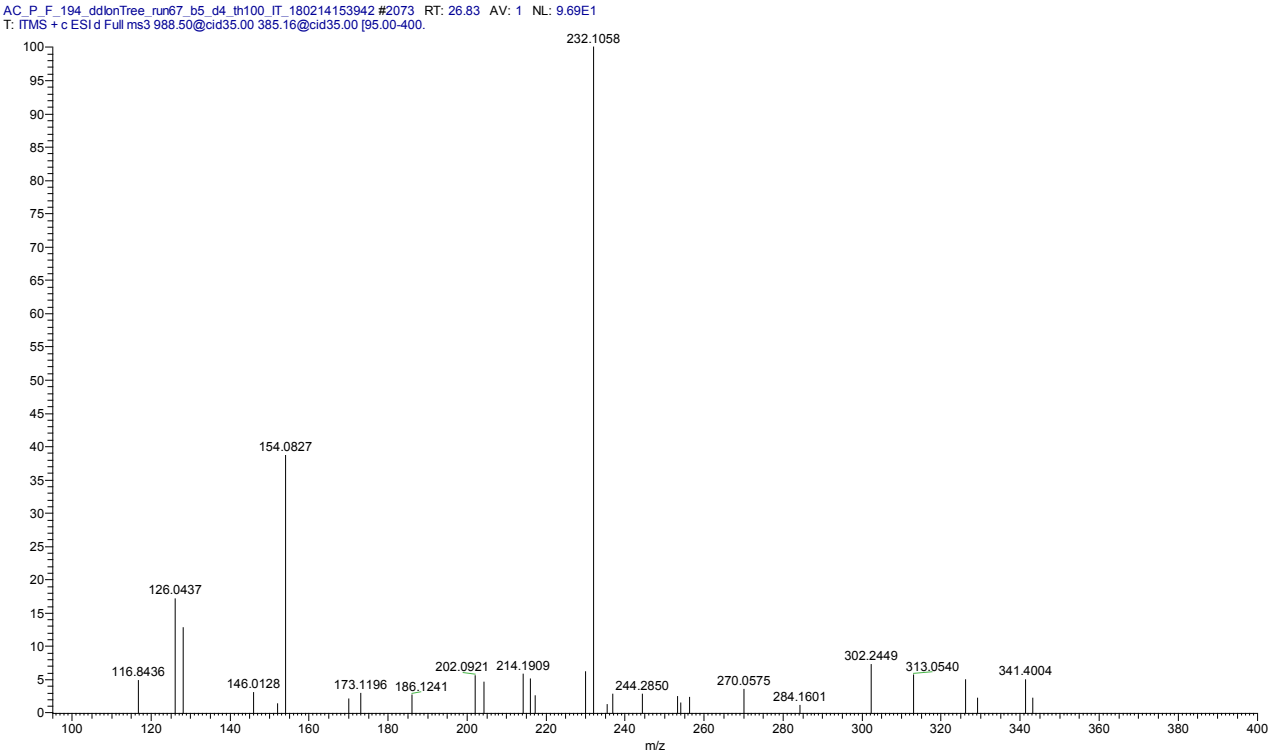

Figure 133. MS 3 spectrum of the fragment with *m/z* value of 385.16 of the *m/z* feature annotated as putative cyclic-depsipeptide with a *m/z* value of 988.50 at rt 26.83 min.

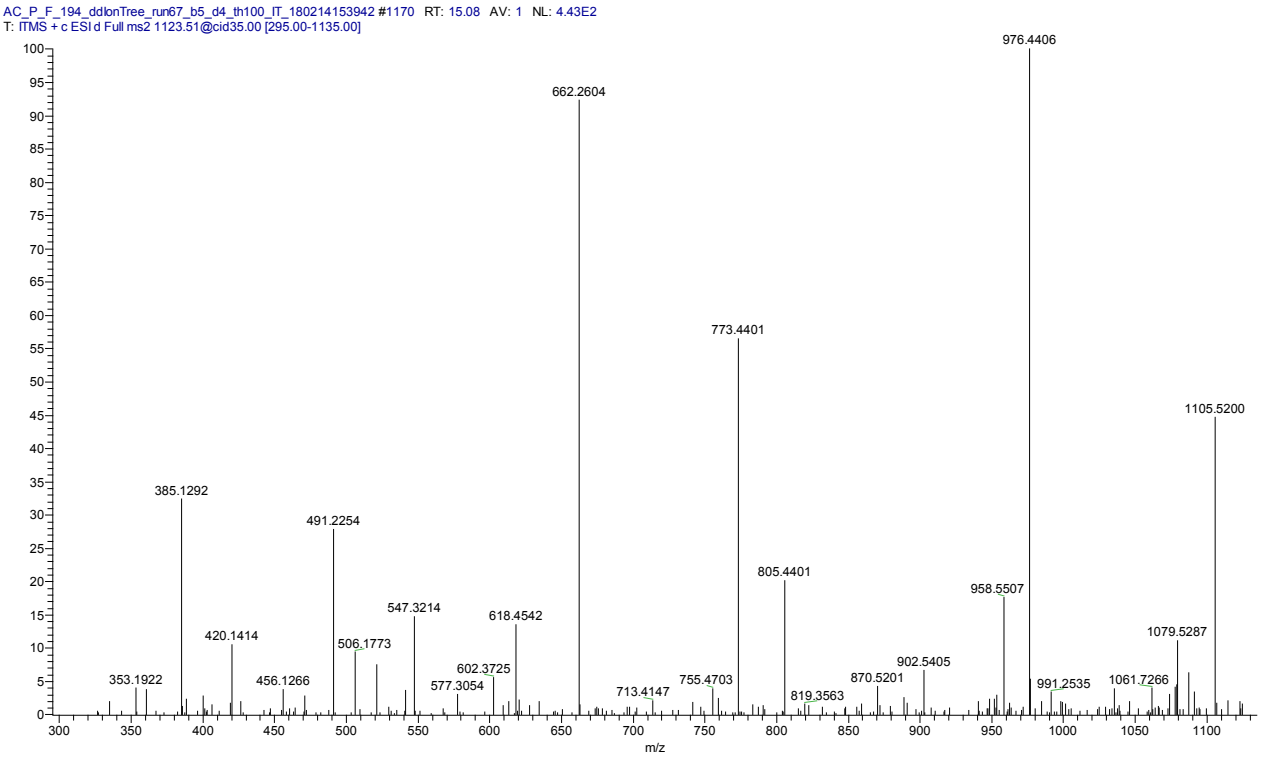

Figure 134. MS 2 spectrum of the *m/z* feature annotated as putative cyclic-depsipeptide with a *m/z* value of 1123.51 at rt 15.08 min.

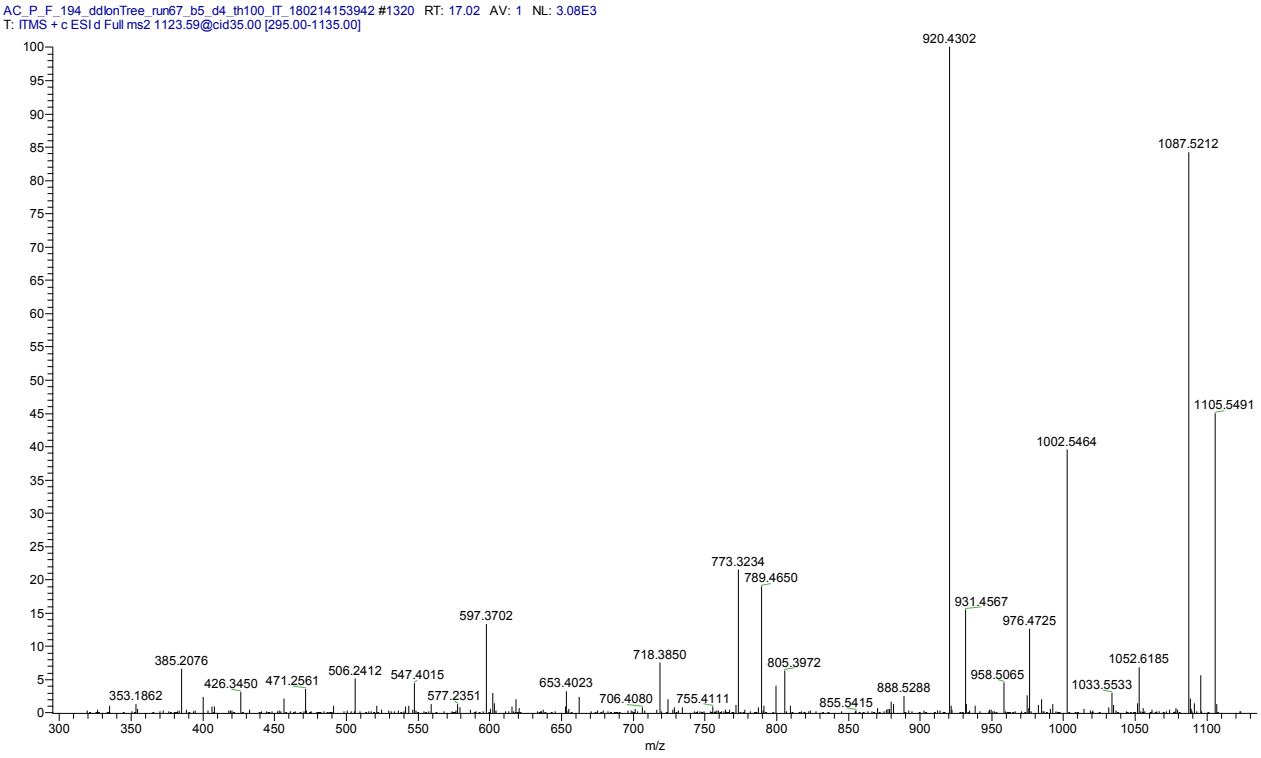

Figure 135. MS 2 spectrum of the *m/z* feature annotated as putative cyclic-depsipeptide with a *m/z* value of 1123.59 at rt 17.02 min.

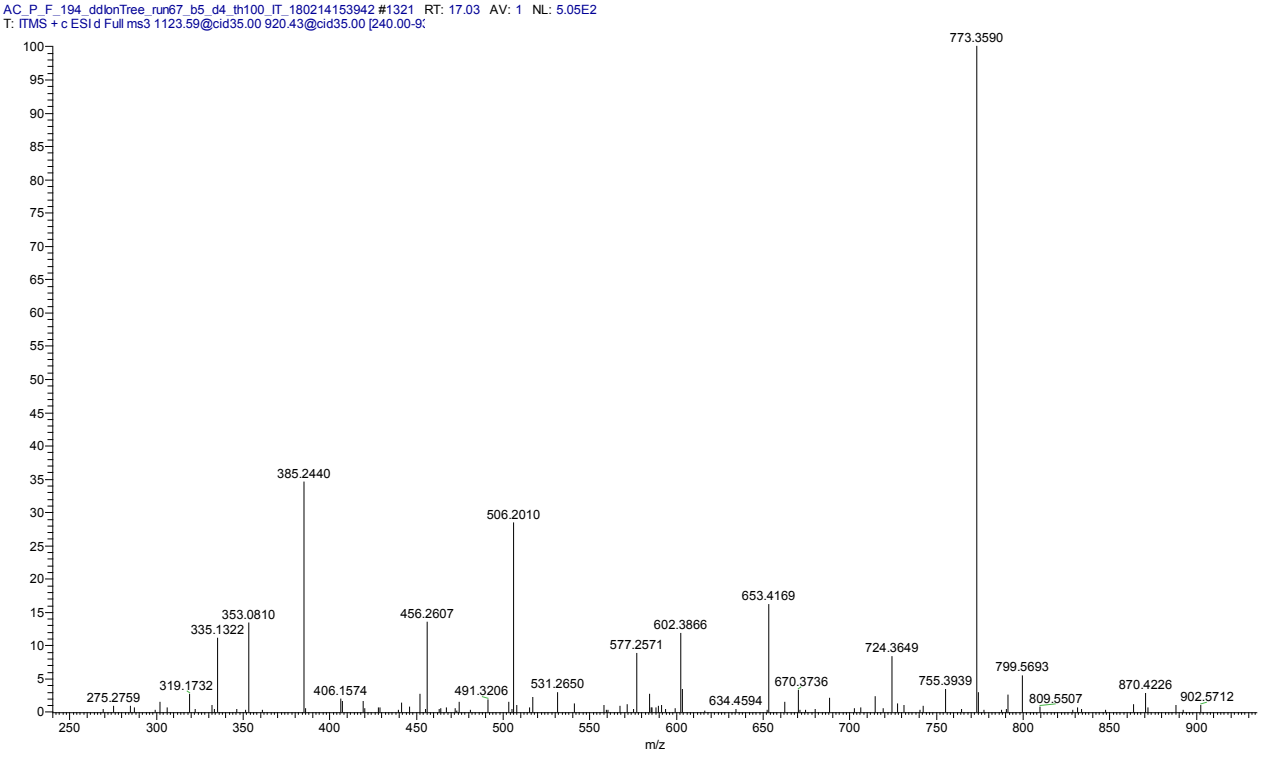

Figure 136. MS 3 spectrum of the fragment with *m/z* value of 920.43 of the *m/z* feature annotated as putative cyclic-depsipeptide with a *m/z* value of 1123.59 at rt 17.03 min.

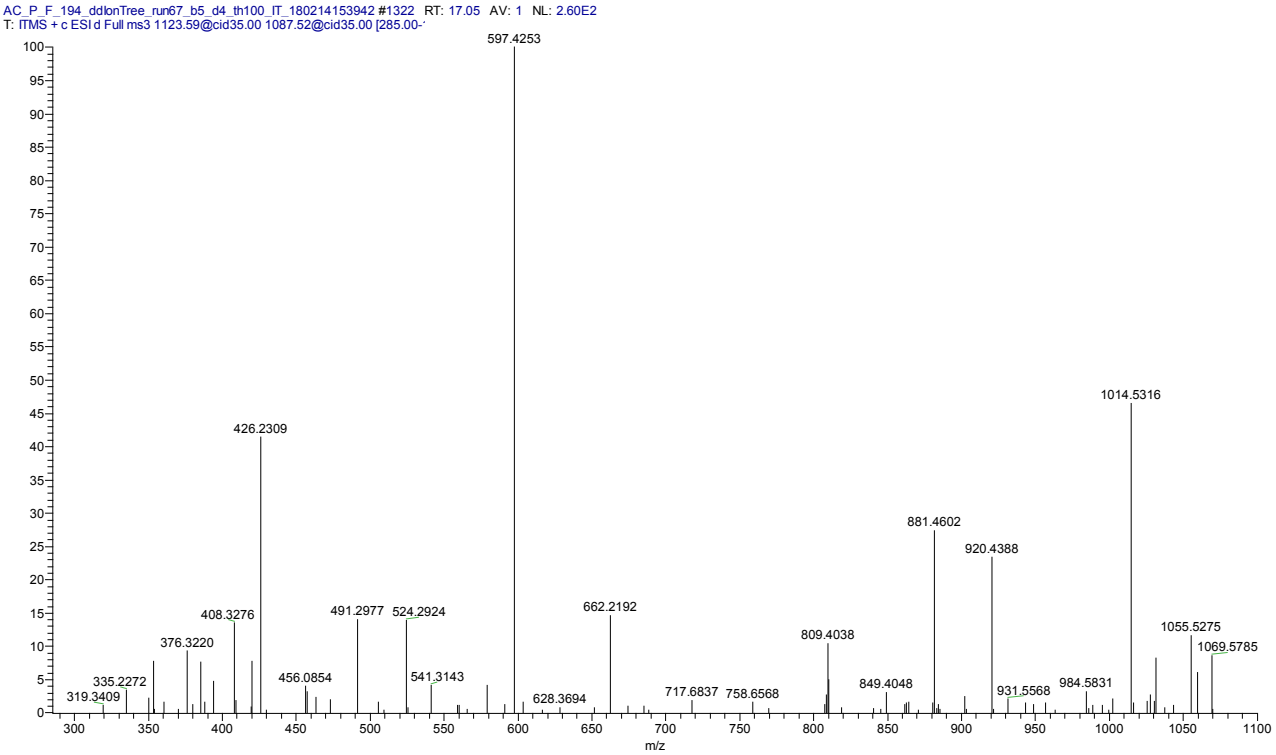

Figure 137. MS 3 spectrum of the fragment with *m/z* value of 1087.52 of the *m/z* feature annotated as putative cyclic-depsipeptide with a *m/z* value of 1123.59 at rt 17.05 min.

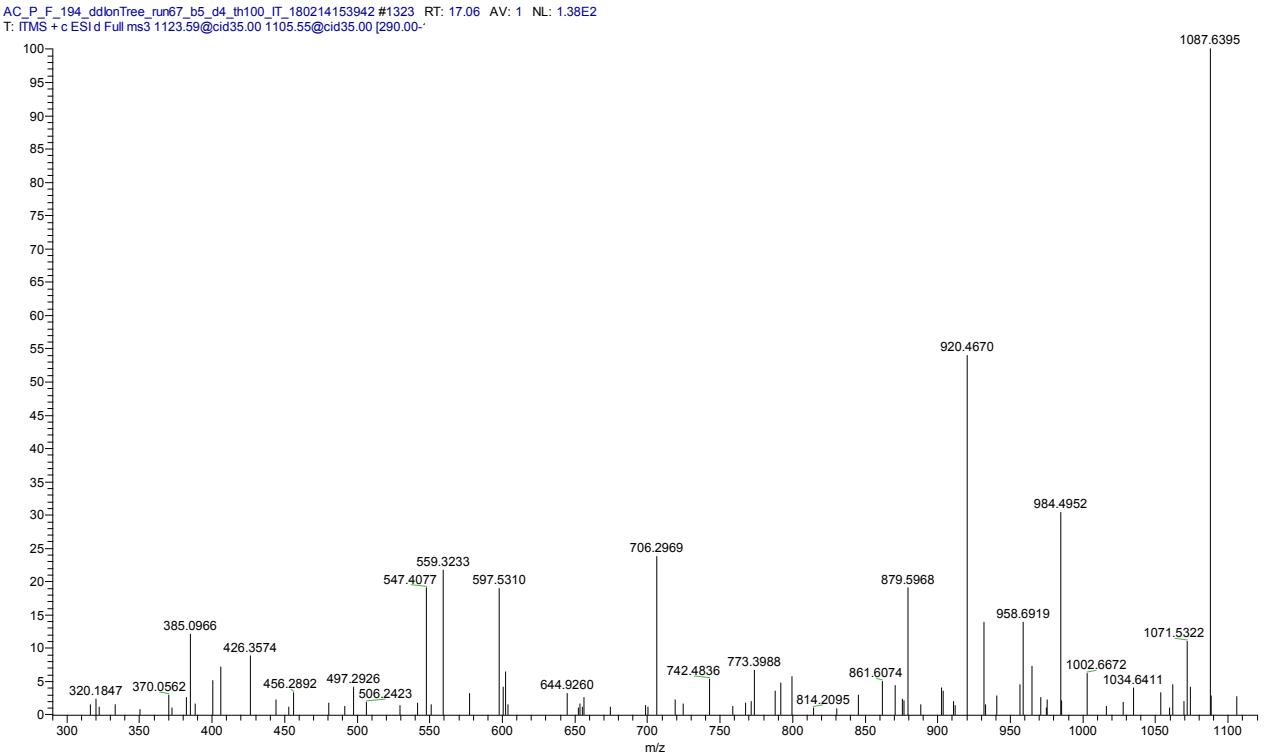

Figure 138. MS 3 spectrum of the fragment with *m/z* value of 1105.55 of the *m/z* feature annotated as putative cyclic-depsipeptide with a *m/z* value of 1123.59 at rt 17.06 min.

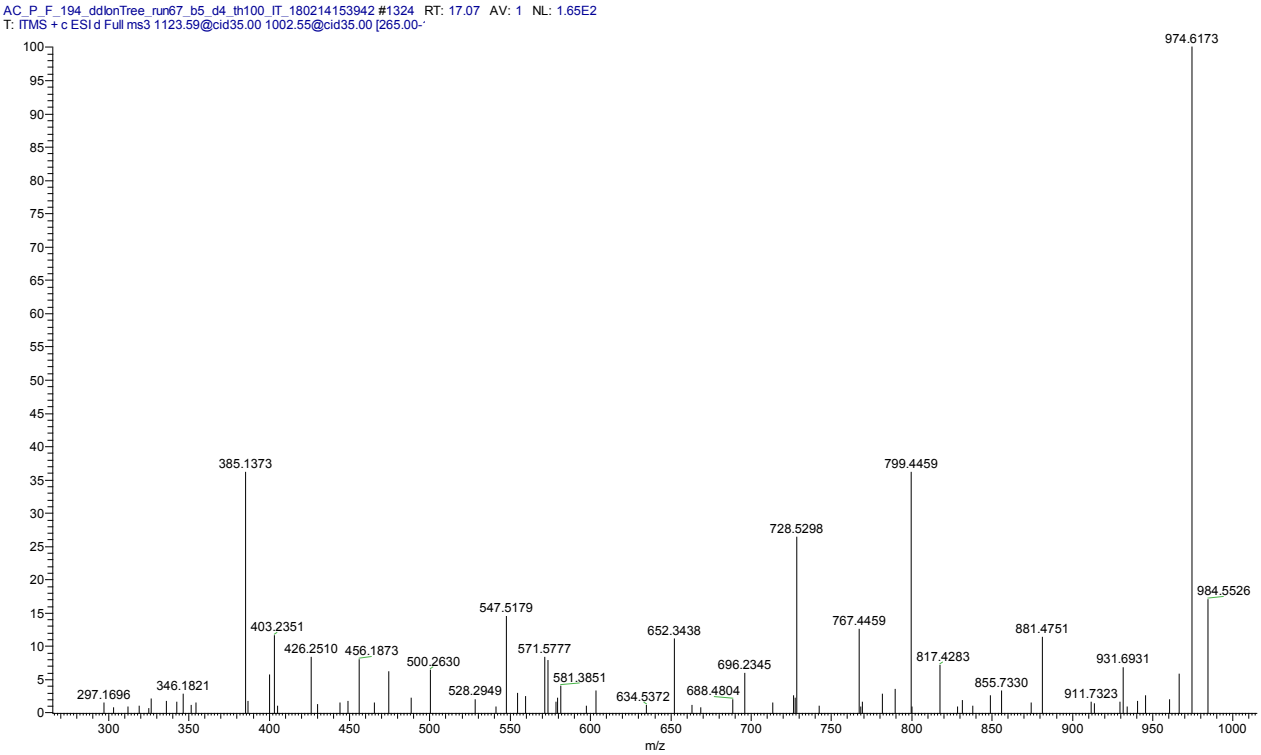

Figure 139. MS 3 spectrum of the fragment with *m/z* value of 1002.55 of the *m/z* feature annotated as putative cyclic-depsipeptide with a *m/z* value of 1123.59 at rt 17.07 min.

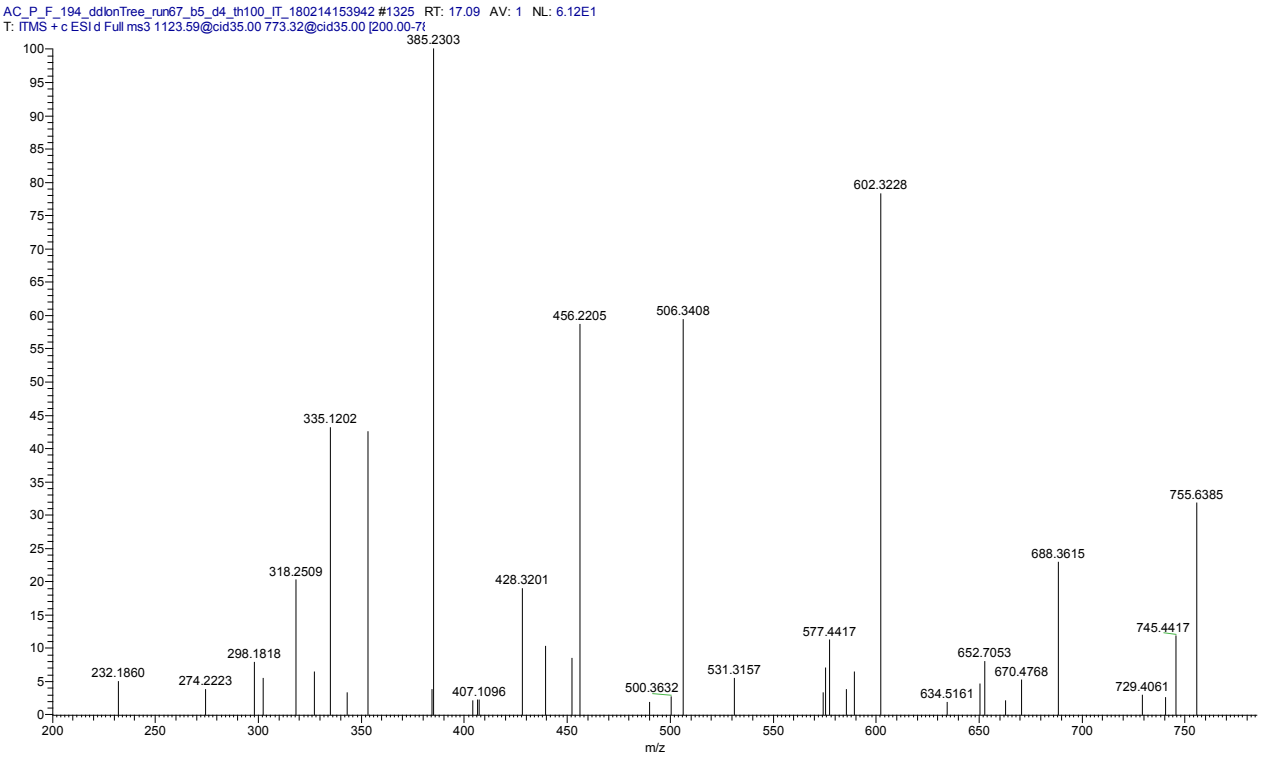

Figure 140. MS 3 spectrum of the fragment with *m/z* value of 773.32 of the *m/z* feature annotated as putative cyclic-depsipeptide with a *m/z* value of 1123.59 at rt 17.09 min.

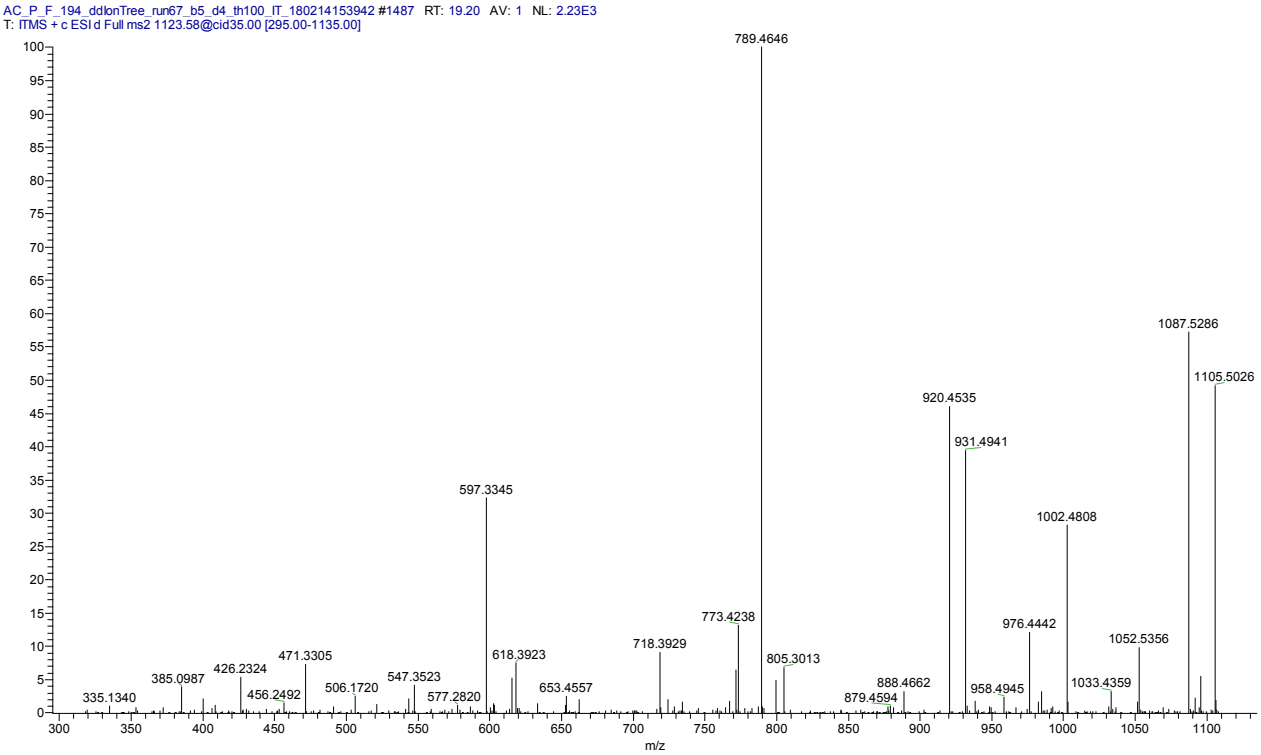

Figure 141. MS 2 spectrum of the *m/z* feature annotated as putative cyclic-depsipeptide with a *m/z* value 1123.58 at rt 19.20 min.

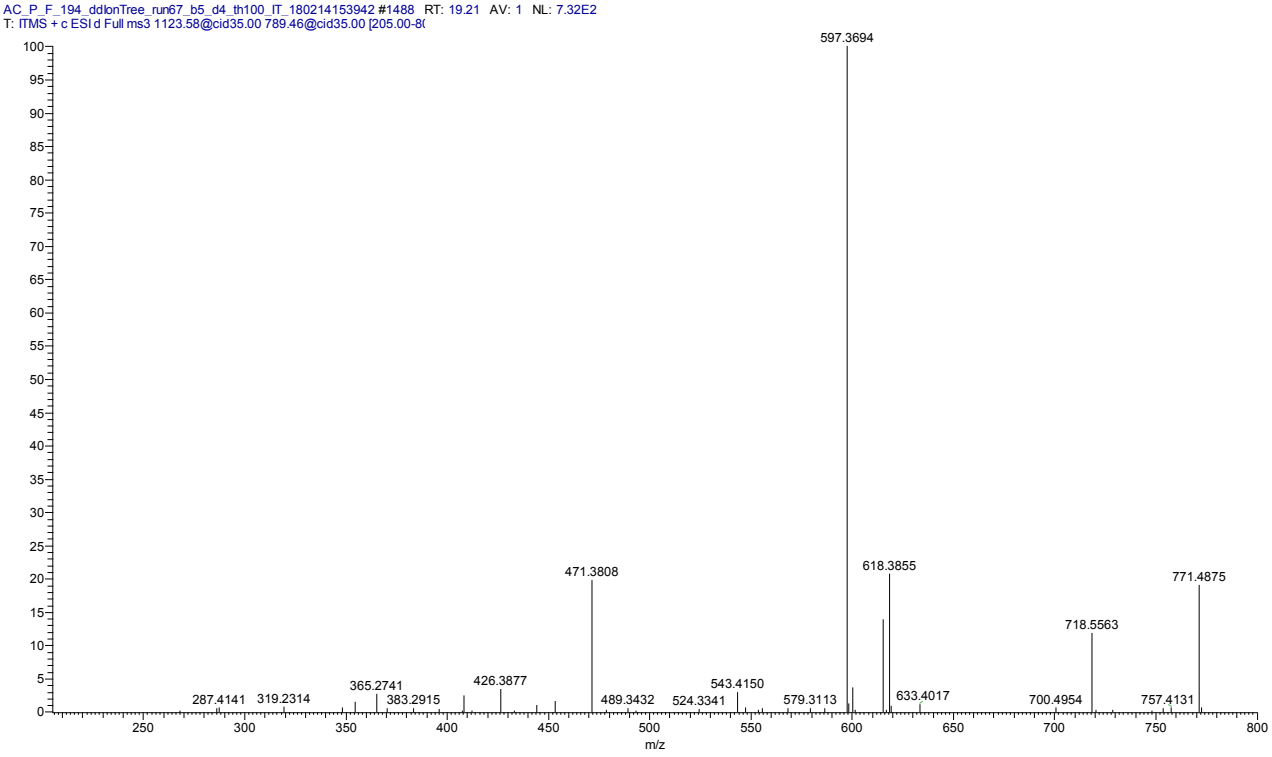

Figure 142. MS 3 spectrum of the fragment with *m/z* value of 789.45 of the *m/z* feature annotated as putative cyclic-depsipeptide with a *m/z* value 1123.58 at rt 19.21 min.

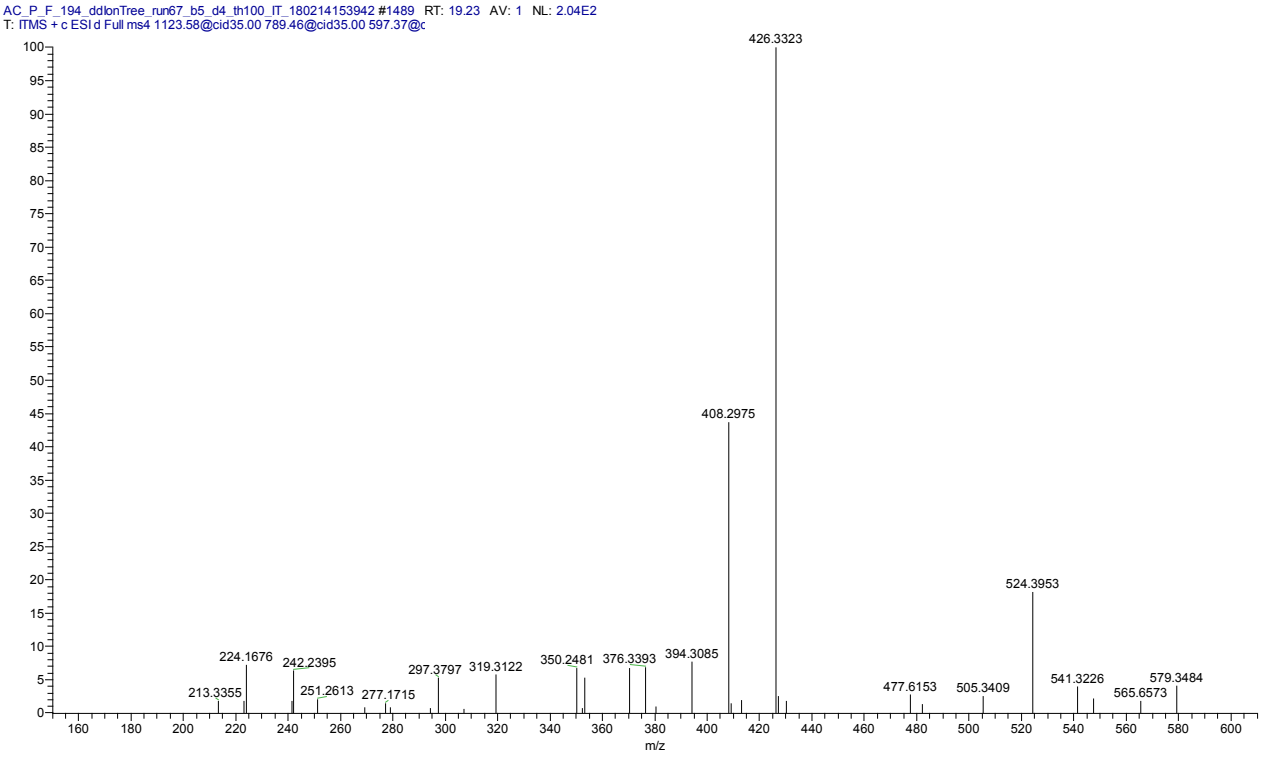

Figure 143. MS 4 spectrum of the fragment with *m/z* value of 597.37 of the fragment with *m/z* value of 789.45 of the *m/z* feature annotated as putative cyclic-depsipeptide with a *m/z* value 1123.58 at rt 19.23 min.

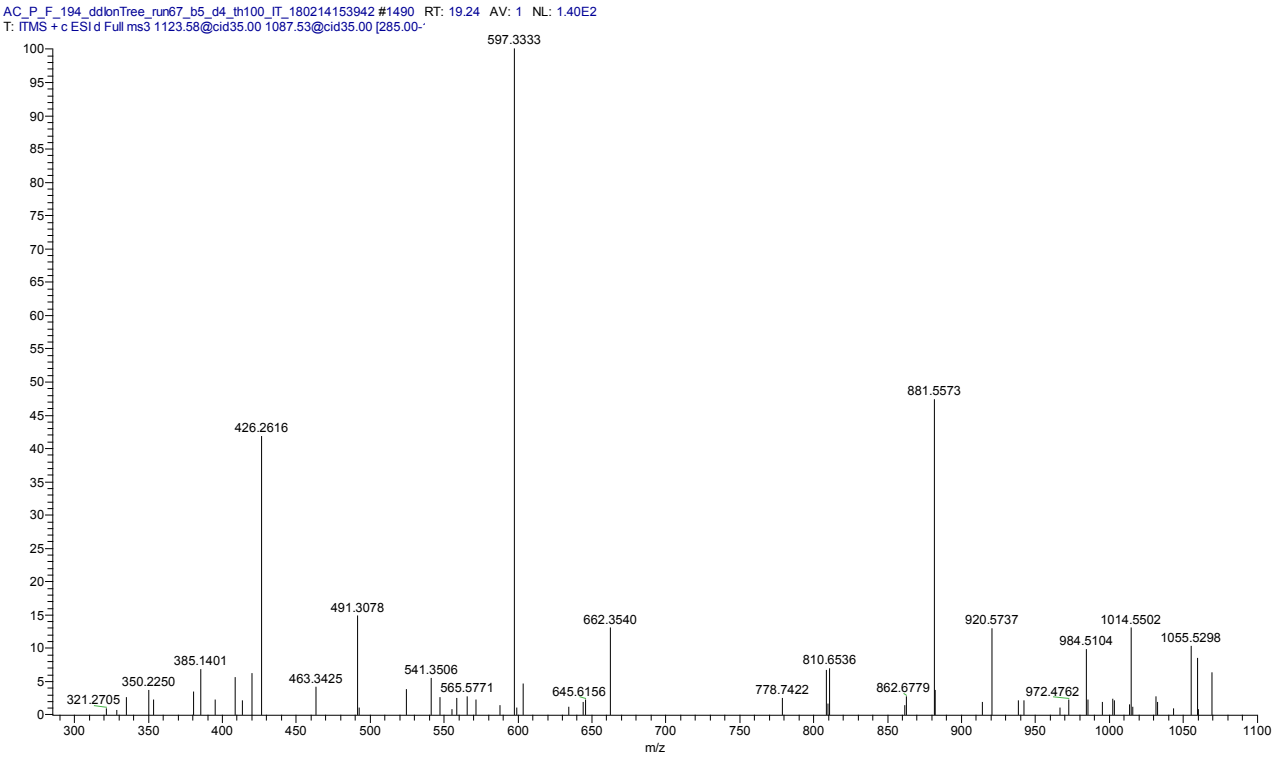

Figure 144. MS 3 spectrum of the fragment with *m/z* value of 1087.53 of the *m/z* feature annotated as putative cyclic-depsipeptide with a *m/z* value 1123.58 at rt 19.24 min.

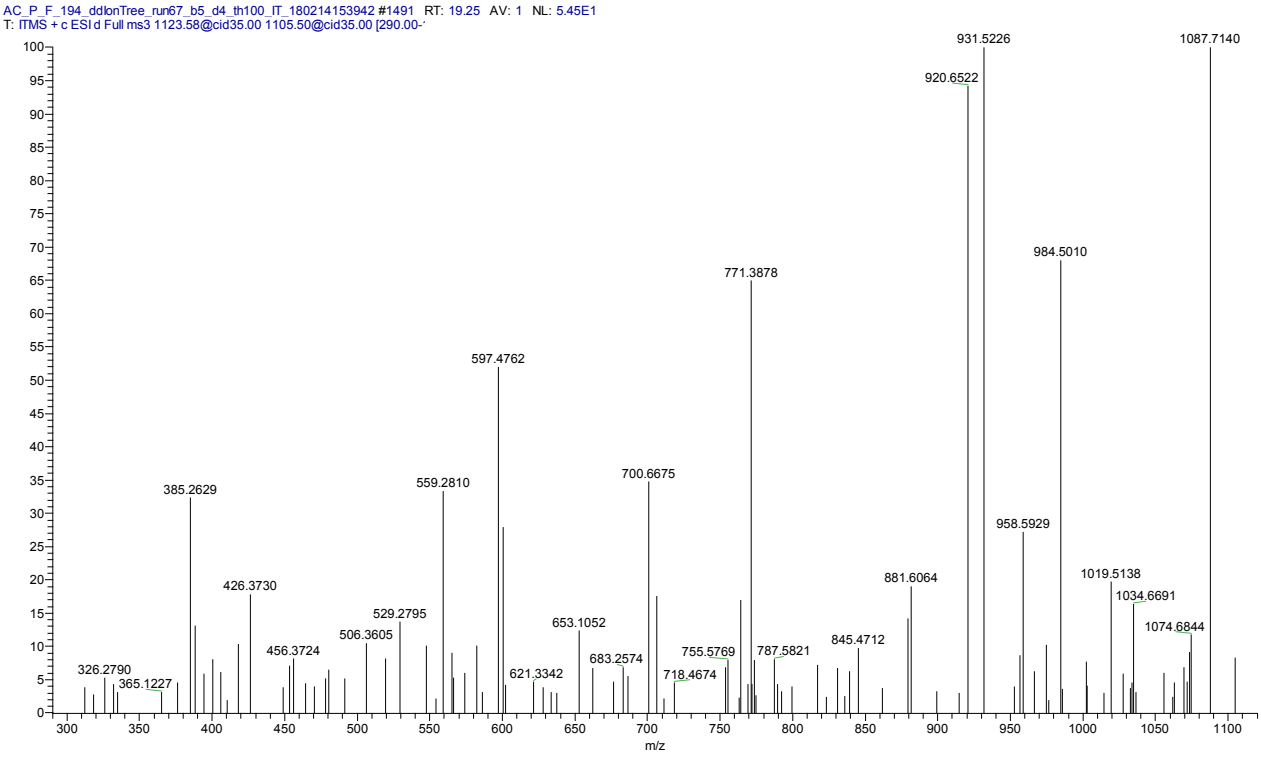

Figure 145. MS 3 spectrum of the fragment with *m/z* value of 1105.50 of the *m/z* feature annotated as putative cyclic-depsipeptide with a *m/z* value 1123.58 at rt 19.25 min.

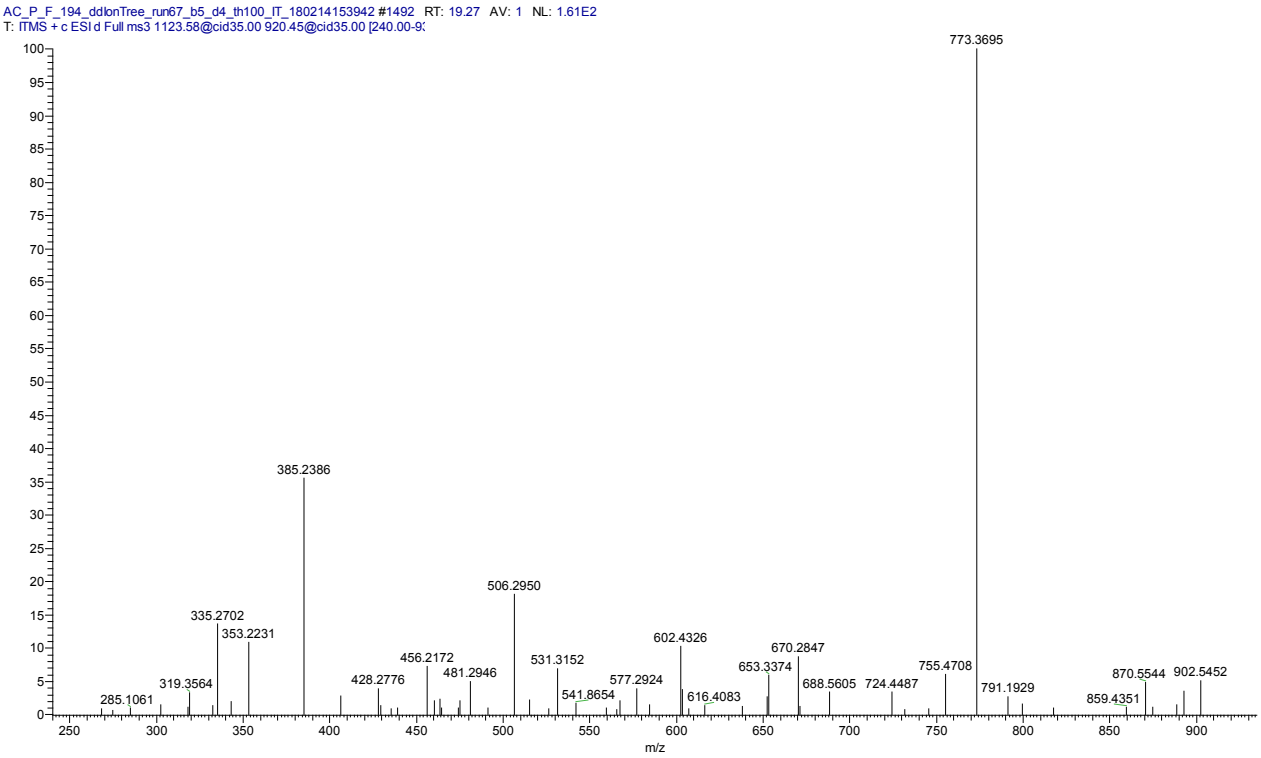

Figure 146. MS 3 spectrum of the fragment with *m/z* value of 920.45 of the *m/z* feature annotated as putative cyclic-depsipeptide with a *m/z* value 1123.58 at rt 19.27 min.

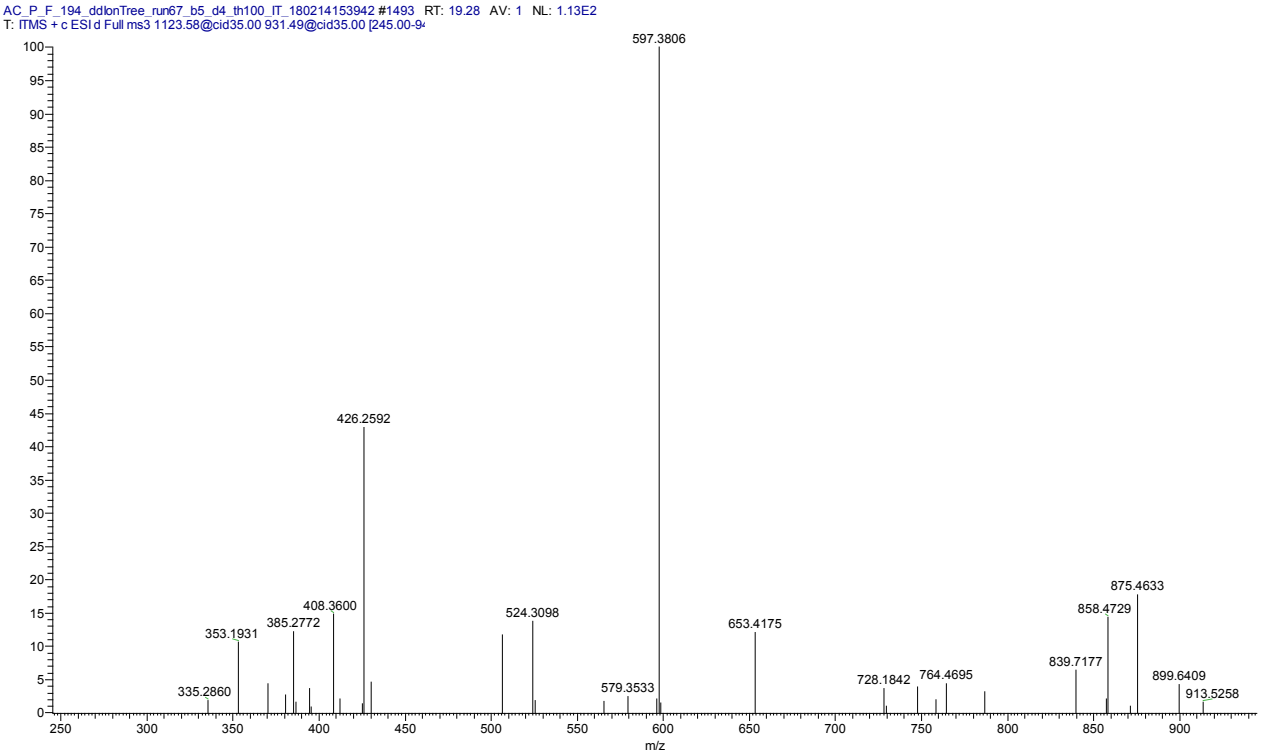

Figure 147. MS 3 spectrum of the fragment with *m/z* value of 931.49 of the *m/z* feature annotated as putative cyclic-depsipeptide with a *m/z* value 1123.58 at rt 19.28 min.

IV. Isolation of natural products from nodulated *Ardisia crenata* Sims (Primulaceae) leaf tissue

Isolation of natural products from nodulated *Ardisia crenata* Sims (Primulaceae) leaf tissue

ARTICLE INFO

Keywords:
Ardisia crenata
Primulaceae
Candidatus Burkholderia crenata
Burkholderiaceae
Natural product isolation
Catechines
Cyclic-depsipeptides
Epicatechin-3-hydroxy-2-methyl-propanoate
FR900359

ABSTRACT

Ardisia crenata Sims belongs to the ethno-botanically used genus *Ardisia* in the family Primulaceae sensu lato, which is rich in biologically active substances with great chemo diversity. The species also lives in obligate leaf endosymbiosis, wherein the plant harbours their bacterial endosymbionts in specialised glands at the leaf margin, referred to as leaf nodules. Genetic studies of the bacterial endosymbiont revealed the non-ribosomal peptide synthetase (frs) gene cluster. Expression of frs in *Escherichia coli* leads to the synthesis of the cyclic-depsipeptide FR900359, which displays strong and selective inhibition of Gq proteins. This makes it not only a promising drug candidate but also an interesting lead structure for the development of novel pharmaceuticals. A non-targeted metabolomics approach shows substantial differences in secondary metabolite profiles of nodulated and non-nodulated tissues. Examination of MS data revealed novel putative derivatives of FR900359. The following procedure aimed at isolating these new compounds. A novel depsipeptide candidate was isolated but it degraded before its structure could be elucidated. Other substances which were successfully isolated were catechin, epicatechin and the novel natural product epicatechin-3-hydroxy-2-methyl-propanoate.

IV.1. Introduction

The plant species *Ardisia crenata*, belonging to the family Primulaceae sensu lato, is widely distributed in East Asia and is commonly used as an ornamental plant. It is also used in Eastern traditional medicine and as a source for biologically active phytochemicals (Kitajima et al., 2006; Kobayashi and de Mejía, 2005). The leaves of *A. crenata* bear specialized structures on their margin containing symbiotic bacteria. These structures are referred to as leaf nodules (Carlier et al., 2016). Leaf nodule symbiosis is known from diverse taxa: Primulaceae sensu lato (ca. 30 nodulated species), Rubiaceae (ca. 430 nodulated species) and Styracaceae (one species) as dicot families and Dioscoraceae (at least one nodulated species) as monocot family (Pinto-Carbó et al., 2018; Yang and Hu, 2018). The occurrence of internal cavities in the leaf lamina harboring symbiotic bacteria, defines the leaf nodule symbiosis. These structures are often visible as nodules on the leaf surface (HORNER JR and LERSTEN, 1972). The symbiotic bacteria are transmitted vertically i.e. the bacteria are transported from one generation to the next by colonization of the plant's seeds (Miller and Donnelly, 1987). This symbiosis is considered as obligatory, since the plant cannot survive past the seedling stage without the bacterial symbiont. Besides the production of secondary metabolites, the biological function and obligatory nature of this symbiosis remains unstudied (Carlier et al., 2016).

The symbiotic bacterium of *A. crenata* is *Candidatus Burkholderia crenata*. Up to now, in vitro cultivation attempts failed, which could be related to the tight symbiosis between host and bacterium. Recently the genome of *Candidatus Burkholderia crenata* was sequenced. It is the smallest genome from a species of the genus *Burkholderia* to date and contains a large amount of insertion sequences and pseudogenes. These results lead to the assumption that this genome is undergoing reductive evolution (Carlier et al., 2016). Such patterns are often found in symbiotic bacteria in comparison with non-symbiotic relatives. Free-living organisms are subjected to a greater variety of environmental parameters and therefore have to allocate a larger proportion of their genome to transcriptional regulators than host-restricted symbionts or pathogens (Cases et al., 2003). It was noticed that the genome of *Candidatus B. crenata* does not encode functions commonly associated with plant symbioses such as nitrogen fixation (nitrogenase) or plant hormone metabolism. In comparison to the genes belonging to the core genome of Burkholderiaceae and genes conserved within the endosymbionts of Primulaceae and Rubiaceae, the genome of *Candidatus B. crenata* also contains 24 unique genes. These genes are organized in two clusters localized on two different plasmids and encode for putative enzymes involved in polyketide- and non-ribosomal peptide synthesis. (Carlier et al., 2016). Heterologous expression of the frs gene cluster in *Escherichia coli* leads to the production of FR900359, therefore confirming it as the FR non-ribosomal peptide synthetase gene cluster (Crüsemann et al., 2018).

The cyclic-depsipeptide FR900359 was first isolated from *A. crenata* and described in 1988 (Fujioka et al., 1988). FR900359 has the ability to interfere with cell signaling by selectively blocking heterotrimeric guanine nucleotide binding proteins (G proteins) (Crüsemann et al., 2018). Many essential processes in eukaryotic cells are regulated by Gq-mediated signaling pathways (Link and Müller, 2016). Therefore, FR900359 could have value as a pharmaceutical. G proteins are very important for homoeostasis in response to extracellular cues. Since the discovery of the G protein family no pharmacological agent that targets these proteins, is available yet (Schrage et al., 2015). Beside the cyclic-depsipeptide YM254890 (Nishimura et al., 2010), FR900359 is the only available compound so far, which interdicts Gq signaling with high selectivity and potency (Schrage et al., 2015).

Besides pharmacological use and better understanding of the physiology of Gq-proteins and Gq-protein coupled receptors (GqPCRs), the ecological function of FR900359 *in planta* is of interest. A previous study showed that kirkamide, a metabolite of the nodule-bearing species *Psychotria kirkii* (Rubiaceae) is toxic to insects, which suggests a protective function against herbivory (Sieber et al., 2015). In a study the effects of FR900359 on mice and bean bug nymphs was tested. The results showed significant decrease in mouse blood pressure and lower survival rates of the nymphs. Toxic effects on insects were likely caused by the high affinity of FR900359 to Gq proteins of various pest insects. These results likewise suggest that FR900359 protects the host plant against herbivores (Crüsemann et al., 2018).

The structure of FR900359 was first determined by nuclear magnetic resonance spectroscopic and mass spectrometric analysis. The structure consists of ten units: alanine, *N*-methylalanine, β-hydroxyleucine (three residues), 3-phenyllactic acid, acetic acid, propionicacid, and the uncommon amino acids *N*-methyldehydroalanine and *N,O*-dimethylthreonine. (Figure 148) (Fujioka et al., 1988).

The following procedure aimed to isolate FR900359 and possible derivatives from fresh leaves of *A. crenata* and analyze the purified substances by RP-HPLC-UV, RP-HPLC-HRESIMS and nuclear magnetic resonance spectroscopy (NMR). A novel depsipeptide candidate was isolated but it degraded before its structure could be elucidated. Other substances which were successfully isolated were catechin, epicatechin and the novel natural product epicatechin-3-hydroxy-2-methyl-propanoate.

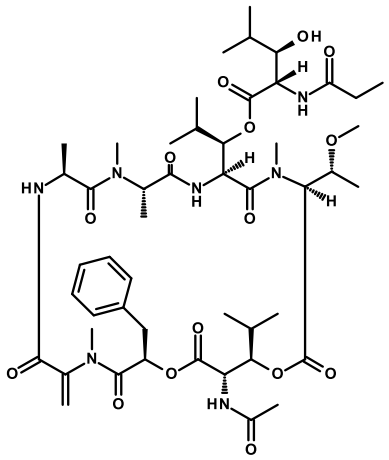

Figure 148. Chemical structure of FR900359 (Fujioka et al., 1988).

IV.2. Results and discussion

The following extraction scheme was used for the natural product isolation from *A. crenata* leaf tissue (Figure 149).

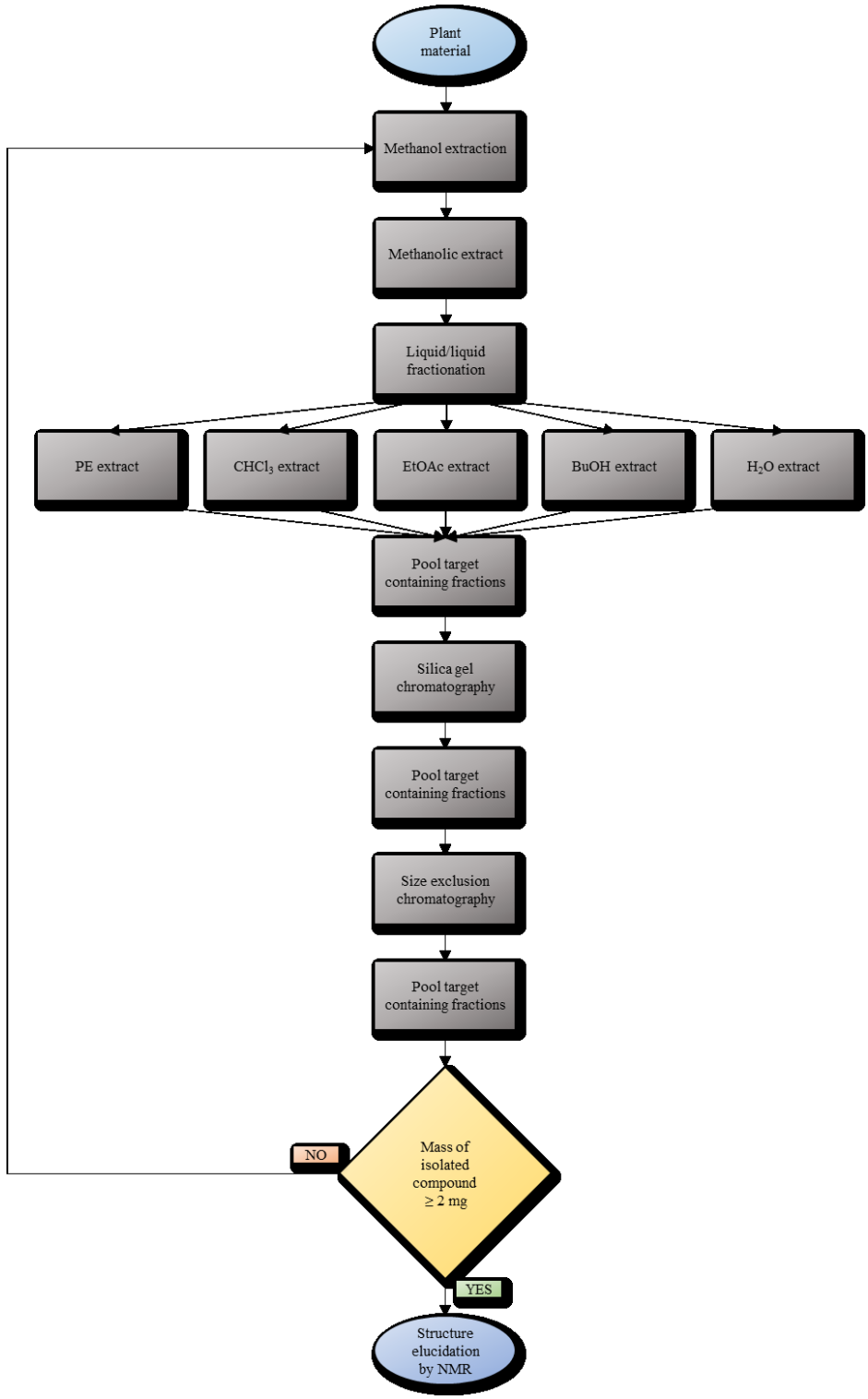

Figure 149. Extraction scheme used for the natural product isolation from nodulated *A. crenata* leaf tissue.

The presence of the target compounds was analyzed by reversed phase high pressure liquid chromatography (RP-HPLC) and high-resolution electrospray ionization mass spectrometry (HRESIMS) in positive ion mode. All *m/z* values given correspond to the singly protonated molecular ion species $[M+H]^+$, of the respective analytes, if not stated otherwise. The plant extract and corresponding fractions were screened for cyclic-depsipeptides, as well as putative depsipeptide candidates with the following *m/z* values: 817.4342, 988.5309, 1002.5394, 1032.5500 and 1123.5629. 1002.5394 is the *m/z* value of FR900359 (**1**), 1032.5500 (**2**) is the *m/z* value of AC-1, 817.4342 (**3**) is the *m/z* value of AC-SC (Figure 150), the *m/z* value of 988.5309 belongs to two putative FR900359 derivatives and the *m/z* value of 1123.5629 belongs to three putative depsipeptide candidates.

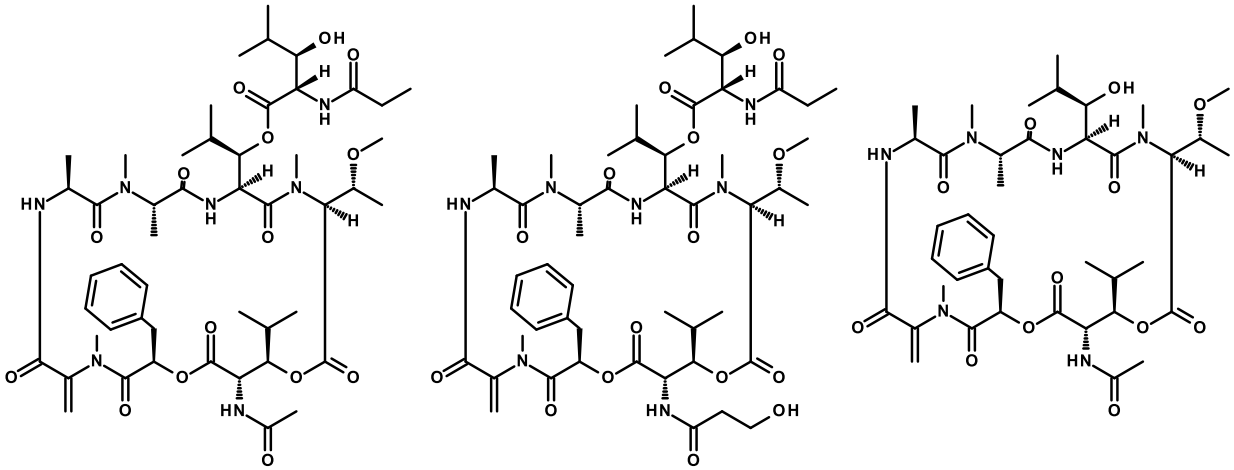

FR900359 (**1**)

Exact mass : 1001.5321 g/mol
Formula : $C_{49}H_{75}N_7O_{15}$

AC-1 (**2**)

Exact mass : 1031.5427 g/mol
Formula : $C_{50}H_{77}N_7O_{16}$

AC-SC (**3**)

Exact mass : 816.4269 g/mol
Formula : $C_{40}H_{60}N_6O_{12}$

Figure 150. Chemical structures of FR900359 (**1**), AC-1 (**2**) and AC-SC (**3**) (Crüsemann et al., 2018).

IV.2.1. Analysis of crude plant extract and liquid/liquid fractions of the crude extract

The target compounds and isolated compounds are displayed here (Figure 151 and Figure 152) In the solvent fractionation step the targets are distributed between all fractions except the H_2O phase), which allowed removing very polar compounds such as sugars and glycosides (Figure 153 and Figure 154). This is likely because the different phases weren't extracted completely. The $CHCl_3$, EtOAc and BuOH phases were then subjected to a silica gel column chromatography.

IV.2.2. Analysis of silica gel chromatography fractions

A separation of the targets by polarity can be seen (Figure 155, Figure 156, Figure 157, Figure 158, Figure 159 and Figure 160). At the point of the size exclusion chromatography (SEC) the MS analysis of the different silica gel column chromatography fractions was not completed yet, also no UV or thin layer chromatography (TLC) signature of the targets was known at this point. The SEC was therefore conducted with the fractions that seemed most promising based on their UV spectra, which was expected to be uncharacteristic due to the lack of pronounced chromophores in the target cyclic-depsipeptides. Maybe a better separation could be achieved by using finer silica gel and adding the dissolved extract directly onto the column instead of dripping it onto dry silica gel first.

IV.2.3. Analysis of the silica gel chromatography fractions AC_KG8 and AC_KG9 after SEC

The silica gel column chromatography fractions selected for SEC were AC_KG8 and AC_KG9. The MS analysis reveals a separation by size, with the bigger compounds eluting first (Figure 161, Figure 162, Figure 163 and Figure 164).

IV.2.4. Analysis of the silica gel chromatography fractions AC_KG18, AC_KG19+20, AC_KG21+22, AC_KG23+24 and AC_KG32 after SEC

The silica gel column chromatography fractions selected for the second SEC were AC_KG18, AC_KG19+20, AC_KG21+22, AC_KG23+24 and AC_KG32. The MS analysis reveals a separation by size, with the bigger compounds eluting first (Figure 165, Figure 166, Figure 167 and Figure 168).

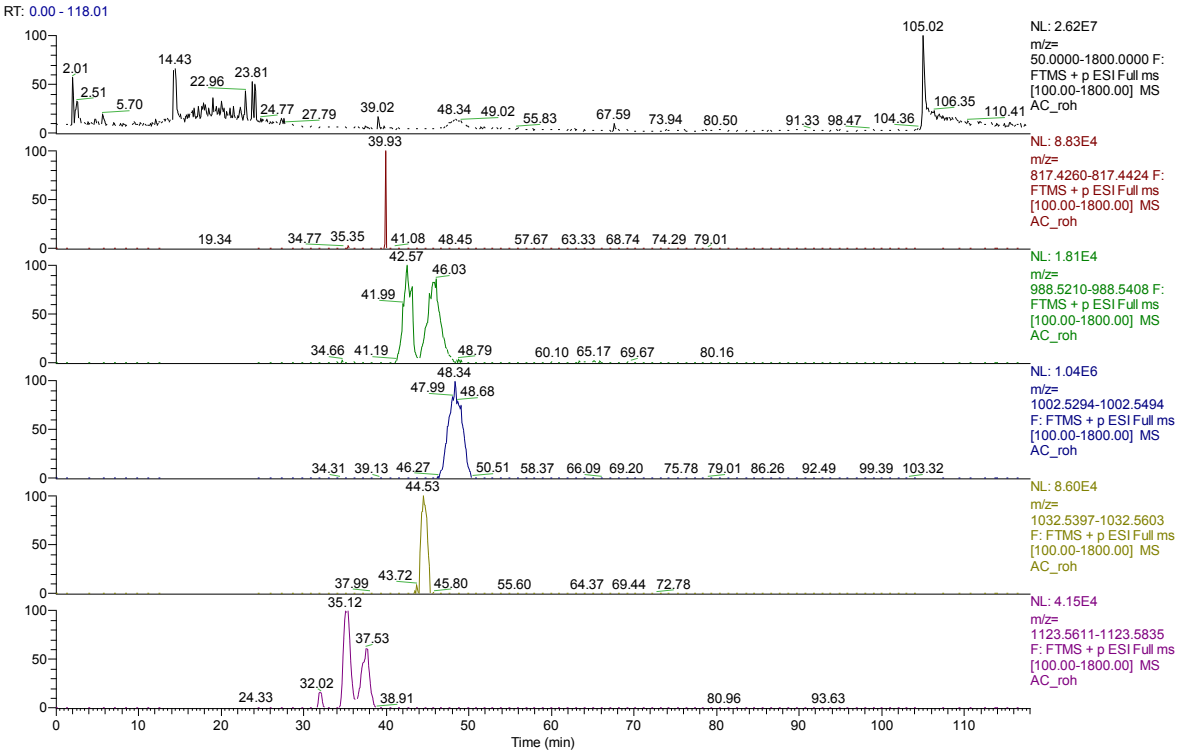

Figure 151. Top to bottom: total ion current (TIC) of the *A. crenata* leaf margin crude extract and extracted-ion chromatograms (XIC´s) of the *A. crenata* leaf margin crude extract showing the cyclic-depsipeptides and cyclic-depsipeptide candidates with the *m/z* values: 817.4342, rt 39.93 min (**3**); 988.5309, rt 42.57 min, rt 45.03 min; 1002.5394, rt 48.34 min (**1**); 1032.5500, rt 44.53 (**2**) and 1123.5629, rt 32.02 min, rt 35.12 min, rt 37.53 min.

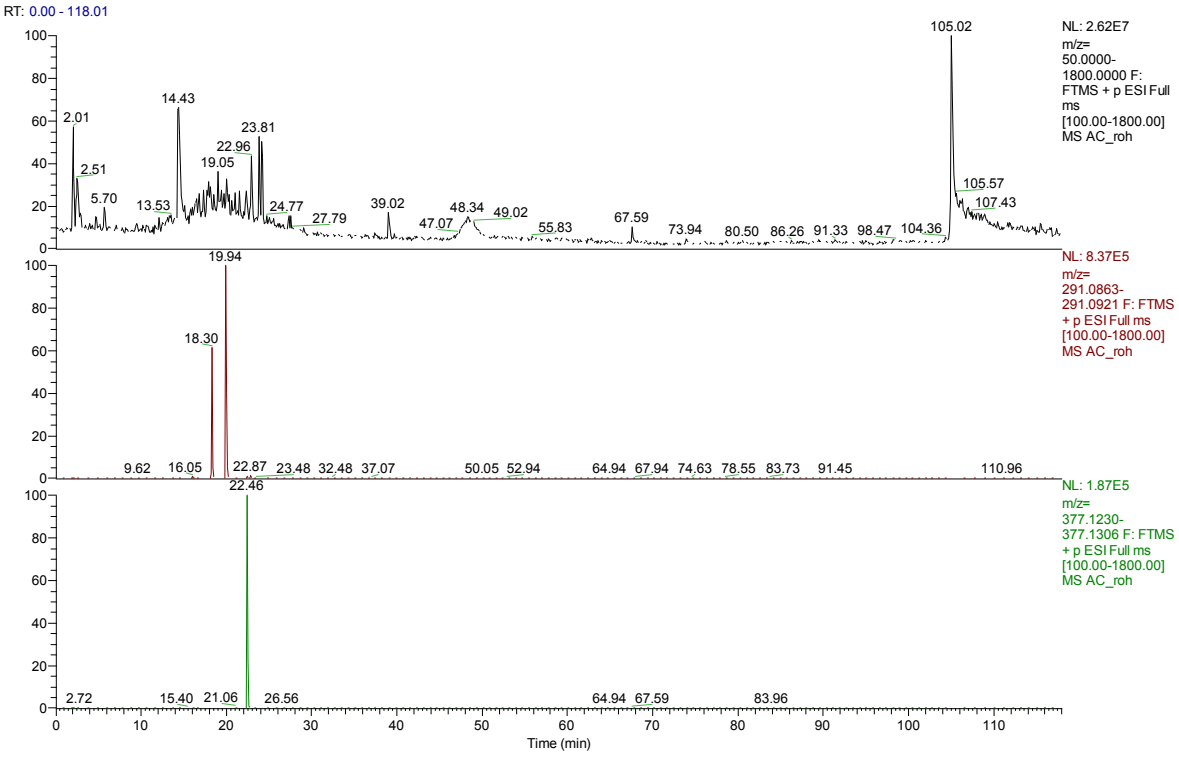

Figure 152. Top to bottom: total ion current (TIC) of the *A. crenata* leaf margin crude extract and extracted-ion chromatograms (XIC´s) of the *A. crenata* leaf margin crude extract showing (+)-catechin (**4**), (-)-epicatechin (**5**) and epicatechin-3-hydroxy-2-methyl-propanoate (**6**) with the *m/z* values: 291.0858, rt 18.30 min, rt 19.94 min and 377.1211, rt 22.46 min.

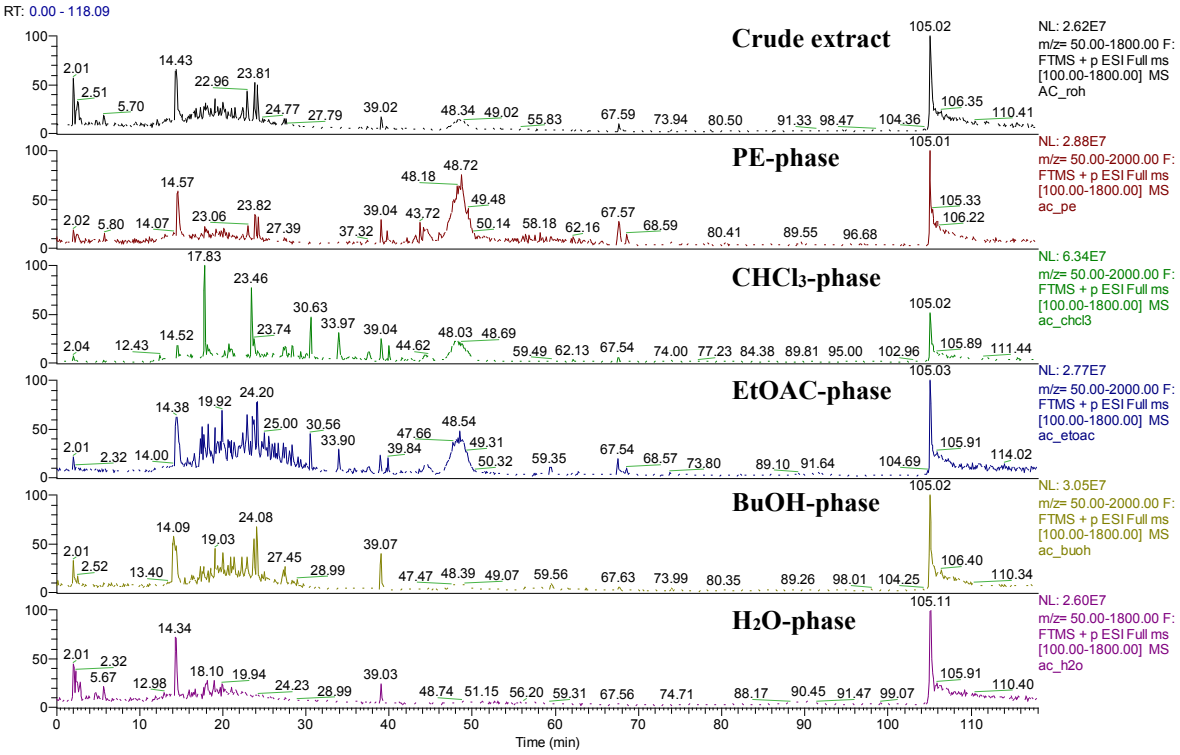

Figure 153. TIC of the crude extract and liquid/liquid fractions of *A. crenata* leaf margin crude extract. Top to bottom: crude extract, AC_PE, AC_$CHCl_3$, AC_EtOAc, AC_BuOH, AC_H_2O. Note the targets at retention time: 39.84 min (**3**), 44.62 min (**2**), 48.69 min (**1**).

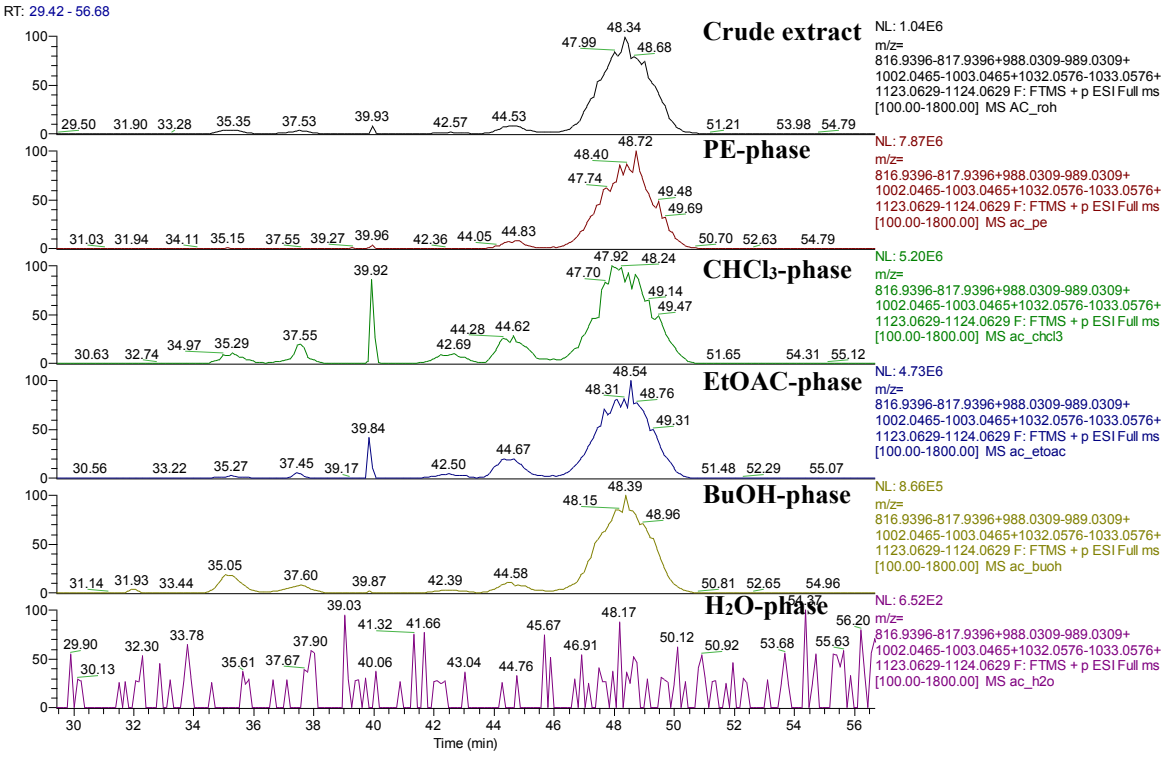

Figure 154. XICs of following *m/z* values for, top to bottom: crude extract, AC_PE, AC_$CHCl_3$, AC_EtOAc, AC_BuOH, AC_H_2O, selected *m/z* values are: 817.4342, rt 39.92 min (**3**); 988.5309, rt 42.50 min, rt 44.67 min; 1002.5394, rt 48.39 min (**1**); 1032.5500, rt 44.62 (**2**) and 1123.5629, rt 31.93 min, rt 35.05 min, rt 37.60 min.

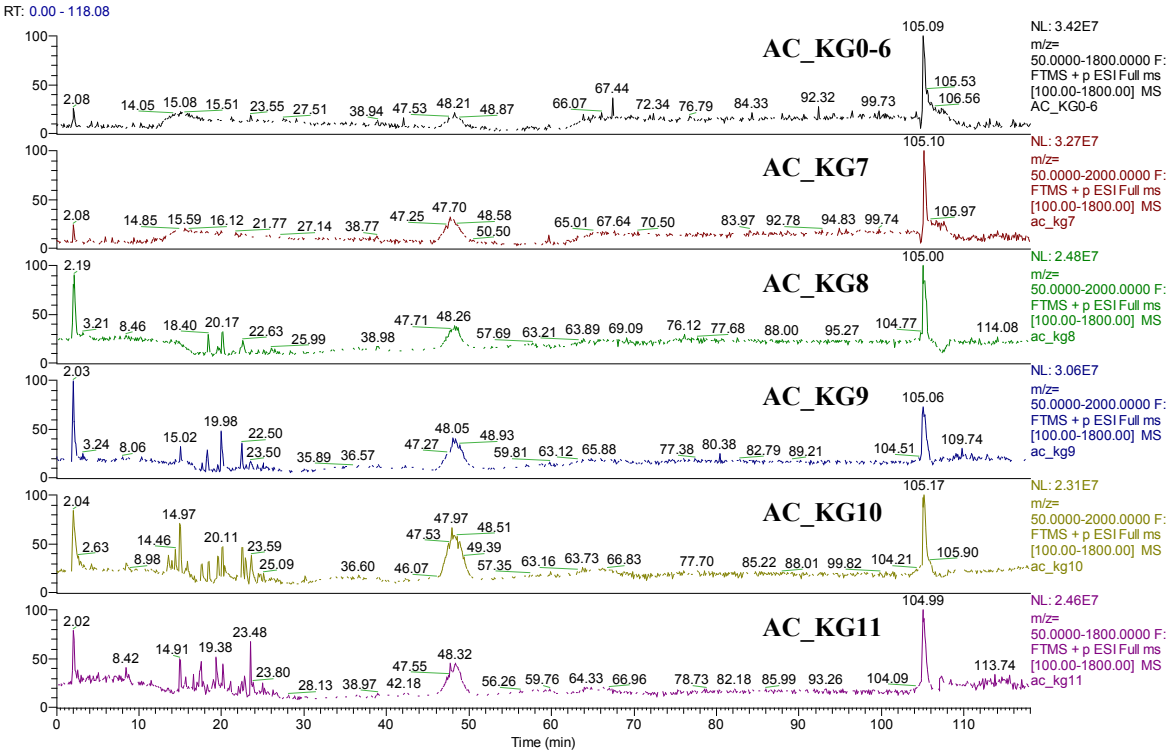

Figure 155. TIC of the fractions obtained by subjecting the $CHCl_3$, EtOAc and BuOH phases of the crude extract of *A. crenata* leaf margins to silica gel column chromatography. Top to bottom: AC_KG0-6, AC_KG7, AC_KG8, AC_KG9, AC_KG10, AC_KG11.

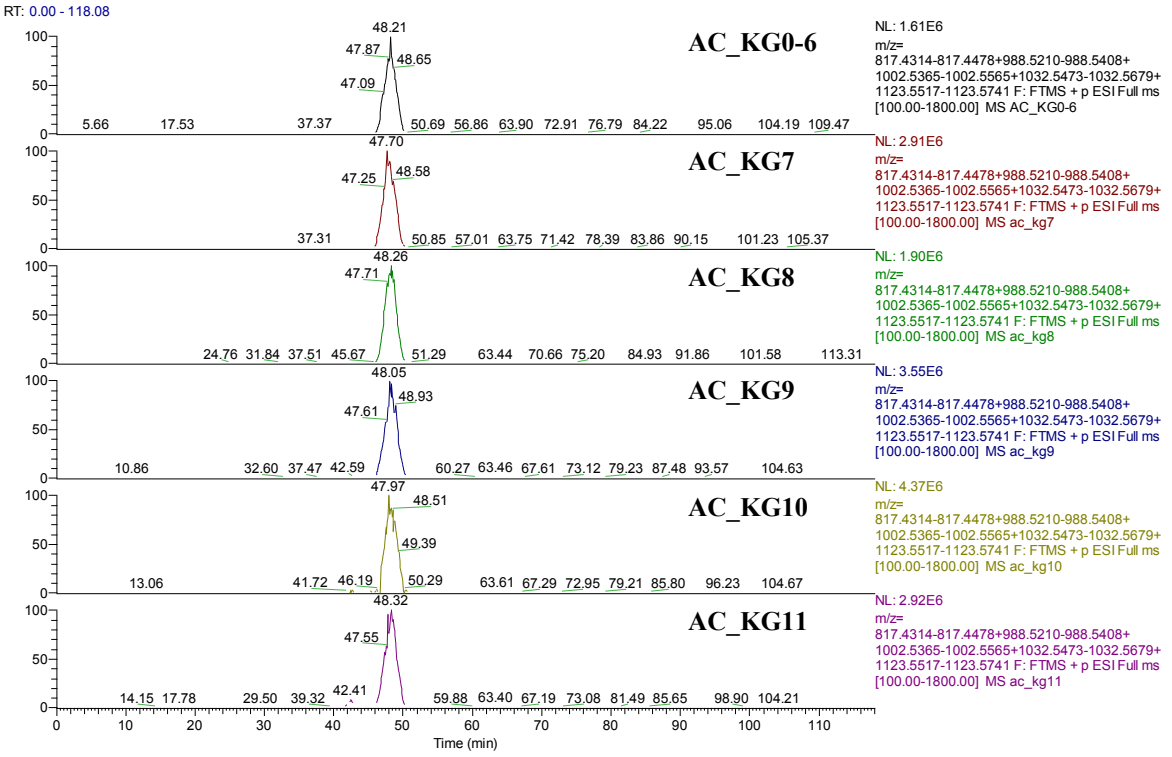

Figure 156. XICs of following *m/z* values for, top to bottom: AC_KG0-6, AC_KG7, AC_KG8, AC_KG9, AC_KG10, AC_KG11, selected *m/z* values are: 817.4342; 988.5309, rt 42.41 min; 1002.5394, rt 48.21 min (**1**); 1032.5500 and 1123.5629.

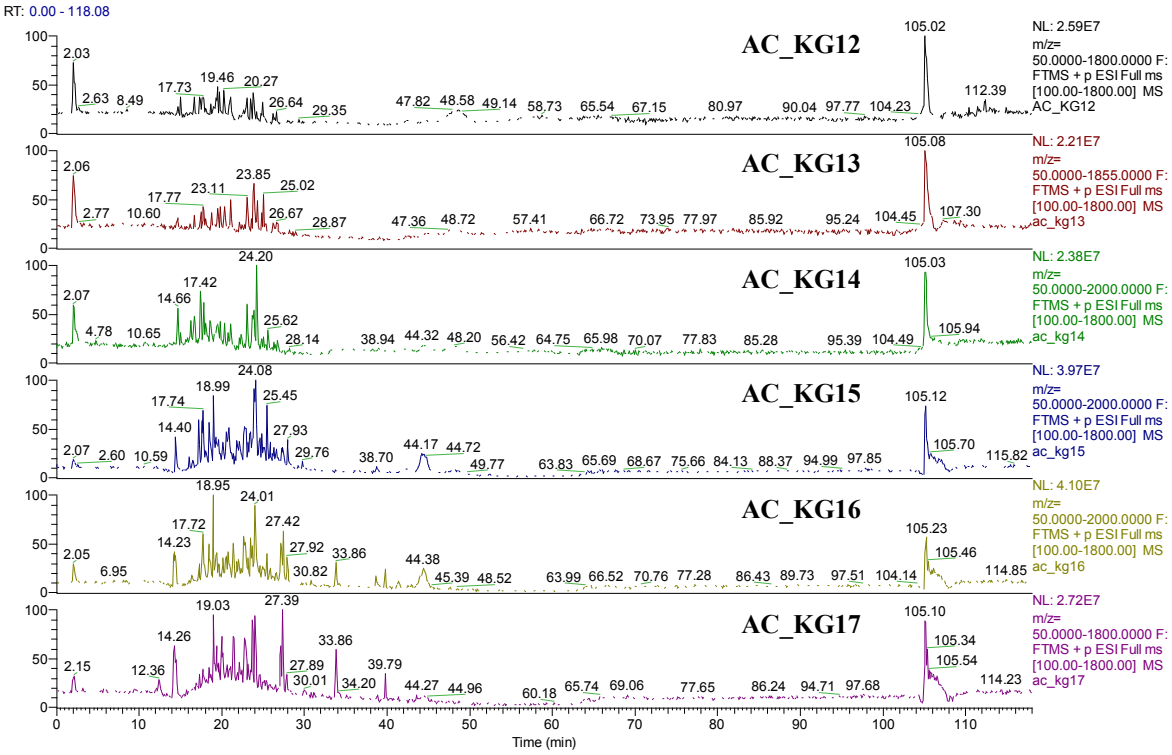

Figure 157. TIC of the fractions obtained by subjecting the $CHCl_3$, EtOAc and BuOH phases of the crude extract of *A. crenata* leaf margins to silica gel column chromatography. Top to bottom: AC_KG14, AC_KG15, AC_KG16, AC_KG17.

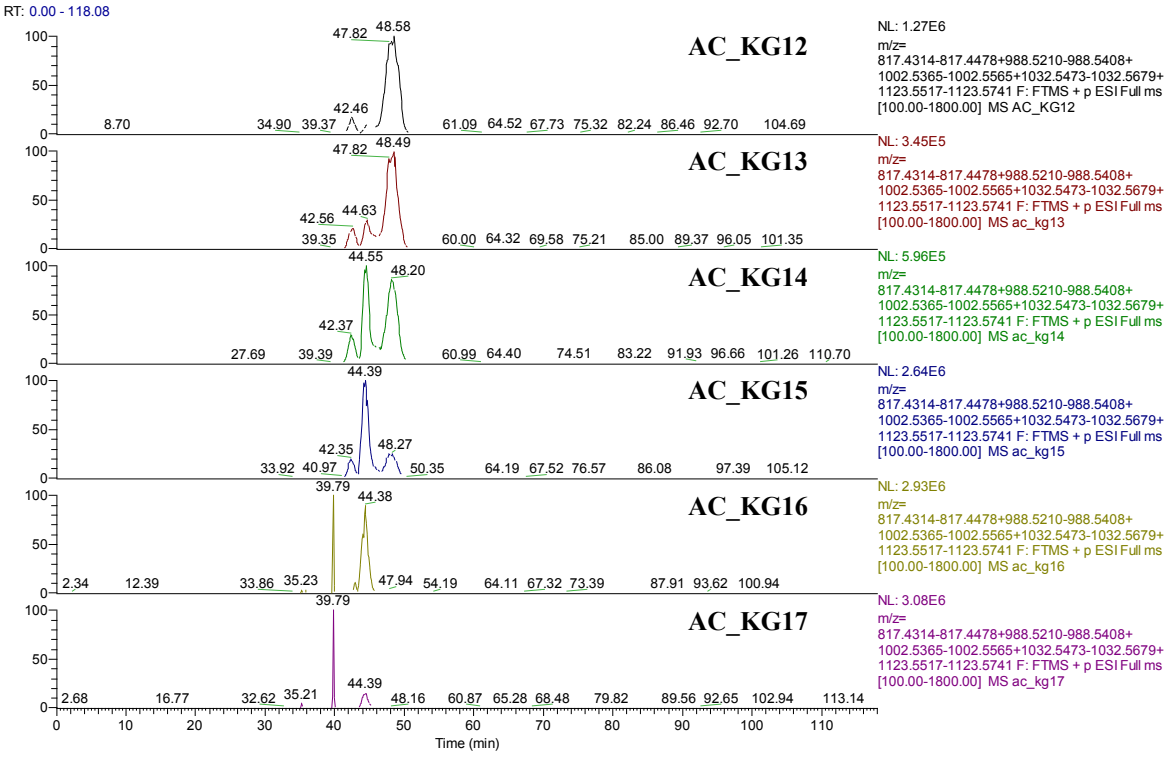

Figure 158. XICs of following *m/z* values for, top to bottom: AC_KG14, AC_KG15, AC_KG16, AC_KG17, AC_KG18, AC_KG19+20, AC_KG21+22, AC_KG23+24, selected *m/z* values are: 817.4342, rt 39.79 min (**3**); 988.5309, rt 42.46 min, rt 44.55 min; 1002.5394, rt 48.58 min (**1**); 1032.5500, rt 44.63 min (**2**) and 1123.5629.

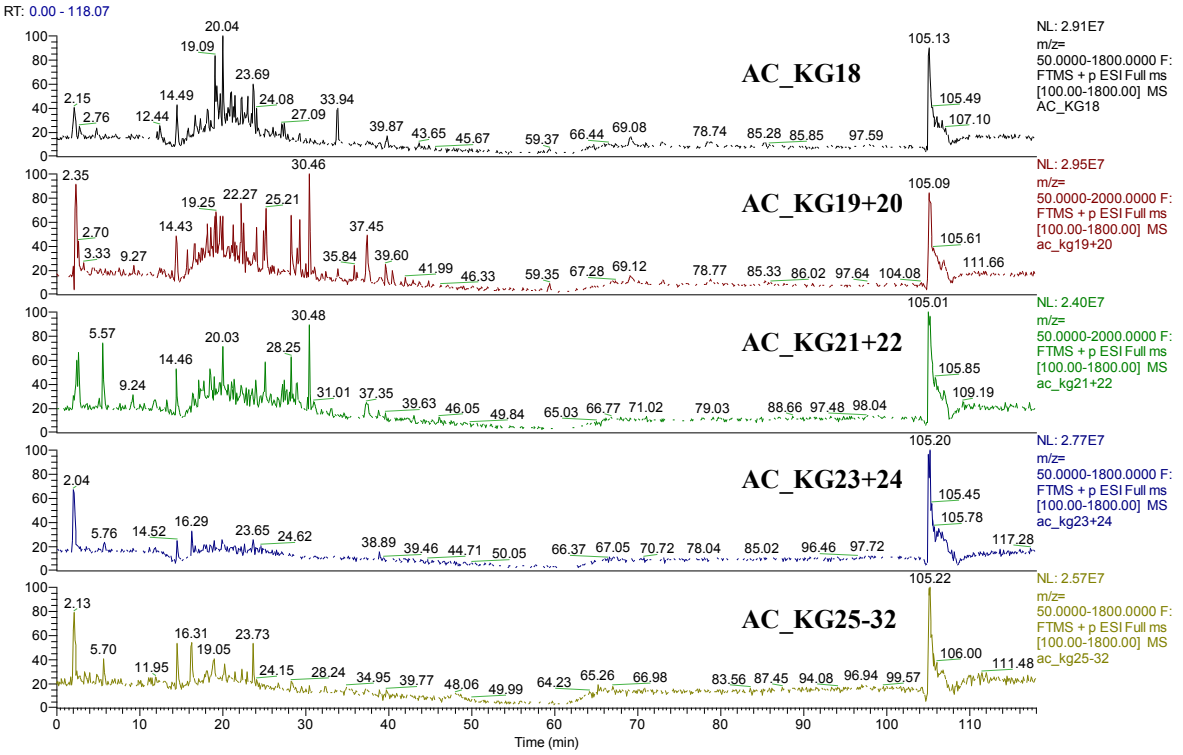

Figure 159. TIC of the fractions obtained by subjecting the $CHCl_3$, EtOAc and BuOH phases of the crude extract of *A. crenata* leaf margins to silica gel column chromatography. Top to bottom: AC_KG18, AC_KG19+20, AC_KG21+22, AC_KG23+24, AC_KG25-32.

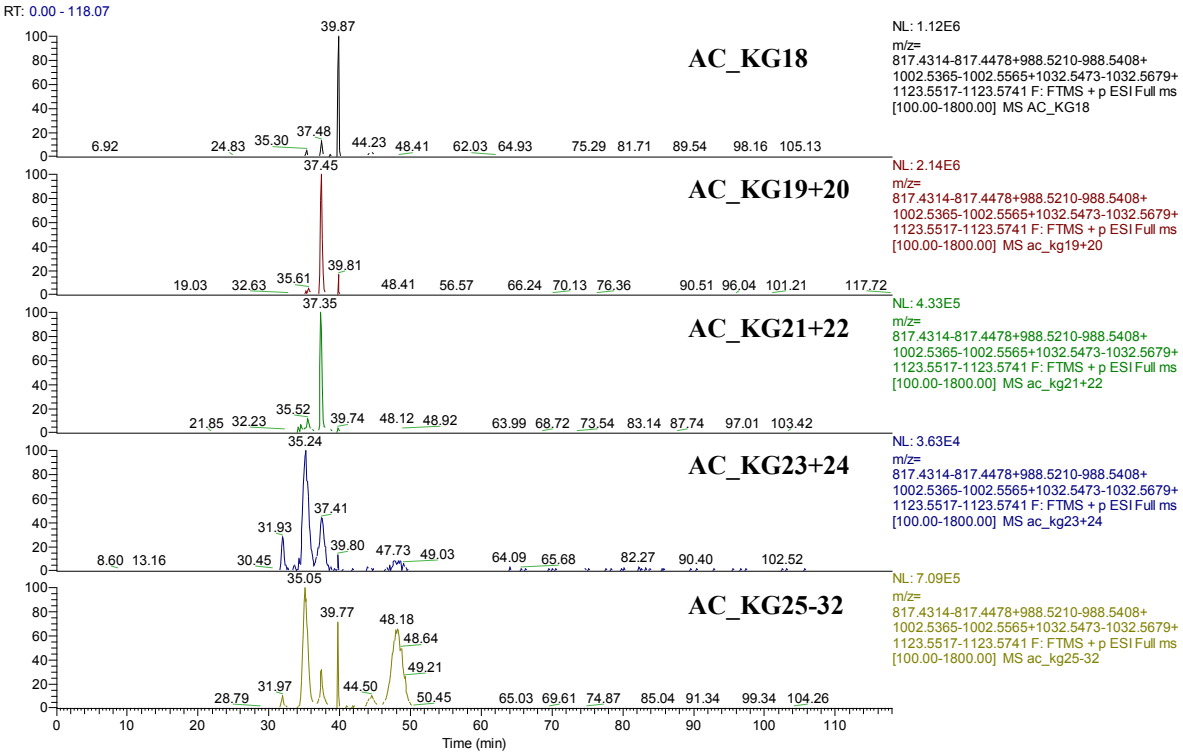

Figure 160. XICs of following *m/z* values for, top to bottom: AC_KG18, AC_KG19+20, AC_KG21+22, AC_KG23+24, AC_KG25-32, selected *m/z* values are: 817.4342, rt 39.87 min (**3**); 988.5309, rt 42.46 min, rt 44.50 min; 1002.5394, rt 48.18 min (**1**); 1032.5500, rt 44.63 min (**2**) and 1123.5629, rt 31.93 min, rt 35.24 min, rt 37.45 min.

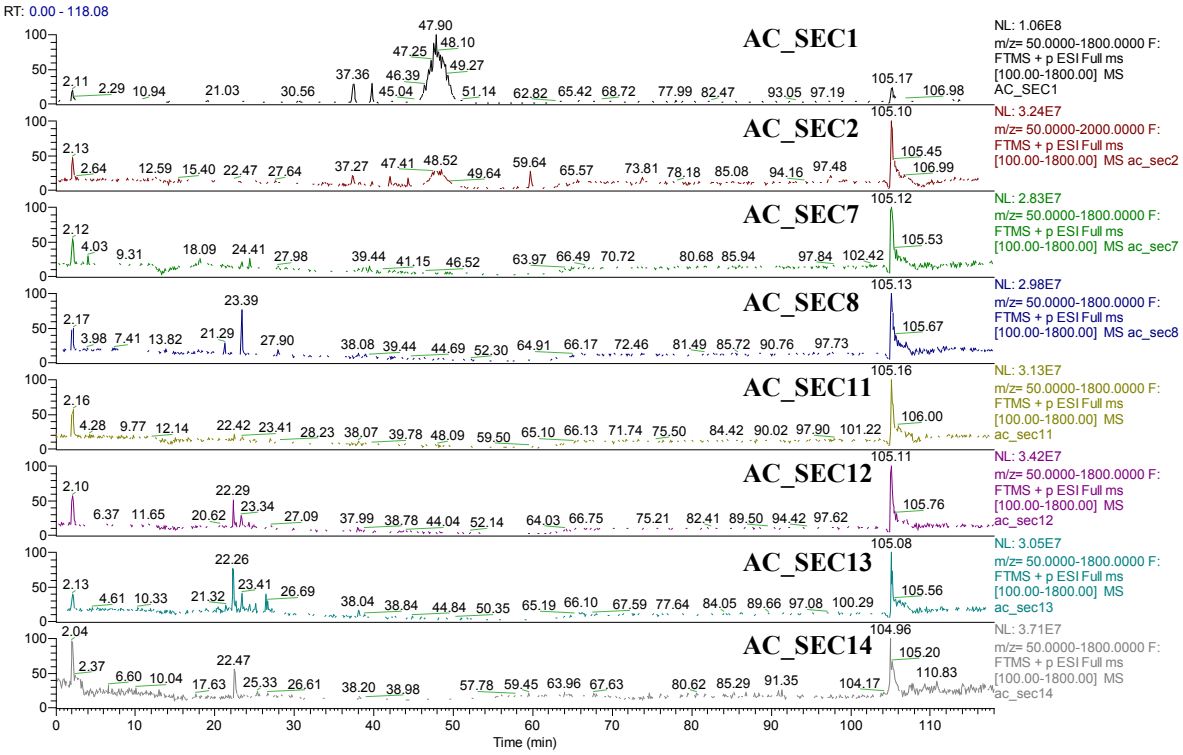

Figure 161. TIC of the fractions obtained by subjecting the united fractions AC_KG8 and AC_KG9 to SEC. Top to bottom: AC_SEC1, AC_SEC2, AC_SEC7, AC_SEC8, AC_SEC11, AC_SEC12, AC_SEC13, AC_SEC14.

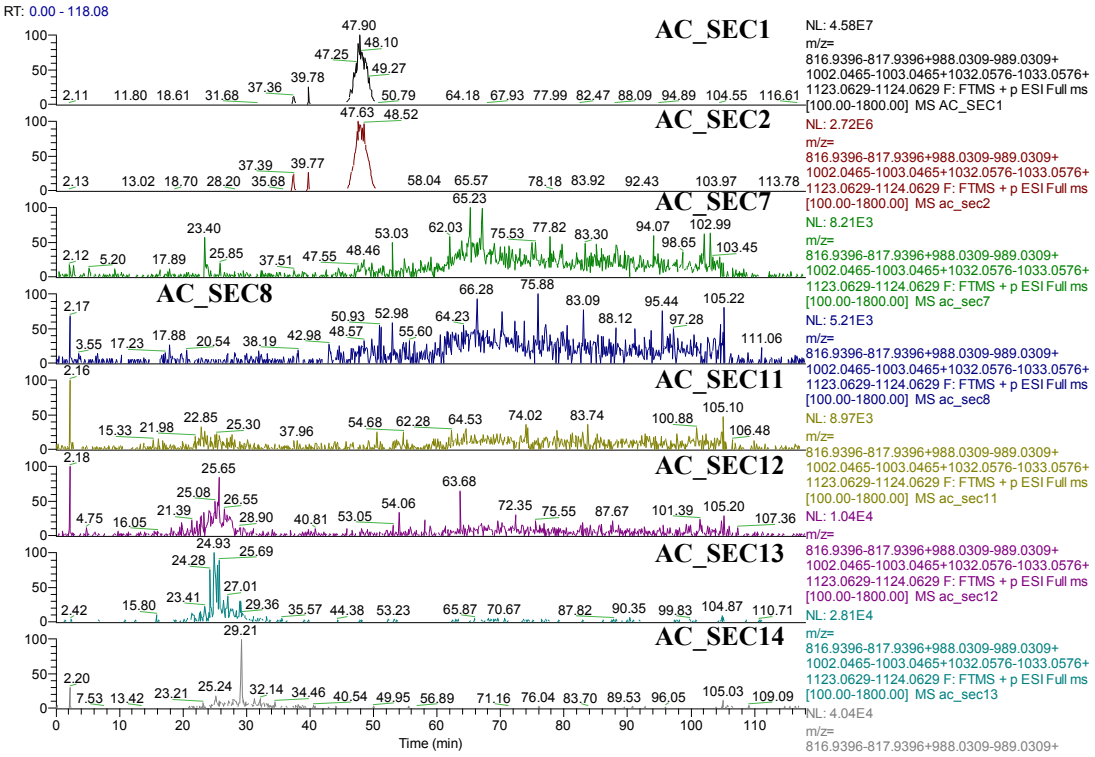

Figure 162. XICs of following *m/z* values for, top to bottom: AC_SEC1, AC_SEC2, AC_SEC7, AC_SEC8, AC_SEC11, AC_SEC12, AC_SEC13, AC_SEC14, selected *m/z* values are: 817.4342; 988.5309; 1002.5394, rt 47.90 min (**1**); 1032.5500 and 1123.5629.

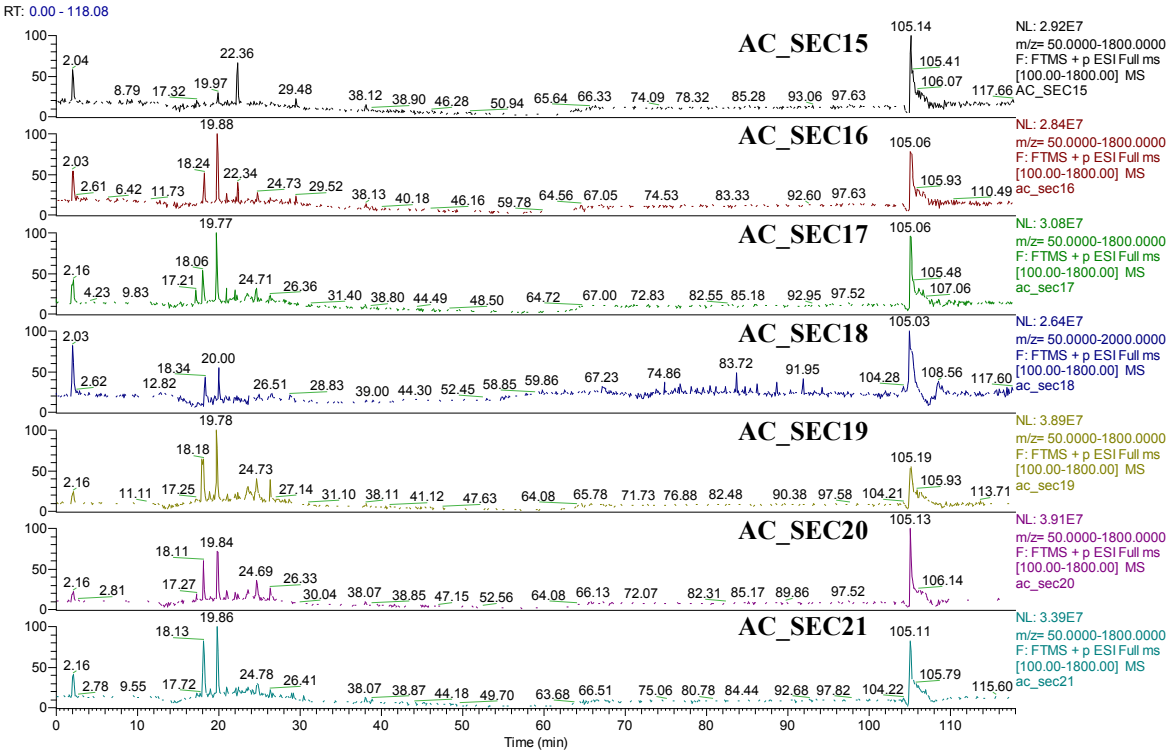

Figure 163. TIC of the fractions obtained by subjecting the united fractions AC_KG8 and AC_KG9 to SEC. Top to bottom: AC_SEC15, AC_SEC16, AC_SEC17, AC_SEC18, AC_SEC19, AC_SEC20, AC_SEC21.

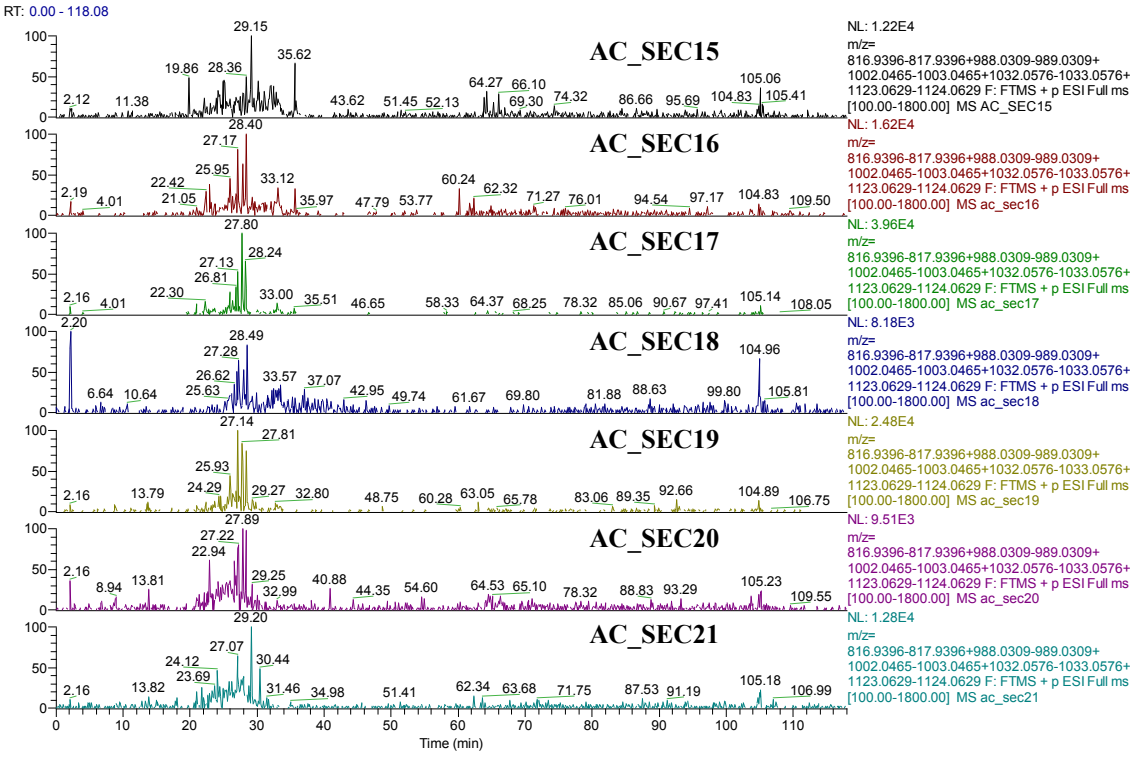

Figure 164. XICs of following *m/z* values for, top to bottom: AC_SEC15, AC_SEC16, AC_SEC17, AC_SEC18, AC_SEC19, AC_SEC20, AC_SEC21, selected *m/z* are: 817.4342; 988.5309; 1002.5394; 1032.5500 and 1123.5629.

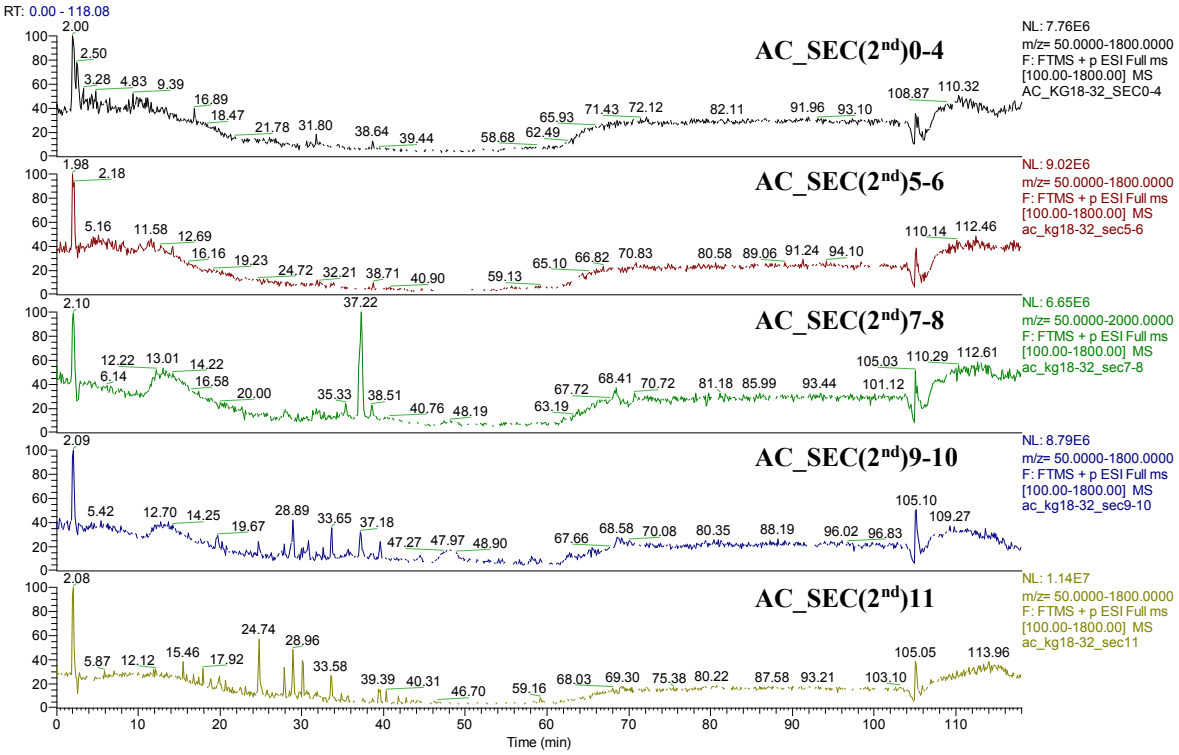

Figure 165. TIC of the fractions obtained by subjecting the united fractions AC_KG18, AC_KG19+20, AC_KG21+22, AC_KG23+24 and AC_KG32 to SEC. Top to bottom: AC_SEC(2nd)0-4, AC_SEC(2nd)5-6, AC_SEC(2nd)7-8, AC_SEC(2nd)9-10, AC_SEC(2nd)11.

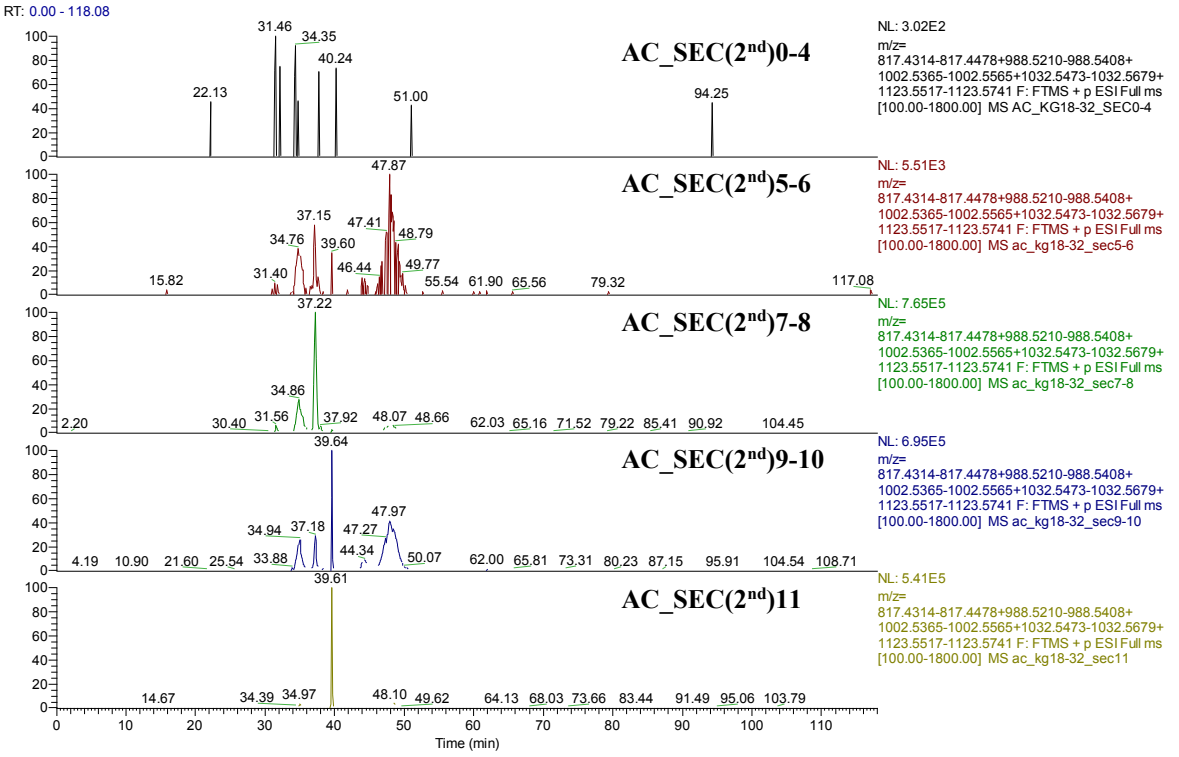

Figure 166. XICs of following *m/z* values for, top to bottom: AC_SEC(2nd)0-4, AC_SEC(2nd)5-6, AC_SEC(2nd)7-8, AC_SEC(2nd)9-10, AC_SEC(2nd)11, selected *m/z* values are: 817.4342, rt 39.64 min (**3**); 988.5309, rt 42.46 min, rt 44.34 min; 1002.5394, rt 47.97 min (**1**); 1032.5500, rt 44.34 min (**2**) and 1123.5629, rt 31.56 min, rt 34.94 min, rt 37.18 min.

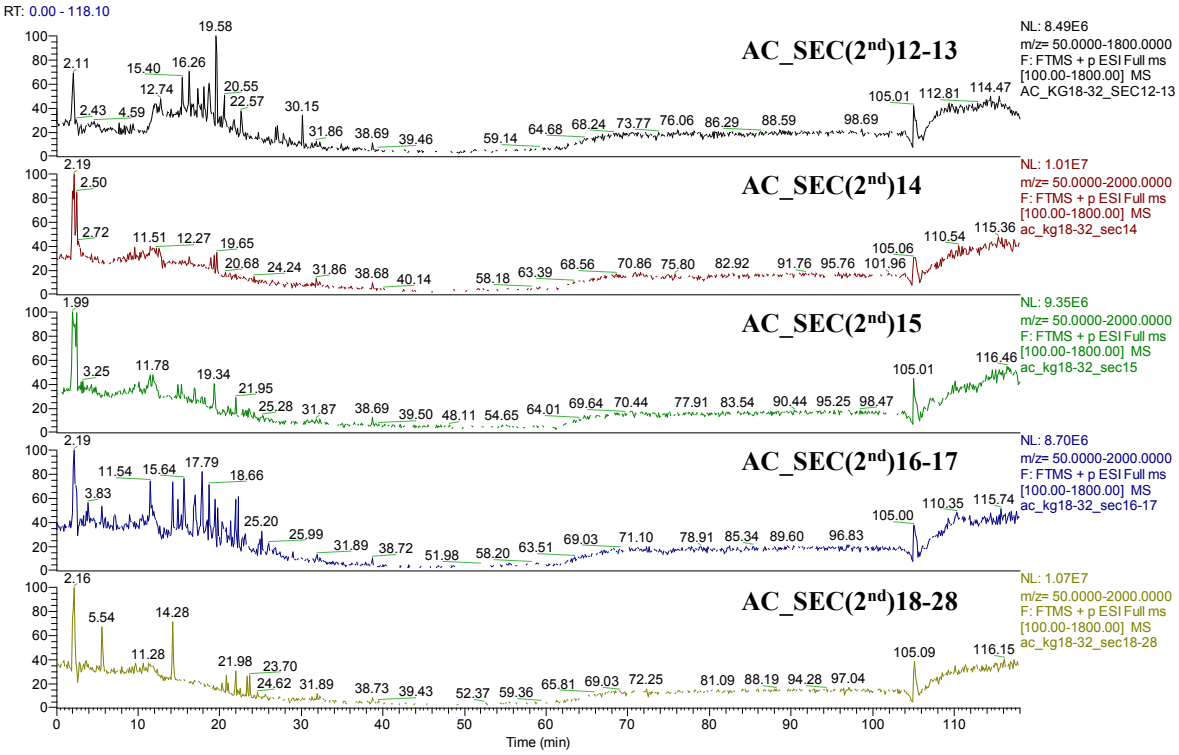

Figure 167. TIC of the fractions obtained by subjecting the united fractions AC_KG18, AC_KG19+20, AC_KG21+22, AC_KG23+24 and AC_KG32 to SEC. Top to bottom: AC_SEC(2nd)12-13, AC_SEC(2nd)14, AC_SEC(2nd)15, AC_SEC(2nd)16-17, AC_SEC(2nd)18-28.

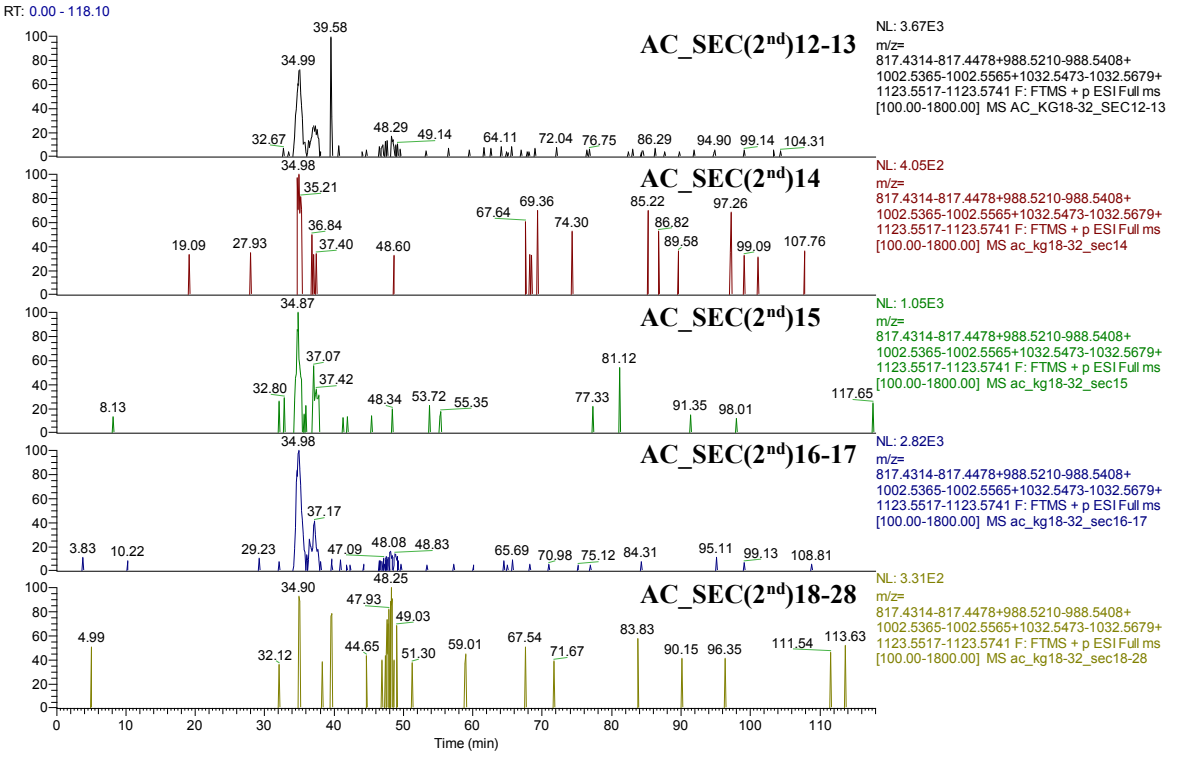

Figure 168. XICs of following *m/z* values for, top to bottom: AC_SEC(2nd)12-13, AC_SEC(2nd)14, AC_SEC(2nd)15, AC_SEC(2nd)16-17, AC_SEC(2nd)18-28, selected *m/z* values are: 817.4342, rt 39.58 min (**3**); 988.5309; 1002.5394; 1032.5500 and 1123.5629, rt 34.99 min, rt 37.17 min.

IV.2.5. Purified natural compounds

The fractions AC_SEC1 and AC_SEC2 yielded 0.1 mg of purified substance. Based on MS analysis of MS 1 and MS 2 spectra the fractions contain the cyclic-depsipeptide FR900359 (**1**) with a *m/z* value of 1002.5369 (rt 47.90 min) (Figure 169, Figure 170 and Figure 171). The measured *m/z* value lies within 5 ppm of the calculated *m/z* value (1002.5394) of the singly protonated $[M+H]^+$ ion. The amount isolated was not sufficient for nuclear magnetic resonance (NMR) analysis.

The fractions AC_SEC13 and AC_SEC14 were pooled and yielded 1.4 mg of purified substance. The amount was sufficient for NMR analysis and a novel natural product was discovered, which was determined as epicatechin-3-hydroxy-2-methyl-propanoate (**6**) (*m/z* value of 377.1211, rt 22.47 min) (Figure 172, Figure 173 and Figure 174). The measured *m/z* value lies within 5 ppm of the calculated *m/z* value (377.1231) of the singly protonated $[M+H]^+$ ion. To determine the configuration polarimetry should be used on the isolated compound.

The fractions AC_SEC17, AC_SEC18, AC_SEC19, AC_SEC20 and AC_SEC21 were combined and yielded 7.7 mg of purified substance. The amount was sufficient for NMR analysis and the combined fractions were determined to contain a mixture of catechin (**4**) (*m/z* value of 291.0856, rt 18.34 min) and epicatechin (**5**) (*m/z* value of 291.0858, rt 20.00 min) (Figure 175, Figure 176, Figure 177, Figure 178 and Figure 179). The measured *m/z* values lie within 5 ppm of the calculated *m/z* values (291.0863) of the singly protonated $[M+H]^+$ ions. For the NMR data and NMR spectra (see: *IV.7.2. Appendix B: NMR data of the isolated natural products*, Table 23, Table 24 and Table 25; IV.7.3. Appendix C: NMR spectra of the isolated natural *products*, Figure 198, Figure 199, Figure 200, Figure 201, Figure 202, Figure 203, Figure 204, Figure 205, Figure 206, Figure 207, Figure 208, Figure 209, Figure 210, Figure 211, Figure 212, Figure 213, Figure 214, Figure 215, Figure 216, Figure 217 and Figure 218).

The fractions AC_SEC(2^{nd})7-8 yielded 0.4 mg of purified substance. Based on MS analysis of MS 1 and MS 2 spectra, as well as UV spectra, the fractions contain a novel cyclic-depsipeptide candidate with a *m/z* value of 1019.5662 (rt 37.22 min), which seems to be a derivative of FR900359 (Figure 180, Figure 181, Figure 182.) For the UV spectra (see: *IV.7.1. Appendix A: UV spectra of the isolated cyclic-depsipeptides*, Figure 195, Figure 196 and Figure 197).

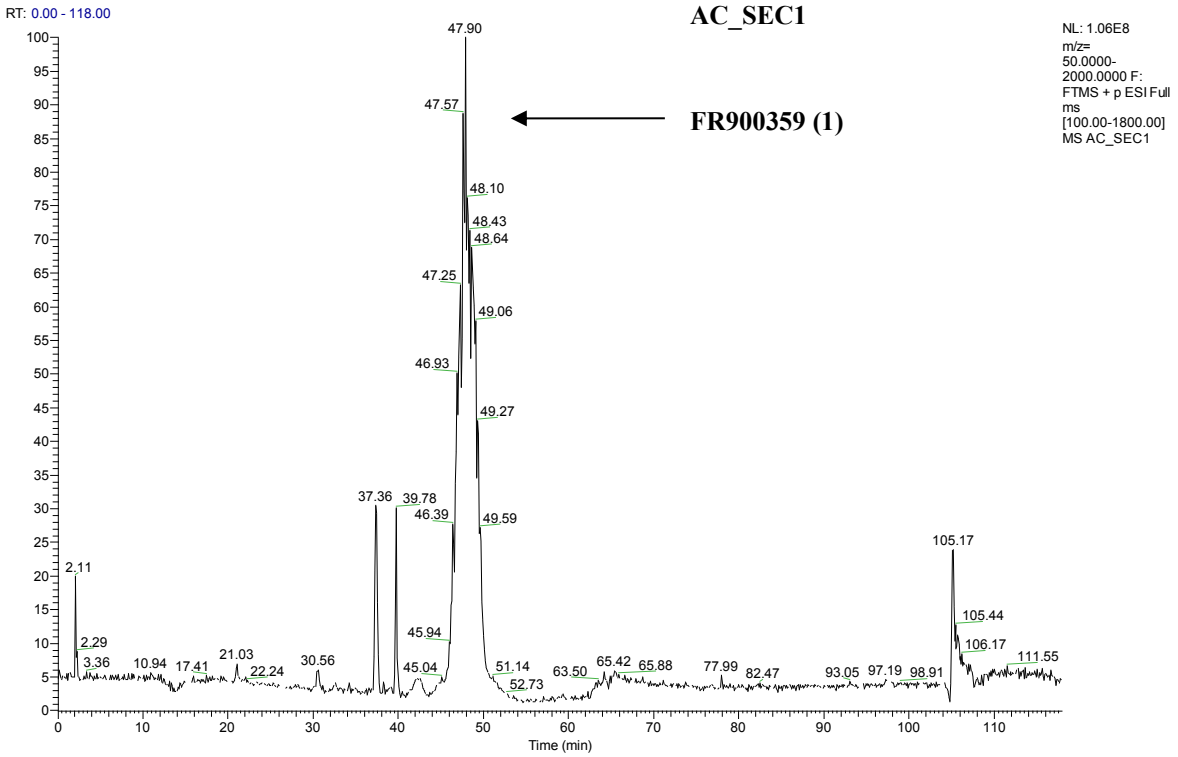

Figure 169. TIC of AC_SEC1 obtained by subjecting the united fractions AC_KG8 and AC_KG9 to SEC. The broad peak of the cyclic-depsipeptide target FR900359 (**1**) with a *m/z* value of 1002.5394 (rt 47.90 min) is visible.

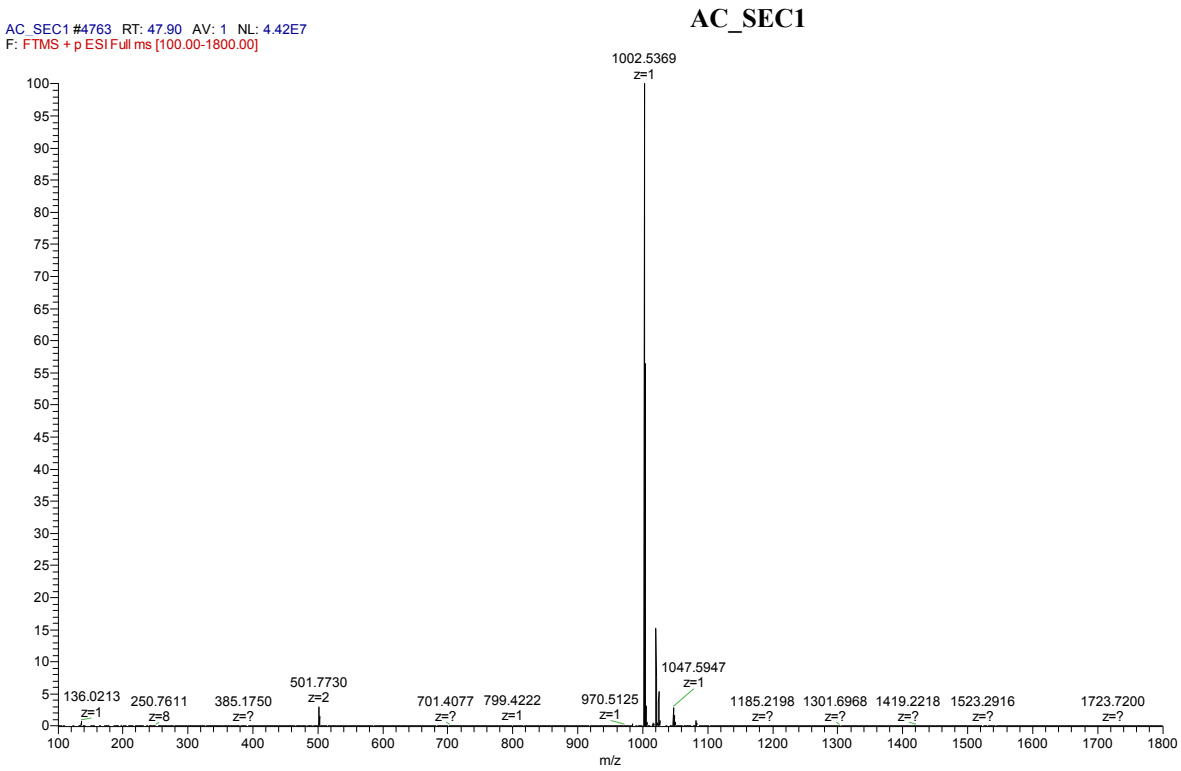

Figure 170. MS 1 fullscan of AC_SEC1 at rt 47.90 min showing the singly protonated (*m/z* value of 1002.5369) and doubly protonated (*m/z* value of 501.7730) ions of FR900359 (**1**).

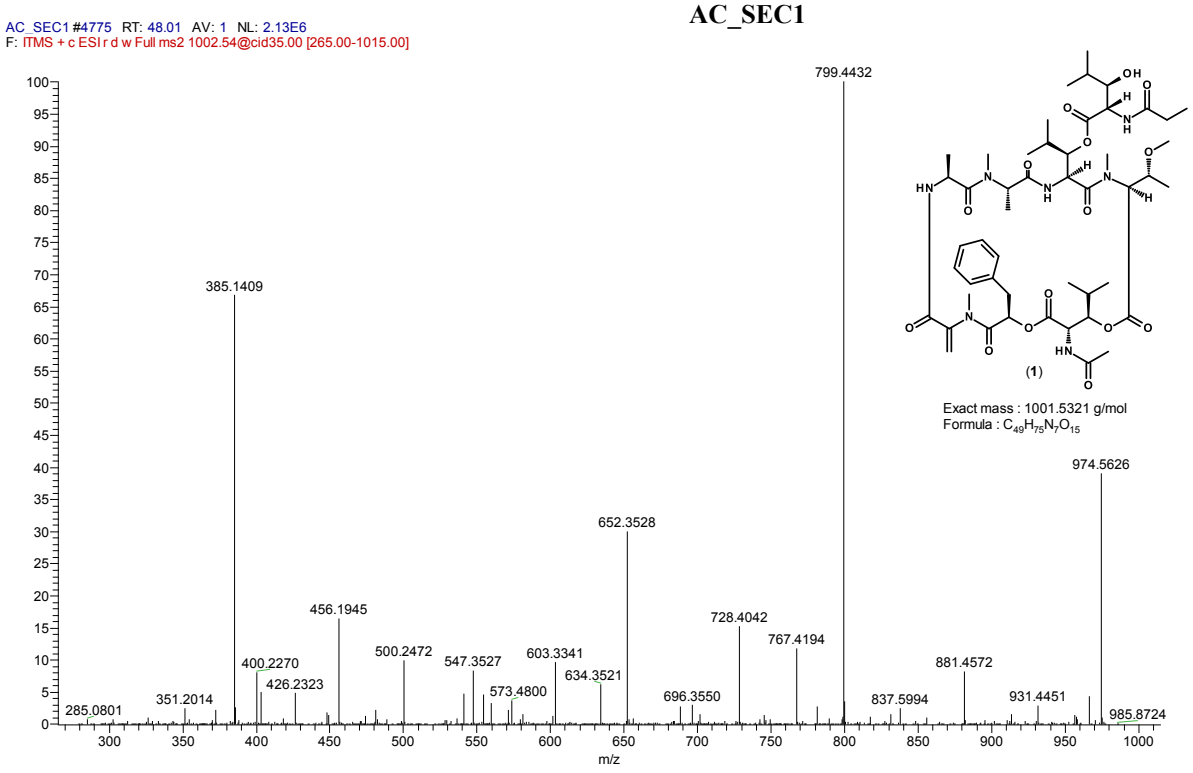

Figure 171. MS 2 of AC_SEC1 at *m/z* 1002.54 (rt 48.01 min) showing the fragmentation pattern of FR900359 (**1**). The structure of the analyte is illustrated in the top right corner.

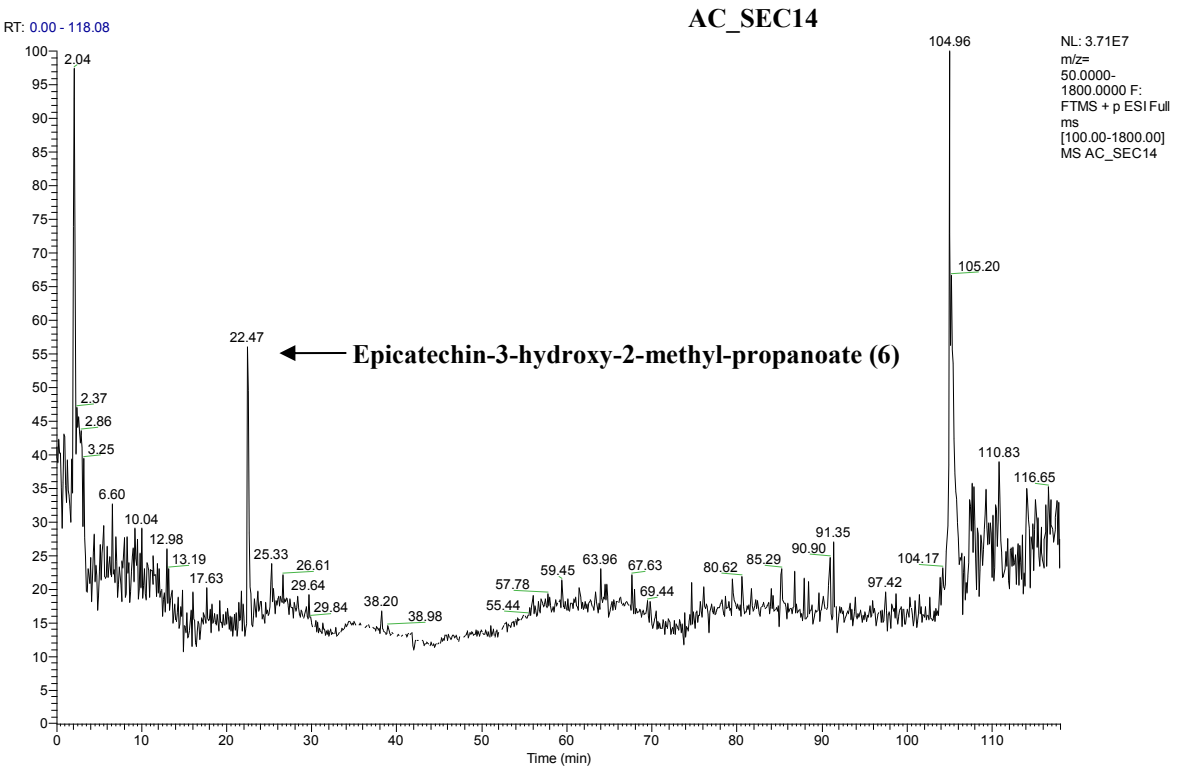

Figure 172. TIC of AC_SEC14 obtained by subjecting the united fractions AC_KG8 and AC_KG9 to SEC. The peak of epicatechin-3-hydroxy-2-methyl-propanoate (**6**) with a *m/z* value of 377.1211 (rt 22.47 min) is visible.

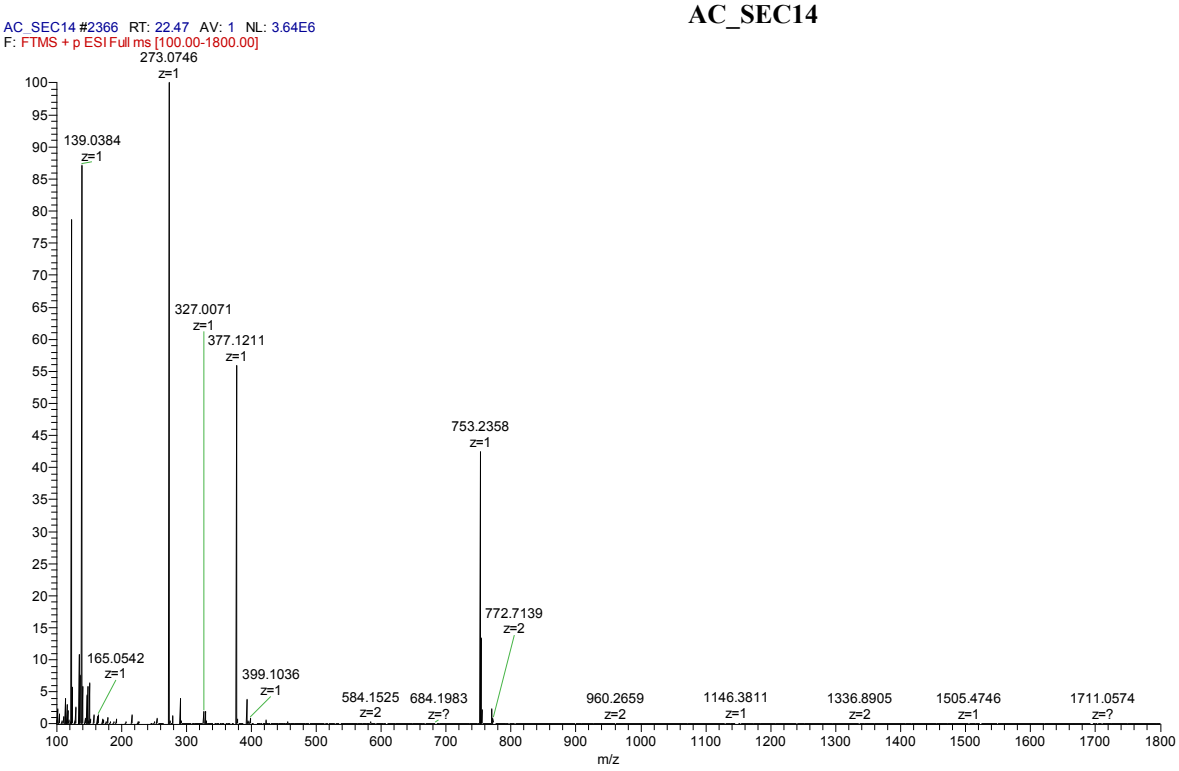

Figure 173. MS 1 fullscan of AC_SEC14 at rt 22.47 min showing the singly protonated (*m/z* value of 377.1212) ion of epicatechin-3-hydroxy-2-methyl-propanoate (**6**).

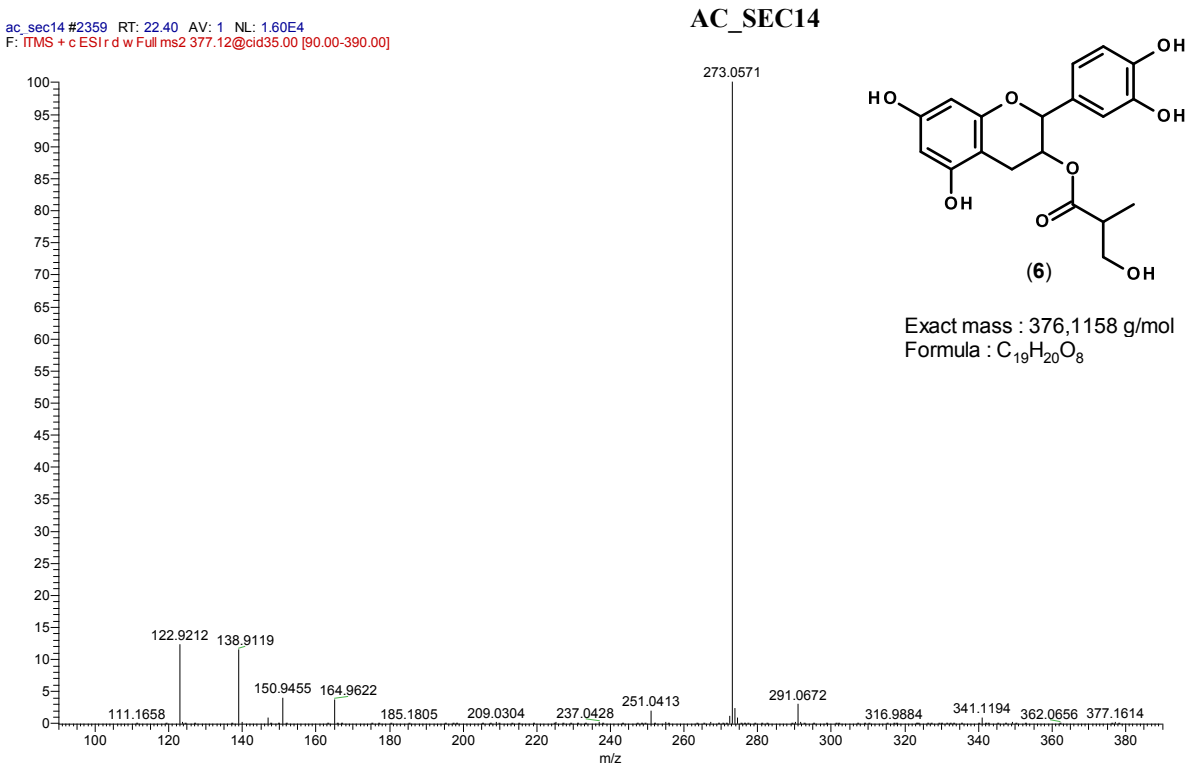

Figure 174. MS 2 of AC_SEC14 at *m/z* 377.12 (rt 22.40 min) showing the fragmentation pattern of epicatechin-3-hydroxy-2-methyl-propanoate (**6**). The structure of the analyte is illustrated in the top right corner.

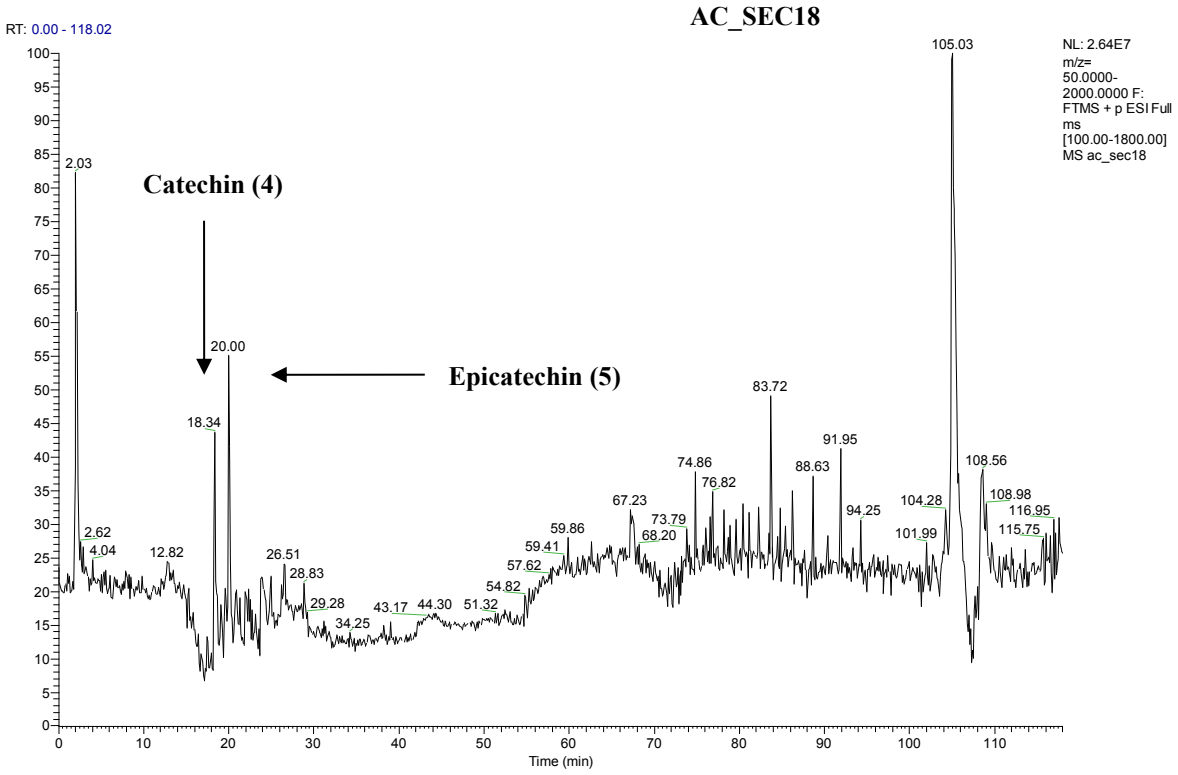

Figure 175. TIC of AC_SEC18 obtained by subjecting the united fractions AC_KG8 and AC_KG9 to SEC. The peaks of catechin (**4**) with a *m/z* value of 291.0856 (rt 18.34 min) and epicatechin (**5**) with a *m/z* value of 291.0858 (rt 20.00 min) are visible.

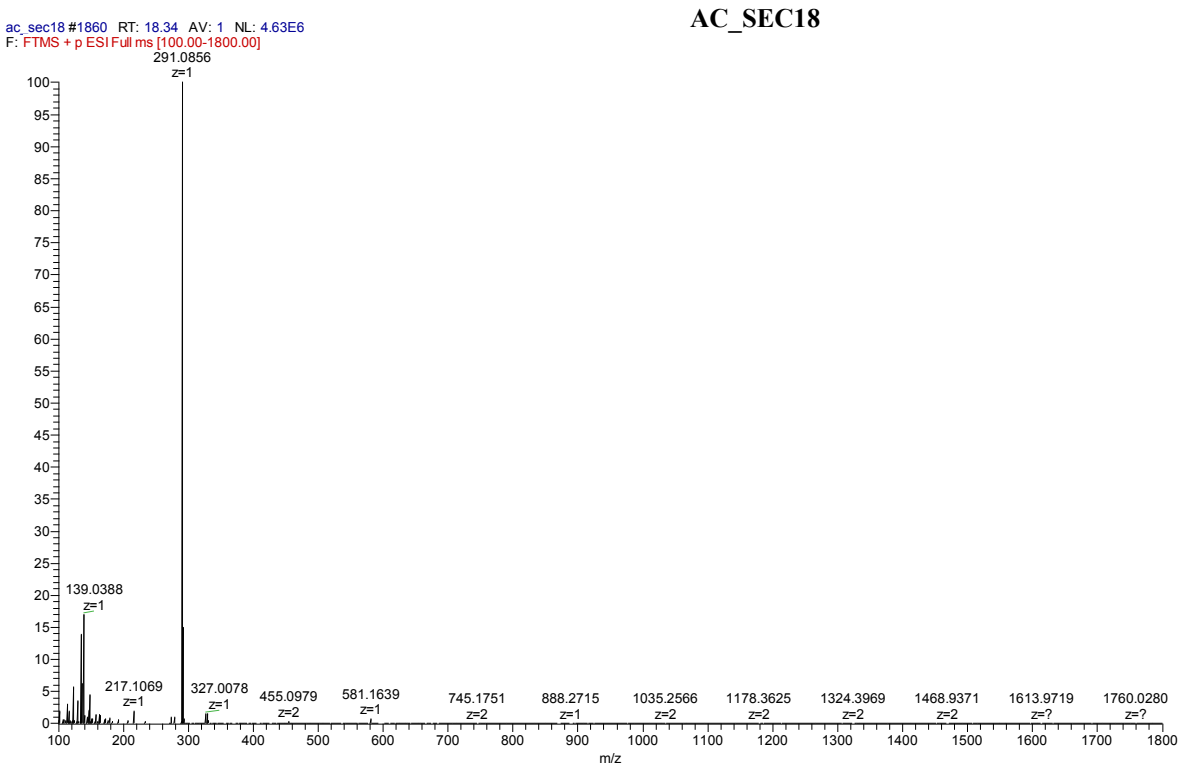

Figure 176. MS 1 fullscan of AC_SEC18 at rt 18.34 min showing the singly protonated (*m/z* value of 291.0856) ion catechin (**4**).

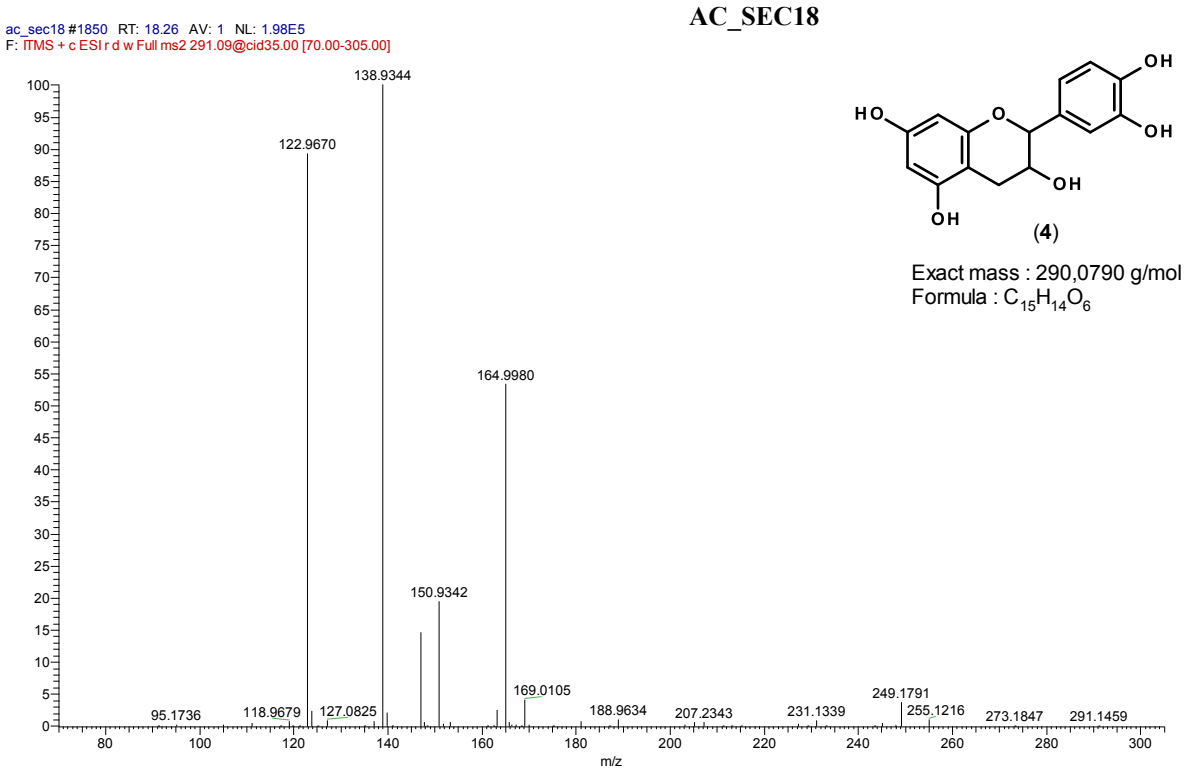

Figure 177. MS 2 of AC_SEC18 at *m/z* 291.09 (rt 18.26 min) showing the fragmentation pattern of catechin (**4**). The structure of the analyte is illustrated in the top right corner.

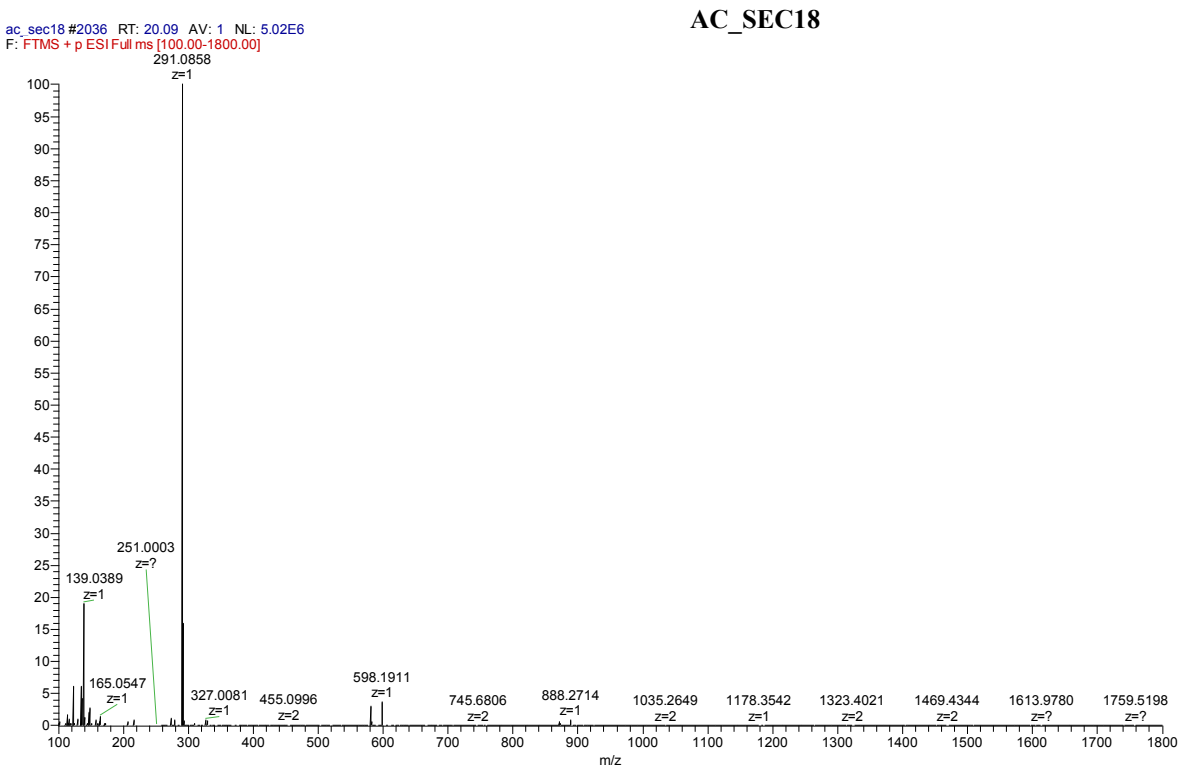

Figure 178. MS 1 fullscan of AC_SEC18 at rt 20.09 min showing the singly protonated (*m/z* value of 291.0858) ion epicatechin (**5**).

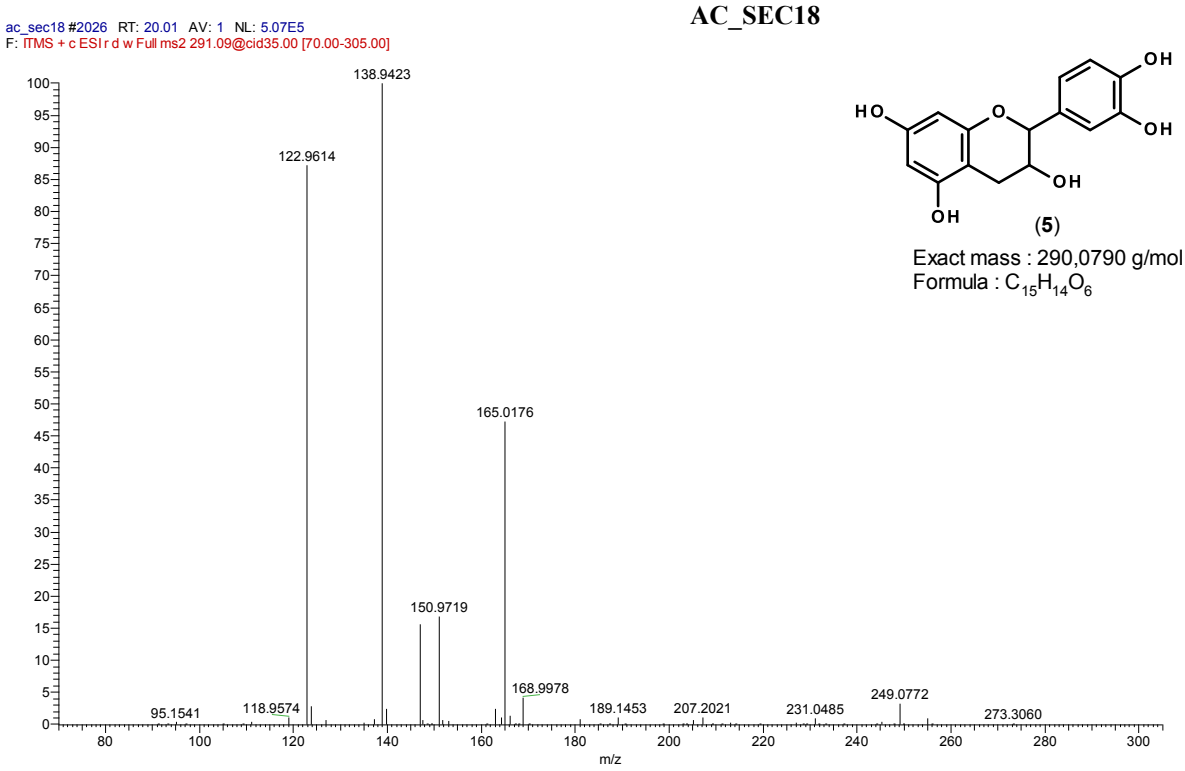

Figure 179. MS 2 of AC_SEC18 at *m/z* 291.09 (rt 20.01 min) showing the fragmentation pattern of epicatechin (**5**). The structure of the analyte is illustrated in the top right corner.

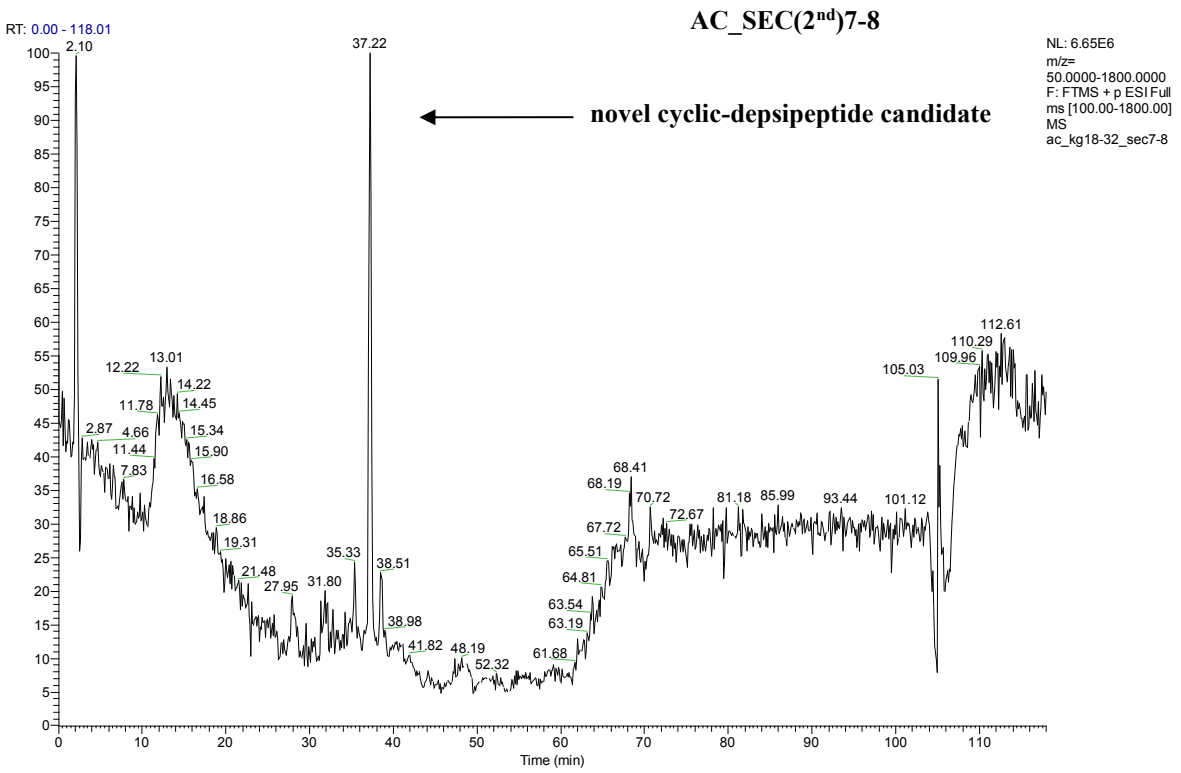

Figure 180. TIC of AC_SEC(2nd)7-8 obtained by subjecting the united fractions AC_KG18, AC_KG19+20, AC_KG21+22, AC_KG23+24 and AC_KG32 to SEC. The peak of a novel cyclic-depsipeptide candidate with a *m/z* value of 1019.5662 (rt 37.22 min) is visible.

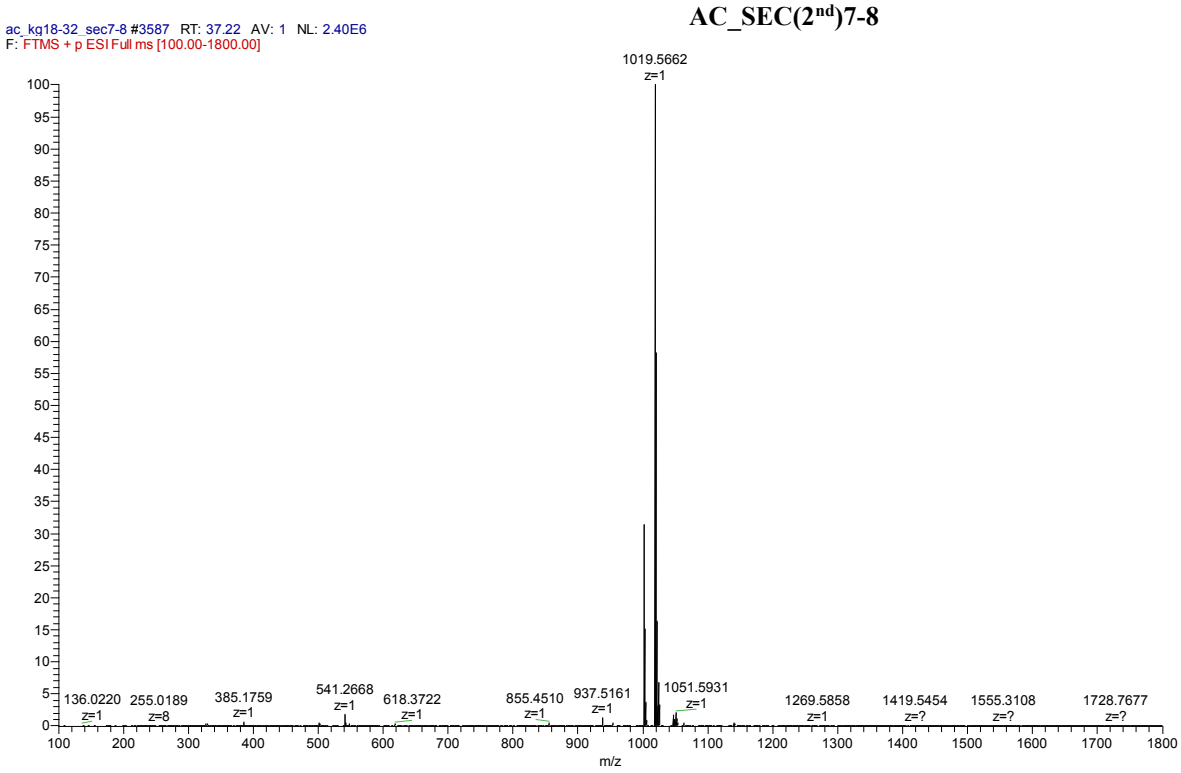

Figure 181. MS 1 fullscan of AC_SEC(2nd)7-8 at rt 37.22 min showing the singly protonated (*m/z* value of 1019.5662) ion of a novel cyclic-depsipeptide candidate.

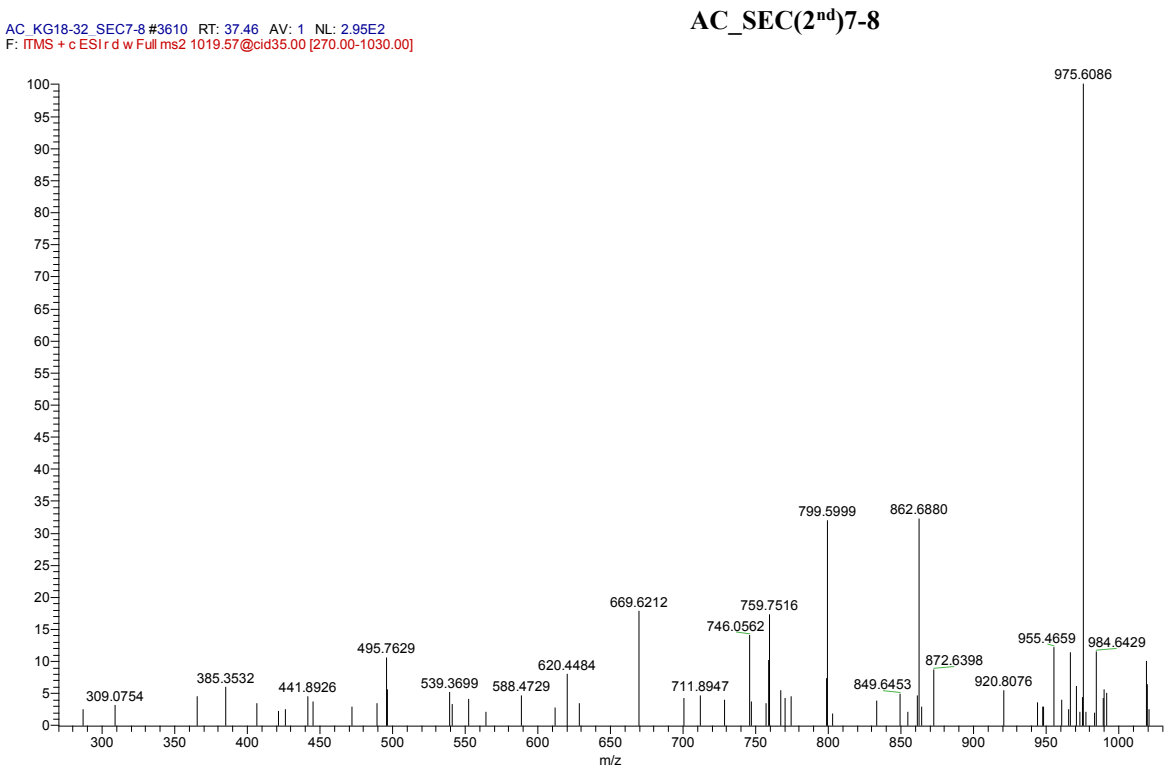

Figure 182. MS 2 of AC_SEC(2nd)7-8 at *m/z* 1019.57 (rt 37.46 min) showing the fragmentation pattern of the novel cyclic-depsipeptide candidate.

IV.2.6. Improved liquid/liquid extraction method

Since the previously used liquid/liquid extraction failed at enriching the target compounds in one specific fraction, a different liquid/liquid extraction method was used (Figure 194). The newly developed liquid/liquid extraction method achieves to enrich the target compounds in a singular phase (Figure 183 and Figure 184), while also removing carotenoids, chlorophylls, glycosides and sugars. Although the extract could be used after the first liquid/liquid separation, the second liquid/liquid extraction provides further concentration of the target compounds. A search for the singly protonated $[M+H]^+$ ions of catechin (**4**) (*m/z* value of 291.0863), epicatechin (**5**) (*m/z* value of 291.0863) and epicatechin-3-hydroxy-2-methyl-propanoate (**6**) (*m/z* value of 377.1231), indicates the enrichment of certain catechins in the ethyl acetate phase (Figure 185 and Figure 186). In the formed precipitate (pellet fraction), which seems to consist mostly of unidentified peptides and proteins, the singly protonated $[M+H]^+$ ions of glutathione (**7**) (*m/z* value of 308.0911) and glutathione disulfide (**8**) (*m/z* value of 613.1593) were annotated based on MS 1 and MS 2 analysis (Figure 187, Figure 188, Figure 189, Figure 190, Figure 191 and Figure 192). The MS 1 and MS 2 spectra for glutathione (**7**) and glutathione disulfide (**8**) match the reference spectra of the external massspectrometry-database mzcloud: https://www.mzcloud.org/DataViewer#Creference472#T858#c#113687, https://www.mzcloud.org/DataViewer#Creference471#T856#c#113319.

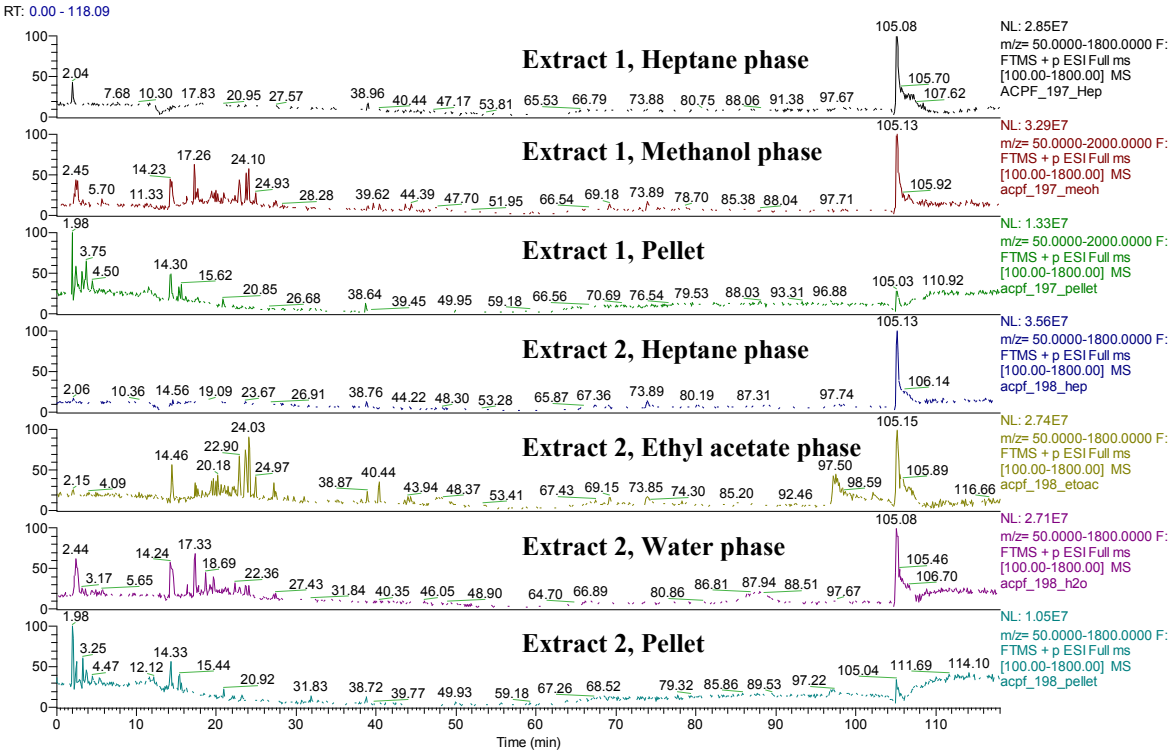

Figure 183. TIC of the fractions obtained by subjecting the crude extracts of combined tissue samples of *A. crenata* to the improved liquid/liquid extraction method. Top to bottom: Extract 1, Heptane phase; Extract 1 Methanol phase; Extract 1, Pellet; Extract 2, Heptane phase; Extract 2, Ethyl acetate phase; Extract 2, Water phase; Extract 2, Pellet.

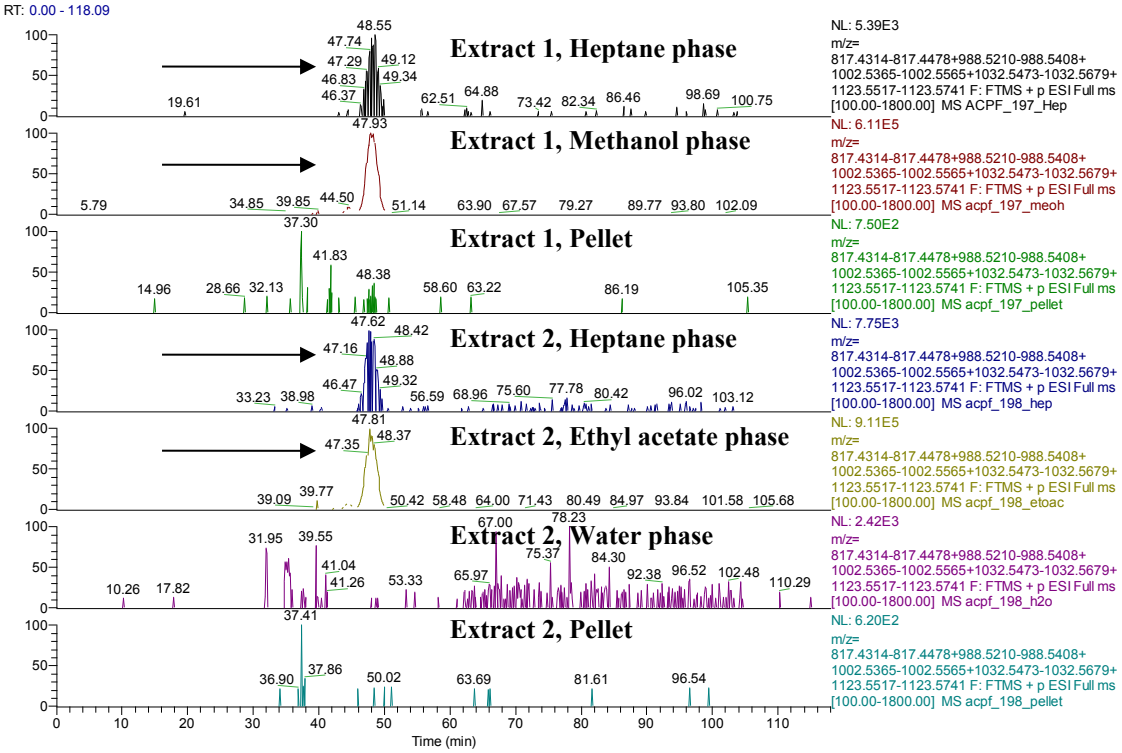

Figure 184. XICs of following *m/z* values showing cyclic-depsipeptides and cyclic-depsipeptide candidates for, top to bottom: Extract 1, Heptane phase; Extract 1 Methanol phase; Extract 1, Pellet; Extract 2, Heptane phase; Extract 2, Ethyl acetate phase; Extract 2, Water phase; Extract 2, Pellet; selected *m/z* values are: 817.4342, rt 39.77 min (**3**); 988.5309, rt 42.50 min, rt 44.50 min; 1002.5394, rt 47.93 min (**1**); 1032.5500, rt 44.50 (**2**) and 1123.5629, rt 31.93 min, rt 35.05 min, rt 37.60 min.

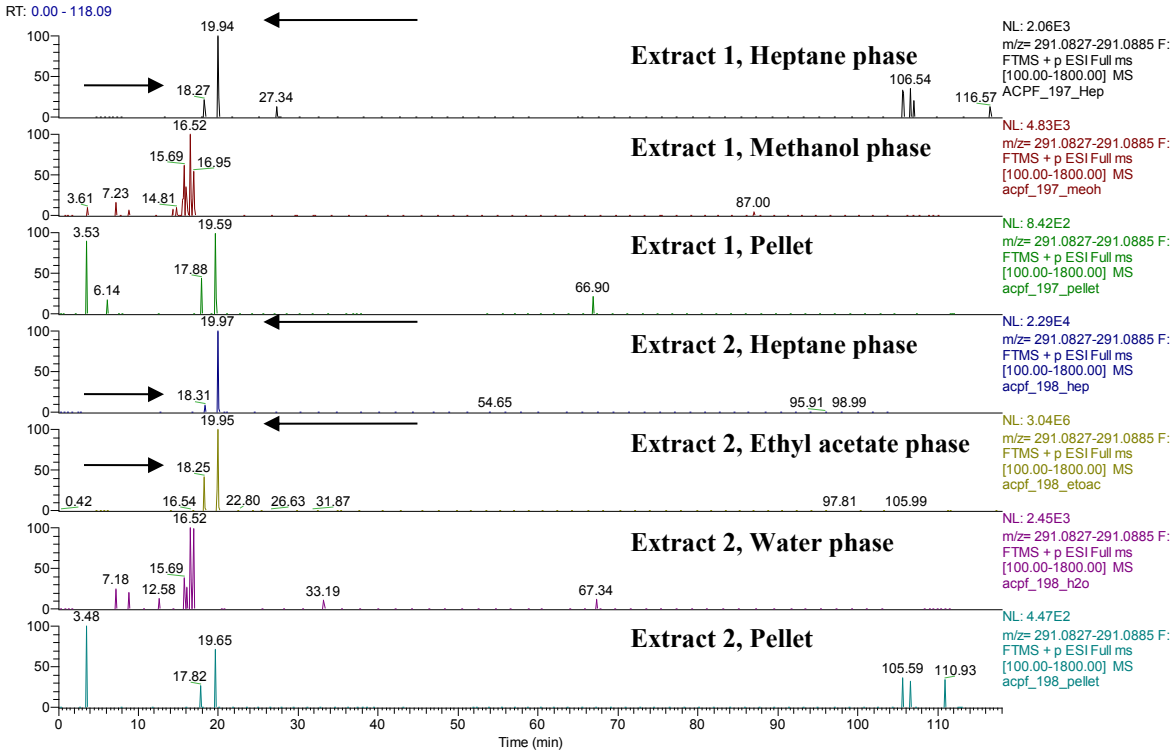

Figure 185. XICs of following *m/z* value showing catechin and epicatechin for, top to bottom: Extract 1, Heptane phase; Extract 1 Methanol phase; Extract 1, Pellet; Extract 2, Heptane phase; Extract 2, Ethyl acetate phase; Extract 2, Water phase; Extract 2, Pellet; selected *m/z* value is: 291.0856, rt 18.25 min (**4**), rt 19.95 min (**5**).

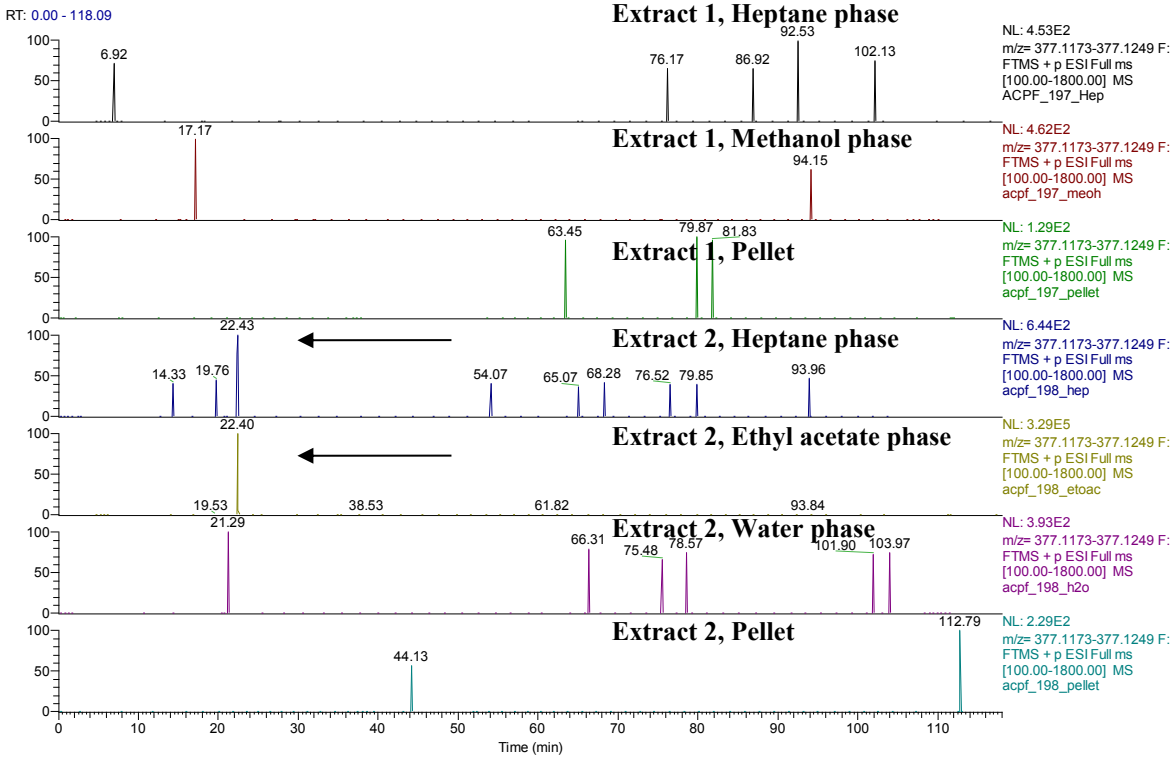

Figure 186. XICs of following *m/z* value showing epicatechin-3-hydroxy-2-methyl-propanoate for, top to bottom: Extract 1, Heptane phase; Extract 1 Methanol phase; Extract 1, Pellet; Extract 2, Heptane phase; Extract 2, Ethyl acetate phase; Extract 2, Water phase; Extract 2, Pellet; selected *m/z* value is: 377.1211, rt 22.40 min (**6**).

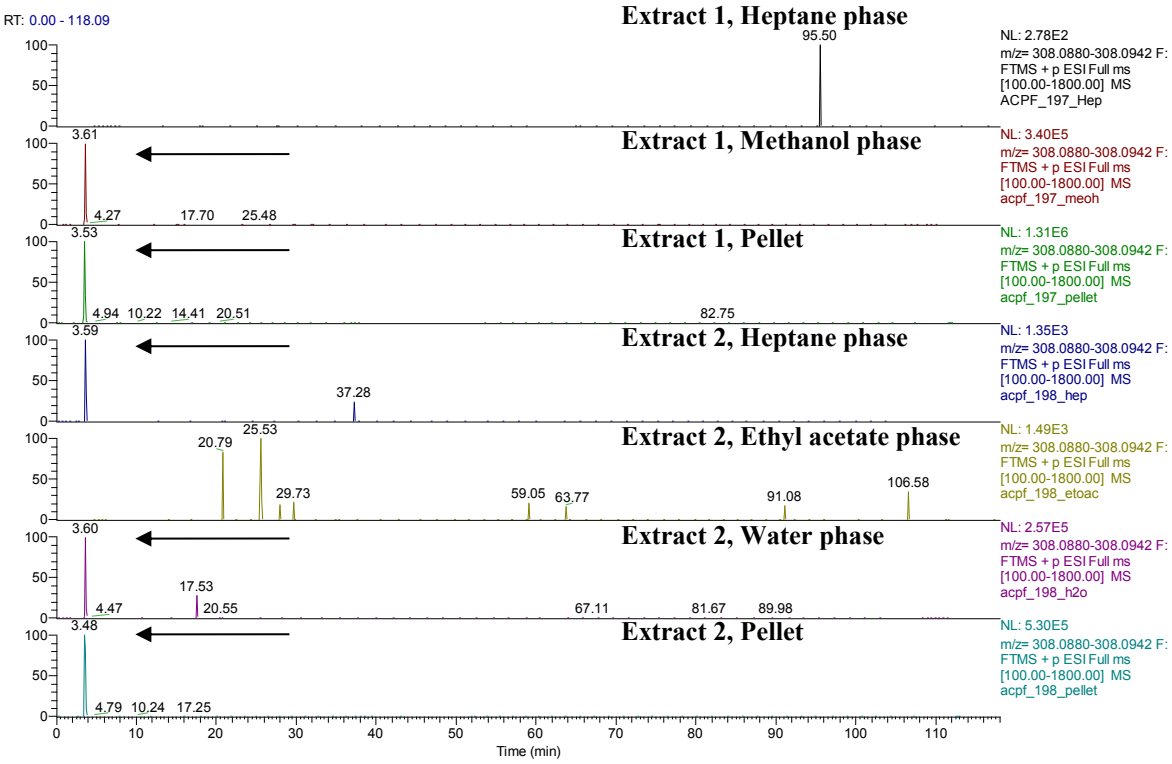

Figure 187. XICs of following *m/z* value showing glutathione for, top to bottom: Extract 1, Heptane phase; Extract 1 Methanol phase; Extract 1, Pellet; Extract 2, Heptane phase; Extract 2, Ethyl acetate phase; Extract 2, Water phase; Extract 2, Pellet; selected *m/z* value is: 308.0911, rt 3.61 min (**7**).

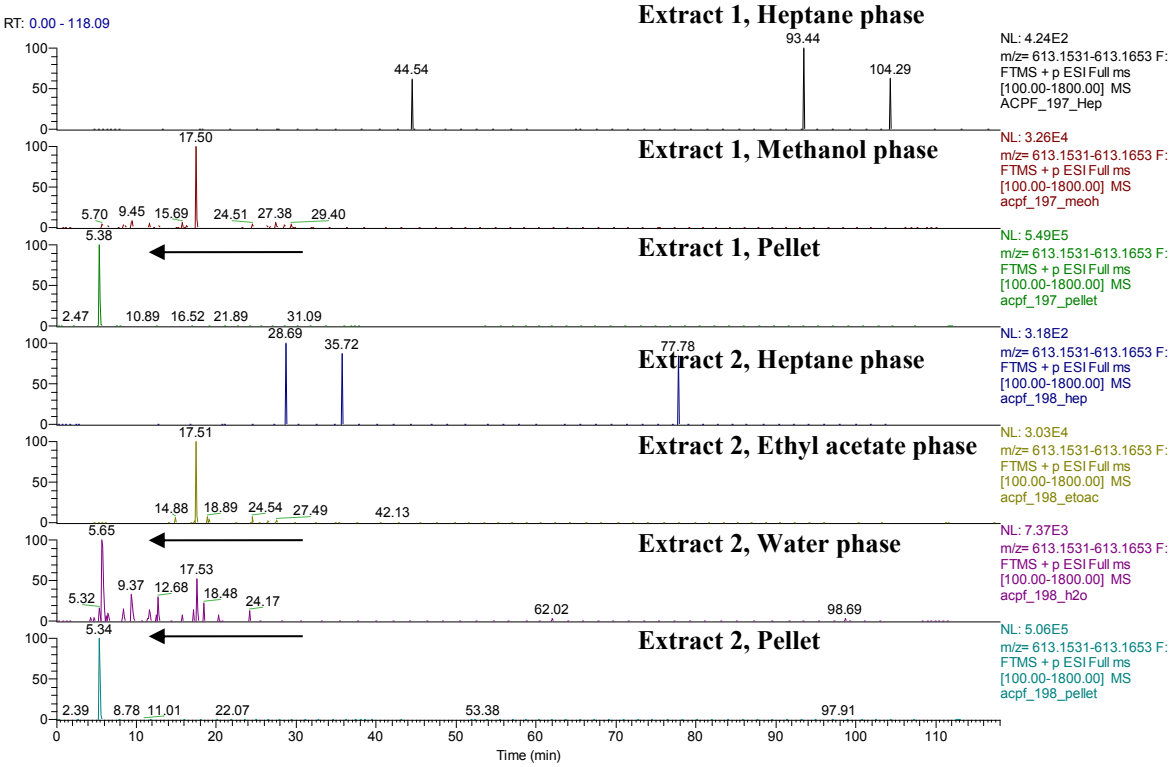

Figure 188. XICs of following *m/z* value showing glutathione disulphide for, top to bottom: Extract 1, Heptane phase; Extract 1 Methanol phase; Extract 1, Pellet; Extract 2, Heptane phase; Extract 2, Ethyl acetate phase; Extract 2, Water phase; Extract 2, Pellet; selected *m/z* value is: 613.1593, rt 5.38 min (**8**).

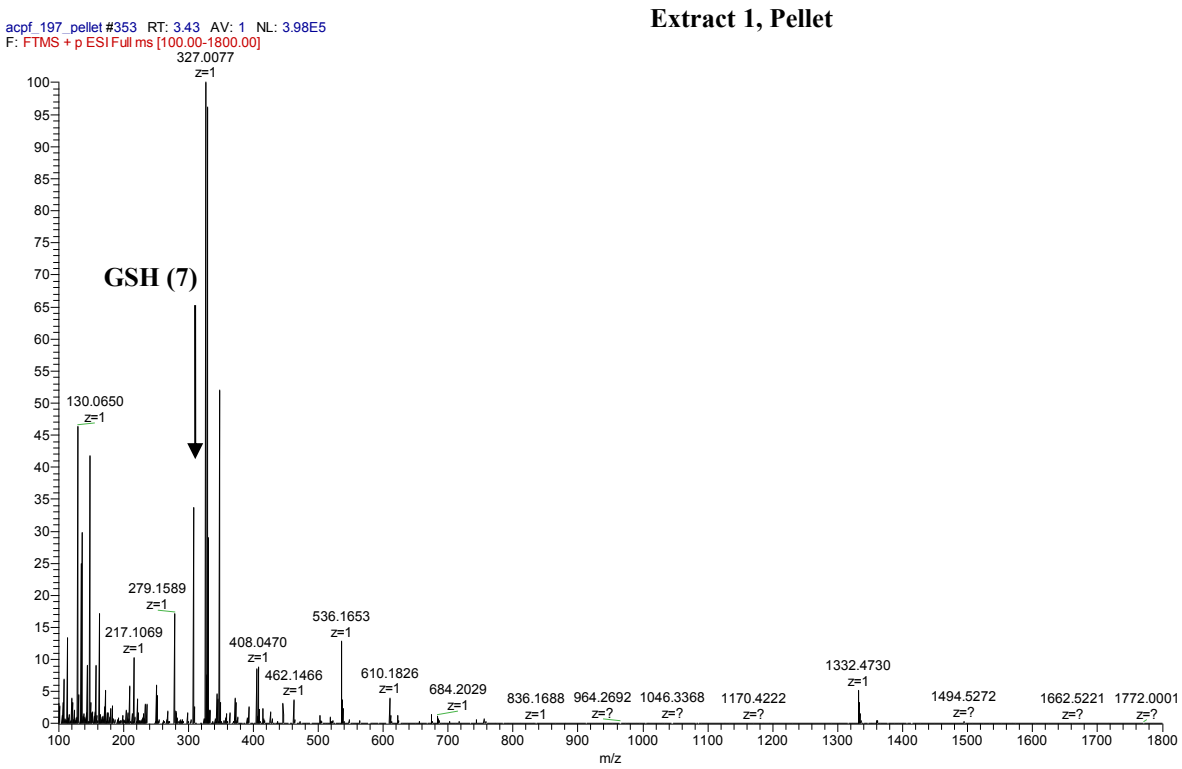

Figure 189. MS 1 fullscan of Extract 1, Pellet at rt 3.43 min showing the singly protonated (*m/z* value of 308.0911) ion of glutathione (**7**).

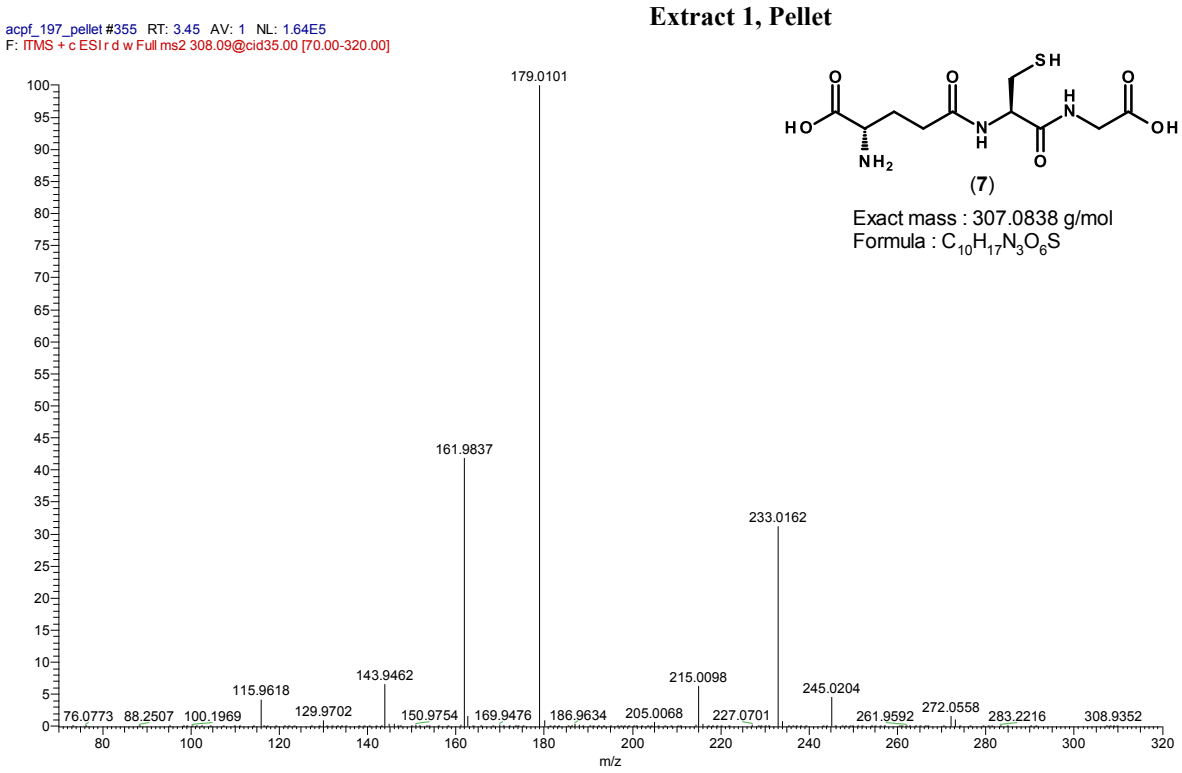

Figure 190. MS 2 of Extract 1, Pellet at *m/z* 308.09 (rt 3.45 min) showing the fragmentation pattern of glutathione (**7**). The structure of the analyte is illustrated in the top right corner.

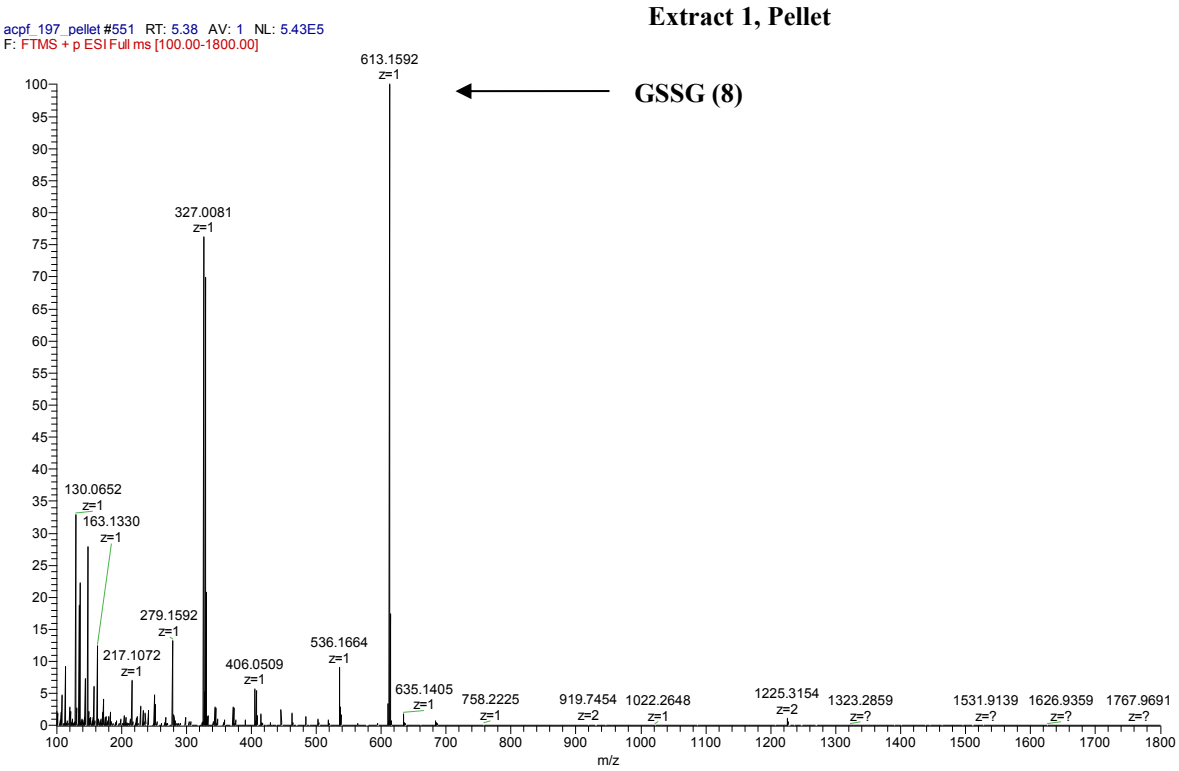

Figure 191. MS 1 fullscan of Extract 1, Pellet at rt 5.38 min showing the singly protonated (*m/z* value of 613.1593) ion of glutathione disulfide (**8**).

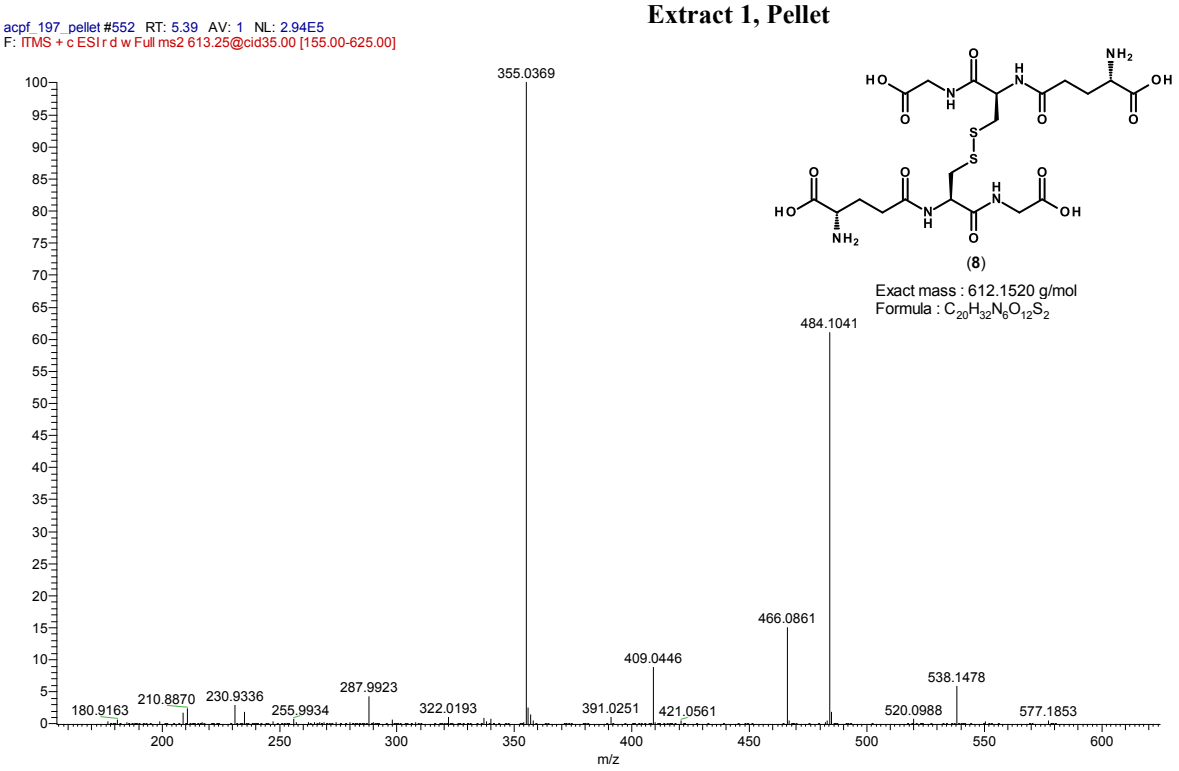

Figure 192. MS 2 of Extract 1, Pellet at *m/z* 613.25 (rt 5.39 min) showing the fragmentation pattern of glutathione disulfide (**8**). The structure of the analyte is illustrated in the top right corner.

IV.3. Conclusion

A new putative depsipeptide candidate was successfully isolated, as well as the already described natural product FR900359 (**1**). UV spectra of the cyclic-depsipeptide FR900359 (**1**) and the novel depsipeptide candidate were obtained. Unfortunately, the amount of FR900359 (**1**) isolated was not sufficient for NMR analysis. NMR analysis of the novel depsipeptide revealed that the natural product seemed to have degraded after prolonged storage, therefore, further isolation attempts need to be undertaken. SEC proved to be successful in enriching and separating the target compounds from the matrix. During the solvent separation procedure of the crude extract care should be taken to do a complete extraction i.e. extracting 3 times with enough volume of each solvent to ensure good separation of the target compounds. Besides that, 3 natural products were isolated, and their structure elucidated by NMR. This yielded the novel natural product epicatechin-3-hydroxy-2-methyl-propanoate (**6**), as well as the previously described natural products catechin (**4**) and epicatechin (**5**) (Figure 193).

The improved liquid/liquid extraction method successfully enriches the target compounds in a singular phase, while also removing carotenoids, chlorophylls, glycosides and sugars. This method should therefore be used in further isolation attempts of cyclic-depsipeptides and their deriatives from *A. crenata* extracts. It can also be used in further isolation of flavonoids, peptides and proteins.

The isolated compounds epicatechin-3-hydroxy-2-methyl-propanoate (**6**), catechin (**4**) and epicatechin (**5**) are secondary plant metabolites that belong to the class of flavonoids, which have a C_3-C_6-C_3 diphenylpropane skeleton. This is thought to be a major factor responsible for their displayed health benefits (Rice-Evans et al., 1996). Research regarding flavonoids on their positive effect on human physiology is being conducted with an emphasis on foodstuffs. Catechins are well known for their antioxidant, anticarcinogenic and anti-inflammatory activity (Scalia et al., 2013). Many plant derived foods e.g. apples, grapes, cacao, guaraná and green tea contain (+)-catechin and (-)-epicatechin (Kofink et al., 2007). *Ardisia compressa*, leaves which are used to prepare a herbal tea in folk medicine were also found to contain (+)-catechin and (-)-epicatechin (Ramırez-Mares et al., 1999). Bactericidal activity of tea catechins and their derivates against human pathogenic bacteria like, *Pleisomonas shigelloides*, *Staphylococcus aureus*, *Vibrio cholerae* and *Vibrio parahaemolyticus* has been observed. It is therefore plausible that catechins protect against pathogenic bacterial infections of the plant as well (Toda et al., 1989; Toda et al., 1992). Besides its toxicity, growth favoring effects of catechin on *Bacillus subtilis* up to a concentration of 4 ppm and on *Escherichia coli* up to 5 ppm were also observed. Only higher concentrations showed a growth inhibitory effect (Fathima and Rao, 2016). *Burkholderia* is a rapidly expanding genus within the group of gram-negative non-fermenting bacteria. Up to now around 80 species have been described. They occur worldwide in very different environments. Some of them are living in soil or in planktonic form in freshwater but most of them are living in symbiosis with a host (Depoorter et al., 2016). The species *Burkholderia oxyphila* sp. nov., which was isolated from acidic forest soil was found to be able to catabolize (+)-catechin and putative aromatic (+)-catechin derivatives (Otsuka et al., 2011). Although *B. oxyphila* sp. nov. lives in a very different environment than *Candidatus B. crenata*, it could be possible that the enzymatic repertory is similar because of ancestry, and *Candidatus B. crenata* is also able to use catechin derivates as substrate. Since *Candidatus B. crenata* cannot be cultivated, physiological tests are limited. Maybe work on the already sequenced genome of *Candidatus B. crenata* by Carlier et al. (2016) can lead to information regarding the capability of the organism of degrading catechin derivates. However, it could also be, that these isolated catechin derivates do not influence the leaf nodule symbiosis. This should be assessed by further research.

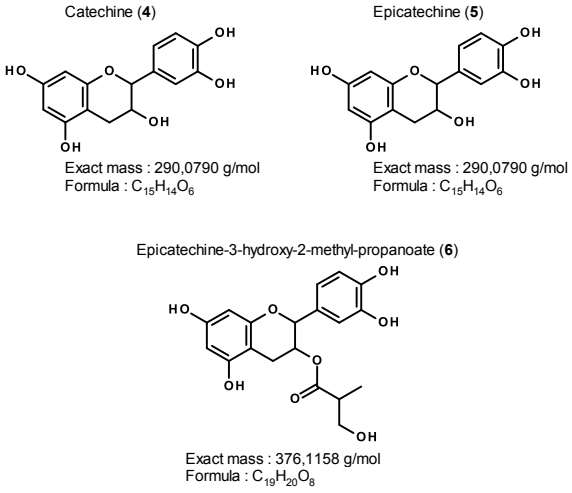

Figure 193. Chemical structure of the isolated compounds.

IV.4. Experimental

IV.4.1. General experimental procedures

The plant material and reagents were weighed using a sartorius Entris® 224I-1S Max 220 g, d=0.1 mg analytical balance. The metabolites were extracted with Methanol HiPerSolv CHROMANORM Reag. PH. Eur. For HPLC – GRADIENT GRADE – suitable for UPLC/UHPLC instruments VWR CHEMICALS BDH PROLABO® and sonicated in a TRANSSONIC 700/H Elma® ultrasonic bath. For the liquid/liquid extraction Petrolether 40-60° DAB, reinst ROTH, Chloroform ≥99.5% for HPLC Alfa Aesar, Ethyl acetate for HPLC, ≥99.7% SIGMA-ALDRICH, 1-Butanol ≥99.8%, HiPerSolv CHROMANORM® for HPLC VWR Chemicals and Water, HiPerSolv CHROMANORM® for HPLC VWR Chemicals were used. Centrifugation was carried out using a HERAEUS FRESCO 21 Centrifuge Thermo SCIENTIFIC. The extract was dried using a REACTI-VAP III #TS-18826 Evaporation Unit Thermo SCIENTIFIC apparatus supplied with Nitrogen ≥ 99,999 % H2O ≤ 3.0 ppm-mol O2 2.0 ppm-mol CnHm 0.5 ppm-mol. Pre-coated TLC-sheets ALUGRAM® SIL G/UV_{254} Layer 0.20 mm siliga gel 60 with fluorescent indicator UV_{254} (MACHEREY-NAGEL) were used for TLC seperation. The silica gel column chromatography was carried out using Silica gel 60 0,2-0,5 mm (ROTH). Sephadex LH-20 (GE Healthcare) was used for the size exclusion chromatography. For the RP-HPLC-UV measurements the extract was dissolved in Methanol HiPerSolv CHROMANORM Reag. PH. Eur. For HPLC – GRADIENT GRADE – suitable for UPLC/UHPLC instruments VWR CHEMICALS BDH PROLABO®. Ammonium acetate ≥97%, p.a., ACS ROTH dissolved in Water, HiPerSolv CHROMANORM® for HPLC VWR Chemicals was used for solvent A. For the RP-HPLC-HRESIMS metabolite measurements the extract was dissolved in a mixture of Milli-Q 18.2 MΩcm TC 27.2 °C TOC 3 ppb H_2O supplied by a Millipore Elix 15.0 MΩcm TC 16.8 °C unit, Acetonitrile HiPerSolv CHROMANORM HPLC LC-MS grade VWR CHEMICALS BDH PROLABO® and Formic acid Optima LC/MS. For the RP-HPLC-UV measurements the separation was carried out using an Agilent 1100 series Pump system connected to a UV diode array detector equipped with a Hypersil BDS C-18 column (250·4.6 mm; 5 µm particle size) Agilent. For the RP-HPLC-HRESIMS measurements the separation was carried out using an Ultimate 3000 XRS Pump system

connected to a RS Autosampler, Column Compartment and SR-3000 Solvent Rack DIONEX equipped with an Accucore 150 –C18 10x2.1 mm, 2.5 µm Defender guards pk4 Thermo SCIENTIFIC Guard Column and Accucore Vanquish C18+ Length (mm): 100, I.D. (mm): 2.1, Particle Size (µm): 1.5 Thermo SCIENTIFIC Column. HRESIMS measurements were conducted using a HESI2 ionisation source in positive ion mode connected to a VELOS PRO, leading into an ORBITRAP ELITE Thermo SCIENTIFIC instrument equipped with Xcalibur software Thermo SCIENTIFIC. For the improved extraction method, Methanol HiPerSolv CHROMANORM Reag. PH. Eur. For HPLC – GRADIENT GRADE – suitable for UPLC/UHPLC instruments VWR CHEMICALS BDH PROLABO®, Heptane, CHROMASOLV® for HPLC, ≥96% SIGMA-ALDRICH, Milli-Q 18.2 MΩcm TC 27.2 °C TOC 3 ppb H_2O supplied by a Millipore Elix 15.0 MΩcm TC 16.8 °C unit and Ethyl acetate for HPLC, ≥99.7% SIGMA-ALDRICH were used. The NMR measurements were carried out on a Bruker AVANCE III 600 NMR Spectrometer and a Bruker AVANCE III HD 700 NMR Spectrometer with CryoProbe™ using Topspin 3.1 software (Bruker). The samples were dissolved in Methanol-d4 ≥99.8 atom % D SIGMA-ALDRICH.

IV.4.1. Extraction with methanol

123 g of nodulated *A. crenata* leaf margins were harvested and immediately preserved in liquid nitrogen. The frozen plant material was homogenized with mortar and pestle. The material was extracted two times by addition of 1000 mL redistilled methanol (MeOH) for approximately 40 hours in darkness each time and then filtrated. The extract was dried under vacuo to yield 10.21 g of crude extract.

IV.4.2. Liquid/liquid extraction

The dried crude extract was suspended in water and then subsequently extracted with petroleum ether (PE), chloroform ($CHCl_3$), ethyl acetate (EtOAc), 1-butanol (1-BuOH) and water (H_2O). The yields were 1.93 g from the PE-phase, 0.01 g from the $CHCl_3$-phase, 0.3 g from the EtOAc-phase, 2.23 g from the 1-BuOH-phase and 5.22 g from the H_2O-phase.

IV.4.3. Silica gel column chromatography

MS-analysis of the extracts suggests that the target compounds (cyclic-depsipeptides) are enriched within the $CHCl_3$, EtOAc and BuOH-phases. Therefore, these phases are pooled for separation by silica gel column chromatography. Silica gel 60 0,2-0,5 mm was used for the silica gel column chromatography. The silica gel is equilibrated in a mixture of EtOAc/PE 50/50. 0.8 g of the combined extracts were combined with 2.0 g silica gel and loaded onto the column. Then the column was stepwise eluted with 100 mL of solvent mixtures (Table 17). The collected fractions were dried under vacuo and the weight was recorded (Table 18).

Table 17
Solvent mixtures for silica gel column chromatography.

Solvent	Volume [mL]	V_{PE} [mL]	V_{EtOAc} [mL]	V_{MeOH} [mL]
I	300	50	50	
II	100	40	60	
III	100	30	70	
IV	100	20	80	
V	100	10	90	
VI	100		100	
VII	100		90	10
VIII	100		80	20
IX	100		70	30
X	100		60	40

Table 18
Yield of extract from the different fractions.

Fraction	Dry weight [mg]
AC_KG0-6	12.9
AC_KG7	1.0
AC_KG8-9	17.8
AC_KG10	18.5
AC_KG11-12	32.6
AC_KG13-14	63.9
AC_KG15-17	223.6
AC_KG18-24	165
AC_KG25-32	9.9

IV.4.4. Size exclusion chromatography by Sephadex LH-20

Since the cyclic-depsipeptide-targets have a mass around ~800-1200 Da, SEC was chosen as the next separation step. The fractions AC_KG8 and AC_KG9 from the silica gel column chromatography were selected based on thin layer chromatography results for SEC. The column was loaded with Sephadex LH-20 and equilibrated with MeOH, which was also used as the eluting solvent. The column was coupled to a UV-spectrometer and 210 nm was chosen as the wavelength for detection. After MS analysis the fractions AC_KG18, AC_KG19+20, AC_KG21+22, AC_KG23+24 and AC_KG32 were combined and a second SEC was performed using the same technique as described earlier.

IV.4.5. Thin layer chromatography

TLC was used to quickly gain information of the composition of individual fractions and if those fractions seemed homogenous they were pooled. Unfortunately, it was not possible to determine the TLC signature of the targets; therefore, fractions were pooled based on other TLC constituents. TLC plates were checked for fluorescence under UV light at 366 nm and extinction under 254 nm. Visual inspection was performed by using an acidic 4-anisaldehyde spray solution followed by developing with a heat gun.

IV.4.6. High performance liquid chromatography

To gain deeper insight into the constituents of the fractions, RP-HPLC-UV and RP-HPLC-HRESIMS techniques were used. For the RP-HPLC-UV analysis the stationary phase consisted of a Hypersil BDS C-18 column (250·4.6 mm; 5 µm particle size). The mobile phase system consisted of a mixture of solvent A, an aqueous solution containing 10 mM ammonium acetate and solvent B being MeOH. A gradient elution method was used for the analysis (Table 19). 10 µL of sample were injected with a flowrate of 1.0 mL/min. The wavelength of detection was set at 230 nm (reference wavelength 360 nm)

Table 19
HPLC Gradient used for sample analysis.

Time [min]	Solvent A [%]	Solvent B [%]
0	90	10
15	0	100
22	0	100

For the RP-HPLC-HRESIMS analysis the samples were transferred into glass vials and placed under a stream of dry nitrogen for desiccation until weight consistency was achieved. (The vials containing the dried samples were sealed by a non-perforated crimp

cap and stored at -20 °C if not measured immediately.) For the measurement the samples were dissolved in a concentration of 10 mg/L in a solvent consisting of (98 % H_2O, 2 % ACN) + 0.1 % FA. After the solvent was added the samples were vortexed and sonicated to aid solvation. The samples were centrifuged at 14800 rpm (21.1·g) at 4 °C for 10 min. 100 µL of the supernatant were transferred into a glass insert for analysis. The pellet was discarded. The samples were placed into an autosampler at 4 °C. The stationary phase consisted of an Accucore™ Vanquish™ C-18+ UHPLC column (100·2.1 mm; 1.5 µm particle size). The mobile phase system consisted of a mixture of solvent A, an aqueous solution of 0.1 % formic acid (FA) and solvent B acetonitrile containing 0.1 % FA. A gradient elution method was used for the analysis (Table 20). 10 µL of sample were injected with a flowrate of 0.1 mL/min. A 25 µL loop was used. The column compartment was kept at 30 °C. Between each measurement a column washing step was performed by injecting a solution composed of (99 % H_2O, 1 % ACN) + 0.1 % FA using the following gradient (Table 21).

Table 20
HPLC Gradient used for sample analysis.

Time [min]	Solvent A [%]	Solvent B [%]
0	99	1
5	99	1
60	1	99
89	1	99
110	99	1
120	99	1

Table 21
HPLC Gradient used for column washing.

Time [min]	Solvent A [%]	Solvent B [%]
0	99	1
1	99	1
2	1	99
47	1	99
48	99	1
68	99	1

MS-analysis was performed in positive ion mode using a Velos PRO Iontrap leading into an Orbitrap Elite Instrument. Resolution was set at 120000, a spray voltage of 3.8 kV was used, and the capillary temperature was set at 250 °C. The mass scanning range of the MS 1 fullscan was set at 100-1800 *m/z*. Nitrogen sheath gas and nitrogen auxiliary gas were set at a flow rate of 5 [a.u.] and 0 [a.u.], respectively. Cyclomethicone_N5 was used as lock mass with a *m/z* value of 371.101230. Each MS 1 fullscan was followed up by 10 data dependent MS 2 fragmentation spectra, of the most abundant ion species. The time for dynamic exclusion duration of previously measured analytes was set at 30 s. The collision energy for CID was set at 35 eV. Before the samples were measured, two measurements, each followed by a column washing step were performed to ensure system equilibrium. A solution composed of (99 % H_2O, 1 % ACN) + 0.1 % FA was injected for all non-sample-type measurements.

IV.4.7. Structure elucidation by nuclear magnetic resonance spectroscopy

Structure elucidation of the isolated compounds was performed via 1D and 2D NMR analysis in a similar manner to (Berger et al., 2017). For the NMR measurements ~2.0 mg of isolated analyte was dissolved in 0.7 mL CD_3OD and transferred into 5 mm high precision NMR sample tubes. The ^{1}H, ^{13}C and 2D spectra were recorded on a Bruker AVANCE III 600 NMR Spectrometer 600.13 MHz (^{1}H), 150.61 MHz (^{13}C) and a Bruker AVANCE III HD 700 NMR Spectrometer 700.40 MHz (^{1}H), 176.12 MHz (^{13}C) with CryoProbe™ and performed using Topspin 3.1 software. The measurement temperature was set at 298 K ± 0.05 K. Residual CH_3OD was used as internal standard for ^{1}H (δH 3.34) and CD_3OD for ^{13}C (δC 49.0) measurements (see: *IV.7.2. Appendix B: NMR data of the isolated natural products*, Table 23, Table 24 and Table 25; IV.7.3. Appendix C: NMR spectra of the isolated natural *products*, Figure 198, Figure 199, Figure 200, Figure 201, Figure 202, Figure 203, Figure 204, Figure 205, Figure 206, Figure 207, Figure 208, Figure 209, Figure 210, Figure 211, Figure 212, Figure 213, Figure 214, Figure 215, Figure 216, Figure 217 and Figure 218).

IV.4.8. Improved liquid/liquid extraction method

Since the previously used liquid/liquid extraction failed at enriching the target compounds in one specific fraction, a different liquid/liquid extraction method was used (Figure 194).

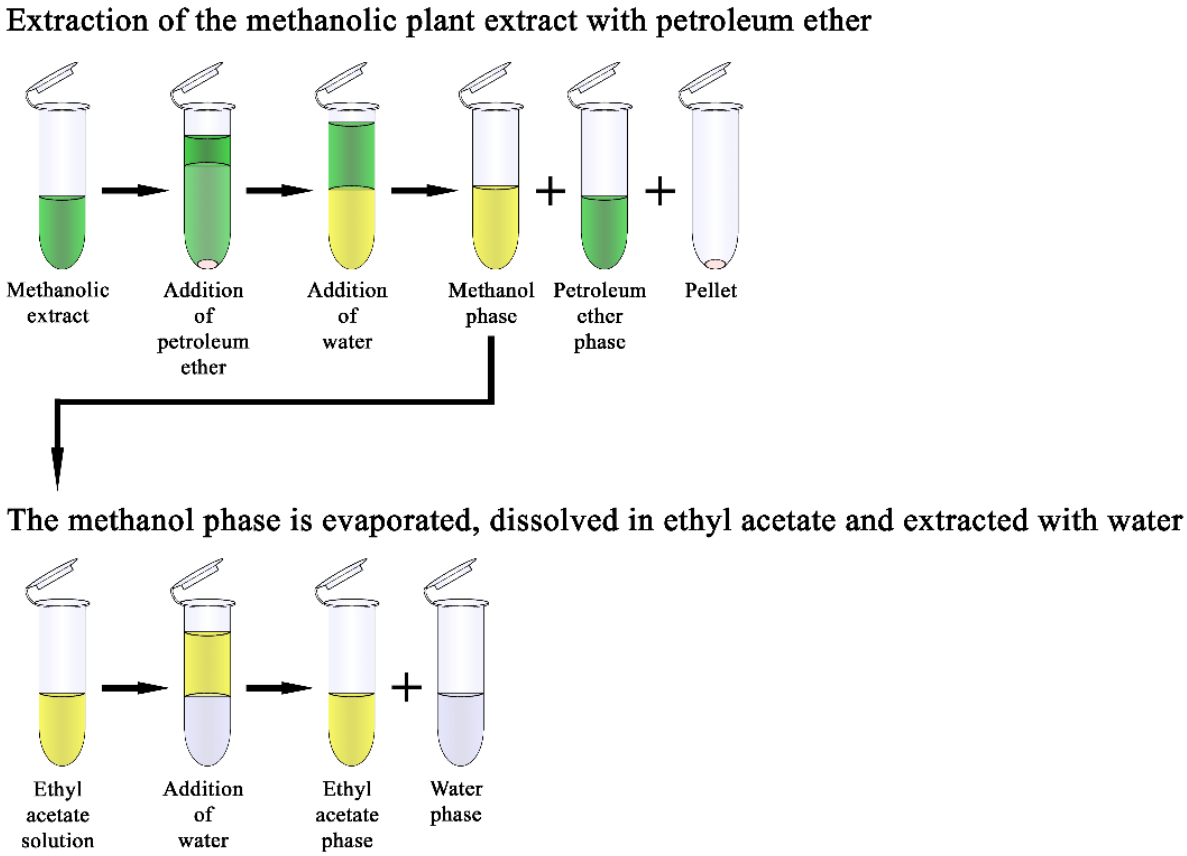

Figure 194. Scheme of the improved liquid/liquid extraction method.

Approximately an equal amount of young and old leaves of *A. crenata* were harvested, frozen with liquid nitrogen and ground using mortar and pestle. For each *A. crenata* combined leave tissue crude extract about 30-50 mg of the homogenized plant material at -196 °C was weighed into pre-chilled 2 mL Eppendorf® Safe-Lock Tubes. For the extraction the samples were placed on ice and 1 mL of ice-cold methanol was added. The samples were vortexed. To increase extraction efficiency, as well as possibly rupturing intact endophytes the samples were sonicated for 20 min at 0 °C. The extraction mixture was vortexed and centrifuged at 14800 rpm (21.1·g) at 4 °C for 4 minutes. The supernatant was transferred into an amber glass vial and placed under a stream of dry nitrogen for desiccation. 1 mL of ice-cold methanol was added to the pellet and the extraction procedure was carried out again for a total of 4 times. After the last extraction the supernatant was colourless. The extracts were dried until weight consistency was achieved. (The vials containing the dry extracts were sealed by a non-perforated crimp cap and stored at -20 °C.) The crude extracts of the combined *A. crenata* leave tissues were dissolved in 1 mL of methanol. To the methanolic crude extract an equal amount of n-heptane was added. This resulted in a pink precipitate being formed. The sample was centrifuged. at 14800 rpm (21.1·g) at 4 °C for 4 min. The biphasic supernatant was separated from the precipitate. Water was added to achieve a methanol concentration of 83.3 % (not accounting for n-heptane). This resulted in a better phase separation with most of the carotenes and chlorophylls in the n-heptane phase. The xanthopylls remained mostly in the methanolic phase with the most apolar xanthophylls being distributed between the two phases. The n-heptane phase was separated and the methanolic phase was extracted two more times with n-heptane. The n-heptane phases were combined. The extracts were dried under dry nitrogen. To enrich the target compounds further the methanolic extract was dissolved in water and extracted 3 times with EtOAc. The organic phases were combined. The extracts were dried under dry nitrogen. The precipitate which formed by adding n-heptane to the methanolic extract was washed by redissolving it in methanol and precipitating it again with n-heptane, followed by centrifugation. This was done for a total of three times including the initial precipitation. The washing solutions were discarded. The washed precipitate was dried under dry nitrogen. The weight of the extracts of the different fractions was recorded (Table 22). RP-HPLC-HRESIMS analysis was performed on each of the phases and the precipitate like previously described.

Table 22
Yield of extract from the different fractions.

Fraction	Dry weight [mg]
Extract 1, original	12.1
Extract 1, Heptane phase	0.8
Extract 1, Methanol phase	8.4
Extract 1, Pellet	1.4
Extract 2, original	17.5
Extract 2, Heptane phase	1.4
Extract 2, Ethyl acetate phase	4.1
Extract 2, Water phase	9.1
Extract 2, Pellet	1.1

IV.5. Acknowledgements

The authors thank Wolfram Weckwerth, head of the Department of Molecular Systems Biology (*mosys*), Lena Fragner for support at the laboratory at *mosys*. Further we thank Karin Vetschera, head of the Chemodiversity research group at the Department of Botany and Biodiversity research and Johann Schinnerl, as well as Lothar Brecker (Institute of Organic Chemistry). We thank Ferdinand Hartmann for assistance. Finally, special thanks to Andreas Berger for the professional advice during the natural product isolation.

IV.6. References

Berger, A., Tanuhadi, E., Brecker, L., Schinnerl, J., Valant-Vetschera, K., 2017. Chemodiversity of tryptamine-derived alkaloids in six Costa Rican Palicourea species (Rubiaceae–Palicoureeae). Phytochemistry 143, 124-131. https://dx.doi.org/10.1016/j.phytochem.2017.07.016.

Carlier, A., Fehr, L., Pinto‐Carbó, M., Schäberle, T., Reher, R., Dessein, S., König, G., Eberl, L., 2016. The genome analysis of Candidatus Burkholderia crenata reveals that secondary metabolism may be a key function of the Ardisia crenata leaf nodule symbiosis. Environmental microbiology. https://dx.doi.org/10.1111/1462-2920.13184.

Cases, I., de Lorenzo, V., Ouzounis, C. A., 2003. Transcription regulation and environmental adaptation in bacteria. Trends in microbiology 11, 248-253. https://dx.doi.org/10.1016/S0966-842X(03)00103-3.

Crüsemann, M., Reher, R., Schamari, I., Brachmann, A. O., Ohbayashi, T., Kuschak, M., Malfacini, D., Seidinger, A., Pinto‐Carbó, M., Richarz, R., 2018. Heterologous Expression, Biosynthetic Studies, and Ecological Function of the Selective Gq‐Signaling Inhibitor FR900359. Angewandte Chemie International Edition 57, 836-840. https://dx.doi.org/10.1002/anie.201707996.

Davis, A. L., Cai, Y., Davies, A. P., Lewis, J., 1996. 1H and 13C NMR assignments of some green tea polyphenols. Magnetic resonance in Chemistry 34, 887-890. https://dx.doi.org/10.1002/(SICI)1097-458X(199611)34:11<887::AID-OMR995>3.0.CO;2-U.

Depoorter, E., Bull, M. J., Peeters, C., Coenye, T., Vandamme, P., Mahenthiralingam, E., 2016. Burkholderia: an update on taxonomy and biotechnological potential as antibiotic producers. Applied microbiology and biotechnology 100, 5215-5229. https://dx.doi.org/10.1007/s00253-016-7520-x.

El-Razek, M. A., 2007. NMR assignments of four catechin epimers. Asian Journal of Chemistry 19, 4867.

Fathima, A., Rao, J. R., 2016. Selective toxicity of Catechin—a natural flavonoid towards bacteria. Applied microbiology and biotechnology 100, 6395-6402. https://dx.doi.org/10.1007/s00253-016-7492-x.

Fujioka, M., Koda, S., Morimoto, Y., Biemann, K., 1988. Structure of FR900359, a cyclic depsipeptide from Ardisia crenata sims. The Journal Of Organic Chemistry 53, 2820-2825. https://dx.doi.org/10.1021/jo00247a030.

HORNER JR, H. T., LERSTEN, N. R., 1972. Nomenclature of bacteria in leaf nodules of the families Myrsinaceae and Rubiaceae. International Journal of Systematic and Evolutionary Microbiology 22, 117-122. https://dx.doi.org/10.1099/00207713-22-2-117.

Karplus, M., 1959. Contact electron‐spin coupling of nuclear magnetic moments. The Journal of chemical physics 30, 11-15. https://dx.doi.org/10.1063/1.1729860.

Kitajima, K., Fox, A. M., Sato, T., Nagamatsu, D., 2006. Cultivar selection prior to introduction may increase invasiveness: evidence from Ardisia crenata. Biological Invasions 8, 1471. https://dx.doi.org/10.1007/s10530-005-5839-9.

Kobayashi, H., de Mejía, E., 2005. The genus Ardisia: a novel source of health-promoting compounds and phytopharmaceuticals. Journal of Ethnopharmacology 96, 347-354. https://dx.doi.org/10.1016/j.jep.2004.09.037.

Kofink, M., Papagiannopoulos, M., Galensa, R., 2007. Enantioseparation of catechin and epicatechin in plant food by chiral capillary electrophoresis. European Food Research and Technology 225, 569-577. https://dx.doi.org/10.1007/s00217-006-0455-1.

Link, A., Müller, C. E., 2016. G‐Protein‐Coupled Receptors: Sustained Signaling via Intracellular Megaplexes and Pathway‐Specific Drugs. Angewandte Chemie International Edition 55, 15962-15964. https://dx.doi.org/10.1002/anie.201609015.

Miller, I., Donnelly, A., 1987. Location and distribution of symbiotic bacteria during floral development in Ardisia crispa. Plant, Cell & Environment 10, 715-724. https://dx.doi.org/10.1111/1365-3040.ep11604753.

Nishimura, A., Kitano, K., Takasaki, J., Taniguchi, M., Mizuno, N., Tago, K., Hakoshima, T., Itoh, H., 2010. Structural basis for the specific inhibition of heterotrimeric Gq protein by a small molecule. Proceedings of the National Academy of Sciences 107, 13666-13671. https://dx.doi.org/10.1073/pnas.1003553107.

Otsuka, Y., Muramatsu, Y., Nakagawa, Y., Matsuda, M., Nakamura, M., Murata, H., 2011. Burkholderia oxyphila sp. nov., a bacterium isolated from acidic forest soil that catabolizes (+)-catechin and its putative aromatic derivatives. International Journal of Systematic and Evolutionary Microbiology 61, 249-254. https://dx.doi.org/10.1099/ijs.0.017368-0.

Pinto-Carbó, M., Gademann, K., Eberl, L., Carlier, A., 2018. Leaf nodule symbiosis: function and transmission of obligate bacterial endophytes. Current opinion in plant biology 44, 23-31. https://dx.doi.org/10.1016/j.pbi.2018.01.001.

Ramırez-Mares, M., Fatell, S., Villa-Trevino, S., de Mejía, E. G., 1999. Protection of extract from leaves of Ardisia compressa against benomyl-induced cytotoxicity and genotoxicity in cultured rat hepatocytes. Toxicology in vitro 13, 889-896. https://dx.doi.org/10.1016/S0887-2333(99)00071-5.

Rice-Evans, C. A., Miller, N. J., Paganga, G., 1996. Structure-antioxidant activity relationships of flavonoids and phenolic acids. Free radical biology and medicine 20, 933-956. https://dx.doi.org/10.1016/0891-5849(95)02227-9.

Scalia, S., Marchetti, N., Bianchi, A., 2013. Comparative evaluation of different co-antioxidants on the photochemical-and functional-stability of epigallocatechin-3-gallate in topical creams exposed to simulated sunlight. Molecules 18, 574-587. https://dx.doi.org/10.3390/molecules18010574.

Schrage, R., Schmitz, A.-L., Gaffal, E., Annala, S., Kehraus, S., Wenzel, D., Büllesbach, K. M., Bald, T., Inoue, A., Shinjo, Y., 2015. The experimental power of FR900359 to study Gq-regulated biological processes. Nature communications 6, 10156. https://dx.doi.org/10.1038/ncomms10156.

Sieber, S., Carlier, A., Neuburger, M., Grabenweger, G., Eberl, L., Gademann, K., 2015. Isolation and total synthesis of kirkamide, an aminocyclitol from an obligate leaf nodule symbiont. Angewandte Chemie International Edition 54, 7968-7970. https://dx.doi.org/10.1002/anie.201502696.

Toda, M., Okubo, S., Hiyoshi, R., Shimamura, T., 1989. The bactericidal activity of tea and coffee. Letters in applied microbiology 8, 123-125. https://dx.doi.org/10.1111/j.1472-765X.1989.tb00255.x.

Toda, M., Okubo, S., Ikigai, H., Suzuki, T., Suzuki, Y., Hara, Y., Shimamura, T., 1992. The protective activity of tea catechins against experimental infection by Vibrio cholerae O1. Microbiology and immunology 36, 999-1001. https://dx.doi.org/10.1111/j.1365-2672.1991.tb04435.x.

Yang, C.-J., Hu, J.-M., 2018. Bacterial Leaf Nodule Symbiosis in Flowering Plants. Symbiosis. IntechOpen. https://dx.doi.org/10.5772/intechopen.73078.

IV.7. Appendix

IV.7.1. Appendix A: UV spectra of the isolated cyclic-depsipeptides

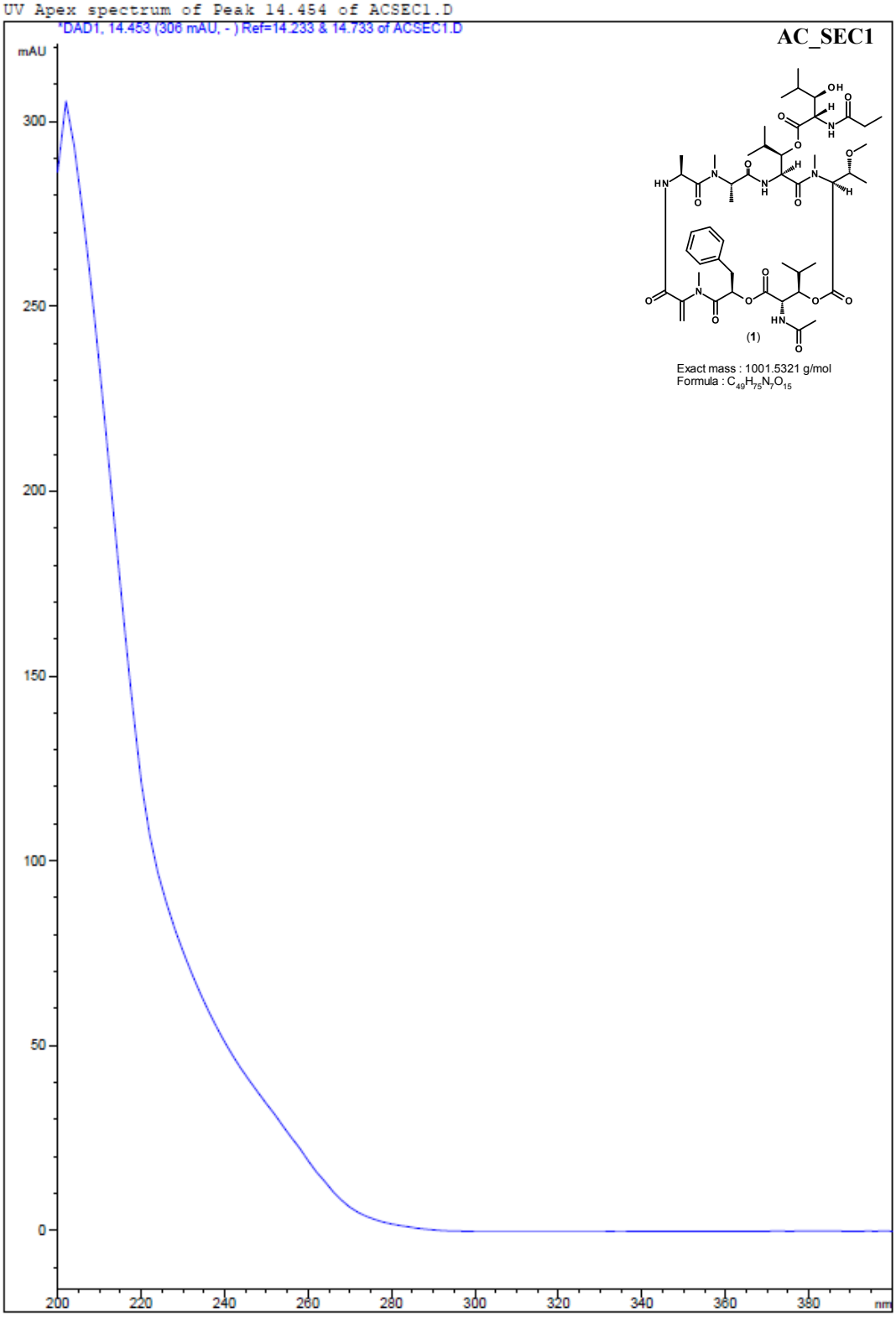

Figure 195. UV apex spectrum of the fraction AC_SEC1 at rt 14.45 min containing FR900359 (**1**).

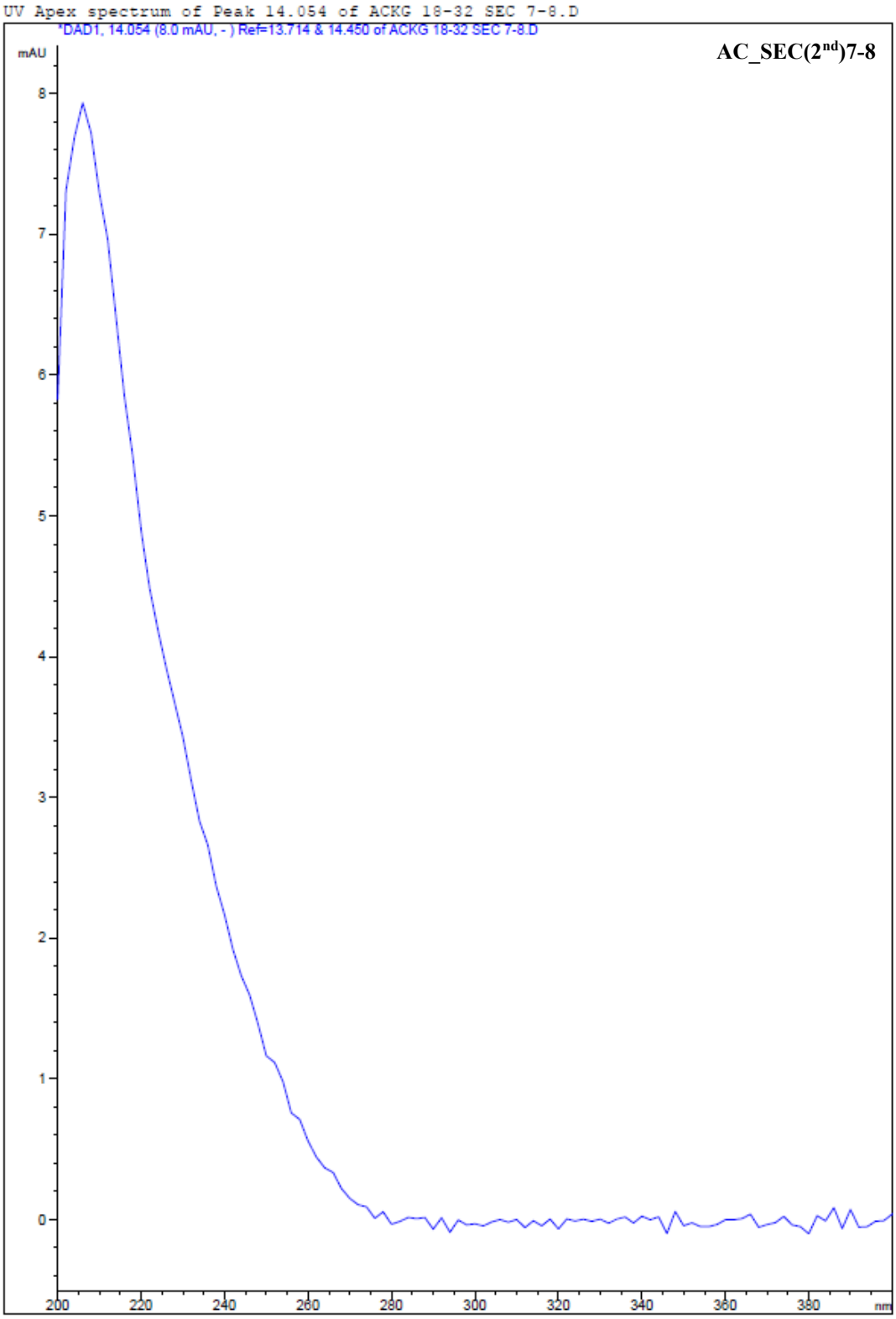

Figure 196. UV apex spectrum of the fraction AC_SEC(2^{nd})7-8 at rt 14.05 min.

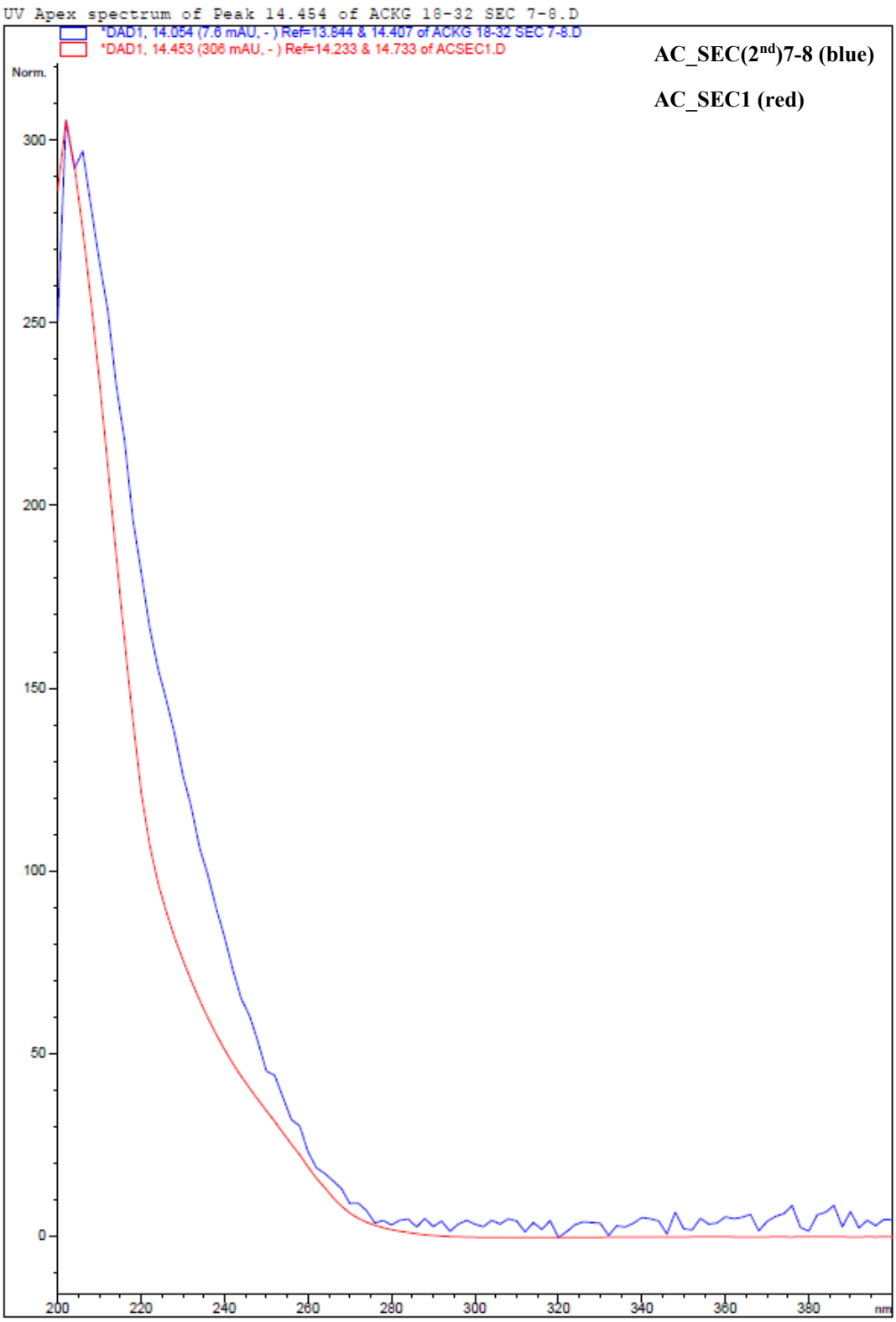

Figure 197. Overlay of the UV apex spectra of the fractions AC_SEC(2nd)7-8 at rt 14.05 min (blue) and AC_SEC1 at rt 14.45 min containing FR900359 (**1**) (red).

IV.7.2. Appendix B: NMR data of the isolated natural products

Epicatechin-3-hydroxy-2-methyl-propanoate (**6**): white solid: **^{1}H-NMR (600.13 MHz, CD_3OD)** δ = 6.960 (s *apparent pattern*, 1H), 6.787 (m, 1H), 6.778 (m, 1H), 5.972 (d, *J* = 1.6 Hz, 1H), 5.948 (d, *J* = 1.6 Hz, 1H), 5.424 (t *apparent pattern*, *J* = 1.6 Hz, 1H), 5.007 (s *apparent pattern*, 1H), 3.602 (dd, *J* = 10.8, 7.5 Hz, 1H), 3.431 (dd, *J* = 10.8, 6.0 Hz, 1H), 2.967 (dd, *J* = 17.4, 4.6 Hz, 1H), 2.840 (d *apparent pattern*, *J* = 17.4 Hz, 1H), 2.533 (tq, *J* = 7.4, 6.8 Hz, 1H), 0.937 (d, *J* = 7.1 Hz, 3H); **^{13}C-NMR (150.61 MHz, CD_3OD)** δ = 176.10, 157.90, 157.11, 146.04, 145.98, 131.33, 119.01, 115.90, 114.95, 99.22, 96.48, 95.74, 78.16, 69.90, 65.01, 43.61, 26.65, 13.89; **HRMS (ESI)** calculated for $C_{19}H_{21}O_8^+$: $[M+H]^+$ 377.1231; Found $[M+H]^+$ 377.1211.

Table 23
NMR spectroscopic data (600 MHz, CD3OD) of epicatechin-3-hydroxy-2-methyl-propanoate (**6**). [a] Apparent splitting pattern.

C no.	δ_C, Type	δ_H (*J* in Hz)
2	78.16, CH	5.007, s[a]
3	69.90, CH	5.424, t[a] (1.6)
4a	26.65, CH_2	2.967, dd (17.4, 4.6)
4b		2.840, d[a] (17.4)
5	157.90 a, C	
6	96.48, CH	5.972, d (1.6)
7	157.85 a, C	
8	95.74, CH	5.948, d (1.6)
9	157.11, C	
10	99.22, C	
1’	131.33, C	
2’	114.95, CH	6.960, s[a]
3’	145.98 b, C	
4’	146.04 b, C	
5’	115.90, CH	6.778, m
6’	119.01, CH	6.787, m
1’’	176.10, C	
2’’	43.61, CH	2.533, tq (7.4, 6.8)
3’’a	65.01, CH_2	3.602, dd (10.8, 7.5)
3’’b		3.431, dd (10.8, 6.0)
4’’	13.89, CH_3	0.936, d (7.1)

Catechin (**4**): white solid: **^{1}H-NMR (600.13 MHz, CD_3OD)** δ = 6.866 (d, *J* = 1.8 Hz, 1H), 6.759 (m, 1H), 6.722 (m, 1H), 5.956 (d, *J* = 2.3 Hz, 1H), 5.883 (d, *J* = 2.3 Hz, 1H), 4.593 (d, *J* = 7.6 Hz, 1H), 4.003 (ddd, *J* = 13.2, 7.9, 5.4 Hz, 1H), 2.844 (m, 1H), 2.534 (dd, *J* = 16.1, 8.1 Hz, 1H); **^{13}C-NMR (150.61 MHz, CD_3OD)** δ = 157.85, 157.59, 156.92, 146.26, 146.23, 132.21, 120.03, 116.07, 115.24, 100.80, 96.27, 95.58, 82.86, 68.82, 28.53; **HRMS (ESI)** calculated for $C_{15}H_{15}O_6^+$: $[M+H]^+$ 291.0863; Found $[M+H]^+$ 291.0856.

Table 24
NMR spectroscopic data (600 MHz, CD3OD) of catechin (**4**).

C no.	δ_C, Type	δ_H (*J* in Hz)
2	82.86, CH	4.593, d (7.6)
3	68.82, CH	4.003, ddd (13.2, 7.9, 5.4)
4a	28.53, CH_2	2.844, m
4b		2.534, dd (16.1, 8.1)
5	157.59 a, C	
6	96.27, CH	5.956, d (2.3)
7	157.85 a, C	
8	95.58, CH	5.883, d (2.3)
9	156.92 a, C	
10	100.80, C	
1’	132.21, C	
2’	115.24, CH	6.866, d (1.8)
3’	146.23 b, C	
4’	146.26 b, C	
5’	116.07, CH	6.759, m
6’	120.03, CH	6.722, m

Epicatechin (**5**): white solid: **^{1}H-NMR (600.13 MHz, CD_3OD)** δ = 7.004 (d, *J* = 1.9 Hz, 1H), 6.794 (m, 1H), 6.759 (m, 1H), 5.970 (d, *J* = 2.4 Hz, 1H), 5.945 (d, *J* = 2.4 Hz, 1H), 4.847 (s *apparent pattern*, 1H), 4.208 (m, 1H), 2.861 (m, 1H), 2.766 (dd, *J* = 16.7, 2.8 Hz, 1H); **^{13}C-NMR (150.61 MHz, CD_3OD)** δ = 158.01, 157.68, 157.31, 145.95, 145.78, 132.29, 119.38, 115.88, 115.31, 100.05, 96.37, 95.87, 79.88, 67.49, 29.26; **HRMS (ESI)** calculated for $C_{15}H_{15}O_6^+$: $[M+H]^+$ 291.0863; Found $[M+H]^+$ 291.0858.

Table 25
NMR spectroscopic data (600 MHz, CD3OD) of epicatechin (**5**). [a] Apparent splitting pattern.

C no.	δ_C, Type	δ_H (*J* in Hz)
2	79.88, CH	4.847, s[a]
3	67.49, CH	4.208, m
4a	29.26, CH_2	2.861, m
4b		2.766, dd (16.7, 2.8)
5	158.01 a, C	
6	96.37, CH	5.970, d (2.4)
7	157.68 a, C	
8	95.87, CH	5.945, d (2.4)
9	157.31 a, C	
10	100.05, C	
1’	132.29, C	
2’	115.31, CH	7.004, d (1.9)
3’	145.95 b, C	
4’	145.78 b, C	
5’	115.88, CH	6.759, m
6’	119.38, CH	6.794, m

The spectroscopic data seems consistent with data for catechin (**4**) and epicatechin (**5**) described in the literature (Davis et al., 1996; El-Razek, 2007). The cis conformation can be inferred by the small coupling constant between the protons of 2 and 3. This could be caused by the near 90 ° dihedral angle between the protons, which occurs in the cis conformation of the molecule and following the Karplus equation should yield a $^{3}J_{H,H}$ of near 0, whereas for the trans conformation, the dihedral angle of these protons would be near 180 ° and therefore, yield a higher $^{3}J_{H,H}$ (Karplus, 1959) . For epicatechin-3-hydroxy-2-methyl-propanoate (**6**) the conformation at the stereocenter at 2’’ could not be resolved.

IV.7.3. Appendix C: NMR spectra of the isolated natural products

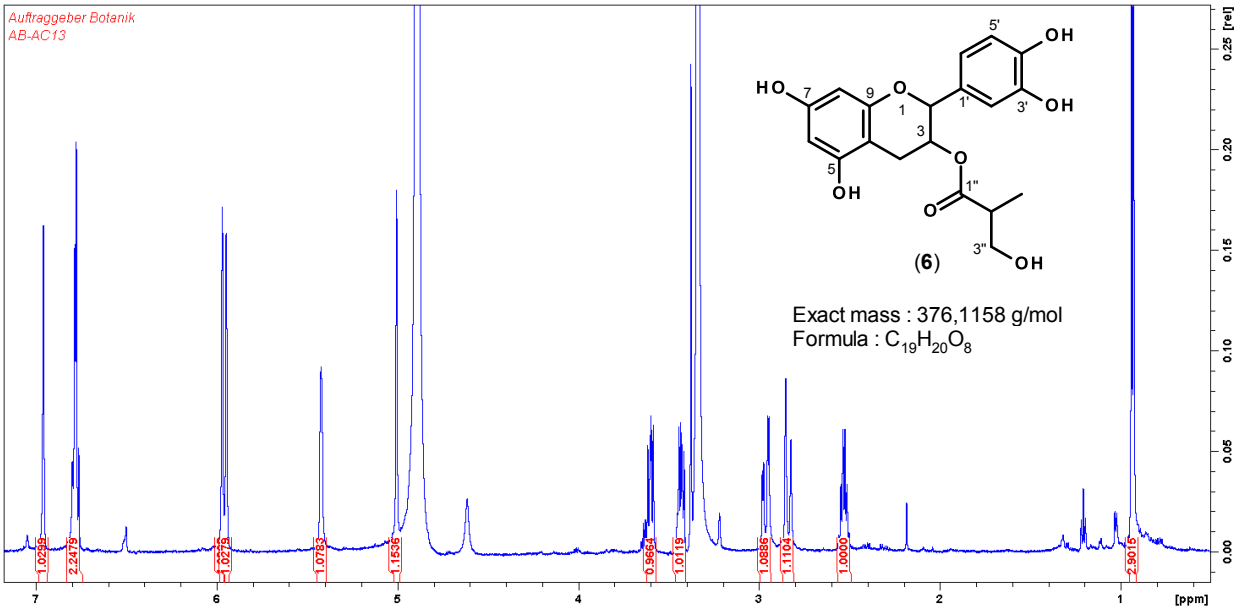

Figure 198. ^{1}H-NMR Spectrum of isolated epicatechin-3-hydroxy-2-methyl-propanoate (**6**) in CD_3OD (600.13 MHz).

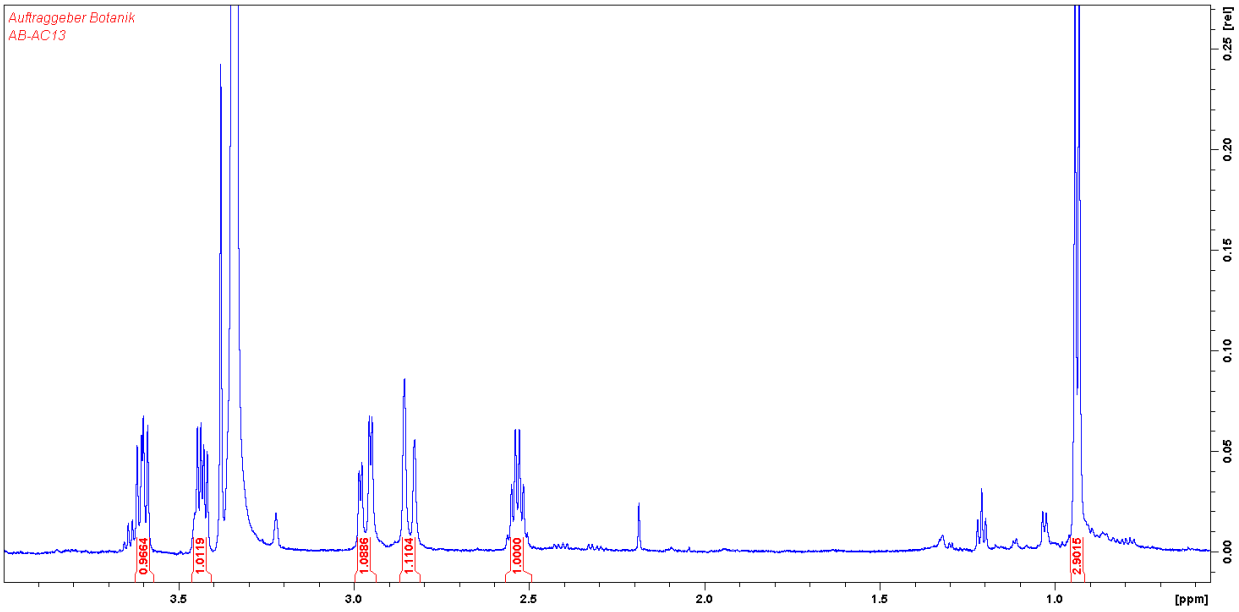

Figure 199: Section of ^{1}H-NMR Spectrum of isolated epicatechin-3-hydroxy-2-methyl-propanoate (**6**) in CD_3OD (600.13 MHz).

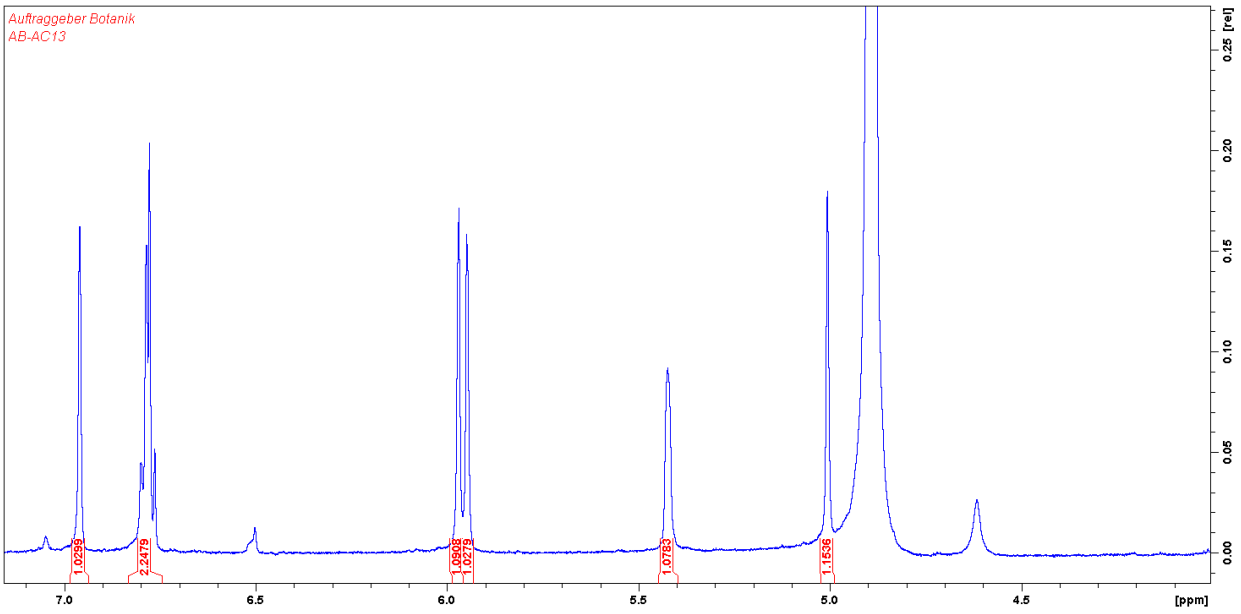

Figure 200. Section of ^{1}H-NMR Spectrum of isolated epicatechin-3-hydroxy-2-methyl-propanoate (**6**) in CD_3OD (600.13 MHz).

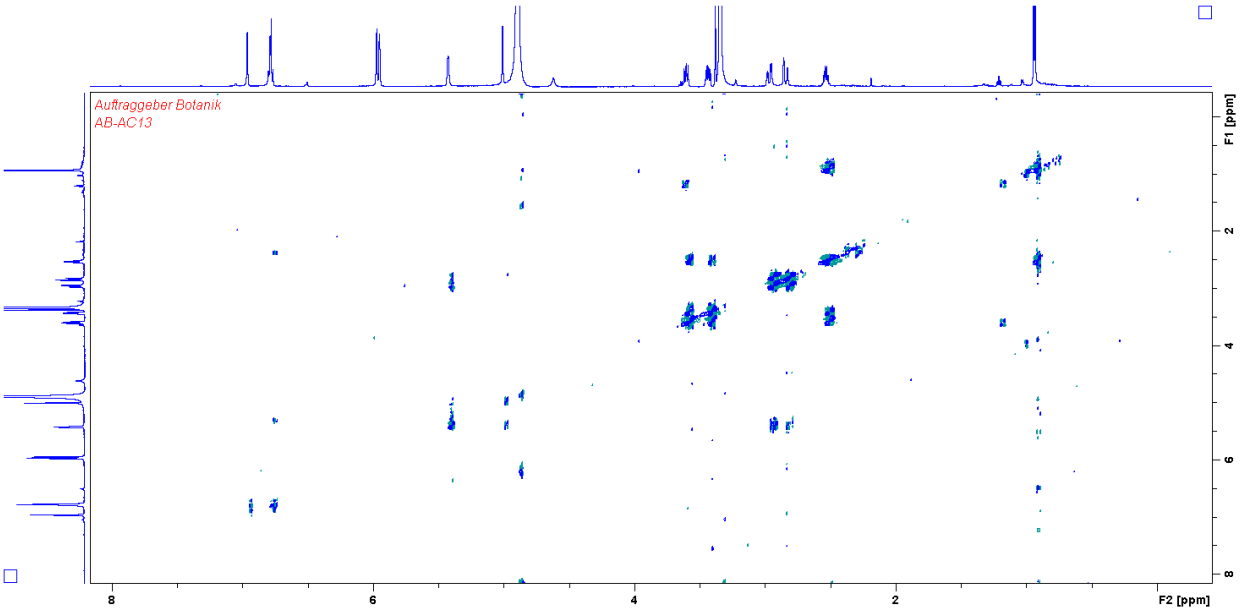

Figure 201. ^{1}H-^{1}H COSY NMR Spectrum of isolated epicatechin-3-hydroxy-2-methyl-propanoate (**6**) in CD_3OD (600.13 MHz).

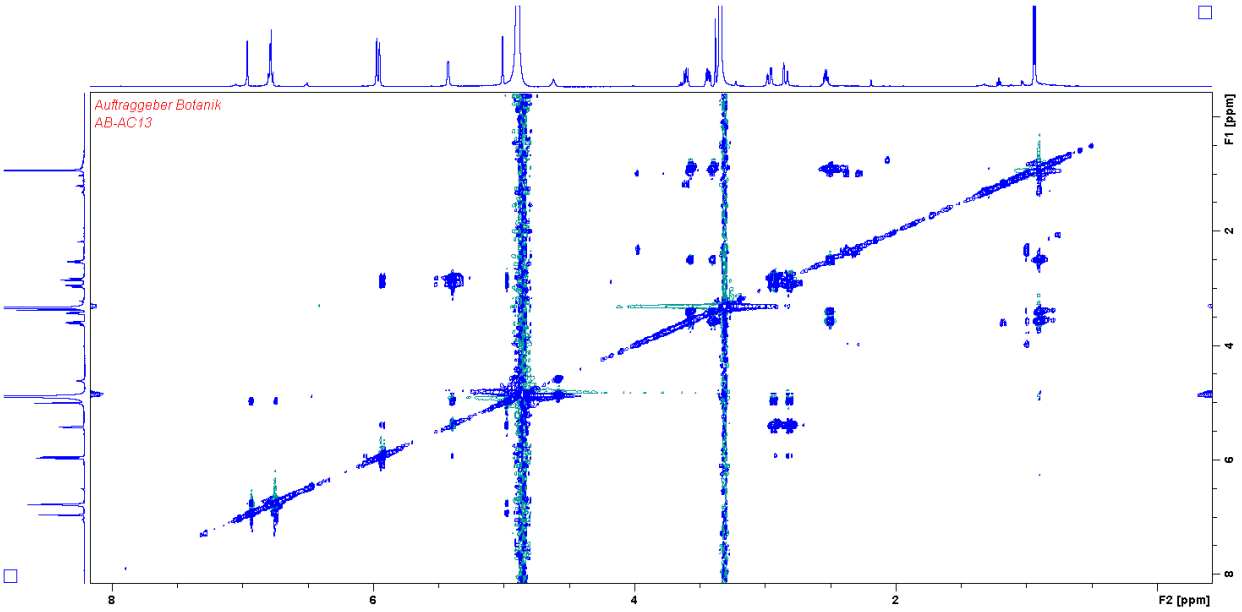

Figure 202. ^{1}H-^{1}H TOCSY NMR Spectrum of isolated epicatechin-3-hydroxy-2-methyl-propanoate (**6**) in CD_3OD (600.13 MHz).

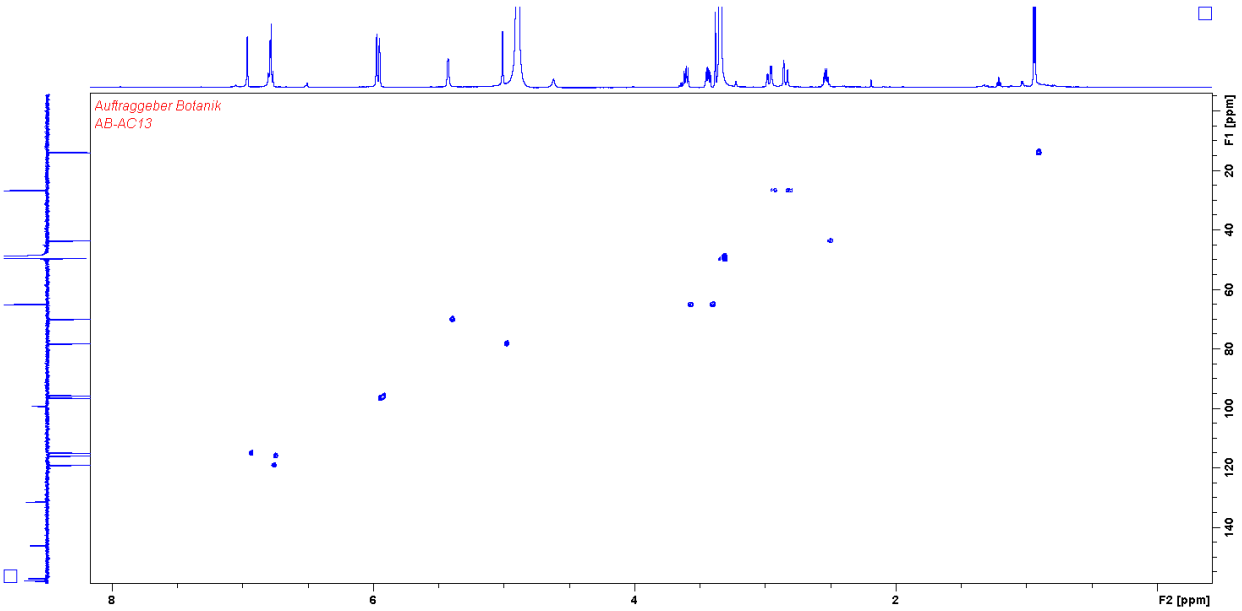

Figure 203. ^{1}H-^{13}C HSQC NMR Spectrum of isolated epicatechin-3-hydroxy-2-methyl-propanoate (**6**) in CD_3OD (600.13 MHz).

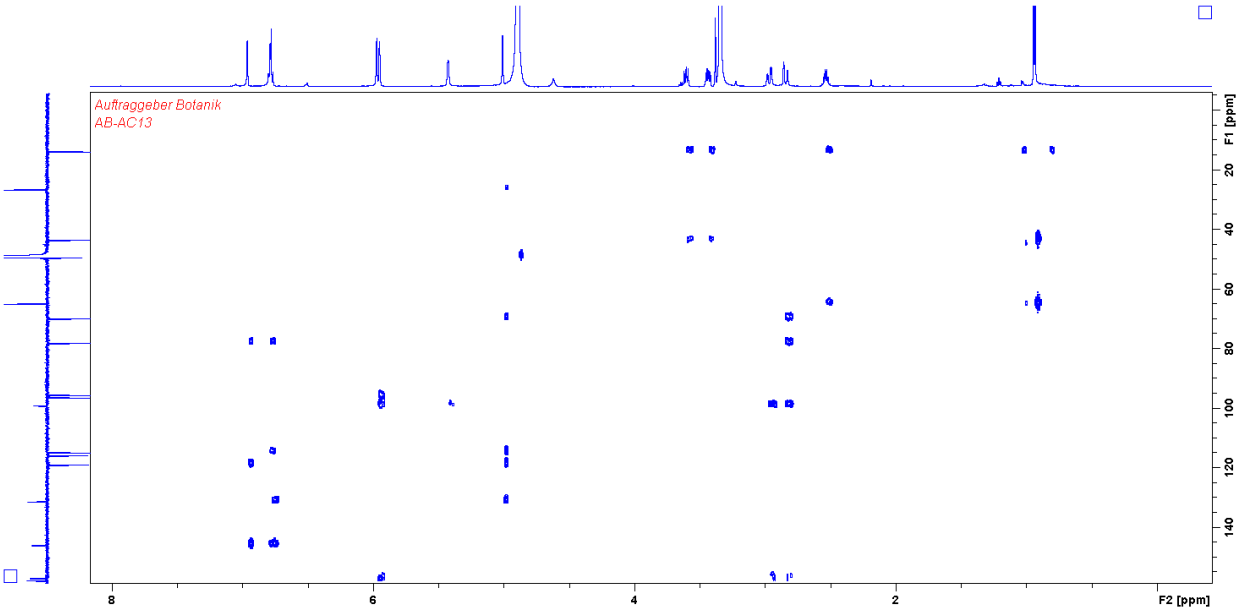

Figure 204. ^{1}H-^{13}C HMBC NMR Spectrum of isolated epicatechin-3-hydroxy-2-methyl-propanoate (**6**) in CD_3OD (600.13 MHz).

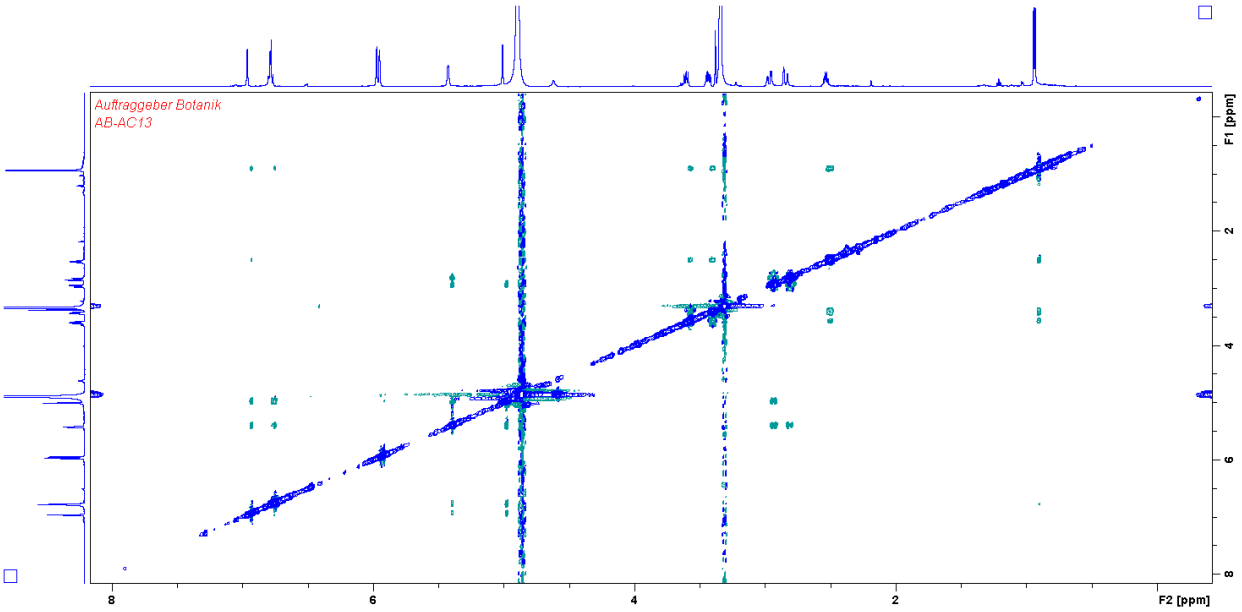

Figure 205. ^{1}H-^{1}H NOESY NMR Spectrum of isolated epicatechin-3-hydroxy-2-methyl-propanoate (**6**) in CD_3OD (600.13 MHz).

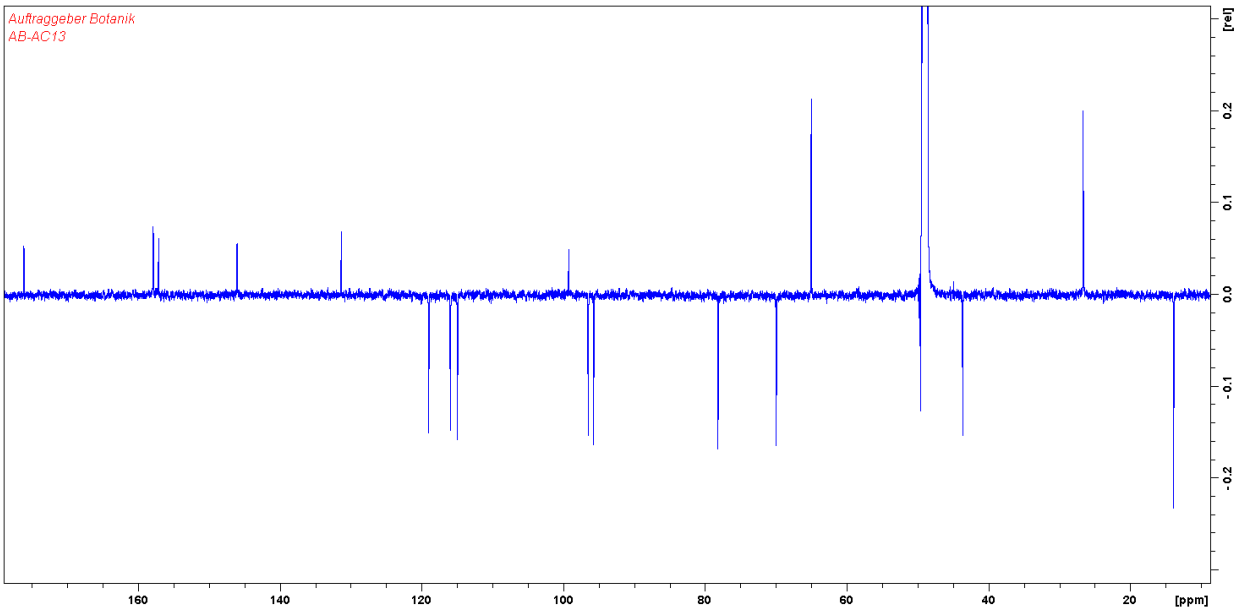

Figure 206. ^{13}C-NMR Spectrum of isolated epicatechin-3-hydroxy-2-methyl-propanoate (**6**) in CD_3OD (600.13 MHz).

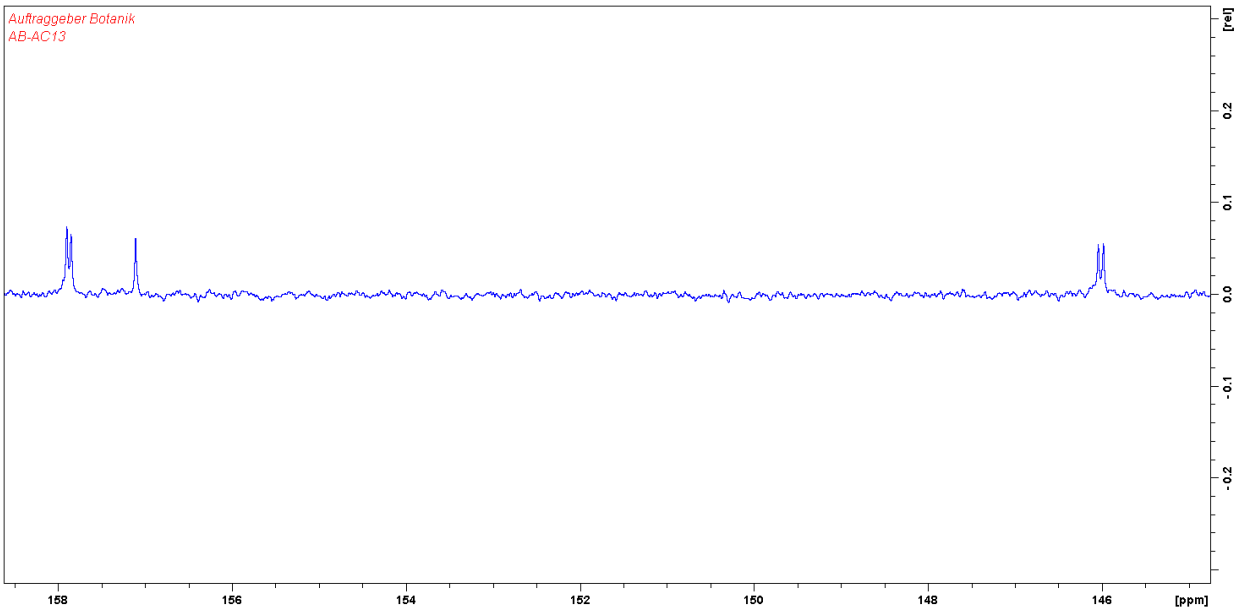

Figure 207. Section of ^{13}C-NMR Spectrum of isolated epicatechin-3-hydroxy-2-methyl-propanoate (**6**) in CD_3OD (600.13 MHz).

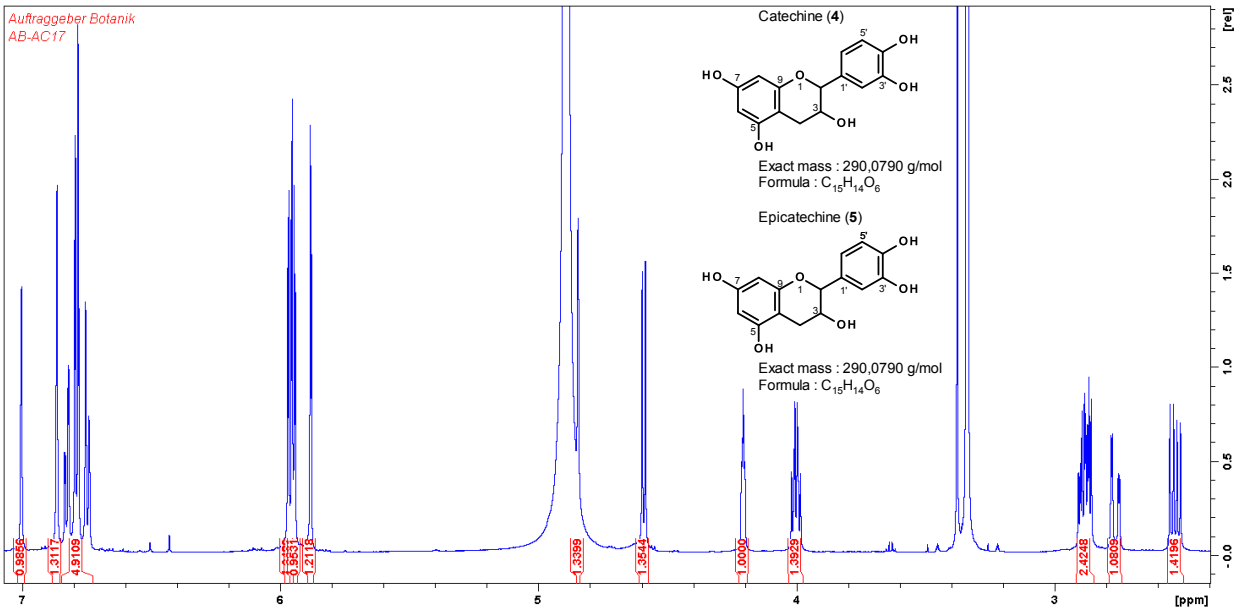

Figure 208. ^{1}H-NMR Spectrum of isolated catechin (**4**) and epicatechin (**5**) in CD_3OD (600.13 MHz).

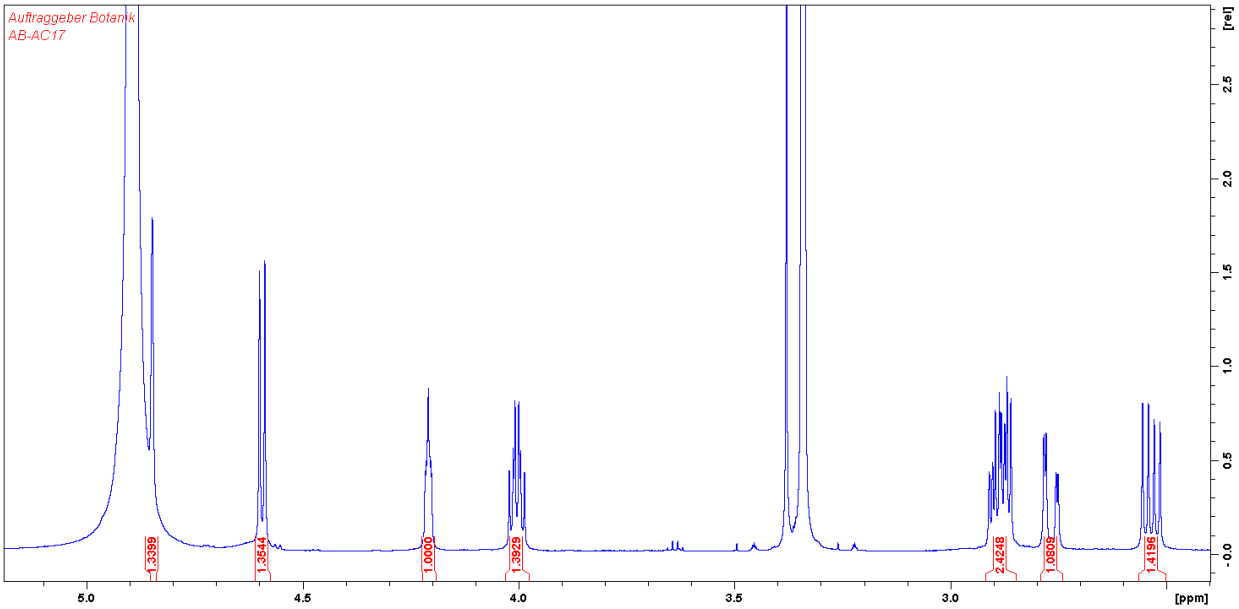

Figure 209. Section of ^{1}H-NMR Spectrum of isolated catechin (**4**) and epicatechin (**5**) in CD_3OD (600.13 MHz).

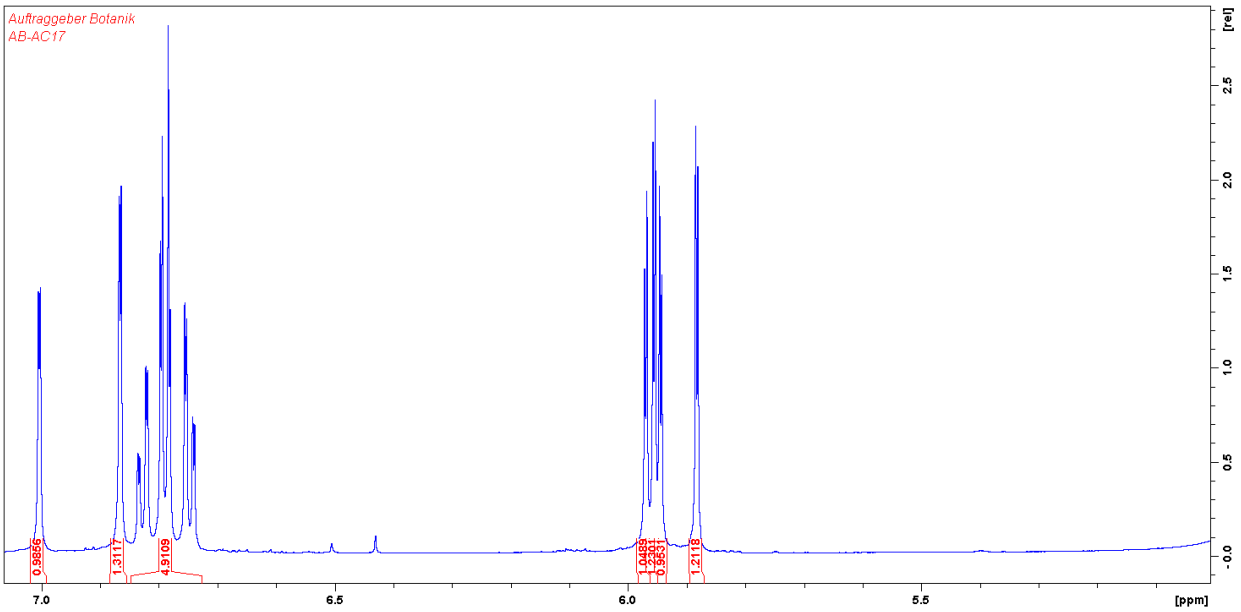

Figure 210. Section of ^{1}H-NMR Spectrum of isolated catechin (**4**) and epicatechin (**5**) in CD_3OD (600.13 MHz).

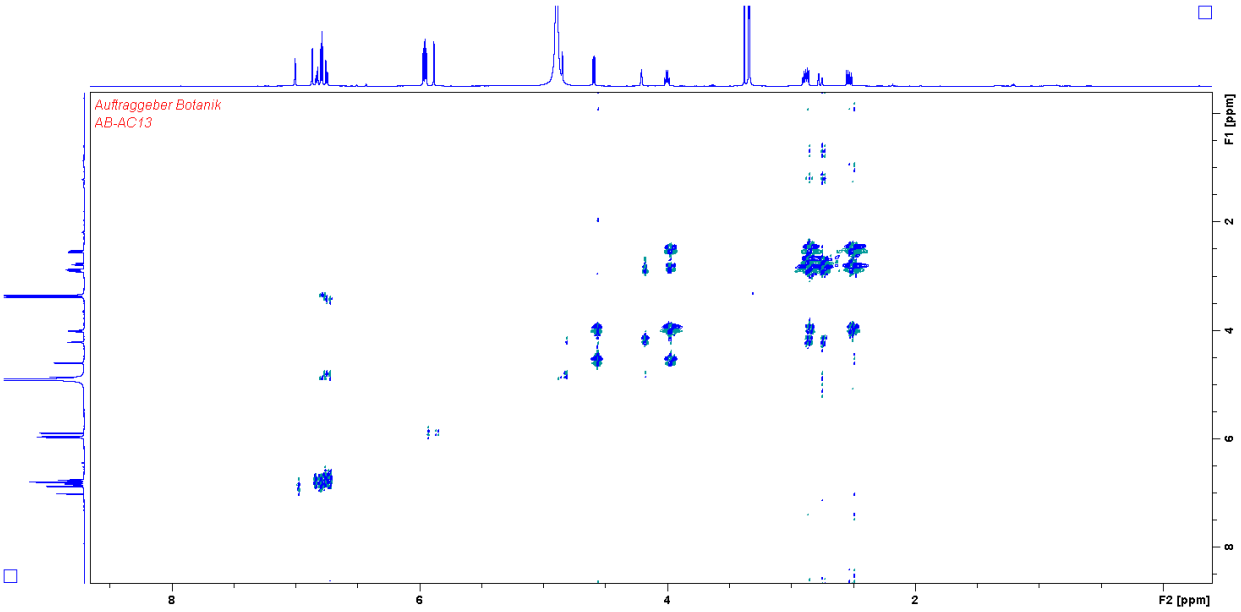

Figure 211. ^{1}H-^{1}H COSY NMR Spectrum of isolated catechin (**4**) and epicatechin (**5**) in CD_3OD (600.13 MHz).

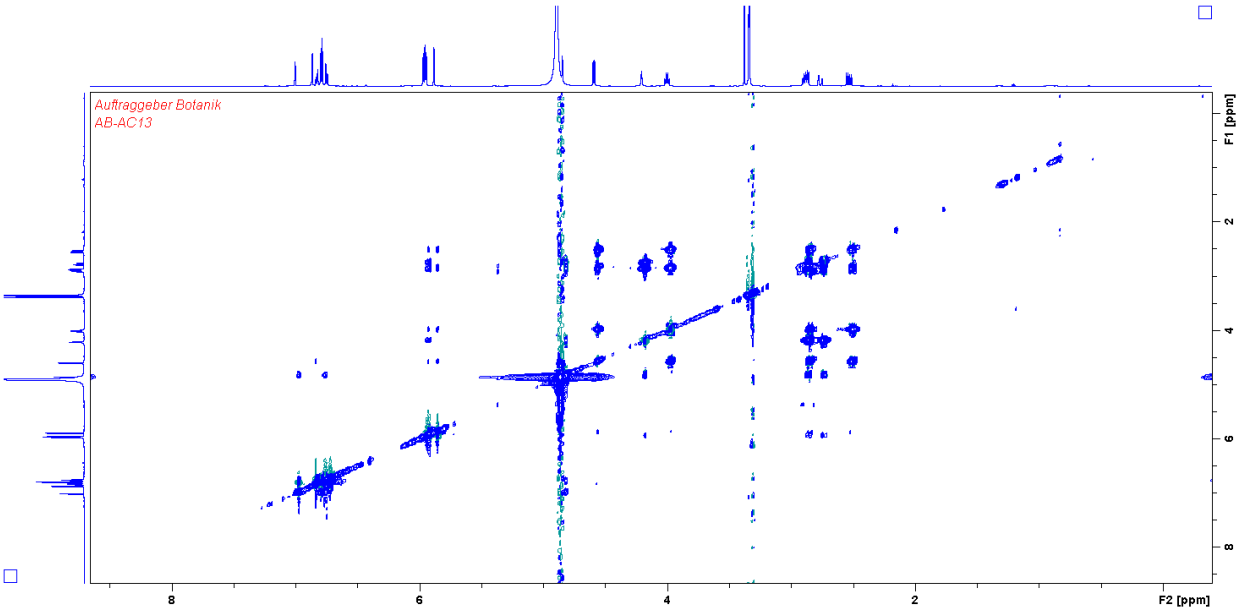

Figure 212. ^{1}H-^{1}H TOCSY NMR Spectrum of isolated catechin (**4**) and epicatechin (**5**) in CD_3OD (600.13 MHz).

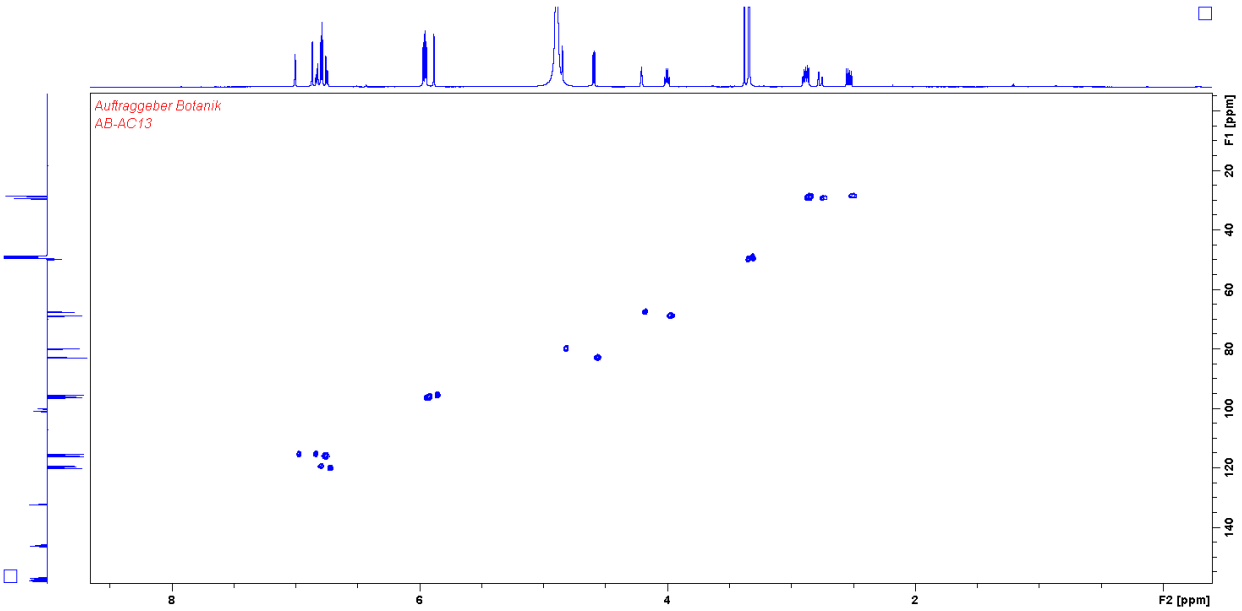

Figure 213. ^{1}H-^{13}C HSQC NMR Spectrum of isolated catechin (**4**) and epicatechin (**5**) in CD_3OD (600.13 MHz).

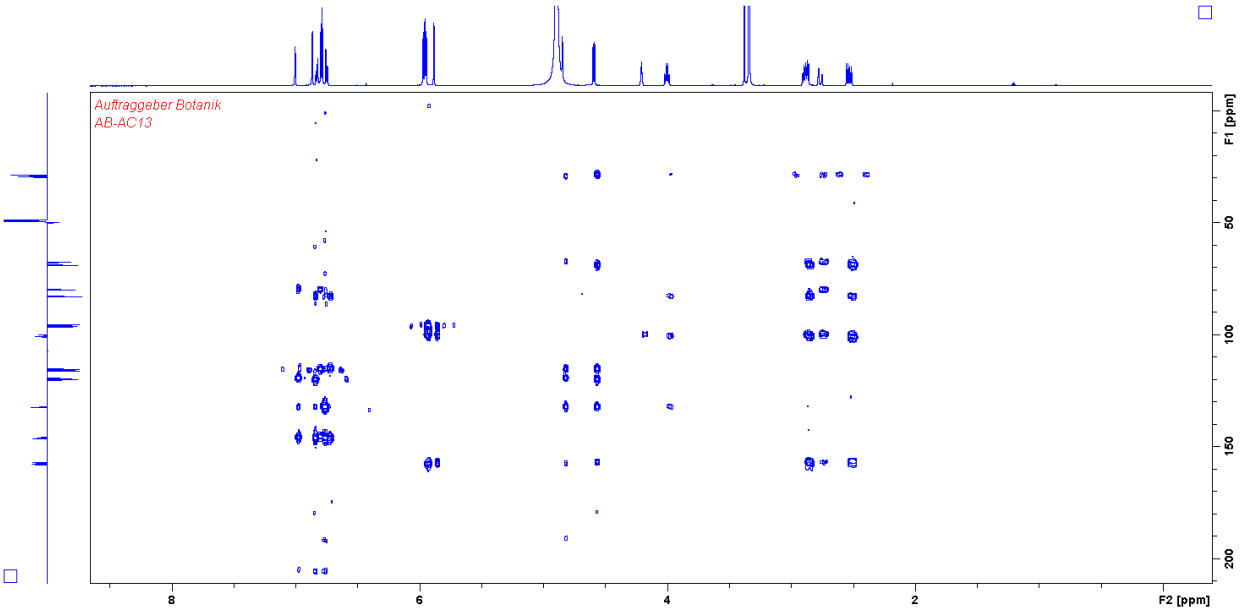

Figure 214. ^{1}H-^{13}C HMBC NMR Spectrum of isolated catechin (**4**) and epicatechin (**5**) in CD_3OD (600.13 MHz).

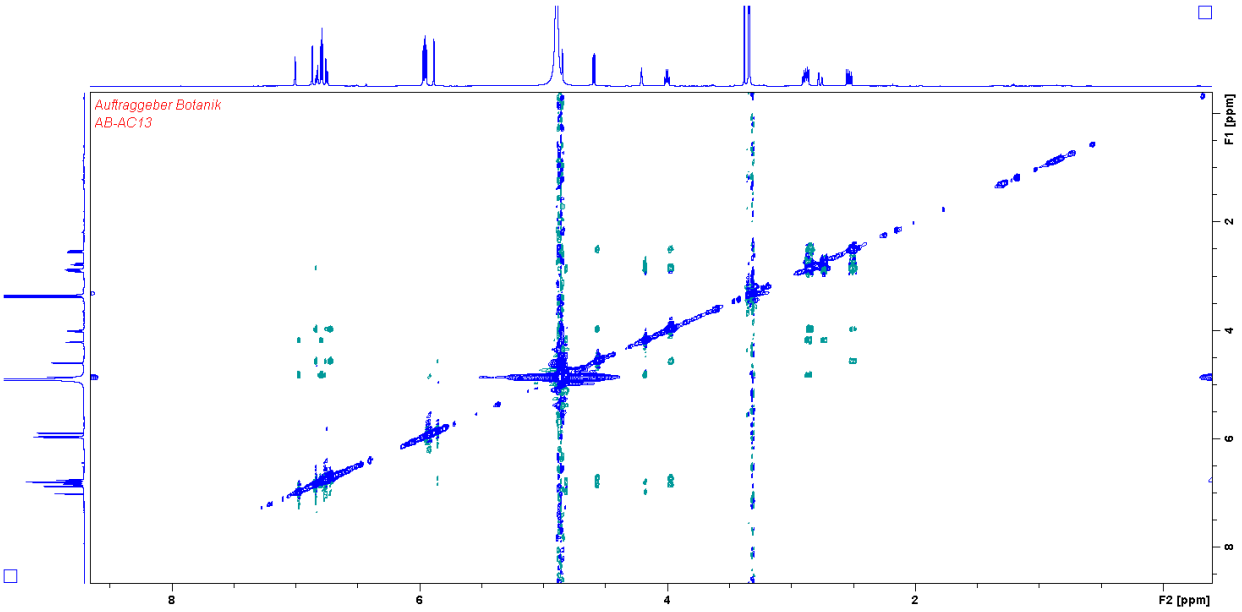

Figure 215. ^{1}H-^{1}H NOESY NMR Spectrum of isolated catechin (**4**) and epicatechin (**5**) in CD_3OD (600.13 MHz).

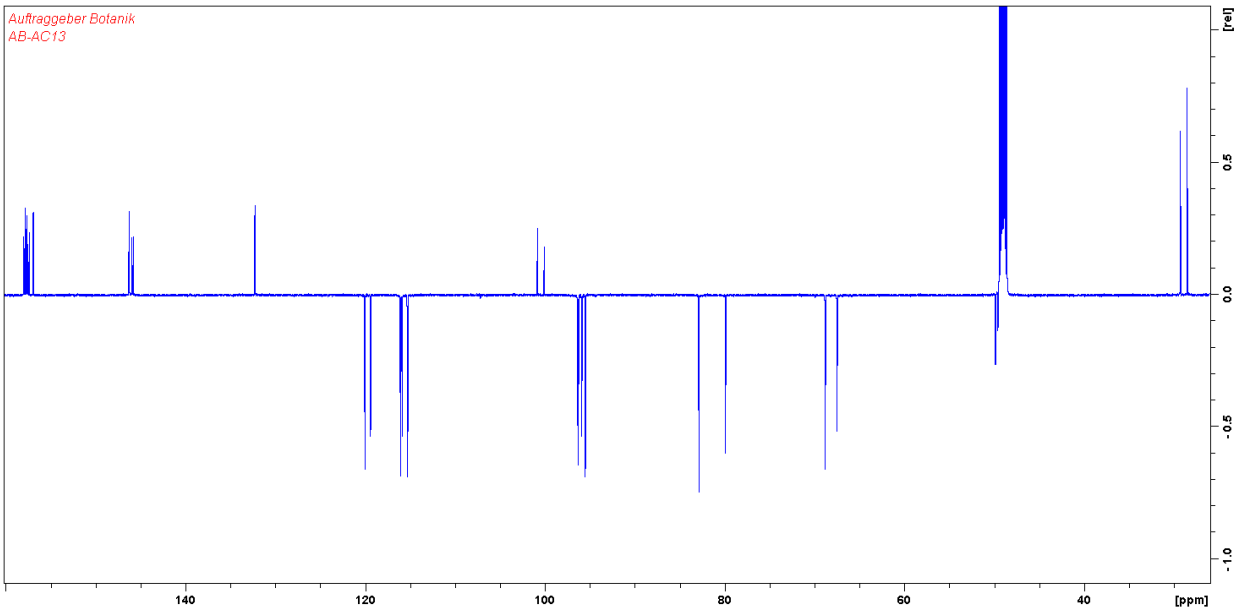

Figure 216. ^{13}C-NMR Spectrum of isolated catechin (**4**) and epicatechin (**5**) in CD_3OD (600.13 MHz).

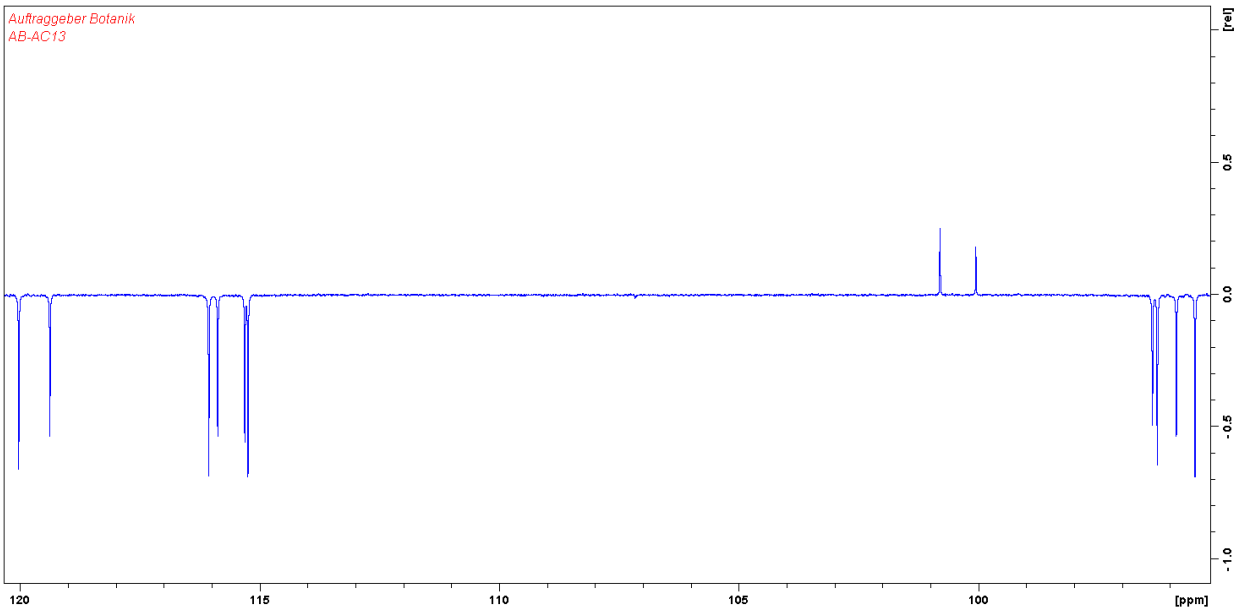

Figure 217. Section of ^{13}C-NMR Spectrum of isolated catechin (**4**) and epicatechin (**5**) in CD_3OD (600.13 MHz).

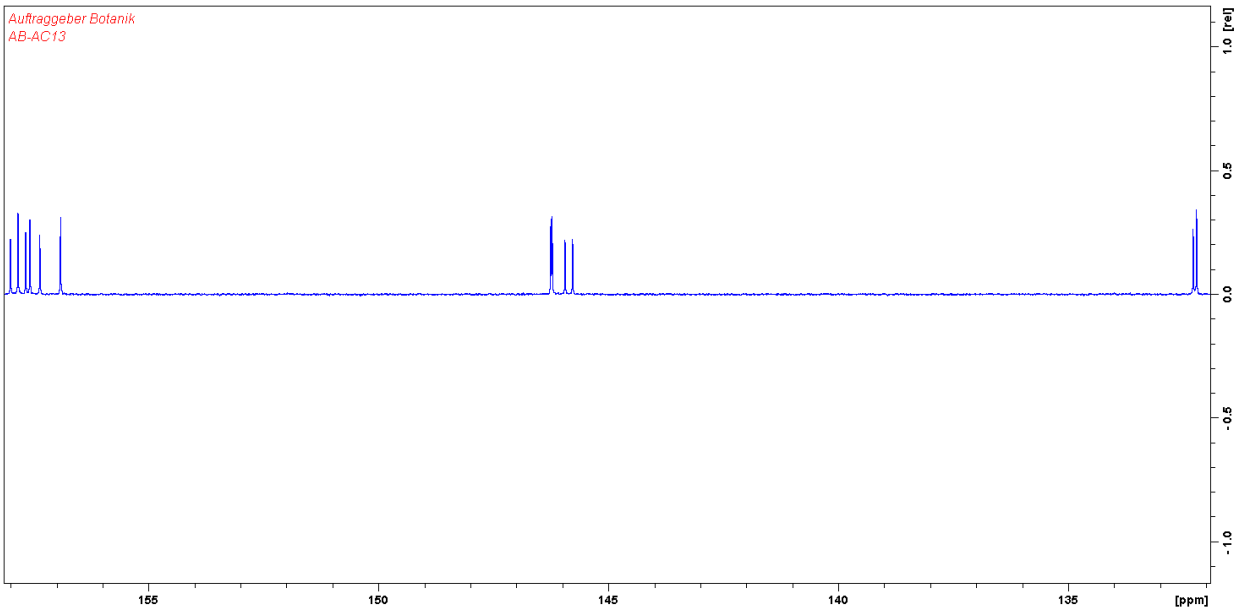

Figure 218. Section of ^{13}C-NMR Spectrum of isolated catechin (**4**) and epicatechin (**5**) in CD_3OD (600.13 MHz).

V. Conclusion

The results indicate that the metabolite composition of the investigated species differ greatly from each other. This is likely attributed for by the different evolutionary lineages of the species and their variation in natural habitat with resulting characteristic adaptations. A distinct metabolome can be seen for each different tissue type within a species.

For all species the difference in the metabolic composition between tissue types seem to increase with age. This is likely attributed by tissue differentiation and development.

For *A. crenata* and *P. kirkii* the difference in the metabolic composition between nodulated and non-nodulated tissue types seem to increase with age. This effect seems to be stronger pronounced in *A. crenata* compared to *P. kirkii*. For *A. crenata* an additional stage of leaf development was included in the experiment, interestingly the metabolome of these very old tissues seems to be almost identical to the old tissue types. These results indicate that the bacterial endosymbionts start producing secondary metabolites early on in leaf development, but the full capacity of secondary metabolite production is only reached later on in leaf development. For *A crenata* it can also be seen that at a certain stage of leaf development of the secondary metabolome seems to be established and persists probably until leaf senescence.

For *D. bulbifera* the results show a clear difference in the metabolic composition between leaf acumen and leaf lamina tissue types and smaller differences between the leaf lamina tissue types at different leaf developmental stages. Interestingly the metabolome of the leaf acumen tissue types at different leaf developmental stages seem to be almost identical to each other. This indicates that while the leaf lamina tissues seem to differentiate and develop with age, this process probably happens very early on in the development of the leaf acumen tissue. This could be since the leaf acumen is already present at a very early stage of leaf development and the present extrafloral nectaries already start secreting before the main leaf is even present.

Within this experiment 17 compounds could be annotated at various levels of confidence. Caffeoylquinic acid, catechin, epicatechin, naringenin and quercetin-3-glucoside were annotated based on the targeted matching of the in-house developed software mzFun using a database of locally measured standard compounds. These results were confirmed by manual reevaluation of the MS spectra and comparison with an external database (mzCloud). Catechin, epicatechin and epicatechin-3-hydroxy-2-methyl-propanoate could later be isolated from *A. crenata* leaves and their structure was elucidated by NMR (see: Isolation of natural products from nodulated *Ardisia crenata* Sims (Primulaceae) leaf tissue, 7.2. Appendix B: NMR data of the isolated natural products, Table 7, Table 8 and Table 9; 7.3. Appendix C: NMR spectra of the isolated natural products, Figure 51, Figure 52, Figure 53, Figure 54, Figure 55, Figure 56, Figure 57, Figure 58, Figure 59, Figure 60, Figure 61, Figure 62, Figure 63, Figure 64, Figure 65, Figure 66, Figure 67, Figure 68, Figure 69, Figure 70 and Figure 71). Glutathione and glutathione disulfide were confirmed by manual reevaluation of the MS spectra and comparison with an external database (mzCloud). The compounds annotated as cyclic-depsipeptides and pavettamine were confirmed by manual reevaluation of the MS spectra unfortunately comparison with an external database wasn't possible due to the lack of MS spectra measured with similar MS settings.

For *A. crenata* the compounds annotated as cyclic-depsipeptides seem to be characteristic for developed nodulated tissue while catechin and epicatechin seem to be characteristic for developed non-nodulated tissue. The compounds annotated as epicatechin-3-hydroxy-2-methyl-propanoate, glutathione and quercetin-3-glucoside seem to be characteristic for tissues still in development. Interestingly a *m/z* feature annotated as quercetin-3-glucoside also seems to be characteristic for the developed nodulated tissues.

This could indicate that the cyclic-depsipeptides are either produced at a high rate within the developed nodules and/or lack a transporter or diffuse slowly through the leaf tissue. Glutathione within the developing tissue could be responsible for coping with oxidative stress while epicatechin-3-hydroxy-2-methyl-propanoate might be a signaling-compound for the interaction between plant and bacteria.

For *D. bulbifera* the compounds annotated as catechin, glutathione, glutathione disulfide and one of the *m/z* features annotated as naringenin seem to be characteristic for the leaf acumen tissue types, while the compounds annotated as caffeoylquinic acid, one of the *m/z* features annotated as naringenin and quercetin-3-glucoside seem to be characteristic for the leaf lamina tissue types. This could indicate that the bacterial endosymbionts require glutathione to cope with increased oxidative stress within the leaf or that glutathione and glutathione disulfide are enriched by the increased number of bacterial cells within the tissue. The flavonoids present might be used for signaling between plant and bacteria.

For *P. kirkii* the compound annotated as glutathione disulfide seems to be characteristic for the old nodulated tissue, while the compounds annotated as caffeoylquinic acid, glutathione, pavettamine and quercetin-3-glucoside seem to be characteristic for the old non-nodulated tissue. This could indicate that the bacterial endosymbionts cope with increased oxidative stress within the developed leaf by oxidation of glutathione, while pavettamine either diffuses or is transported from the nodulated tissue into the surrounding non-nodulated tissue.
Since the full capacity of secondary metabolite production by the bacterial endosymbionts is only reached at a later developmental stage it would be interesting if the potency of the produced substances is high enough to already deter herbivory at the lower concentrations found in younger leaves or if at this stage other compounds can be found that fulfill a similar role.
It seems that leaf-nodulated plants contain a vast amount of different secondary metabolites within their endosymbiont harboring glands. Most of these substances are probably not yet characterized. Natural product isolation and structure elucidation by NMR could help to further increase the insight into this kind of symbiosis. Especially the potential secondary metabolites produced by the bacteria through the PKS pathway could be a potential target for further research.
Although 17 compounds could be annotated within this experiment still thousands of unknowns remain. It is likely that some of these *m/z* features were already characterized and are present in other databases. Therefore, even more compounds could probably be annotated by using these resources. Although other databases for secondary metabolites are established the lack of a universal LC-MS based metabolomics protocol still remains as great bottleneck for the technique. This indicates that although steadily improving there is still great room for improvement for secondary metabolite analysis using LC-MS techniques coupled with statistical analysis and database matching. Especially the need for laborious and expensive manual reevaluation of the generated data should be reduced by method improvements to make the technique more accurate, reliable and accessible.
A new putative depsipeptide candidate was successfully isolated, as well as the already described natural product FR900359. UV spectra of the cyclic-depsipeptide FR900359 and the novel depsipeptide candidate were obtained. Unfortunately, the amount of FR900359 isolated was not sufficient for NMR analysis. NMR analysis of the novel depsipeptide revealed that the natural product seemed to have degraded after prolonged storage, therefore, further isolation attempts need to be undertaken. SEC proved to be successful in enriching and separating the target compounds from the matrix. During the solvent separation procedure of the crude extract care should be taken to do a complete extraction i.e. extracting 3 times with enough volume of each solvent to ensure good separation of the target compounds. Besides that, 3 natural products were isolated, and their structure elucidated by NMR. This yielded the novel natural product epicatechin-3-hydroxy-2-methyl-propanoate, as well as the previously described natural products catechin and epicatechin.
The improved liquid/liquid extraction method successfully enriches the target compounds in a singular phase, while also removing carotenoids, chlorophylls, glycosides and sugars. This method should therefore be used in further isolation attempts of cyclic-depsipeptides and their deriatives from *A. crenata* extracts. It can also be used in further isolation of flavonoids, peptides and proteins.
The isolated compounds epicatechin-3-hydroxy-2-methyl-propanoate, catechin and epicatechin are secondary plant metabolites that belong to the class of flavonoids, which have a C_3-C_6-C_3 diphenylpropane skeleton. This is thought to be a major factor responsible for their displayed health benefits (Rice-Evans et al., 1996). Research regarding flavonoids on their positive effect on human physiology is being conducted with an emphasis on foodstuffs. Catechins are well known for their antioxidant, anticarcinogenic and anti-inflammatory activity (Scalia et al., 2013). Many plant derived foods e.g. apples, grapes, cacao, guaraná and green tea contain (+)-catechin and (-)-epicatechin (Kofink et al., 2007). *Ardisia compressa*, leaves which are used to prepare a herbal tea in folk medicine were also found to contain (+)-catechin and (-)-epicatechin (Ramırez-Mares et al., 1999). Bactericidal activity of tea catechins and their derivates against human pathogenic bacteria like, *Pleisomonas shigelloides*, *Staphylococcus aureus*, *Vibrio cholerae* and *Vibrio parahaemolyticus* has been observed. It is therefore plausible that catechins protect against pathogenic bacterial infections of the plant as well (Toda et al., 1989; Toda et al., 1992). Besides its toxicity, growth favoring effects of catechin on *Bacillus subtilis* up to a concentration of 4 ppm and on *Escherichia coli* up to 5 ppm were also observed. Only higher concentrations showed a growth inhibitory effect (Fathima and Rao, 2016). *Burkholderia* is a rapidly expanding genus within the group of gram-negative non-fermenting

bacteria. Up to now around 80 species have been described. They occur worldwide in very different environments. Some of them are living in soil or in planktonic form in freshwater but most of them are living in symbiosis with a host (Depoorter et al., 2016). The species *Burkholderia oxyphila* sp. nov., which was isolated from acidic forest soil was found to be able to catabolize (+)-catechin and putative aromatic (+)-catechin derivatives (Otsuka et al., 2011). Although *B. oxyphila* sp. nov. lives in a very different environment than *Candidatus B. crenata*, it could be possible that the enzymatic repertory is similar because of ancestry, and *Candidatus B. crenata* is also able to use catechin derivates as substrate. Since *Candidatus B. crenata* cannot be cultivated, physiological tests are limited. Maybe work on the already sequenced genome of *Candidatus B. crenata* by Carlier et al. (2016) can lead to information regarding the capability of the organism of degrading catechin derivates. However, it could also be, that these isolated catechin derivates do not influence the leaf nodule symbiosis. This should be assessed by further research.

VI. Acknowledgments

This section is dedicated to the people who made this thesis possible.
I want to thank my principal investigator Wolfram Weckwerth for the opportunity to participate in this area of research and for his excellent advise and supervision.
Special thanks to Lena Fragner for her additional supervision and mentorship.
Further I want to thank Gert Bachmann, Anke Bellaire, Andreas Berger, Lothar Brecker, Martin Brenner, Ferdinand Hartmann, Johannes Herpell, Johann Schinnerl, Xiaoliang Sun, Sonja Tischler, and Karin Vetschera for their additional support.
I want to thank my parents and my grandfather for their moral and financial support, without their effort my studies would not have been possible.
Finally, I want to thank my friends for their moral support.

VII. References

Becking, J., 1971. The physiological significance of the leaf nodules of Psychotria. Plant and soil 35, 361-374.

Berger, A., Tanuhadi, E., Brecker, L., Schinnerl, J., Valant-Vetschera, K., 2017. Chemodiversity of tryptamine-derived alkaloids in six Costa Rican Palicourea species (Rubiaceae–Palicoureeae). Phytochemistry 143, 124-131.

Carlier, A., Fehr, L., Pinto-Carbó, M., Schäberle, T., Reher, R., Dessein, S., König, G., Eberl, L., 2016. The genome analysis of Candidatus Burkholderia crenata reveals that secondary metabolism may be a key function of the Ardisia crenata leaf nodule symbiosis. Environmental microbiology.

Carlier, A. L., Eberl, L., 2012. The eroded genome of a Psychotria leaf symbiont: hypotheses about lifestyle and interactions with its plant host. Environmental microbiology 14, 2757-2769.

Cases, I., de Lorenzo, V., Ouzounis, C. A., 2003. Transcription regulation and environmental adaptation in bacteria. Trends in microbiology 11, 248-253.

Challinor, V. L., Bode, H. B., 2015. Bioactive natural products from novel microbial sources. Annals of the New York Academy of Sciences 1354, 82-97.

Crüsemann, M., Reher, R., Schamari, I., Brachmann, A. O., Ohbayashi, T., Kuschak, M., Malfacini, D., Seidinger, A., Pinto-Carbó, M., Richarz, R., 2018. Heterologous Expression, Biosynthetic Studies, and Ecological Function of the Selective Gq-Signaling Inhibitor FR900359. Angewandte Chemie International Edition 57, 836-840.

Davis, A. L., Cai, Y., Davies, A. P., Lewis, J., 1996. 1H and 13C NMR assignments of some green tea polyphenols. Magnetic resonance in Chemistry 34, 887-890.

Depoorter, E., Bull, M. J., Peeters, C., Coenye, T., Vandamme, P., Mahenthiralingam, E., 2016. Burkholderia: an update on taxonomy and biotechnological potential as antibiotic producers. Applied microbiology and biotechnology 100, 5215-5229.

El-Razek, M. A., 2007. NMR assignments of four catechin epimers. Asian Journal of Chemistry 19, 4867.

Fathima, A., Rao, J. R., 2016. Selective toxicity of Catechin—a natural flavonoid towards bacteria. Applied microbiology and biotechnology 100, 6395-6402.

Fujioka, M., Koda, S., Morimoto, Y., Biemann, K., 1988. Structure of FR900359, a cyclic depsipeptide from Ardisia crenata sims. The Journal Of Organic Chemistry 53, 2820-2825.

HORNER JR, H. T., LERSTEN, N. R., 1972. Nomenclature of bacteria in leaf nodules of the families Myrsinaceae and Rubiaceae. International Journal of Systematic and Evolutionary Microbiology 22, 117-122.

Karplus, M., 1959. Contact electron-spin coupling of nuclear magnetic moments. The Journal of chemical physics 30, 11-15.

Kitajima, K., Fox, A. M., Sato, T., Nagamatsu, D., 2006. Cultivar selection prior to introduction may increase invasiveness: evidence from Ardisia crenata. Biological Invasions 8, 1471.

Kobayashi, H., de Mejía, E., 2005. The genus Ardisia: a novel source of health-promoting compounds and phytopharmaceuticals. Journal of Ethnopharmacology 96, 347-354.

Kofink, M., Papagiannopoulos, M., Galensa, R., 2007. Enantioseparation of catechin and epicatechin in plant food by chiral capillary electrophoresis. European Food Research and Technology 225, 569-577.

Li, Y., Gan, L., Li, Y., Deng, L., 2015. The HPLC–MS/MS Method for Determination of Diosbulbin B in the Plasma of Rats Administered with Rhizoma Dioscoreae Bulbiferae Combinations: Application to Comparative Pharmacokinetic Study. Journal of Liquid Chromatography & Related Technologies 38, 847-854.

Link, A., Müller, C. E., 2016. G-Protein-Coupled Receptors: Sustained Signaling via Intracellular Megaplexes and Pathway-Specific Drugs. Angewandte Chemie International Edition 55, 15962-15964.

Ludwig-Müller, J., 2015. Plants and endophytes: equal partners in secondary metabolite production? Biotechnology letters 37, 1325-1334.

Miller, I., Donnelly, A., 1987. Location and distribution of symbiotic bacteria during floral development in Ardisia crispa. Plant, Cell & Environment 10, 715-724.

Miller, I., Reporter, M., 1987. Bacterial leaf symbiosis in Dioscorea sansibarensis: morphology and ultrastructure of the acuminate leaf glands. Plant, Cell & Environment 10, 413-424.

Neuwinger, H. D., 2004. Plants used for poison fishing in tropical Africa. Toxicon 44, 417-430.

Nishimura, A., Kitano, K., Takasaki, J., Taniguchi, M., Mizuno, N., Tago, K., Hakoshima, T., Itoh, H., 2010. Structural basis for the specific inhibition of heterotrimeric Gq protein by a small molecule. Proceedings of the National Academy of Sciences 107, 13666-13671.

Ogbuagu, M., 2008. Nutritive and antinutritive composition of the wild (in-edible) species of Dioscorea bulbifera (Potato Yam) and Dioscorea dumentorum (Bitter Yam). J Food Technol 6, 224-226.

Otsuka, Y., Muramatsu, Y., Nakagawa, Y., Matsuda, M., Nakamura, M., Murata, H., 2011. Burkholderia oxyphila sp. nov., a bacterium isolated from acidic forest soil that catabolizes (+)-catechin and its putative aromatic derivatives. International Journal of Systematic and Evolutionary Microbiology 61, 249-254.

Paizs, B., Suhai, S., 2005. Fragmentation pathways of protonated peptides. Mass spectrometry reviews 24, 508-548.
Pinto-Carbó, M., Gademann, K., Eberl, L., Carlier, A., 2018. Leaf nodule symbiosis: function and transmission of obligate bacterial endophytes. Current opinion in plant biology 44, 23-31.
Ramırez-Mares, M., Fatell, S., Villa-Trevino, S., de Mejı´a, E. G., 1999. Protection of extract from leaves of Ardisia compressa against benomyl-induced cytotoxicity and genotoxicity in cultured rat hepatocytes. Toxicology in vitro 13, 889-896.
Reher, R., Kuschak, M., Heycke, N., Annala, S., Kehraus, S., Dai, H.-F., Müller, C. E., Kostenis, E., König, G. M., Crüsemann, M., 2018. Applying Molecular Networking for the Detection of Natural Sources and Analogues of the Selective Gq Protein Inhibitor FR900359. Journal of natural products 81, 1628-1635.
Rice-Evans, C. A., Miller, N. J., Paganga, G., 1996. Structure-antioxidant activity relationships of flavonoids and phenolic acids. Free radical biology and medicine 20, 933-956.
Scalia, S., Marchetti, N., Bianchi, A., 2013. Comparative evaluation of different co-antioxidants on the photochemical-and functional-stability of epigallocatechin-3-gallate in topical creams exposed to simulated sunlight. Molecules 18, 574-587.
Schrage, R., Schmitz, A.-L., Gaffal, E., Annala, S., Kehraus, S., Wenzel, D., Büllesbach, K. M., Bald, T., Inoue, A., Shinjo, Y., 2015. The experimental power of FR900359 to study Gq-regulated biological processes. Nature communications 6, 10156.
Sieber, S., Carlier, A., Neuburger, M., Grabenweger, G., Eberl, L., Gademann, K., 2015. Isolation and total synthesis of kirkamide, an aminocyclitol from an obligate leaf nodule symbiont. Angewandte Chemie International Edition 54, 7968-7970.
Silver, W., Centifanto, Y. M., Nicholas, D., 1963. Nitrogen fixation by the leaf-nodule endophyte of Psychotria bacteriophila. Nature 199, 396.
Toda, M., Okubo, S., Hiyoshi, R., Shimamura, T., 1989. The bactericidal activity of tea and coffee. Letters in applied microbiology 8, 123-125.
Toda, M., Okubo, S., Ikigai, H., Suzuki, T., Suzuki, Y., Hara, Y., Shimamura, T., 1992. The protective activity of tea catechins against experimental infection by Vibrio cholerae O1. Microbiology and immunology 36, 999-1001.
Van Elst, D., Nuyens, S., Van Wyk, B., Verstraete, B., Dessein, S., Prinsen, E., 2013. Distribution of the cardiotoxin pavettamine in the coffee family (Rubiaceae) and its significance for gousiekte, a fatal poisoning of ruminants. Plant physiology and biochemistry 67, 15-19.
Yang, C.-J., Hu, J.-M., 2018. Bacterial Leaf Nodule Symbiosis in Flowering Plants. Symbiosis. IntechOpen.

VIII.Table of figures